UNIVERSITÀ DEGLI STUDI DI TRIESTE

XXXIII CICLO DEL DOTTORATO DI RICERCA IN

SCIENZE DELLA TERRA, FLUIDODINAMICA E MATEMATICA. INTERAZIONI E METODICHE

PO FRIULI VENEZIA GIULIA - FONDO SOCIALE EUROPEO 2014/2020

GRAVIMETRY FOR MONITORING WATER MASS MOVEMENTS IN KARSTIC AREAS

Disciplinary Sector: **GEO/10**
GEOFISICA DELLA TERRA SOLIDA

PhD candidate:
TOMMASO PIVETTA FERRUCCIO, MARIA

Coordinator of the PhD program:
PROF. STEFANO MASET

Supervisor:
PROF. CARLA BRAITENBERG

Co-supervisor:
PROF. FRANCI GABROVŠEK

ACADEMIC YEAR 2019/2020

Contents

Abstract

Karst aquifers represent a significant source of drinkable water for about a quarter of the world's population. The water circulation in this environment occurs mostly underground and it is controlled by alternation of small conduits and large voids present in the rock massif. Such intricate void distribution combined with an irregular recharge provided by the rain results in fast and complex water flows with temporary accumulation of huge water volumes in the voids. The knowledge of the dynamics of such system is usually limited to the areas where a direct access to the vadose zone through speleological exploration is possible. Given the importance of such aquifers and their intrinsic vulnerability it is important to have a detailed picture of the water dynamics and of the underground water paths.

Gravimetry offers a valid complement to classical hydrologic measurements in order to characterize such systems and monitor the recharge process.

In this contribution, I show an innovative integration of continuous gravimetric observations and hydrologic data to constrain a hydrodynamic model of the Škocjan cave system (Slovenia). The Škocjan caves hydrology is mostly governed by the allogenic contribution of the Reka River, which during flood event causes the accumulation of large volumes of water in the cave system for few hours. In July 2018 I installed a continuous recording gravimeter nearby the cave system which allowed the detection of several gravity transients related to the local hydrologic contribution.

Gravity observations are sensitive to several other contributions apart the hydrology, such as Earth and marine tides, atmospheric mass redistribution, large scale water mass variations in oceans and seas. All these phenomena superpose their effects and should be carefully evaluated and removed before unveiling the contributions related to the local hydrology. Before discussing the hydrologic related gravity signals, this thesis illustrates the efforts in modelling and removing all gravity contributions linked to these other phenomena. The study area is close to the Adriatic Sea, hence global models of tidal and non-tidal gravity effects could be inadequate for the correction. I show and prove that tidal models are sufficiently accurate to remove the main marine tidal influence while a dedicated correction of the non-tidal component is required. This was fulfilled by including the modelling of the gravity variations due to a 4D mass model of the non-tidal ocean component constrained by tide gauge observations. The final gravity residuals, obtained after reducing the observations for all the non-hydrologic contributions, revealed several large residuals correlated to the Reka flooding; such transients lasted for several hours (up to 1 day) with amplitudes ranging from 10 nm/s^2 up to several hundreds of nm/s^2. I focused my analysis on a particular flood event occurred in February 2019 that caused water level variations of more than 90 m inside the Škocjan caves and gravity variations exceeding 400 nm/s^2. The gravity transient was then employed together with hydrologic data to constrain a hydraulic model of the cave system which approximated the cavity through a series of interconnected conduits with rectangular

cross-section. I fitted both hydrologic and gravimetric observations obtaining a 4D model of the water mass variations in the cave system.

I estimated that more than 3 10^6 m^3 of water were temporary accumulated during the peak's flood and lasted for about 6 hours.

I demonstrated how the inclusion of gravity observations improves water mass budget estimates for this cave system, which previously were based relying only on hydrological observations. In addition to this the hydraulic model shed new lights into the complex hydrodynamics of this karstic system in particular unveiling the critical role of the conduit system downstream Škocjan in regulating the water storage variations in the cave system.

Finally, the Škocjan cave gravity observations and the modelling allowed to draw some general conclusions about the detectability of water storage variations in karst through gravimetry. I assessed the noise level of the Škocjan gravity station which is about 10 nm/s^2 in the diurnal spectral band and which can be taken as representative of the noise level of a typical spring based gravimeter. Relying on realistic water level variations I estimated the expected gravity signals on surface due to temporary water accumulation in other caves of the Classical Karst. For all the considered caves the gravity signal is well above the noise threshold, suggesting that a remote monitoring of the storage variations is feasible. In the final discussion I also considered the effect of other geophysical phenomena superposing in the same frequency band of the hydrology and the uncertainties due to neglecting or underestimating such components.

Chapter 1
Introduction

1.1 Motivation

Karst areas on carbonates and evaporites occupy about 15 % of the ice-free continental areas: in Europe the surface reaches almost 22 % (Chen et al., 2017; Figure 1.1a-b). About one fourth of the world's and about one third of Europe's population is supplied by water from karst aquifers: in some regions, like the Dinaric region or in Southwest China, the karst water contributes up to the 50 % of the freshwater supply (Chen et al., 2017).

In karst aquifers most of the water is drained through networks of solution conduits, which evolve along sedimentary or tectonic discontinuities (Ford & Williams, 2007). The evolution of the conduit systems is controlled by complex mechanisms (Dreybrodt et al., 2005), which make the position of drainage pathways hard to predict. In active tectonic environments, the structure and boundary conditions for the evolution of conduit networks continuously change. This makes the conduit systems extremely non-homogenous with rapidly changing geometry, where cross-sections available for flow may change by orders of magnitude within short distances. Large voids with volumes in the order of 10^6 m^3 are common features in such settings. The positions of solution conduits and voids in karst aquifers are largely unknown, except for the parts accessible to direct human exploration. The combination of rapid changes in geometry with irregular recharge processes results into fast fluctuations of the underground level and temporary accumulation of huge water volumes in highly inhomogeneous storage units. Due to these characteristics karst aquifers are difficult to characterize and particularly vulnerable to human impacts.

To assess the structure and the hydrodynamics of karst aquifers, different geophysical and hydrological techniques are used, each of them being applicable to a specific situation. Among the various geophysical methods, gravimetry, which is sensitive to spatial and temporal mass variations, is particularly apt to both reconstruct the geometry of the underground drainage system and to monitor mass variations occurring in it due to the recharge process.

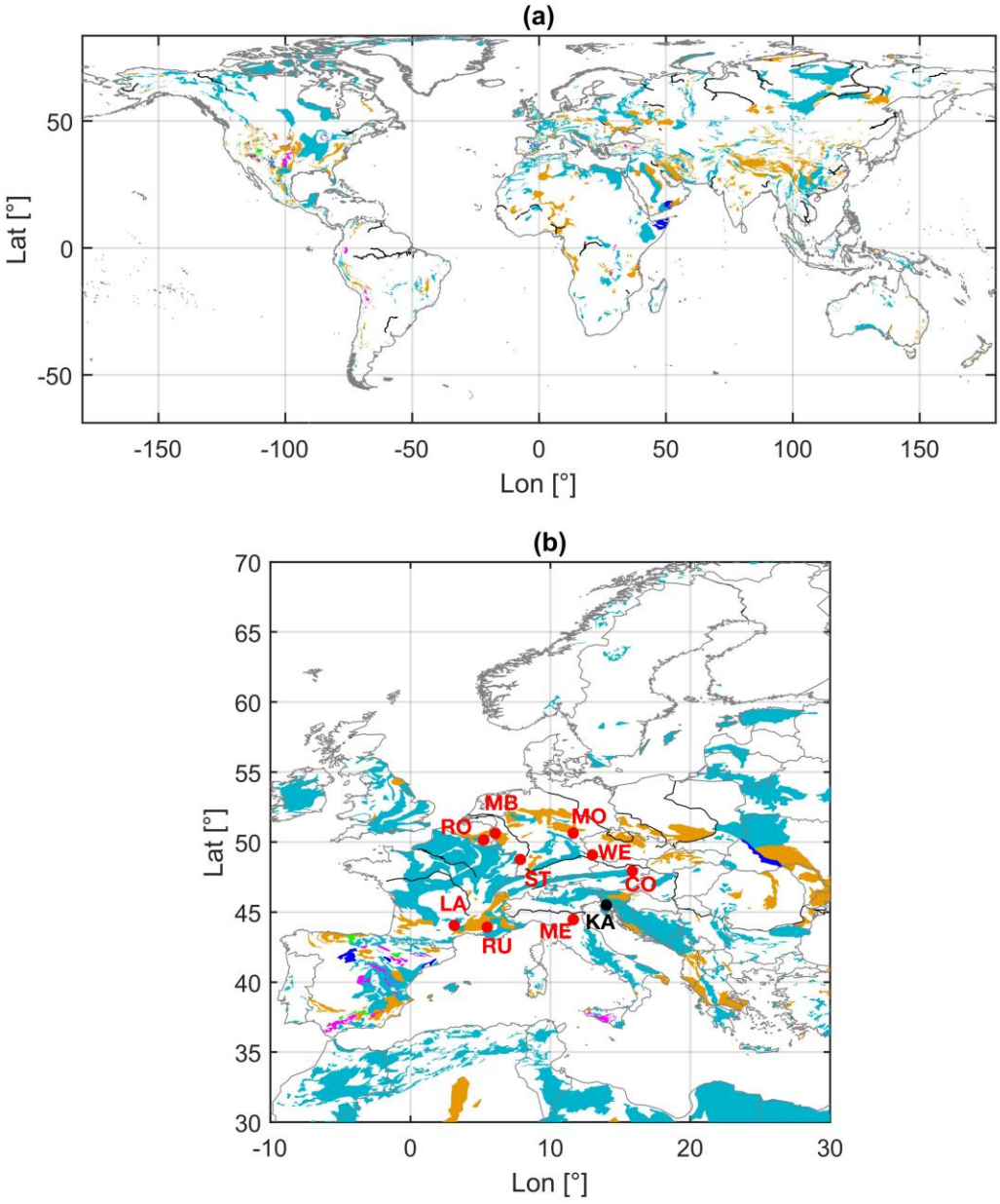

Figure 1.1 a) World map of the karst aquifers (outlines from Chen et al., 2017). Light blue: continuous carbonate rocks; orange: discontinuous carbonate rocks; purple: continuous evaporites; light green: discontinuous evaporites. Coastline and national boundaries reported in gray. Black: main rivers. b) Detail in the European area. Red dots locate continuous gravity stations, mostly Superconducting Gravimeters. LA=Larzac Plateau; RU=Rustrel; ST=Strasbourg; RO=Rochefort; MB=Membach; MO=Moxa; WE=Wettzell; CO=Conrad; ME=Medicina. Black dot KA=Classical Karst.

Recently, the advent of new and performing instruments such as the superconducting gravimeters (SG) and satellite measurements have raised new interest into this method for monitoring water mass movements (Van Camp et al., 2017). Gravity measurements have been successfully applied to study the groundwater flow in other karstic environments (see red dots in Figure 1.1b) as demonstrated by several studies (Fores et al., 2017; Jacob et al., 2010; Mouyen et al., 2019; Watlet et al., 2020) or to monitor the subsidence and underground mass redistribution in sinkhole prone areas (Kobe et al., 2019). Other studies utilized gravimetry to characterize water flow in porous media (Güntner et al., 2017) or to monitor fluids relevant for geothermal exploitation (Portier et al., 2018).

In this PhD thesis, I present a combined gravimetric-hydrological study from Kras/Carso aquifer, a classical karstic region between Italy and Slovenia (black dot in Figure 1.1b). Flood events are dominated by the highly variable allogenic recharge of the Reka River, which causes large water level and storage variations in the epiphreatic zone. The initial part of the Reka River underground flow is formed by the Škocjan Caves, where flow follows a large underground canyon with a total volume of more than 5 10^6 m^3 and water level variations exceeding 100 m. Hence, Škocjan Caves present an ideal site to evaluate the combined gravimetric-hydrological response to flood events, assessing the limits of the method. The focus of the study is on the short term hydrologic variability linked to fast water accumulation during important rain events which is a peculiar characteristic of this system and deserves particular attention.

In July 2018, a continuously recording gravimeter, a gPhone spring based gravimeter, was installed above the caves. Several flood events, including an extreme flood in February 2019, provided excellent gravimetric and hydrologic records.

This work presents the results of the gravity monitoring of the Škocjan caves, demonstrating how the inclusion of gravimetric observations improves the mass balance estimates of a system. I also provide a wider perspective on the feasibility of such an approach to study the structure of karst aquifers and groundwater therein, with a special reference to Classical Karst region.

1.2 Karst hydrogeology

Karst aquifers have distinct features which make them rather different from other types of aquifers (i.e. porous aquifers or fractured). The water circulation in this environment occurs mostly underground since the presence of soluble rocks usually prevents the development of a superficial drainage system as rivers. Inside the karst massif water principally follows a complex network of conduits and voids that were formed by dissolution and erosion on the rocks operated by weather agents. Diffuse fracturing and micropores of the rock massif are

further important types of permeability (Bonacci et al., 2006) able to transfer and store non negligible volumes of water in the system.

The recharge to the system can be provided by the aquifer itself (autogenic) or originating from nearby non karstic areas (allogenic): these two mechanisms can be regarded as end-members, while usually an aquifer shows a combination of these components. As we will see extensively the Škocjan area is mostly dominated by allogenic recharge but in other sectors of the Classical Karst the autogenic component becomes more relevant.

In karst aquifers, water infiltrates through fractures, holes or dolines (Goldscheider & Drew, 2014): allogenic water inputs usually infiltrate through large conduits and shafts while the autogenic component is more diffuse and exploits the subsurface network of fractures of the epikarst (i.e. the most superficial part of the karst massif, Figure 1.2). Such fracture network then usually convoys and concentrates the infiltrated waters into a more organized and hierarchic system of shafts and conduits.

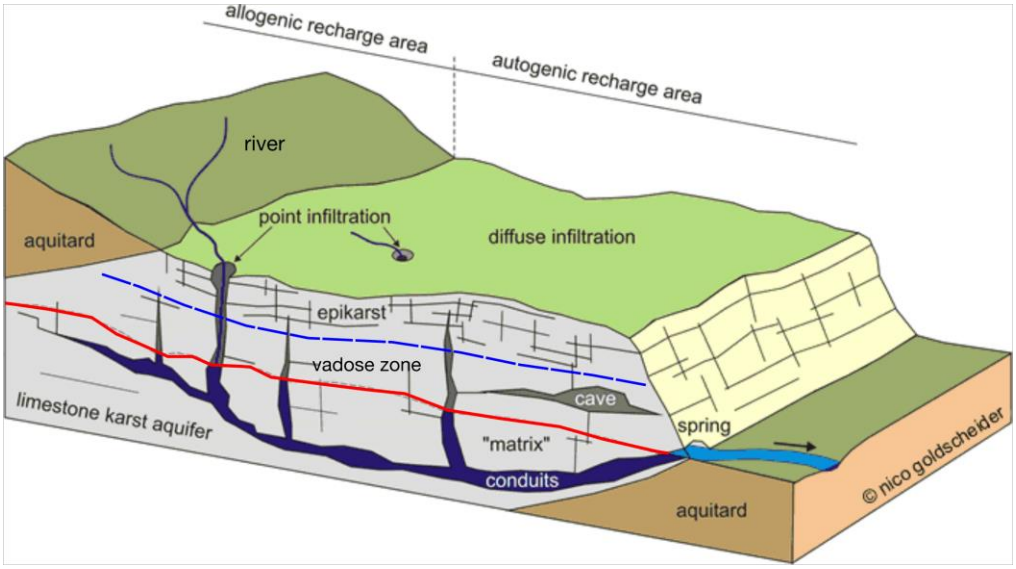

Figure 1.2: Sketch reporting an archetypal karst system (modified from Goldscheider & Drew, 2014)

A karst aquifer has an unsaturated (or vadose zone) which experiences temporary accumulation of water during meteoric events and a saturated zone, in which the conduits and matrix are permanently saturated also on dry conditions.

Due to its geometric structure and large variations in permeability a karstic aquifer shows quite impressive water volume variations during intense rains and very complex and non-linear mechanisms regulating the hydrodynamics.

An archetypal hydrodynamic response of a karst aquifer to the recharge process is shown in the sketches of Figure 1.3, which are modified from Bonacci et al. (2006).

Figure 1.3a depicts the situation during dry conditions: here groundwater level (red line) marks the saturated zone where all the channels and the pores below the line are filled by water.

As rains or discharge variations in the allogenic input are provided to the karstic system the water level in the vadose zone begins to vary. Such situation is shown in Figure 1.3b where high intensity rains result in rapid (few hours) and large variations of water level (over 100 m) in the conduit systems. In this phase the water flows saturate the conduits and the largest fractures, while small fissures and porosity matrix are not yet filled. The groundwater level is still located at the quota corresponding to the dry conditions. During such events the flow in the channels is frequently turbulent making the karst hydrology closer to a fluvial system rather than a typical groundwater flow of a porous aquifer (Bonacci et al., 2006; White, 2002). The similarity between water flow in karst and in a river becomes even more evident in case an allogenic input is provided: in this case the propagation of flood-like transients in the system in system.

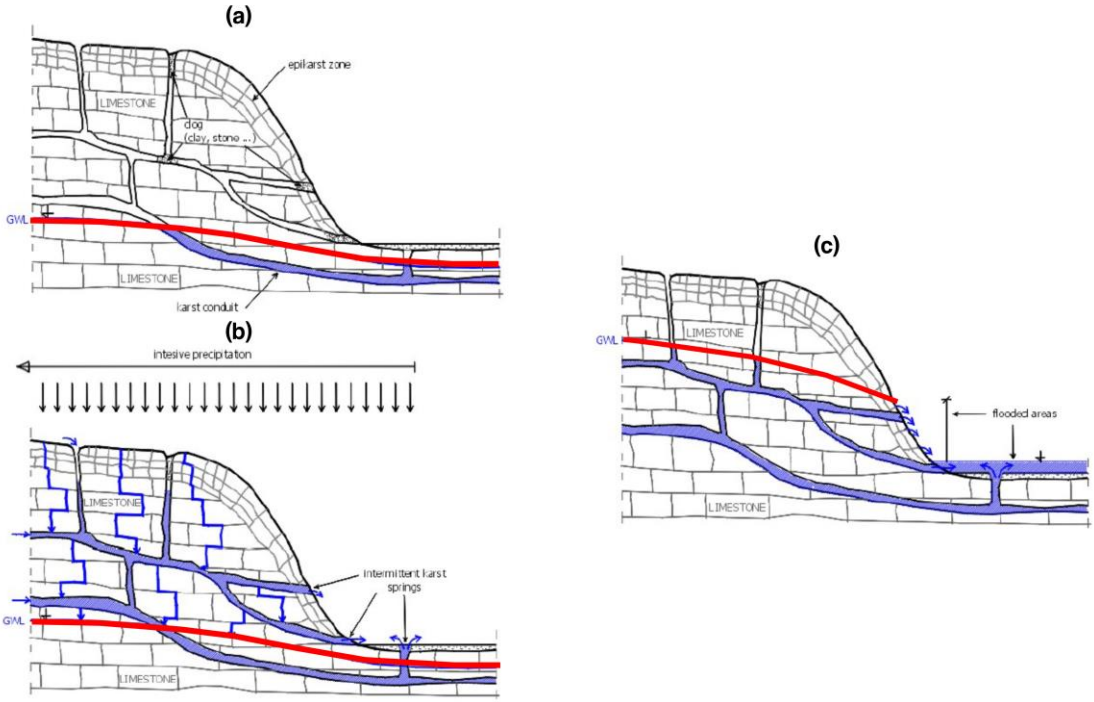

Figure 1.3. Sketches of the hydrodynamic response of a karstic system to intense precipitation (modified from Bonacci et al., 2006). *a) situation on dry conditions; b) response of the aquifer during an intense rain event; c) response immediately after the meteorological event.*

The final phase is shown in Figure 1.3c, when the rain event terminated, and now the water in the aquifer has filled the porosity matrix causing a general increase in the groundwater level. The elevated piezometric level in the aquifer causes an increase of discharge at the springs of the system.

The mechanism described in the sketches is common to basically all the karst system world-wide.

The complex hydrodynamics of a karst system requires targeted monitoring strategies and dedicated modelling techniques in order to study the aquifer. Most of the efforts are devoted to unveil the underground network of conduits, its connectivity and its response to the recharge process, both autogenic and allogenic. The velocity of transmission of the flood transients and the infiltration velocity are fundamental aspects to assess, particularly important for mitigating pollution risks. The hydrologic balance of a karstic system is an important outcome for evaluating eventual effects of the climate change and human impacts on the aquifer and for planning a sustainable use of the resource.

Where the caves are directly accessible, classical hydrological instrumentation as divers recording pressure, temperature and electrical conductivity, may be deployed. This instrumentation is indispensable in order to define the hydraulic connection between cave systems and gain insights into the travel time of flood pulses. Such data together with meteorological observations are fundamental to constrain hydrologic and hydraulic models. These models are useful to obtain mass balances of the system and as we will discuss throughout the thesis, they are precious in physically proving the connection between shaft, conduits and voids in the system.

The identification of underground water paths can also be approached employing tracer tests and geochemical analysis of the waters. With such techniques hints on the water origin are also obtainable; however, also these techniques require a direct access to the vadose zone, for deploying the instrumentation along the underground water paths.

Geophysical methods are complementary tools to these more classical hydrological prospections: in several cases they can provide valuable information on the underground karstic structures and the water storage variations. The added value is that they can be installed on surface. The focus of the thesis is on the application of gravimetry, which is the best method for obtaining quantitatively mass balances of the karstic system.

1.3 Gravimetry and hydrogeodesy

The gravity field on the Earth is non-uniform and non-stationary and it changes in response to basically every phenomenon that redistributes mass around the instrument. Gravimetry is the branch of geodesy which aims at measuring gravity variations, occurring both in space and time, and offers an interpretation to them (Van Camp et al., 2017). The largest variations on the Earth are due to the spatial variations between the poles and equator, where the centrifugal acceleration and Earth's flattening cause a gravity change from about 9.83 m/s^2 to

9.78 m/s^2 (~ 5 10^{-2} m/s^2). Topographic variations and lateral density changes in the crust and mantle represent a secondary effect which is still relevant and it is about 1-2 orders of magnitude lower compared to the Earth's centrifugal contribution. Small-scale density inhomogeneities, like a cavity in the karst, slightly perturb the gravitational field, generating gravity signals up to the order of 10^{-5} m/s^2.

Temporal variations of the gravity field involve a broad band of frequencies and are generally lower in terms of amplitude with respect to the static spatial variations, with the Earth tides (10^{-6} m/s^2) being the largest contributors (Figure 1.4). Redistribution of air and water masses due to atmosphere dynamics and hydrology cause even lower amplitude signals, as we will extensively discuss throughout this thesis.

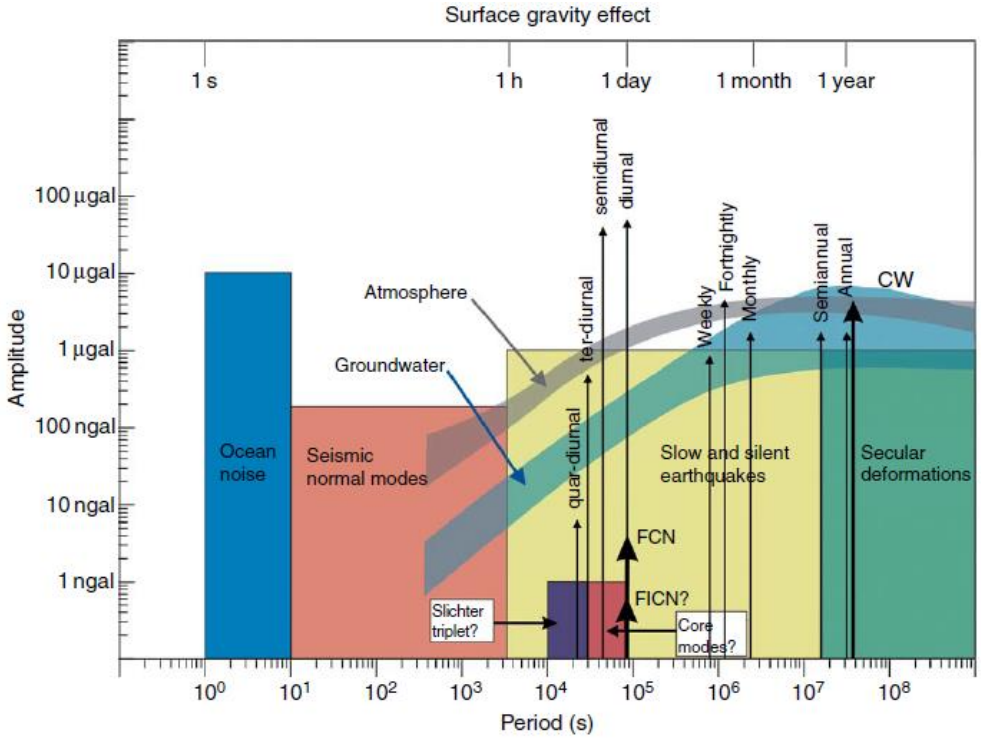

Figure 1.4 Typical amplitudes and frequencies of gravity signals associated to various geophysical phenomena. (From Hinderer et al., 2007*). Note 1 µGal = 10^{-8} m/s^2 = 10 nm/s^2.*

As it is evident, the gravity changes involve different temporal and spatial scales and therefore different instruments and techniques are required for their observation and monitoring. Satellite measurements offer global pictures of gravity changes with spatial resolutions in continental areas up to 80 km and precision sufficient to map large scale geologic structures (Braitenberg, 2015; Ebbing et al., 2018). Large scale oceanic currents (Tapley et al., 2003) and hydrologic-climatic processes (Abdelmohsen et al., 2020; Taylor et al., 2013; Thomas & Famiglietti, 2019) have been detected and studied relying on time variable gravity fields derived from satellite products.

Obviously local phenomena generating tiny gravity signals are only detectable through terrestrial measurements, which offer the highest performances in terms of accuracy and temporal resolution.

There are several types of instruments for performing terrestrial measurements (Van Camp et al., 2017), however the most commonly employed are the following three:

1) Spring based gravimeters, which basically use a micrometer to measure slight length variations of a suspended spring-mass system; length variations are then converted into gravity variations. In modern gravimeters the mechanical apparatus is supplemented by an electronic system that provides a feedback force to keep the mass in the same equilibrium position. The applied force is equal to the magnitude of the gravity variation. There are several applications which used these instruments for continuous monitoring, however since they are easily portable, they are extensively used for surveys in the field (Figure 1.5a).
2) Superconducting gravimeters (SG; Figure 1.5b) employ feedback principle, similar to the spring based instruments, to sustain a small mass in a fixed position inside a vacuum chamber. The instruments operate at low temperatures and pressure in order to minimize the electronic noise and obtain super-stable currents. Given their dimensions and fragility of the apparatus they could be installed only in fixed locations for continuous monitoring.
3) Absolute gravimeters (AG; Figure 1.5c) are basically composed by a laser interferometer that accurately measures the falling time of a known mass inside a vacuum chamber. Knowing the distance and the time the absolute value of gravity acceleration is then easily computable. Absolute gravimeters can be employed for both surveys in campaign (usually complemented with spring based measurements) and for repeated measures, eventually providing time-lapse images of the underground density distribution.

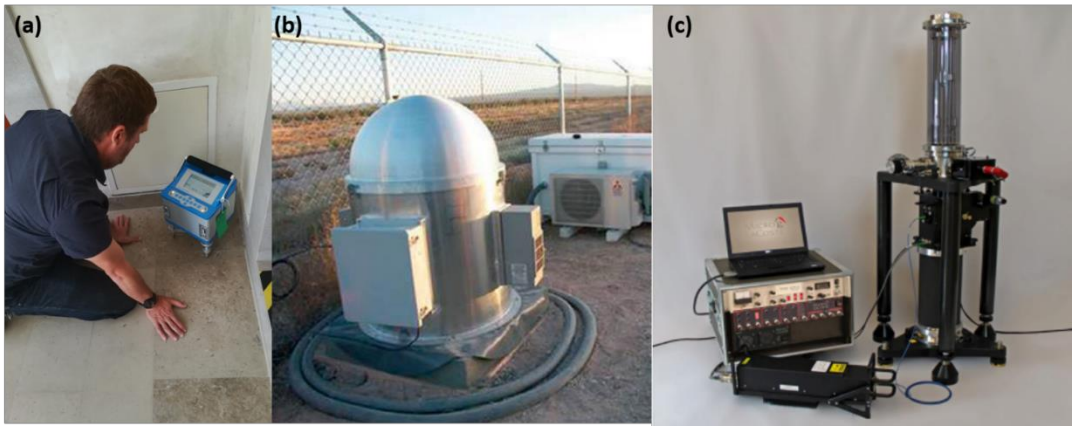

Figure 1.5 a) Scintrex CG-6 spring based gravimeter based at the Karst Research Institute ZRC SAZU of Postojna; b) Superconducting gravimeter (photo from GWR instruments site); c) FG-5 absolute gravimeter (photo from the brochure of the instrument).

The first two instruments offer relative gravity variations tied to a reference time/location, instead, absolute gravimeters are able to measure the absolute value of vertical component of the gravity field. In terms of performance the superconducting gravimeters offer the highest accuracies (< 1 nm/s^2) in a very wide frequency band and even in the seismic band they can compete with broad band seismometers (Rosat & Hinderer, 2018). Spring based gravimeters are noisier in the tidal and seismic bands with accuracies in the order of 10 nm/s^2. Usually such instruments are not particularly affordable at very long periods due to mechanical limits of the spring but recent experiments seemed to prove that an active tilt control of the instrument improves the performance also in the long term (Fores et al., 2019). Absolute gravimeters offer precisions in the order of 10 nm/s^2 and usually are employed for correcting the long period trends in measurements made by relative instruments, however they could not compete with them in terms of temporal resolution of the measurements. All these instruments obviously differ each other in terms of costs: superconducting and absolute gravimeters are more expensive (about 300,000-500,000 €) than spring based meters (< 100,000 €).

I only mention two more instruments, presently in testing phase that seem particularly relevant for future applications in the field: quantum free-fall gravimeters and MicroElectroMechanical Systems (MEMS). Quantum free-fall gravimeters could offer the benefits of an absolute measurement combined with a sampling rate close to the SG (Van Camp et al., 2017). MEMS (Middlemiss et al., 2016) offer an extremely small and light measurement unit (dimensions of few cm). The accuracy is still too low compared to spring based instruments but given the small dimensions and the low costs they could revolutionize the observations making possible the deployment of instrumental arrays or low quota observations through drones.

The three instruments described above have been exploited successfully in hydrologic studies or, as commonly referred, for hydro-geodesy applications.

The link between gravity variations and hydrology is due to the processes that redistribute the water mass both during and after a recharge event. As I have already introduced, in the karst environment the fractures and voids of the system are important storage units, able to temporary accumulate several millions of cubic meters of water. A mass change produces a gravity change via the Newton Law. Exploiting the Newton law we can easily predict the gravity change $\overrightarrow{dg}$ exerted on a test mass (gravimeter) due to an episodic water filling of a cavity (with mass dm), located at a distance r from the gravimeter:

$$\overrightarrow{dg} = -G\frac{dm}{r^3}\vec{r} \tag{1.1}$$

here I have assumed that the cavity is approximated by a sphere. For instance a cavity with radius 20 m filled by water with density 1000 kg/m^3 would cause a gravity variation $|\overrightarrow{dg}|$ of about 50 nm/s^2 at a distance of 200 m. Such gravity change could be detected easily by all the gravity instruments described above. Equation 1.1. informs us that gravity is inversely related to the distance between the source mass and observation point: as a consequence, as the water mass in the cavity system is drained the gravity will decrease accordingly.

The perturbation of the gravity field due to the temporary emplacement of a mass is known as Newtonian effect. However, a mass is also responsible of a deformation of the Earth surface, since the mass acts as a load. As we will see extensively in the thesis this deformation is responsible of a height change of the instrument and a redistribution of the Earth density below the applied load: both these effects lead to further gravity changes, known as loading component. For small scale loads such component is usually smaller than the Newtonian one (Llubes et al., 2004; Meurers et al., 2021), but for large scale phenomena (i.e. global variations of hydrology) the effect becomes important. In karst environment there is evidence of spatially localized deformation associated to large water variations occurring in the vadose zone: tiltmeters (Longuevergne, Florsch, et al., 2009; Meurers et al., 2021; Tenze et al., 2012) and GNSS (Braitenberg et al., 2019; Devoti et al., 2015) testify the presence of loading contribution, as well as uplift associated with overpressure insisting over conduits saturated by water. In any case the tilt and displacement is rather small, up to several microradians and few mm respectively, in case of extraordinary large meteorological events.

The study of hydrologic-related gravity signals is also of interest for a broader geodetic community, since in every time-series the hydrologic noise is present and could interfere with other phenomena of interest. Several studies have been conducted for estimating and optimally removing the hydrologic contribution from SG data: various approaches are employed depending on the hydrologic data availability, on the knowledge of the underground drainage system and its functioning during the recharge process (some examples are found in Creutzfeldt et al., 2008; Meurers et al., 2007; Weise & Jahr, 2017). All these studies evidenced that there is not a standardized approach to the problem.

Other experiments focused on the use of gravity observations to estimate the local water mass balance, the infiltration rates or to constrain the hydrologic models. For instance, SG data were used to estimate the daily evapotranspiration component of the system by stacking of multi-year daily observations (Van Camp et al., 2016). Evapotranspiration is one of the key factors for a hydrologic balance and it is hardly assessable by other methods. Other applications, reviewed in Van Camp et al. (2017), employed gravity data to distinguish between confined and unconfined aquifers, estimate local soil moisture or to enhance the mass fluxes estimates filling the gap of satellite resolution.

The strength of the method is related to its sensitivity to the integrated water mass around the instrument, which makes the technique an ideal complement to the classical hydrologic observations. In addition, the instrument should not be located directly in the saturated or in

the vadose zone of the aquifer, allowing a remote and non-invasive monitoring and control of the water masses.

Gravimetry has been applied in porous and karstic aquifers. Güntner et al. (2017) proved that SG observations gives excellent estimates of storage variations in porous aquifers. They were also able to retrieve temporal variations of evapotranspiration component given the precipitation data and an estimate of the runoff component. The results were in a very good accordance compared with lysimeter measurements demonstrating the importance of gravimeters for improving the integrated mass balance of an area. The authors suggested that an instrument installed on surface is mostly sensitive near-surface moisture variations and hence this configuration would not be optimal to study the variations of deep storage.

Information on the deeper contributions could be found by setting the instrument underground: an example is given in Longuevergne et al. (2009), in which the authors analyzed the data from the SG in Strasbourg, located about 10 m below the ground level. The authors corrected the data for the far field continental hydrologic effects and for the local superficial contribution by modelling the data of a moisture probe. The residuals revealed a long period component, which was mostly due to the water level variations in a deeper aquifer.

In addition to continuous measurements Kennedy et al. (2016) performed repeated absolute measurements in an artificial recharge facility and demonstrate that infiltration rate and depth of the wetting front are directly estimable from the analysis of gravity time-series. Gravity data combined with hydraulic modelling and wells observations give an improved picture of the processes in the vadose zone. This includes a better estimation of vertical and horizontal hydraulic conductivity and specific yield. With the combination of hydrologic and gravity observations Kennedy et al. (2016) were also able to discriminate the storage changes between the shallow saturated zone and those occurring in the deeper aquifer. Other interesting applications for depicting the hydrodynamics in porous media can be found in Christiansen et al. (2011) or Piccolroaz et al. (2015).

In karst environment similar efforts to map and monitor the underground storage units with repeated absolute gravity measurements were made by Van Camp et al. (2006), in the Rochefort caves (Belgium; RO in Figure 1.1b) and by Jacob et al. (2008, 2009, 2010) in the Larzac Plateau in France (LA in Figure 1.1a).

The Rochefort karst area shares some common features with the Škocjan system. Similarly to study case discussed in this thesis, the hydrology is governed by an allogenic contribution of the Lomme River. Van Camp et al. (2006) showed that the recharge in Rochefort caves can be monitored by the gravimeter: the investigation lasted for few weeks when repeated measurements were done during two typical flood events of the Lomme River. Signals up to 90 nm/s^2 amplitude were recorded, which were sensibly higher than the accuracy of the instrument. The authors found different delays between the gravity maxima and the water levels recorded in the cave for the two flood events: the explanation involved the different

saturation conditions in the epikarst and in the porous sub-system insisting before the two floods.

In their applications to the Larzac Plateau, Jacob et al. (2008, 2009, 2010) employed a combination of repeated surface gravity measurements, with absolute gravimeters, and surface to depth measurements (STD) in a 60 m deep pothole with a portable relative gravimeter. In this case the authors focused on long period mass balances in the basin, looking at multi-year data. Through repeated STD and density measurements on samples, they found an average porosity of the massif and estimated that almost 10 % saturation of the pores occur during the recharge process, evidencing the importance of the infiltration process and the primary role of the epikarst as a storage unit rather than the saturated zone.

Exploiting repeated absolute measurements in different locations of the Larzac Plateau, they were also able to map the heterogeneity of the water storage units. Through these 4D observations and the precipitation data, they built a comprehensive water budget of the system, in which gravity data was useful to constrain the water evapotranspiration component during the year.

More recently a SG station (Fores et al., 2017) was installed on the Larzac Plateau. In this work the authors used the gravity data to constrain the water storage changes (WSC) and through the rainfall (R) and evapotranspiration (AET) data they calculated the local discharge (Q) according to:

$$Q = R - AET - WSC \tag{1.2}$$

The local discharge Q is essentially the water leaving the epikarst through the fractures of the system. The local discharge time-series is then modelled through a simple hydraulic model, where the vadose zone is approximated by two serially coupled reservoirs with discharge governed by Maillet law (Deville et al., 2013). Each reservoir has a characteristic time of recharge, which models how fast the water is drained from a reservoir. The first reservoir corresponds to a sub-superficial layer, very sensitive to the meteorological data, while the other to simulates the epikarst. Albeit simple, this model allowed to identify rather complex and non-linear hydrodynamic mechanisms, as the water piston effect, occurred after abundant rain insisted on an already saturated system by previous precipitations.

Additionally, the gravity observations also evidenced the absence of fast transfer of water in the site: this aspect was not investigable by AG measurements due to low temporal resolution and confirmed the complementarity of the two techniques.

Another application of SG data in a karstic context was done recently in Rustrel (France) where an SG was located in a gallery 500 m below the surface (Mouyen et al., 2019). In order to model the gravity observations the authors employed a hydrologic model through which they calculated the local storage (WSC) by knowing the observed rainfall (R), evapotranspiration (AET) and adjusting the model parameters to fit the observed discharge at one spring (Q).

The WCS thickness time-series was then converted into a gravity effect by approximating the water level variation within a homogeneous disk of radius 2 km. The comparison with observed data revealed an overestimation of the observed gravity in spring-summer 2016 (underestimation of the amount of water since the water storage is above the instrument) and an underestimation of the observed gravity in autumn-winter 2016 (overestimation of water). The authors suggested some possible explanations for the misfits: first, the presence of lateral fluxes is not modelled, considering also the vicinity of the SG to another nearby catchment area. A second explanation involved the different sensitivity of the gravity observations (more sensitive to unsaturated zone) and the hydrologic model which includes also the saturated zone in the modelling procedure. The authors suggested to install a further SG on the surface which could help to better deciphering the processes occurring within the 500 m thick vadose zone.

In most of these applications the assumption is that the karst systems, although being a complex media, could be reasonably well approximated by a porous media in which the water is homogeneously stored in the matrix porosity. The approximation seems valid in most of the contexts since the gravity acts as a filter on the mass distribution weighing it by the distance from the instrument.

An attempt to take into account the inhomogeneous distribution of the water masses in the karst was done recently by Watlet et al. (2020) analyzing the continuous data from a spring based gravimeter and a SG nearby the Rochefort caves. Here the gravimeters recorded over 10 flood events occurring in the cave system, in which also the water level is monitored. As already hinted, the water volume in the caves is influenced by both the autogenic recharge as well as the allogenic input from the Lomme River. For these flood events the authors forward modelled the gravity effects in the known cavities, using the diver data as constraint for the water level. The modelled gravity effects are largely underestimated by up to 8 times lower with respect to the observed transients, suggesting the presence of further unknown storage units in the vicinity. Depending on the flood event considered the water unknown volume could be up to 4 times the actual volume of the Rochefort caves.

Interestingly also Watlet et al. (2020) evidenced the presence of a long period positive gravity anomaly insisting for several days after the flood pulse transient has passed. The authors proposed that the source mechanism of such anomaly could be due to the water infiltration process in the massif, that slowly releases the stored waters, while the allogenic flood-pulse transients are fast and are mostly drained by the conduit system of the cavities.

To conclude this brief overview, I mention that repeated gravity measurements have been employed to monitor underground mass changes related to the dissolution of karstifiable rocks, i.e. evaporites (Kobe et al., 2019) and an attempt was also done in order to monitor geothermal fluids (Portier et al., 2018). The evaporites environment is similar to the karstic carbonates environment, although the solubility and dissolution rates are much higher in evaporites. In any case also here the presence of voids is observed and potentially they could temporary store meteoric waters with mechanisms similar to the one discussed in this thesis.

Also geothermal exploitation employs fractured aquifers, frequently also on carbonates, and there the water circulation is similarly controlled by fractures and joints.

1.4 Working hypothesis and outline of the thesis

With this PhD study I aim to demonstrate the added value of gravimetry for the hydrological characterization of the water dynamics in a karst system.

In particular, the following working hypothesis will be tested:

1) Gravimeters, in particular spring based gravimeters, are sufficiently stable and precise to detect the gravity variations associated to the fast recharge process in the underground cavities of the karst environment.
2) Other gravity changes that superpose on the hydrological signal can be effectively estimated and removed through adequate modelling: the study area is challenging for gravity studies due to its proximity to the Adriatic Sea. Hence the ability of retrieving hydrologic signals from gravity observations should be assessed keeping the uncertainties in removing the effects of other geophysical phenomena into account.
3) Gravimetry, associated to hydrologic observations and hydraulic modelling, allows to obtain a refined estimate of mass fluxes insisting on a portion of the karstic aquifer. Gravimetry, in particular, helps in constraining a subset of hydraulic model parameters, reducing the ambiguity in the modelling (Beven, 2006).
4) Besides the Škocjan caves, that represent the upper limit for the expected gravimetric-hydrologic signals due to their large dimension and the extraordinary allogenic input, other caves in the Classical Karst can be effectively monitored with a gravimeter.

The thesis is structured according to the following outline.

1) Chapter 1 is the present general introduction to the scopes of the PhD thesis.
2) Chapter 2 is an introduction to the hydrology of the Classical Karst with a particular emphasis on the Škocjan area, where the gravimeter has been installed. I present in detail all the hydrological data available and the previous studies relevant for the scopes. The response of the Škocjan system is described by analysing the preliminary hydraulic-gravity simulations which were performed for selecting the location for the continuous recording gravity station. Finally, the instrumental characteristics of the station are presented.
3) Chapter 3 gives details on the processing of the gravity data in order to remove the non-hydrologic components, which are basically due to Earth and marine tidal effects, atmospheric contribution, non-tidal ocean contribution and continental far-field hydrologic contribution.

4) Chapter 4 shows the hydrologic related gravity signals for a large flood event that occurred in 2019. I discuss both the hydraulic and gravimetric modelling results and give an estimate of the water mass balance of the system during a flood event.
5) Chapter 5 illustrates the feasibility of monitoring the storage process through gravity measurements in other caves in the Classical Karst. Here the detectability of storage units is assessed with respect to the instrumental noise characteristics and the presence of other geophysical phenomena superposing on the hydrologic signal. I also give some advices on future possible locations in the Classical Karst plateau that could benefit from a continuous gravity monitoring as well as the feasibility of a time-lapse approach (i.e. repeated gravity measurements with a relative/absolute gravimeter).
6) Chapter 6 is the conclusion of the thesis.

Chapter 2
Hydrology and instrumentation of study area

In this chapter, I give an overview of the hydrology of the Classical Karst with a particular emphasis on the Škocjan and Kačna systems. The monitoring network of hydrologic observations is presented and the hydrologic data of interest for the study case are discussed with reference to the more recently published studies. Some elements on the equations involved and on the software used for performing the hydraulic simulations are also provided with a discussion on a simple example employed for selecting the optimal site for gravimeter installation. Further considerations on the hydrology and in particular on the recurrence time of the flood events of the Reka River and on the typical duration of such events are then addressed. Finally, the novel gravity station is presented together with the auxiliary data necessary for processing the gravity records.

2.1 Hydrology of the Classical Karst

The Classical Karst (Kras/Carso) plateau between Slovenia and Italy is about 40 km long and in average 13 km wide and it is underlain by an up to several kilometers thick succession of Cretaceous to Lower Paleogene carbonates (Blatnik et al., 2020b; Jurkovšek et al., 2016). The geological structure of the broader area is a result of the collision between the Apulian and Eurasian lithospheric plates. The Kras/Carso Plateau is an anticlinorium, which structurally belongs to the External Dinaric Imbricated Belt (Placer et al., 2010). The carbonates are surrounded by relatively impermeable flysch with fluvial network providing allogenic recharge to the Karst. Flysch also prevents the outflow along the SW boundary, so that the main flow is forced to follow the Dinaric (SE–NW) direction (cyan dashed line in Figure 2.1a; Gabrovšek et al., 2018; Petrič et al., 2020; Zini et al., 2014). Along the NW coast of the Trieste Bay, the limestone flysch contact is located systematically below the sea level allowing the outflow of the karst waters into the sea through numerous springs. Among these, the Timavo springs with average discharge of 30 m^3/s are the most important (Petrič et al., 2020).

The recharge of the system is manifold: beside diffuse autogenic infiltration from the karst surface, groundwater inflow from the adjacent alluvial aquifer presents a dominant component of spring water at low flow. During floods, the main contribution comes from the Reka River which originates at mount Snežnik and flows for about 30 km along an alluvial valley before disappearing in the Škocjan Caves. The Škocjan Caves are located near the flysch-limestone contact on the SE border of the karst plateau (Figure 2.1a). From here the river starts its underground flow which is about 33 km long until it reaches the Timavo Springs at the NW border. The underground water path has been already depicted by various tracer tests conducted throughout the past century with also several new tracer tests also performed recently; a comprehensive review and analysis of the results can be found in Petrič & Kogovšek (2016).

The long-term (1952–2013) average discharge of the Reka is about 8 m^3/s according to the Environmental Agency of Slovenia (ARSO). The ratio between the highest and the lowest flow rate is about 1700, with the measured maximum discharge of 305 m^3/s. Since the climate in the area is transitional between Mediterranean and Continental, most of the rain events occur in autumn. Annual precipitation in the recharge area of the Reka reaches over 2000 mm with single precipitation events that could exceed 250 mm in 12 h (Gabrovšek et al., 2018).

The groundwater flow in the aquifer of Kras/Carso is characterized by highly variable recharge of the Reka River and an irregular structure of conduits and voids. The thickness of the vadose zone ranges from several tens of meters close to the Timavo springs, to over 300 m at the SE border. The caves, that evolved over 5 Ma, populate the entire vadose zone (Figure 2.1b).

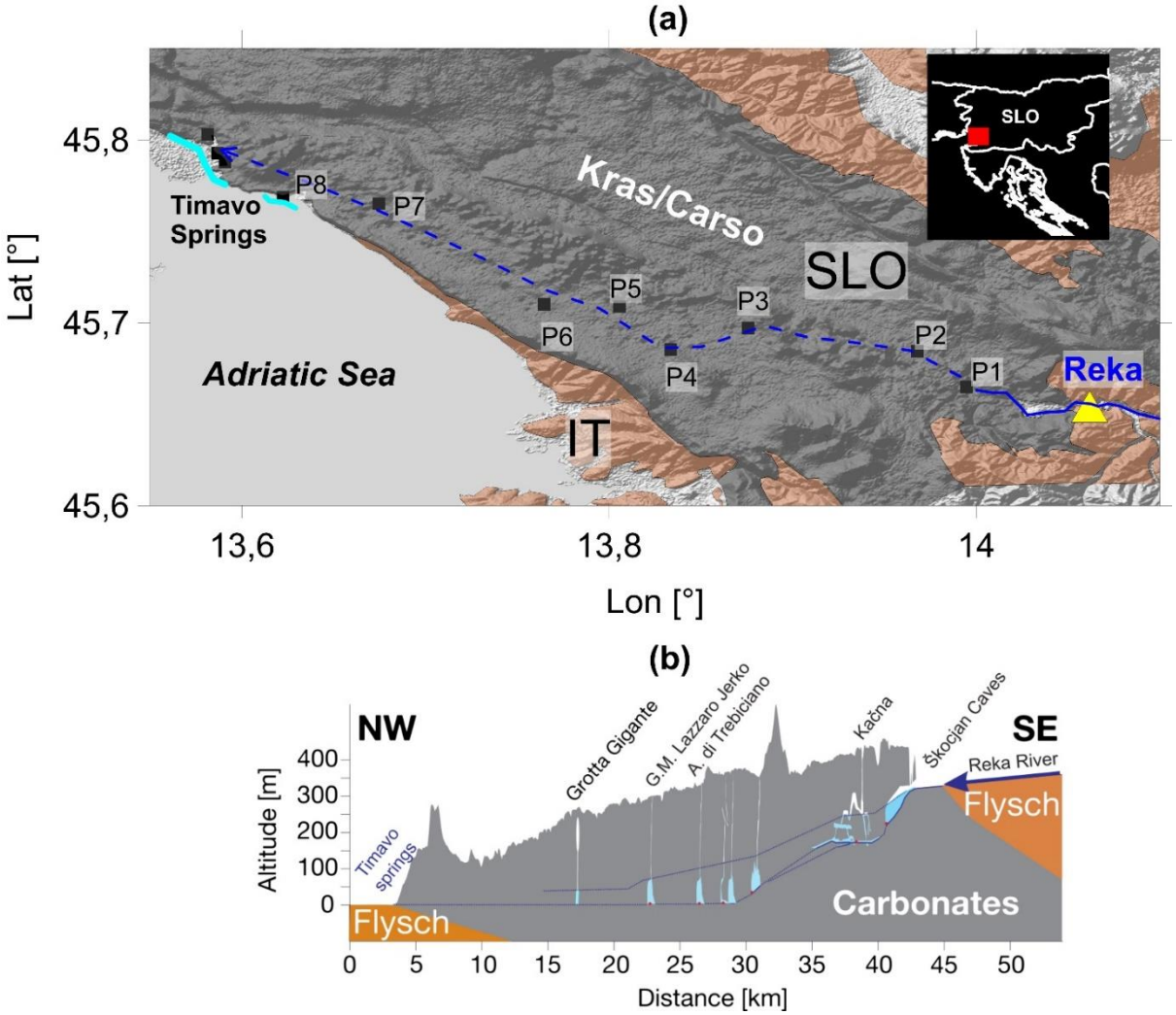

Figure 2.1 a) Classical Karst geology map (gray: Carbonates; brown: flysch; outlines from Jurkovšek et al. 2016*) superposed on a hillshade map of the topography (SRTM data). The black squares locate the principal caves and the Timavo springs (P8). P1: Škocjan caves; P2: Kačna Jama; P3: Kanjaduce; P4: Trebiciano; P5: Lazzaro Jerko; P6: Grotta Gigante; P7: Lindner cave. Yellow triangle shows the Cerkvenikov Mlin, a hydrographic station on the Reka River. The underground water path of the Reka/Timavo is reported with a dashed blue line. b) Simplified geologic section along the Reka water path which shows through the blue line the water level in the caves system during high flow conditions (modified from* Braitenberg et al. 2019*).*

In this study I focus on the caves of the epiphreatic (also flood level) zone. Practically all known epiphreatic caves of the Kras/Carso aquifer have large voids above the base flow water table and experience high and rapid rise of the water level during floods (Gabrovšek et al., 2015a, 2015b). These caves present major temporal storages of floodwater. Most of them have been discovered by following and excavating passages along the air-flow which is pushed out from the epiphreatic passages and voids by the rising water. Many blowholes on the surface with

no connection to the epiphreatic level indicate existence of yet unknown large voids (Gabrovšek et al., 2015a).

Groundwater level, temperature, and specific electric conductivity in the epiphreatic caves are monitored by autonomous instruments (Gabrovšek et al., 2018; Zini et al., 2014). Recorded time series of observed parameters reveal level responses of several tens of meters (up to 120 m) with rates of change of up to 10 m/h. Considering that the planar area of some known chambers reaches 10,000 m^2, the local rate of change of mass is in the order of 10^8 kg/h.

The Škocjan Cave system with a total volume of more than 5 10^6 m^3 and water level variations larger than 100 m are the largest known in the Classical Karst to have such huge storage. The cave system is well known from the speleological and hydrological point of view and water levels are nowadays continuously monitored. Hence, the Škocjan Caves present an ideal site to evaluate the combined gravimetric-hydrological response to flood events. In the following section the data at my disposal and the hydrologic characteristics of the system, according to the most recent publications, is discussed.

2.2 Hydrology in the Škocjan area

2.2.1 General features of the system and hydrologic data

The underground flow path of the Reka River starts in Škocjan Caves, where the flow follows a large canyon for more than 3 km (Figure 2.2a). The cross-section of the canyon is between 2,000 m^2 and 12,000 m^2. Along several sections, the canyon widens into large chambers: Sumeča, the Hanke channel and Martelova which is the last and the largest chamber with a volume of more than 2 10^6 m^3 (Gabrovšek et al., 2018; Šebela, 2009).

The cave system is interrupted at the end of Martelova by a fault plane that causes the channel cross-section to diminish to few tens of square meters (Šebela, 2009). The water flow then follows a system of channels and flooded conduits, which continues in a yet unexplored flooded conduit, and reappears about 800 m NW in a sump in the Kačna Cave (Gabrovšek et al., 2018).

The Kačna Cave is an over 13 km long network of channels, located between the permanent flow level at 150-180 m a.s.l. and the surface of Kras plateau at about 430 m a.s.l (Blatnik et al., 2020a; Rožič et al., 2015). The permanent flow level is constituted by a 5 km long system of channels with variable geometry, interrupted by fully flooded conduits, which are still under exploration.

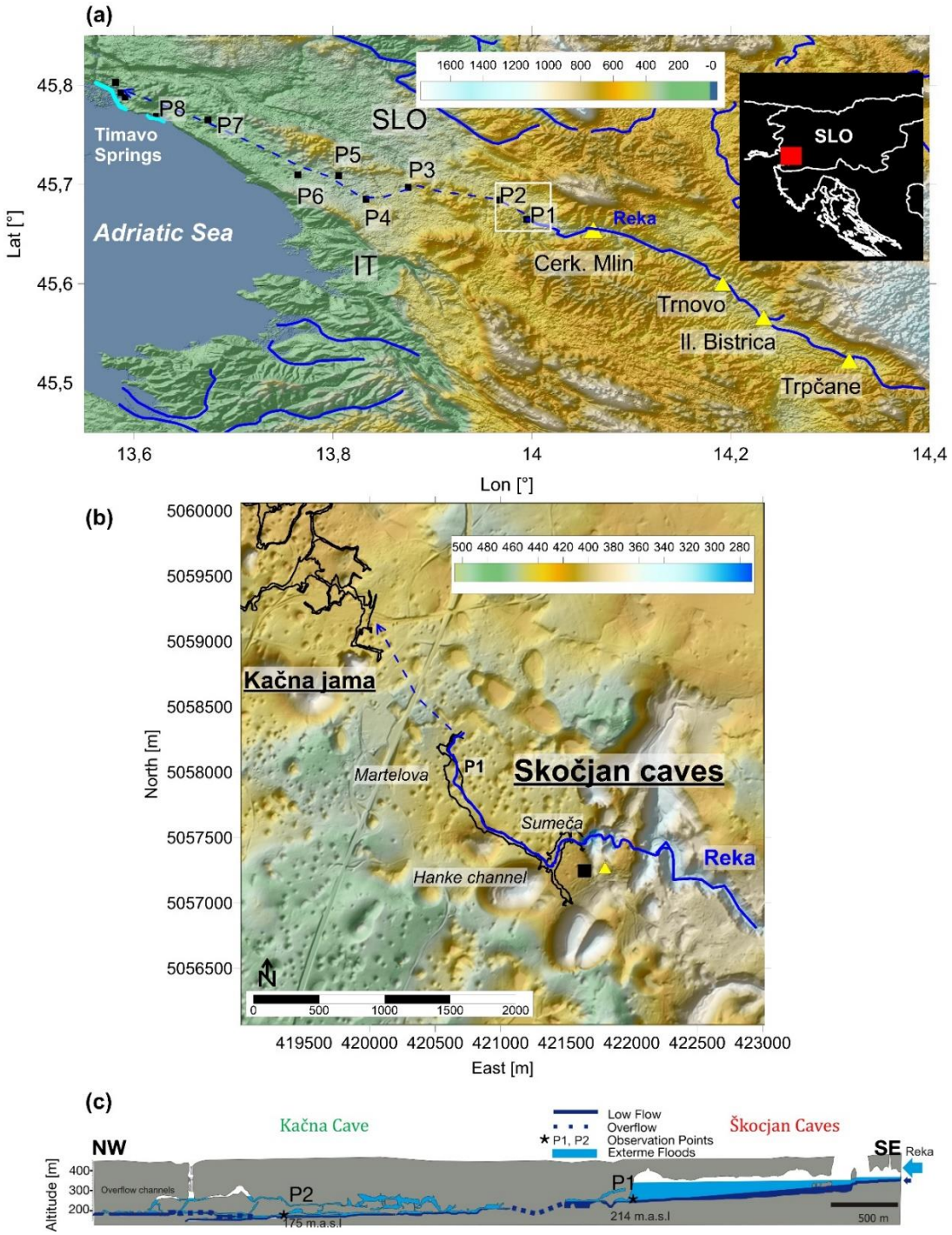

Figure 2.2 a) Classical Karst topography from SRTM data. Colorbar: height above sea level in meters. Black squares: as before. Yellow triangles locate the hydro/meteorological stations along the Reka River. White rectangle bounds the area reported in plot b. b) Detail on the Škocjan cave area: in black outline of the Škocjan and Kačna systems. For Škocjan the names of the main chambers are reported. Blue line: Reka; dashed line: presumed underground water path. Black square: location of the touristic info-center. c) Vertical cross-section along the Škocjan-Kačna cave system. Dark blue areas illustrate the water level in the caves during low flow conditions; light blue during Reka flood events (modified from Blatnik et al. 2020*).*

A large part of the flow from Kačna Cave reappears in Kanjaduce Cave, about 6 km NE from Kačna Cave (P3 in Figure 2.2a). A simplified vertical cross section along the Škocjan and Kačna caves is plotted in Figure 2.2c, showing the hydraulic connection between the two caves system. Here also the typical water levels expected in the caves are depicted, according to different flow conditions of the Reka River: dark blue illustrates the situation during low-flow conditions, while the light blue depicts the situation at high flow conditions.

The long-term monitoring of groundwater parameters in most caves reaching the groundwater flow in Kras/Carso aquifer includes various temperature/pressure loggers. In Figure 2.1a the position of several monitored caves is shown through black squares, the data availability is however variable since many instruments are not operating anymore as reported in Figure 2.3. In the Škocjan area, P1 has been recording pressure and temperature with temporal resolution of 30 minutes since 2005, with a hiatus of 5 years from 2013 to 2018. The sensor P2 located nearby the Škocjan caves, in the Kačna Jama, recorded hydrologic data with some interruptions until 2015.

Other hydrologic data of interest are available from the Environmental Agency of Slovenia (ARSO) which operates a network of hydrographic and meteorological stations along the Reka River. In particular, the river discharge is monitored along its superficial path from Ilirska Bistrica to Škocjan (yellow triangles in Figure 2.2a) by 4 gauging stations. Rain, temperature, pressure and other climatic data are continuously recorded by other 3 meteo stations located in Škocjan, Tatre (close to Trnova station of Figure 2.2a) and Ilirska Bistrica.

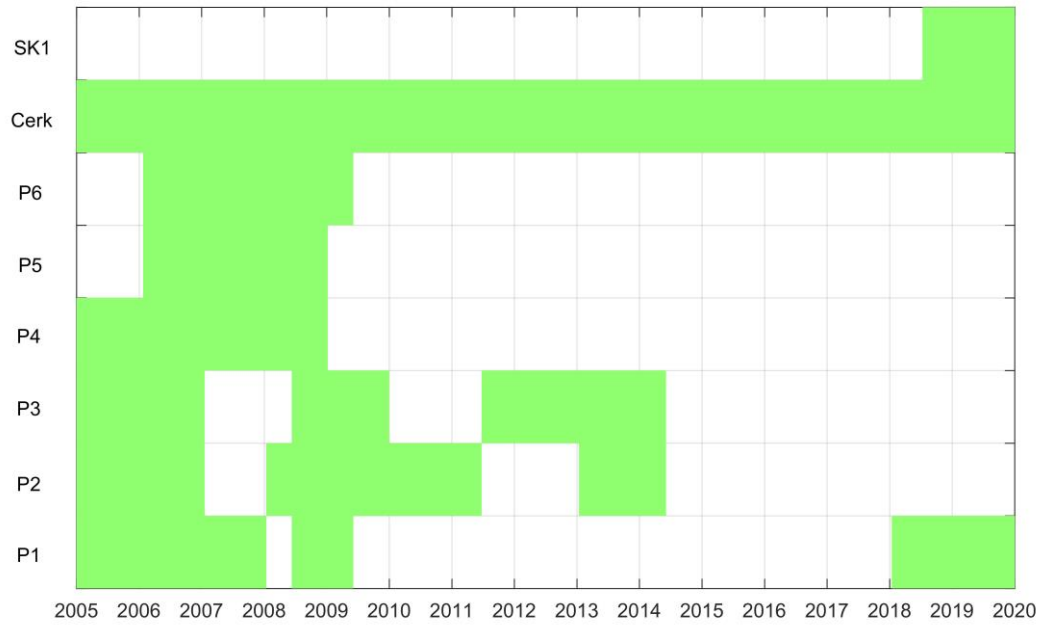

Figure 2.3. Data availability for the various caves (location in Figure 2.1a), for Cerkvenikov Mlin (Cerk) and for the gravimeter station (SK1) installed during this PhD project. In green the available data periods.

2.2.2 Analysis of hydrographs: response of the system to flood events

Such wealth of observations has been the focus of several studies in recent years (Blatnik et al., 2020a; Gabrovšek et al., 2018; Gabrovšek & Peric, 2006) with the aim to interpret the response of the karstic structure to the Reka flood events. The works evidenced that looking at correlation between the Reka discharge and the water level in various caves gives important hints regarding structure of the system and its hydrodynamics. In the following I give an overview of such analysis for the Kačna and Škocjan system.

Figure 2.4 displays the typical flood responses of the Kačna and Škocjan cave systems (2.4b) to two different meteoric events (2.4a): a big event with a discharge exceeding 250 m^3/s (12^{th} December 2008) and a medium event with a peak discharge about 100 m^3/s (17^{th} December 2008). Evidently, the response is dramatically different in terms of water level variations of both cases when the discharge from the river varies. The first event begins almost on dry conditions, with Reka discharge less than 10 m^3/s; the medium event on the other hand superposes its effects on the falling limb of the previous big event.

In the medium event (see inset of Figure 2.4b) the water level variations in Škocjan (P1) are less than 5 m and the phases of rising and recession are both very slow, about 2 m/day (Blatink et al., 2020). In Kačna the water level immediately reacts to the increased Reka flow, rapidly rising the water level up to about 15 m. However, inspecting the recession curve of Kačna in more detail, we see two different trends: an initial phase in which the water level decreases slowly followed by a more rapid decrease when the water level is below 10 m. This is not immediately evident when looking at the raw observations (i.e. inset in Figure 2.4b) but becomes clearer when considering the discharge vs. water level plots (Figure 2.4d). In this plot we see the two different trends in the Kačna curve, with the presence of an inflection point at about 10 m. The presence of such inflection point is interpreted as due to the activation of an overflow channel which alters the stage recharge slope curves as depicted in Figure 2.5 (taken from Blatnik et al. 2020). In addition to this, such plot enhances the different behavior of Škocjan (P1), in which the discharge-stage curve follows a simple power law relation suggesting that for all the duration of the event the flow was in an open channel regime (Blatnik et al., 2020a; Gabrovšek et al., 2018).

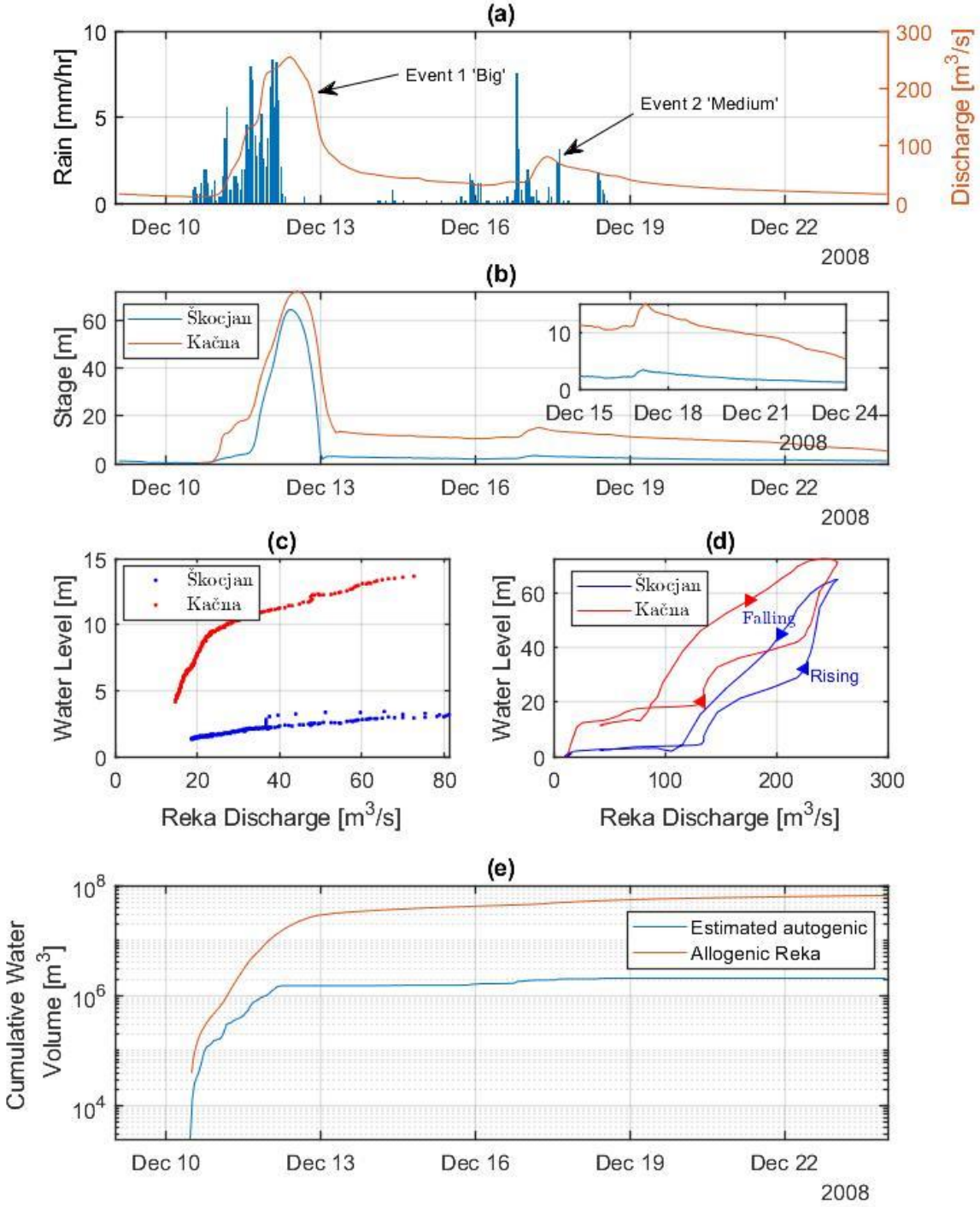

Figure 2.4 Hydrologic recordings in December 2008 in the Škocjan-Kačna system. a) Hourly rain gauge in Škocjan and Reka discharge recorded at Cerkvenikov Mlin. b) Recorded water levels in Škocjan (blue) and Kačna (red). Inset shows a zoom on the 17th December event. c) Discharge vs. water level curves for "medium" event (17th December). d) Discharge vs. water level for the "big" event (12th December). e) integrated water flux during the 2008 flood event at Cerkvenikov Mlin (red) and cumulative water volume due to precipitation occurring over a circular area of radius 2 km centered on Škocjan.

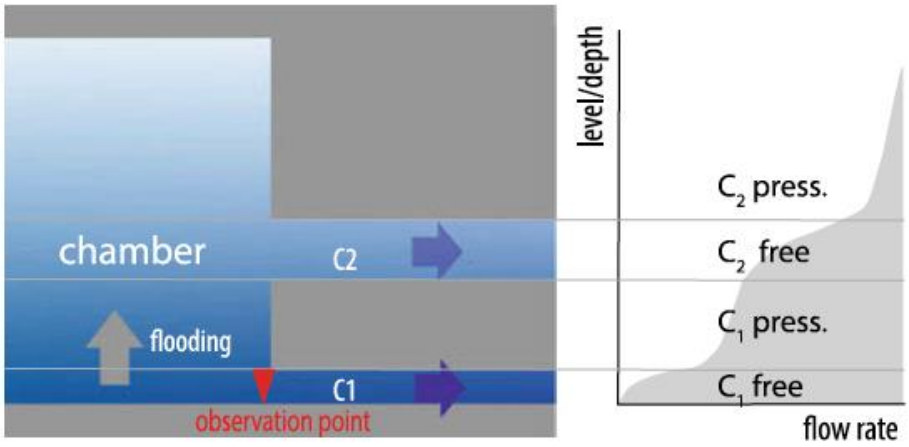

Figure 2.5 Sketch that illustrates the relation between the inflection in the discharge vs. stage plots and the geometry of the drainage system. During a flood event, when an overflow channel is reached, an inflection point in the curve is observed (from Blatnik et al. 2020a*).*

During large flood events, as the one happened on the 12th-13th December 2008, the response of both caves systems is extremely different: a large flood causes the rise of the water levels up to over 60 m in P1 and over 70 m in P2. During the rising phase we observe the inflection stage in P2 at about 15 m which is the first overflow channel. As long as new water inputs are provided and the Reka discharge exceeds the 130 m^3/s another inflection point is reached; again this is more evident in the discharge vs. stage plots (Figure 2.4d). In this case however the inflection is observed also in Škocjan and happens with a slight delay compared to Kačna. Based on this data Gabrovšek et al. (2018) and Blatnik et al. (2020*a*) suggested a possible mechanism for the flooding of the Škocjan and Kačna system: constriction downstream from Kačna Cave causes backflooding with rapid rise of water level reaching also the Škocjan Cave. As the recharge increases, the level at P1 also rises rapidly. The presence of other inflections in the discharge vs. stage plot (Figure 2.4d) is attributable to various overflow channels "activated" during the flood event. As we will see, values of discharge exceeding 250 m^3/s with rates of increase of up to 10 $m^3/s/h$ are critical values for triggering the flooding in Kačna and sequently in Škocjan.

Regarding the hysteretic behavior of the curves in Figure 2.4d Gabrovšek & Peric (2006) proved that the origin is due to the restriction of the drainage system downstream the Martelova chamber. The authors, in particular, showed with synthetic tests that the height of the channel restriction and the length of the chamber upstream the restriction are the main controlling parameters which influence the shape of the hysteresis curve. Slow release of seepage waters contained in fractures could further contribute to the hysteretic behavior; however, in Škocjan the dominant mechanism seems likely to be due to the alternation of large voids and restriction conduits.

We remark that the response of the conduit system depends also on the hydrologic conditions before the flood event: this would lead to different inflection points and a different hysteresis curves in the stage discharge plots. In any case the occurrence of two consecutive large events is rare and the examples discussed throughout the thesis have a similar time evolution of the discharge-stage response as the 2008 event.

During such flood events the total water volume that is drained through the cave system is impressive and easily exceeds 10^7 m^3 (Figure 2.4e), while the autogenic recharge is likely to play a minor role. Figure 2.4e shows the estimated water volumes of the two contributions: the red curve is the integrated water flux of the Reka recorded at Cerkvenikov Mlin for the 2008 event. The blue curve is the autogenic water volume contribution estimated from the rain gauge observations in Škocjan: the water volumes are calculated assuming the rain is uniformly distributed over a circular area within 2 km from Škocjan. Evapotranspiration is neglected and if accounted for it would further reduce the autogenic contribution. The comparison between the two curves let us infer that during large flood events the allogenic contribution is at least one order of magnitude larger than the autogenic one.

To be more quantitative and also to prove physically all the mechanisms described above, Gabrovšek et al. (2018), produced a hydraulic model of the whole Classical Karst system, which is particularly detailed and well constrained in the Škocjan-Kačna area. The authors approximated the different caves and the channels with a series of interlinked conduits with simplified cross-section and then provided the observed Reka discharge of a flood event as a water input. The authors simulated the water level variations in various caves by solving the Saint-Venant equations, used for modelling the unsteady flow in a channel, and compared the results with the observed data.

Since I will employ and modify such model for constraining the mass balance and predicting the gravity changes in Škocjan, I give a rapid overview on the equations and on the software employed for modelling, in the following section. I discuss then a simplified hydraulic model of the Škocjan caves which will also be employed to assess the expected gravity signals for a flood event in Škocjan.

2.3 Modelling the hydraulics of a karst system

2.3.1 Saint-Venant Equations

Several studies (Blatnik et al., 2019; Gabrovšek & Peric, 2006; Kaufmann et al., 2016; Mayaud et al., 2019) demonstrated that the hydrodynamic response of a karstic system subjected to flow variations can be modelled reasonably well with simplified versions of the Navier-Stokes

equations, the so-called Saint-Venant equations (SVe). With respect to the Navier-Stokes equations, the SVe model only 1-D flow, accounting the viscosity and turbulence terms through simple empirical relations and assuming the boundary friction to be approximated as in a steady flow. Due to their simplicity such equations are particularly apt to model unsteady flow occurring in artificial channels and also in natural rivers.

The SVe are derived from the mass and momentum conservation of a small piece of fluid subjected to an external force. As reported in Blatnik et al. (2020a), the mass and momentum conservation equations respectively could be written as:

$$b(h)\frac{\partial h}{\partial t} + \frac{\partial Q}{\partial x} = q \tag{2.1}$$

$$\frac{\partial v}{\partial t} = \frac{1}{\rho A dx}\sum F - v\frac{\partial v}{\partial x} + qv \tag{2.2}$$

The quantities involved in these equations are defined in the table 2.1 and in the sketch 2.6.

b	Width of the channel [m]
h	Depth of the flow [m]
Q	Discharge [m^3/s]
q	Lateral/vertical inflow contributions [m^3/s]
v	Velocity of the parcel [m/s]
A	Cross section area [m^2]
ρ	Fluid density [kg/m^3]
F	External forces acting on the fluid [$kg\ m/s^2$]
i	Gradient of the channel
j	Frictional energy slope
n	Manning coefficient
R	Hydraulic radius [m^{-1}]

Table 2.1. Description of the parameters used in various equations

The right end side of the momentum equation has three terms: the first is the acceleration of the parcel due to the sum of all the external forces, the second term accounts for the change of momentum rate entering and exiting the section and the last term takes into consideration

eventual lateral inflows. The external forces typically considered for modelling the unsteady flow in a channel are: 1) gravitational force, 2) static pressure and 3) frictional forces. For a small slope i of the channel bed the three forces can be approximated as:

$$F_g = \rho g A i dx \tag{2.3}$$

$$F_p = -\rho g A i \frac{\partial h}{\partial x} dx \tag{2.4}$$

$$F_f = -\rho g A j dx \tag{2.5}$$

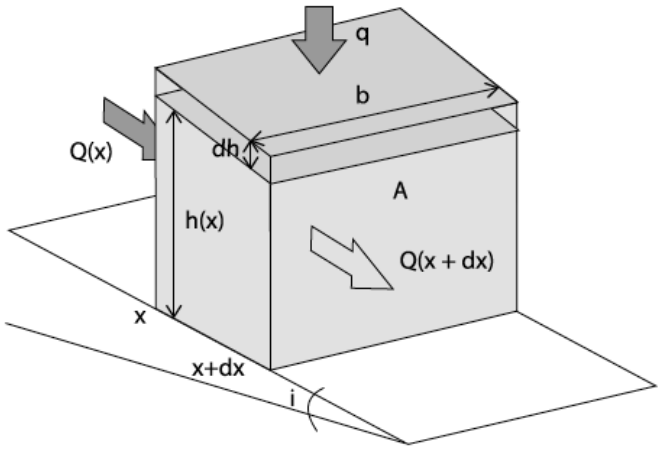

Figure 2.6 Definition of the quantities involved in the equations 2.1 and 2.2. for a small element of fluid (from Blatnik et al. 2020a*).*

Putting equations 2.3-2.5 into 2.2 and using the relation $Q = A\,v$ in eq. 2.1 we obtain the Saint-Venant equations:

$$b(h)\frac{\partial h}{\partial t} + A\frac{\partial v}{\partial x} + v\frac{\partial A}{\partial x} = q \tag{2.6}$$

$$\frac{\partial v}{\partial t} + v\frac{\partial v}{\partial x} + g\frac{\partial h}{\partial x} = g(i - j) + qv \tag{2.7}$$

One crucial parameter is the friction slope j, which takes into account the friction between the fluid and the channel bed. There are several empirical relations such as the Manning formula (Rossman, 2017):

$$j = \frac{n^2 Q^2}{A^2 R^{4/3}} \tag{2.8}$$

where n is the Manning empirical roughness coefficient and R is the hydraulic radius defined as the ratio between the cross-section area and the wetted perimeter (i.e. the perimeter of the channel section that is submerged).

Further simplifications to the SVe can be applied to reduce the number of model parameters or to speed up the computation: for instance, assuming no lateral inputs and neglecting pressure forces and acceleration terms, all the left-hand-side of 2.7 equals 0 leading to the so-called kinematic approximation of the Sve. Practically 2.7 becomes:

$$g(i - j) = 0 \tag{2.9}$$

And 2.6:

$$b(h)\frac{\partial h}{\partial t} + A\frac{\partial v}{\partial x} + v\frac{\partial A}{\partial x} = 0 \tag{2.10}$$

which implies that the friction slope equals the bed slope of the channel. Since no acceleration terms are present, the kinematic solution predicts a flood wave that travels along the channel with uniform velocity dependent principally on the Manning coefficient and on the slope of the channel. Such approach cannot model backwater effects and reverse flow in the channel. Further, assuming there are no temporal variations of discharge, reduces the SVe to a steady state equation for which eq. 2.8 is a solution.

2.3.2 Hydraulic modelling Software

For performing the simulations discussed in the thesis I relied on the Storm Water Management Model (SWMM) software provided by the US Environmental Protection Agency (http://www.epa.gov/ednnrmrl/models/swmm/index.htm). SWMM solves the full or approximated (kinematic approach) 1D-SVe equations for an arbitrary complex network of interconnected conduits. The program is an open source and offers a GUI for easily designing the drainage system. SWMM was firstly developed for simulating the sewage system, but as already outlined there are several applications for studying the karst hydrology as well.

The drainage system can be approximated by designing a network of nodes, to which three spatial coordinates are provided, connected by conduits. The user can assign to each channel different predefined or even customized cross sections and a Manning roughness coefficient. The different nodes act as storage units, if the user assigns a surface area (A) and a relation to model the water level dependence on A, but also as inlets/outlets. A recharge time-series (a

hydrograph) can be supplied to each node; alternatively, the user can also define sub-catchment areas with rain gauge observations that are then drained into the system through inlet nodes. Sketch 2.7 summarizes the various elements implemented for modeling in the SWMM software.

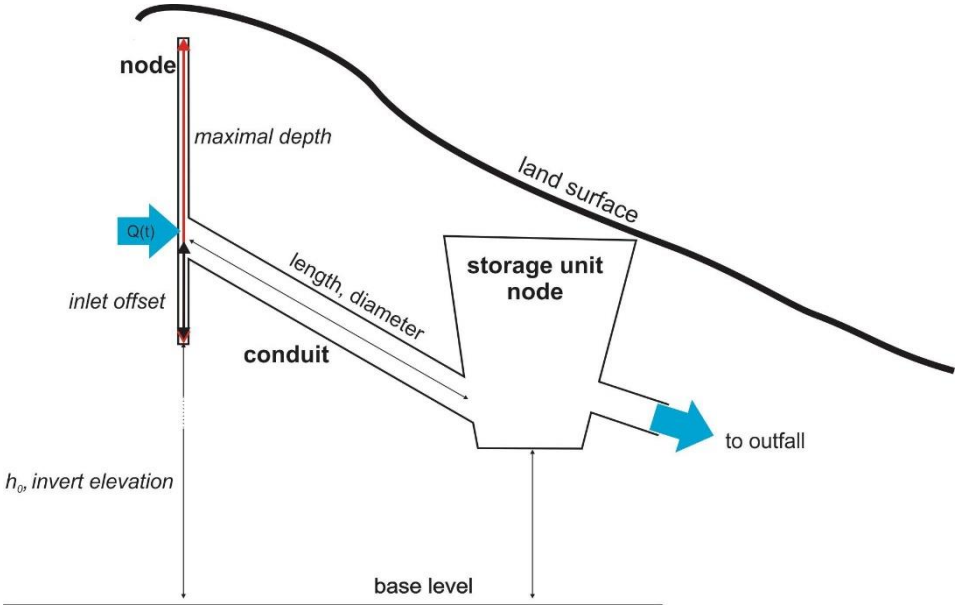

Figure 2.7 Sketch of the SWMM elements employed for constructing the hydraulic models (from Gabrovšek et al., 2018).

Once the network of nodes and conduits is defined, and the input is provided, the program numerically solves the SVe by a finite difference approach, exploiting the explicit forward Euler Method (Rossman, 2017). As already outlined, two approaches could be employed: full or kinematic approximation. I will use the full SVe solution, since back-water, reverse flow is expected in the Škocjan area and such phenomena cannot be taken into account in the kinematic approximation.

2.3.3 Hydraulic Model of the Classical Karst

Gabrovšek et al. (2018) produced a large scale hydraulic model of the whole Classical Karst plateau, exploiting the SWMM routines. The authors discretized the Reka drainage system with 34 conduits with different cross-sections and 31 nodes; the location and geometry of conduits were constrained by speleological observations where a direct access to the vadose zone was possible, otherwise the authors set a realistic initial guess for the geometry that was

sequently adjusted through an inversion procedure. The discharge input was taken from the Cerkvenikov Mlin time-series and was injected in the first node of the model, near the Škocjan caves.

To adjust the parameters, the authors employed an inversion scheme based on the Sambridge algorithm (Sambridge, 1999), that is particularly apt for highly non-linear problems such as that. The algorithm minimized the difference between observed and modelled water level in the various caves of the Classical Karst. A plan view and a vertical cross section along the water path of the model is shown in Figure 2.8.

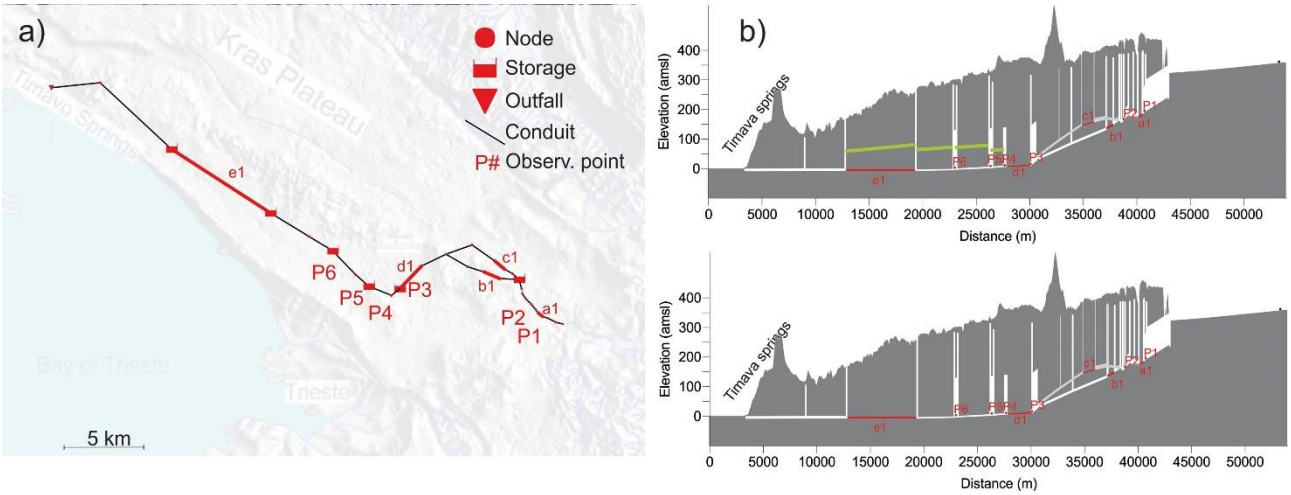

Figure 2.8 a) Plan view of the hydraulic model of Gabrovšek et al. (2018). Red lines: conduits for which the geometry is retrieved by inversion. b) Cross sections along the model; Top: model where the conduits in green reproduce a shallow drainage system with overflow channel; Bottom: model without the overflow channels. (from Gabrovšek et al., 2018*)*

In Figure 2.8 the red lines illustrate the conduits for which an optimized geometry was estimated based on the inversion procedure. In Figure 2.8a a plan view of the model is shown while in 2.8b two vertical sections are shown, which are relative to two slightly different models which have been tested. The model on the top includes a shallower drainage system constituted by some overflow channels, depicted in green, not present in the second model, shown in the bottom of Figure 2.8b.The results showed a satisfactory fit of both models: the inversion procedure improved the Root Mean Square error (RMS) and slightly changed the radius of some conduits as for instance one of the conduits that links the Škocjan cave to Kačna, which has a final diameter of 6.05 m (assuming a parameter range search of 6-8 m in the inversion routine). The model on the top slightly improved the residuals during large flood events. One of the most important outcomes of the research was, that the authors confirmed the important role of the Kačna cave during flood events in Škocjan. The hydraulic model in particular, showed that during large flood events firstly, the Kačna system is flooded, then a reverse flow causes the flooding of the Škocjan caves.

2.4 Preliminary hydraulic/gravimetric simulations for locating the gravimeter

Before gravimeter installation in July 2018, I performed some simple simulations of the expected gravity signals in order to:

1) Define the optimal installation site on the base of simulated amplitudes of the hydrologic induced gravity signals with respect to the noise performance of the gravimeter
2) Evaluate the typical duration of the gravity transients

To do this I modelled the hydraulic response of the Škocjan caves to 2 flood events and then the simulated water volumes were converted into a 4D water mass distribution for which the gravitational effect was calculated.

The events have been selected as representatives of a typical seasonal flood event and of an exceptional one; the recurrence time of the events has been assessed through a statistical analysis on the time-series of the Reka discharge recorded at Cerkvenikov Mlin.

2.4.1 Simplified Hydraulic model of the Škocjan caves

For this simulation I produced a model differing from that by Gabrovšek et al., 2018: my model simplifies the drainage system towards Kačna, but improves the geometry definition of the Škocjan caves. I employed SWMM routines as Gabrovšek et al. (2018) did in their paper. The Škocjan caves were discretized by three wide conduits of rectangular cross-section and a final small tunnel that simulates the series of channels linking the cave system to Kačna. Each conduit is characterized by a length, a mean slope and a Manning coefficient. Figure 2.9a shows a plan view of the 3D geometric model and Figure 2.9b presents a cross section traced along the axis of the channels. Table 2.2 reports the main model parameters. In my modelling procedure I use the hydrograph data recorded at Cerkvenikov Mlin station as input flow at node j1. One could question whether other water inputs along the path Cerkvenikov-Škocjan are present, as well as outlets or constrictions in the river channel that could alter the shape and the magnitude of the hydrographs. In fact, the distance between the two stations is in the range of 7 kilometers and there are no other tributary rivers; hence, the assumption seems reasonable.

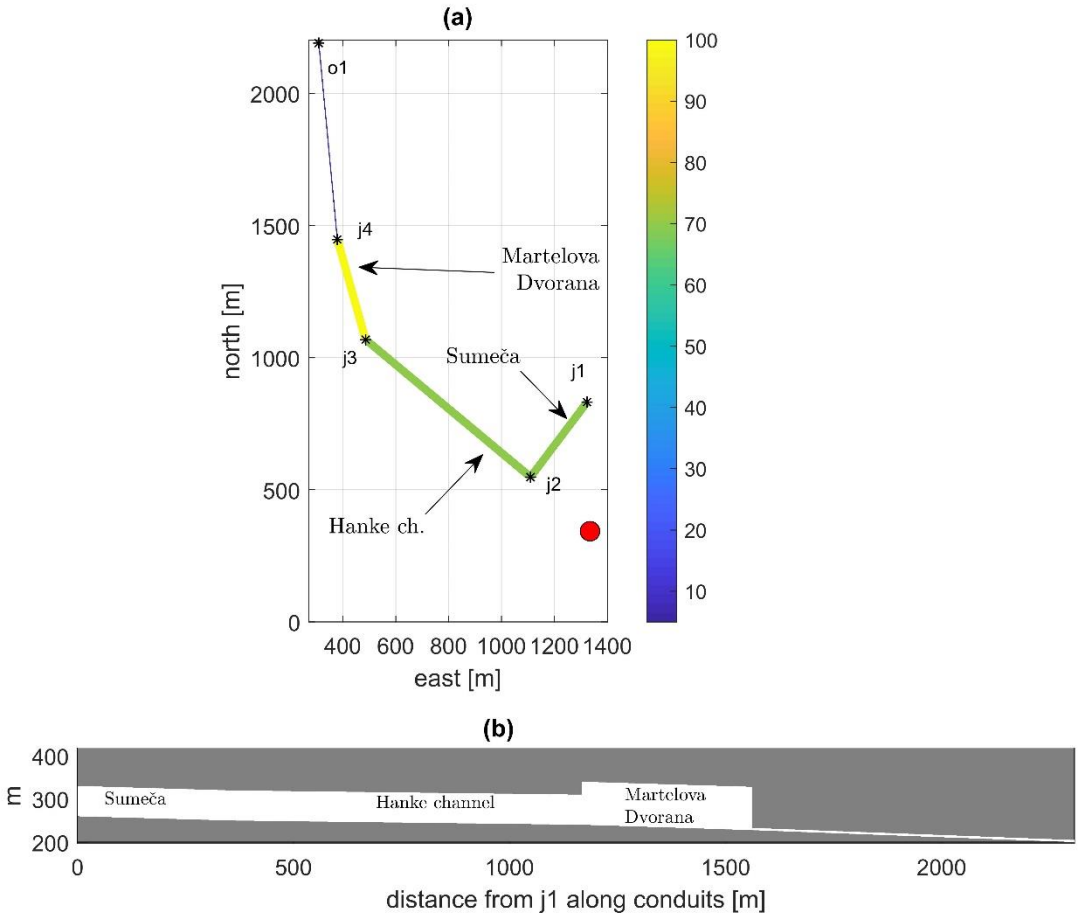

Figure 2.9 a) Plan view of the simplified hydraulic model of the cave; color code proportional to the height of the channel in meters. b) Cross section along the model showing the geometries of the cave. Red dot locates the info-center.

ID	Length [m]	Width [m]	Height [m]	Manning Coefficient	Slope	Input node ID	Output Node ID
c1	360	30	70	0.045	2 %	j1	j2
c2	800	30	70	0.045	2 %	j2	j3
c3	300	30	100	0.045	2 %	j3	j4
c4	800	4.5	5	0.045	2 %	j4	o1

Table 2.2 SWMM input model parameters.

.

The two investigated events occurred in May 2005 and in December 2008 (Figure 2.4). The first event had a peak discharge of 60 m^3/s and it has the typical magnitude of a seasonal event. The flood lasted for about 4 days. The second flooding episode is the December 2008 flood and has a peak discharge of over 200 m^3/s. It started on 10th December 2008 and ended on 14th December. In both cases the hydrographs were resampled in order to decrease the computational effort: the 2005 event was resampled with a 4 hours time-step while 6 hours time-step was selected for the 2008 event. The input hydrographs for the events are plotted in figure 2.10.

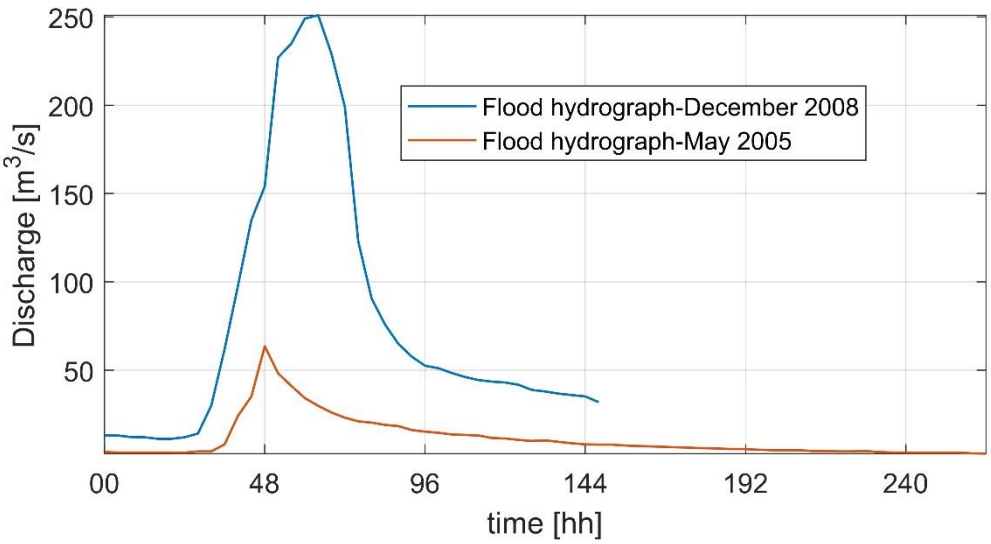

Figure 2.10 Input discharge curves injected at j1 for the hydraulic simulation.

By means of the SWMM software I calculated the expected levels in the nodal points along the water path inside the cave. I calculated the flows according to a dynamic wave solution, every 30 minutes since the selected time step satisfies the Courant-Friedrichs-Lewy condition (Courant et al., 1967) which is a criterion for avoiding numerical instability when solving the SVe (Rossman, 2017) through finite differences.

Node j4 that is located at the end of the Martelova, just before the constriction, is exploited as a control point of my modelling procedure because its level should be similar to the observed level at the diver placed in the Martelova Dvorana.

The water level time-series at node j4 calculated for the two events are plotted in Figure 2.11a and 2.11b together with the observed data from the divers.

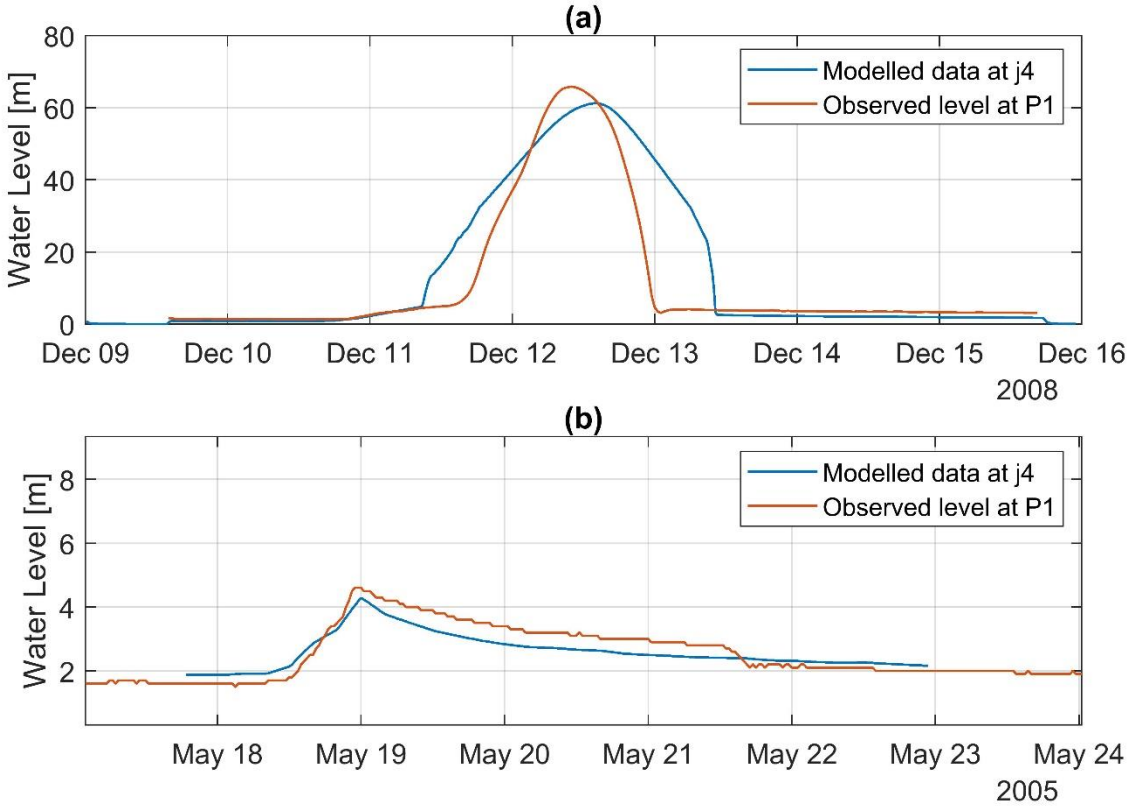

Figure 2.11 Comparison between observed and modelled water level at the node j4. The observed data are extracted from the Martelova level time-series. In a) the event in 2008. In b) the 2005 flood event.

Similarly to the events discussed in section 2.2, the two events are very different in terms of water level response: the 2005 event (plot 2.11b) is characterized by a rapid increase of the water level for about 12 hours followed by a slow exponential decay. The model explains very well the observed data, the shape and the magnitude are almost perfectly reproduced with a final Root Mean Square difference between observed and modelled data of 0.3 m. For the 2005 event I added a 1.5 m shift to the stage level, in order to get a better fit of the model. This shift represents the water column level in absence of the flooding events, when the flow is stationary; in any case this shift will not alter significantly the simulated gravity variations.

The 2008 event has a peculiar bell shape, with a rapid raise of the level and a very steep decrease immediately after the maximum is reached. The model overestimates the event duration, while the maximum water level in the hall is a little bit underestimated. The RMS for this event is about 10 m.

The discrepancy between observed/modelled data for this event could be due to the oversimplification of the model geometries especially in the final part of the model, towards the Kačna cave. However, I remark that the main characteristics of the flood events are captured by the model and the results are quite satisfactory for the gravity signal estimation.

2.4.2 Gravity signals associated to flooding events

Constrained by the hydraulic model simulations, I produced a 4D mass model of the gravity changes due to these two flooding events. The gravity anomalies were calculated discretizing the water mass in the cave at any given time of the simulation by an appropriate number of rectangular prisms. The prisms discretization is widely used in gravimetry for calculating the effect of complex mass distributions. The gravity effect of a prism can be calculated analytically (Nagy et al., 2000) as follows:

$$g_z = G\rho \left| \left| \left| x \ln(y+r) + y \ln(x+r) - z \, tan^{-1} \frac{xy}{zr} \right|_{x1}^{x2} \right|_{y1}^{y2} \right|_{z1}^{z2} \qquad (2.11)$$

Where r is the distance between the prism and the computation point, and $x1, x2, y1, y2, z1, z2$ define the spatial extension of the prism in a Cartesian reference frame; G is the Universal Gravitational Constant and ρ is the density of the prism. The effect of more complex geometries is computed by juxtaposing several prisms and exploiting the superposition principle. For the calculation I exploited the program Tesseroids (Uieda et al., 2016) that implements a routine to compute the gravity effect of a series of prisms through 2.11.

In order to build the prisms model, I discretized the base area of the conduits (figure 2.9) into small square areas of 10 m x 10 m. At each square I then associated the water level that occurs at a specific time and the water density (1000 kg/m^3). In fact, each prism model represents a snapshot of the mass variation during the flooding event.

The gravity field is then calculated for each time step in two points of interest: one is located approximately in the info-center (red dot in Figure 2.9a), where all the facilities for a continuous recording gravity meter are present. The other point is just above the Martelova Dvorana, where we expect the maximum gravity signal to occur. The height of calculation is set to be 420 m which is an average topographic quota for the area. The simulated results are compared to the noise levels of a spring based gravity meter, that are typically in the order of 10 nm/s^2.

The Figure 2.12 shows the simulations for the 2005 event at the info-center (plots 2.12a and 2.12b) and above the Martelova, while 2.13 shows similarly the results for the 2008 event.

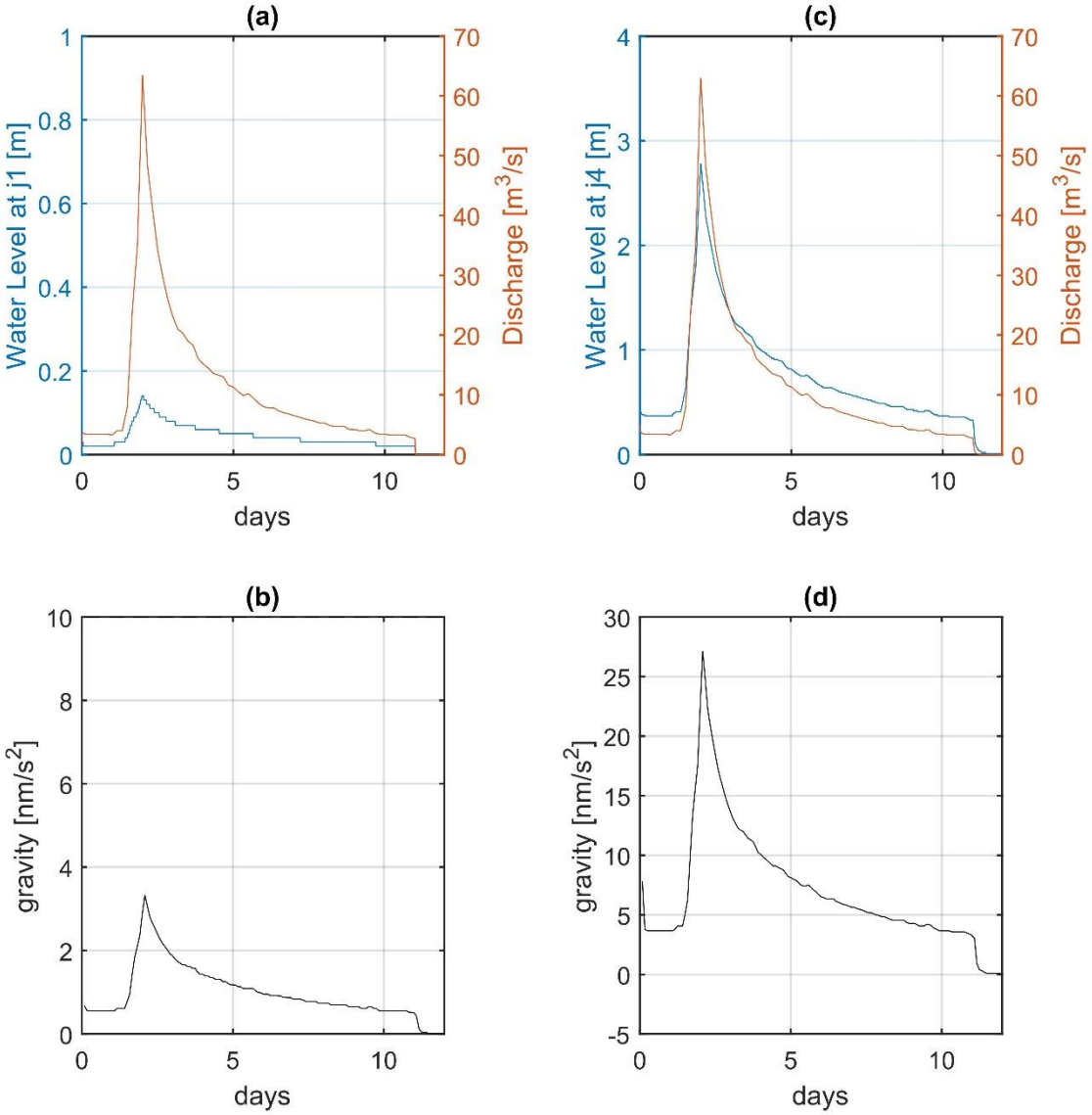

Figure 2.12 2005 flood event simulation: a) in red the discharge at Cerkvenikov Mlin injected at point j1; in blue the simulated water level at the node j1. b) Temporal gravity field variation due to the flooding event; the gravity field was simulated at the info-center. c) and d) same as a) and b) but the simulated water level in j4 and gravity simulation above the Martelova Dvorana (height 420 m a.s.l.).

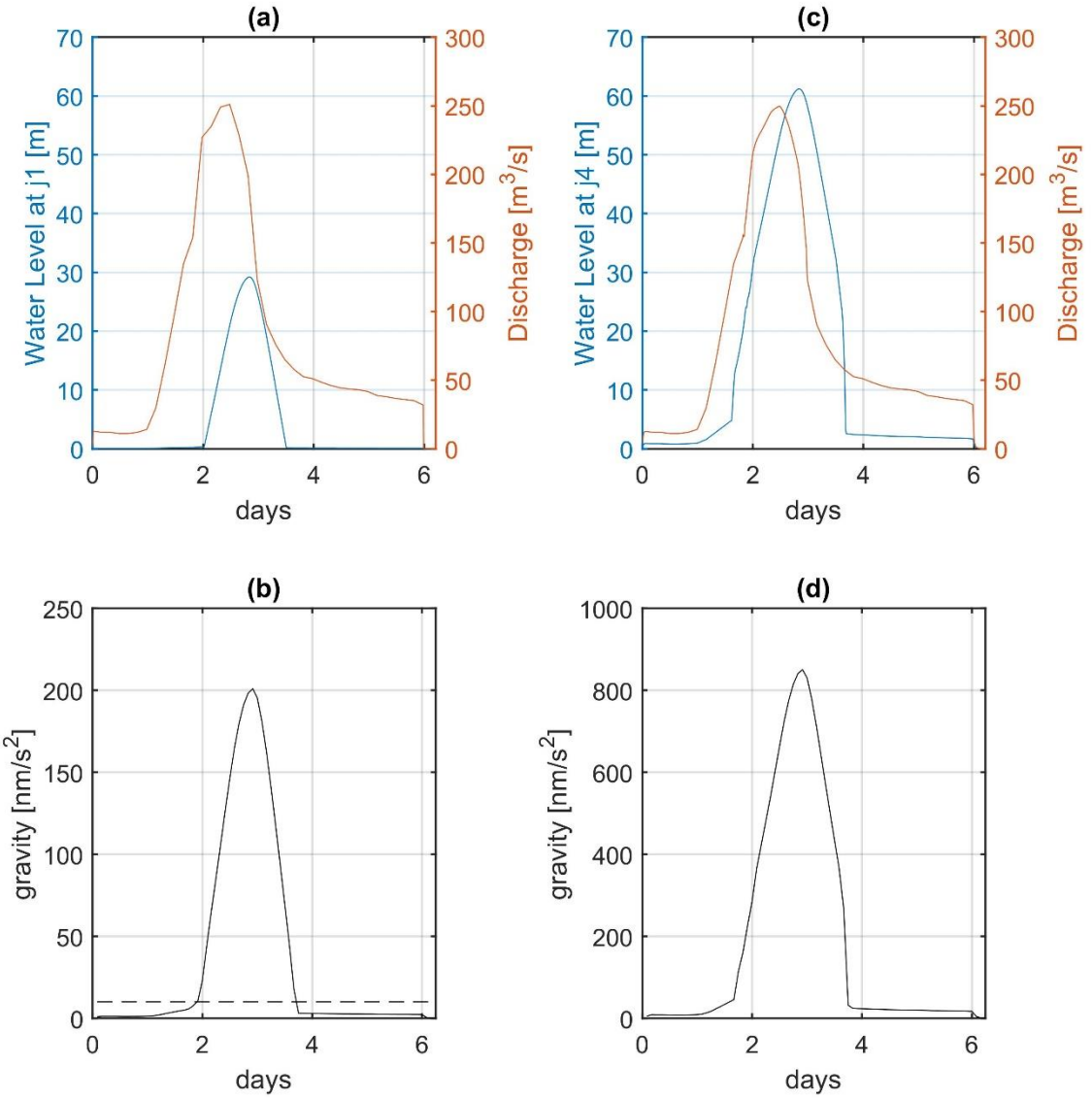

Figure 2.13 2008 flood event simulation: a) in red the discharge at Cerkvenikov Mlin injected at point j1; in blue the simulated water level at the node j1. b) Temporal gravity field variation due to the flooding event; the gravity field was simulated at the info-center. c) and d) same as a) and b) but the simulated water level in j4 and gravity simulation above the Martelova Dvorana (height 420 m a.s.l.). Dashed line 10 nm/s^2, noise level threshold for a typical spring based gravimeter.

Regarding the simulations directly above the Martelova both signals are larger than the noise level (10 nm/s^2). The 2005 event generates a signal with maximum amplitude > 20 nm/s^2; its shape is almost matching the shape of the flow hydrograph and the shape of the water level variation.

The 2008 event produces a signal with greater amplitude (> 800 nm/s^2), the shape of the gravity variation resembles the water variation of the cave.

The gravity anomalies simulated at the info-center are lower by almost a factor 5 with respect to the case where the meter is placed above the Martelova.

In terms of amplitude, the 2005 event seems to be below the noise threshold of common spring gravimeters, while the 2008 event gives an appreciable gravity maximum.

I inspected also gravity vs. discharge and gravity vs. stage at node j4 in a similar way as proposed in figure 2.4c and 2.4d. The hodograph of gravity in relation to discharge at j4 (figure 2.15) has a similar pattern to the stage j4 in relation to discharge, showing some inflection points. The first gravity inflection point is found for a greater discharge value than the first inflection point of stage j4. This is reflected in the relation of gravity to stage j4, where in the increasing phase there are two very different slopes relating gravity to j4: the first slope is much lower than the second one. This indicates that in the first phase the water-volume corresponding to an increase in 1 m stage level is smaller than the volume corresponding to an increase of 1m in stage in the second phase. Also gravity against discharge (figure 2.14b) and gravity against stage j4 (figure 2.14a) show a hysteresis effect, the gravity value being higher in the discharge phase compared to the recharge phase.

It is interesting to observe the stage j4 against the stage j1 (Figure 2.15), which shows that until j4 reaches a level of about 30 m, the j1 stage hardly increases. Only after j4 has reached the level of 30 m, does the stage j1 increase, demonstrating the conduits are filling up backwards, starting from node j4.

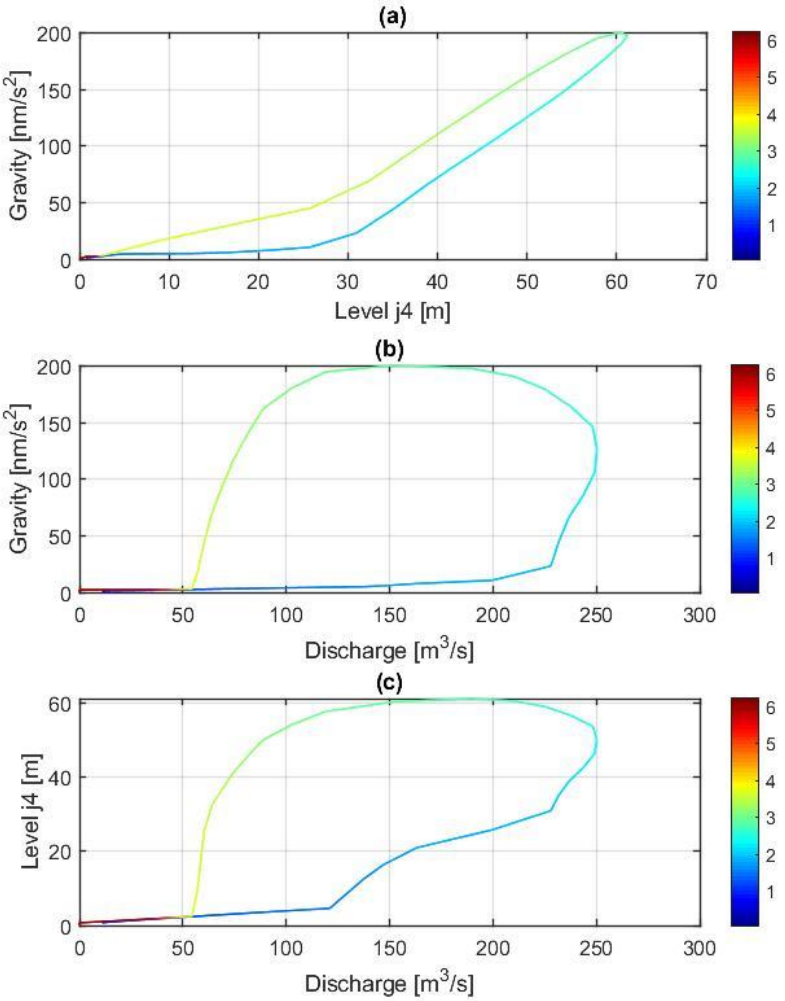

Figure 2.14. time evolution of gravity-level (a) gravity-discharge (b) and level-discharge; color code proportional to days passed since beginning of the simulation.

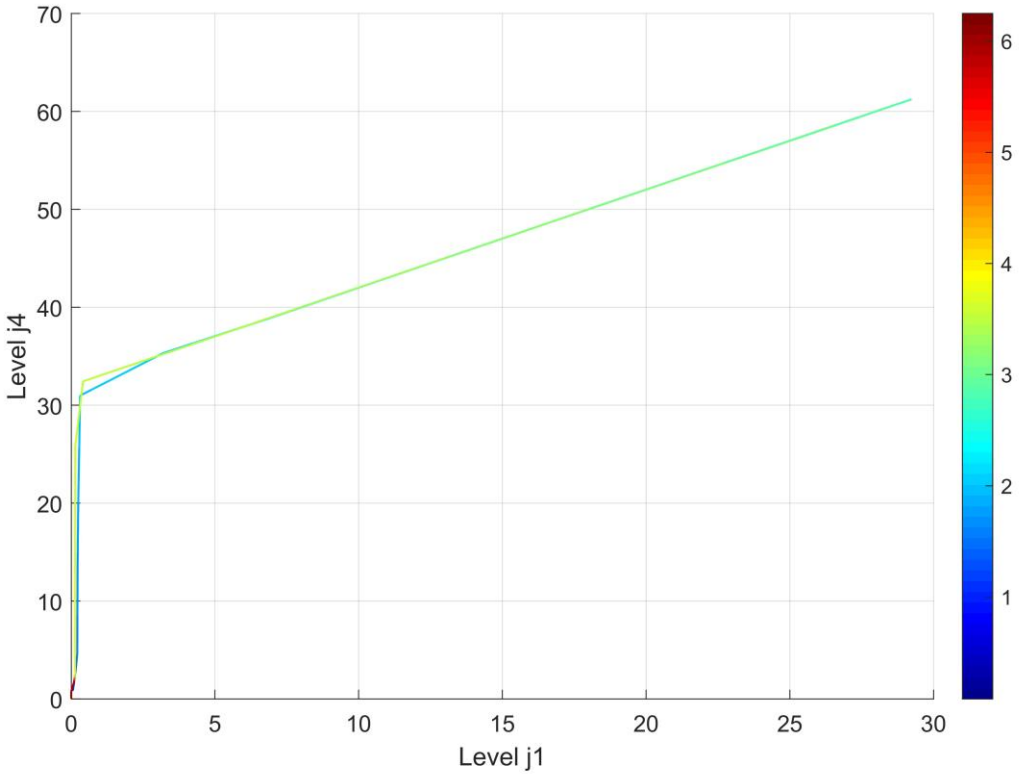

Figure 2.15 Level in j4 vs. level in j1 nodes.

Finally, I also evaluated the sensitivity of the gravity measurements to water level variations in each of the 3 chambers that constitute the cave system. In Figure 2.16a I simulated the gravity contribution at the info-center (black star) due to an increase of 1 m of water occurring in a cave portion delimited by two circles of radii r and r+dr. dr is assumed to be constant and equal to 20 m. The pixels included in the ring in Figure 2.16a are colored proportionally to the gravity change induced in the computation point. The procedure is iterated for all the sectors of the cave, progressively increasing the radial distance from the computation point. Similarly I calculated the effects changing the location of the point, which in Figure 2.16b is above the Martelova chamber. Obviously, the meter is mostly sensitive to water level variations occurring in the Sumeča and Hanke channels in case the instrument is placed in the info-center; while in the other case the measurements would be dominated by water level variations in the Martelova chamber.

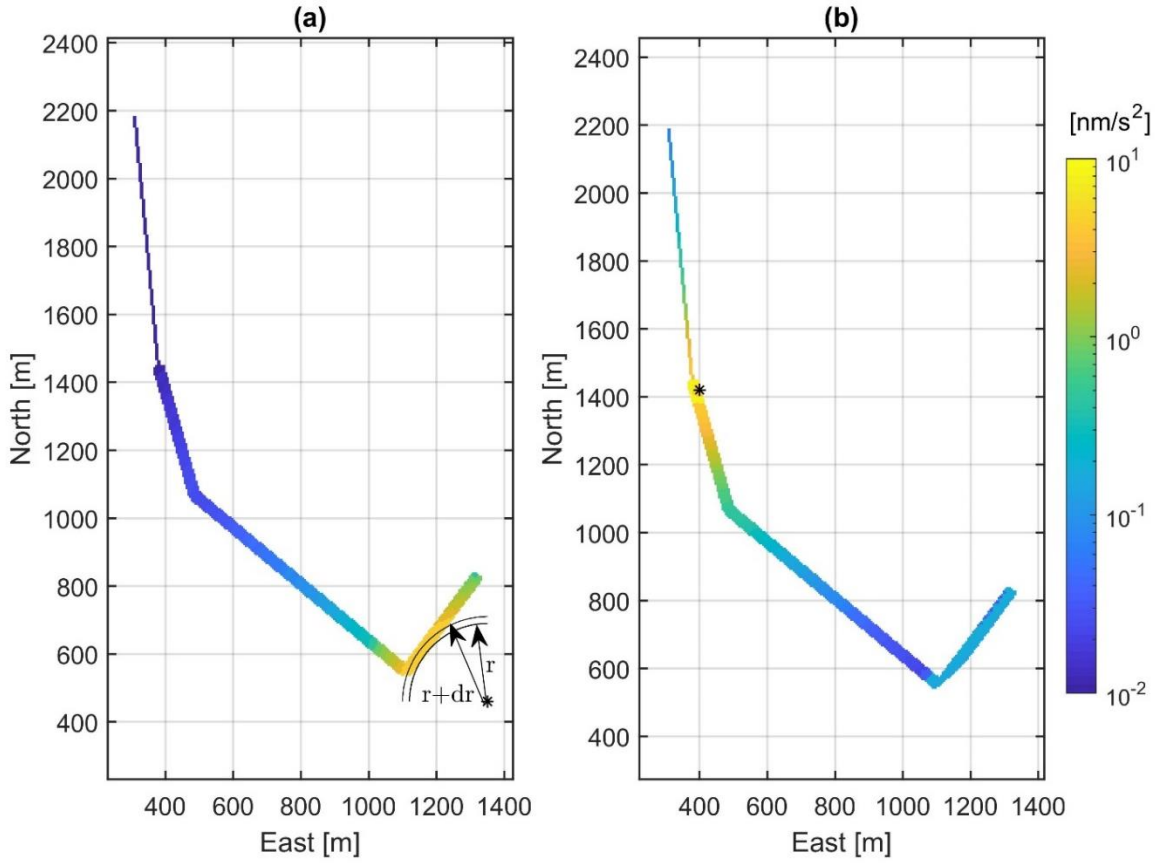

Figure 2.16 Sensitivity of the gravity measurements to 1 m variation of the water level in various cave sectors (see text for details).The two circle sectors, with radii r and r+dr, bound the area of the considered masses. a) Case where the meter is located in the info-center (black star). b) Case where the meter is installed above the Martelova chamber. The color scale is proportional to the gravity effect induced in the calculation point due to the water masses.

2.4.3 Recurrence time of flood events in Škocjan

From a 9-year long time-series of Reka discharge (2005-2014; Figure 2.17a) I extracted the local maxima in order to estimate the recurrence time of some flooding events occurring in the Škocjan area. More than 250 events were detected and their frequency distribution, according to the peak discharge, is reported in plot 2.17b.

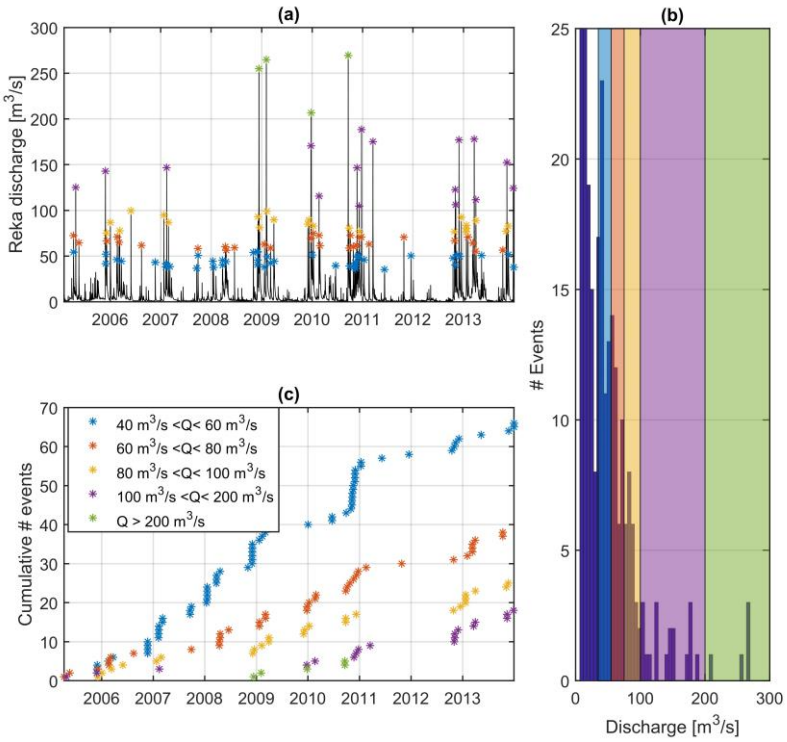

Figure 2.17 a) Reka discharge at Cerkvenikov Mlin; the peak discharge is marked with a star with colour-codes according to the classes identified in plot b). b) Frequency distribution of the peak discharge events of the Reka. The colours subdivide the frequency distribution into 5 different classes. c) Cumulative curve of number of events for each of the five classes.

The histogram has been subdivided into 5 classes, based on the frequency occurrence of the flooding events: each class is coded with a different colour. For each class I plot the cumulative curve of the flooding events that is shown in Figure 2.17c and which help in identifying yearly periodicities and rarer events.

The most frequent classes with discharge 40-60 and 60-80 m^3/s (red and blue stars) represent the typical seasonal events that prevalently occur in autumn or spring periods. With more than 60 events during the 9 years-long records, an average number of 7 events per year is expected for the first class, while for the second an average 4 events/yr has been estimated. The 2005 event, that is at the noise level of the instrument, pertains to this class.

The third class comprises events with peak discharge between 80 and 100 m^3/s (yellow stars) and shows an average recurrence period slightly major to the year. The last two classes comprise events that are more sporadic with recurrence times larger than 1 year. In the considered 9 years time-series, 5 events exceeded the discharge of 200 m^3/s, which could be considered as a threshold for flooding the Martelova Dvorana (e.g. event 2008).

2.5 Gravity station in Škocjan (SK1)

2.5.1 Location

On the base of the hydrologic/gravity simulations I decided to install a continuous gravity station in the info-center in Škocjan. The instrument is a spring-based gravimeter gPhone from MicrogLacoste, gently loaned by the Leibniz Institute of Applied Geophysics (LIAG) at Hannover.

The touristic information center is located nearby the caves at a distance of about 250 m from the Sumeča and Hanke channels (red dot in Figure 2.18a). The instrument, herein referred as SK1, is hosted in a quiet building with all the facilities indispensable for the functioning of the station: power supply and internet connection. A photo of the instrument in its polystyrene case is shown in Figure 2.18b.

Putting the instrument closer to Martelova chamber would be better for maximizing the hydrologic induced gravity signal, however, I preferred the info-center location regarding two aspects:

1) Logistic facilities available in the info-center
2) Higher sensitivity of the instrument to water variations occurring in sectors of the cave (Sumeča and Hanke) not yet monitored, unlike Martelova where the diver P1 is installed.

Based on this configuration I expect to better constrain the water dynamics in the cave and to obtain more reliable mass flux estimates.

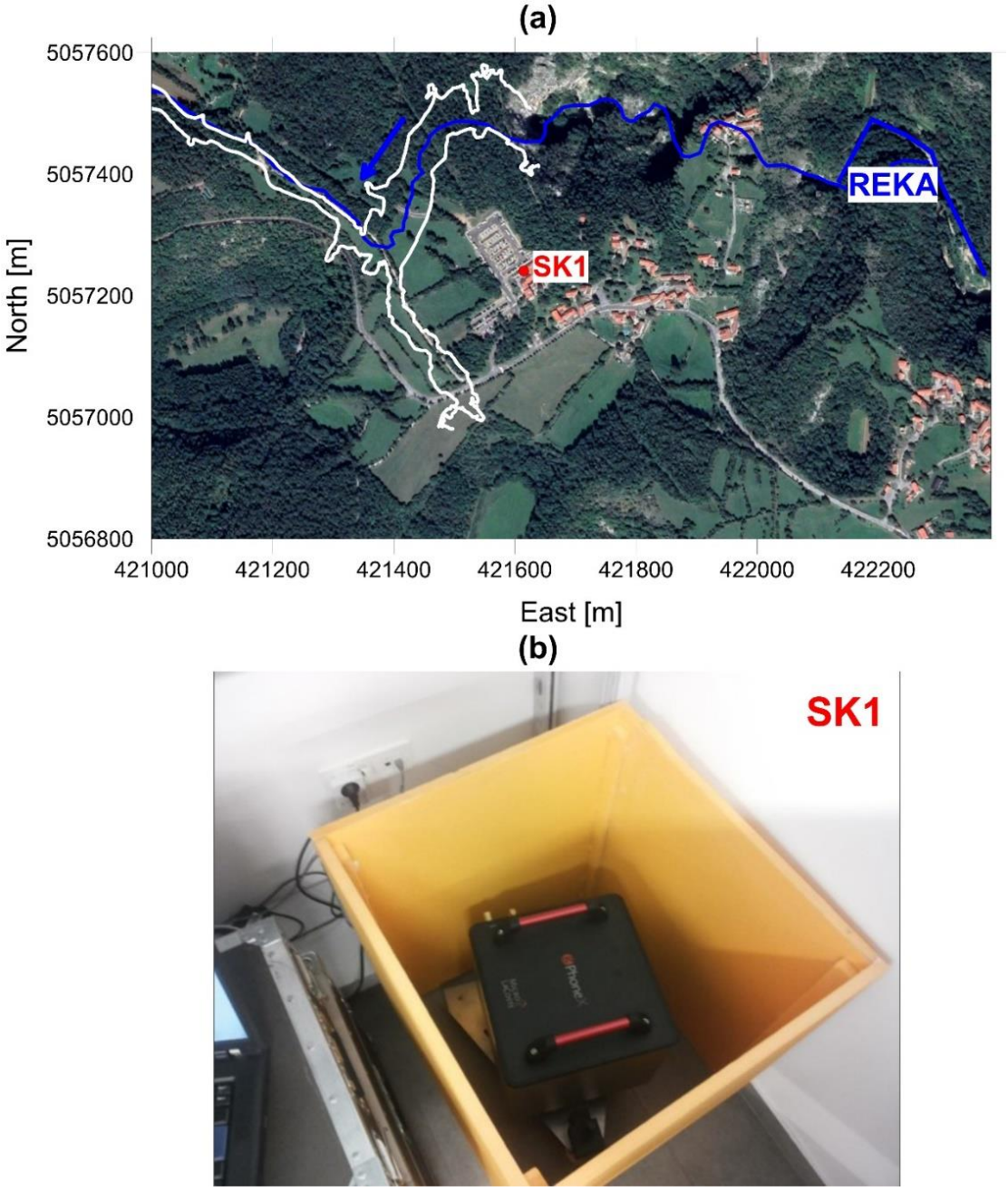

Figure 2.18 a) Location of the gravity station SK1. Blue line: Reka River path; white lines: outline of the Škocjan cave. Orthophoto from Google Earth. b) The gPhone gravimeter.

2.5.2 Instrument characteristics

The gPhone is a spring-based relative gravimeter which can only measure changes of gravity with respect to an arbitrary reference point (or an epoch). It is essentially based on the suspension system designed in the '30s by Lucien LaCoste, a physics student of Prof. Romberg, who assigned him the task of studying a vertical component seismometer with characteristics as good as the horizontal pendulum seismographs. LaCoste came out with a suspension scheme similar to the one shown in Figure 2.19a which is composed by a suspended mass attached at the end of a horizontal beam and by a zero-length spring that counterbalances the gravitational force (red arrow) exerted on the mass. In order to perform the measurement, the two torques (gravitational and elastic) acting on the mass must be equal: a temporal variation of gravity for instance alters the gravitational torque which should be counterbalanced by a slight change in the angle of the beam, resetting the system to the equilibrium position. At the end of the 1930/beginning of 1940 LaCoste-Romberg started producing and selling several gravimeters which become very popular mostly for geophysical exploration purposes.

In the old LaCoste-Romberg gravimeters the re-equilibrium of the mass was performed manually by the user through a dial that controlled the beam position. Nowadays most of the gravimeters, and the gPhone as well, are equipped with an electronic feedback system that measures the change in the gravitational force and automatically counterbalances it, keeping always the mass in the correct position. Additionally, in all the instruments, the measuring unit (i.e. the spring and the beam) are insulated from external variations of pressure and temperature. The first is guaranteed by enclosing the measuring unit into a sealed chamber, the second by controlling the temperature through an oven. The gPhone offers three sealed chambers for a complete insulation from pressure and humidity changes and an insulated double-oven for an accurate temperature control ($\Delta T < 0.1°$)

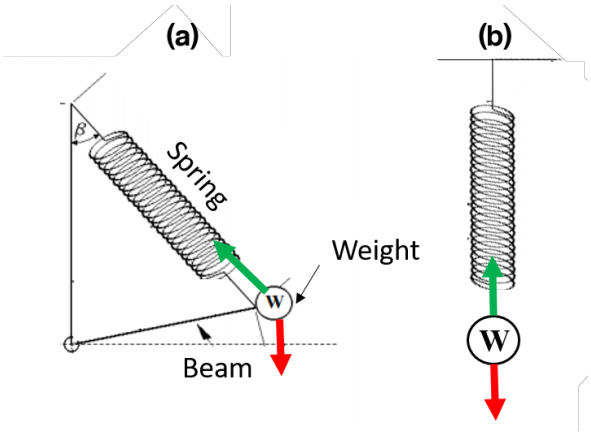

Figure 2.19 a) Simplified scheme of the LaCoste suspension. Green arrow elastic force; red arrow gravity force. Modified from the LaCoste-Romberg manual. b) Simplified scheme of a linear gravimeter.

The configuration invented by LaCoste assures higher sensitivity and hence higher precision compared to the linear gravimeters, in which the system is simply composed by a mass suspended on a spring (2.19b). Both the instruments suffer from the mechanical creeping of the spring which cause length variations of the spring and consequently fictitious non-linear gravity variations, such effect is known as gravimeter drift. By the way the LaCoste suspension has proven to display more stable and lower drift rates compared to the linear suspension configuration, albeit the instrument cannot compete with the Superconducting gravimeters which offer almost linear drift curves with very low drift rates.

Table 2.3 reports the main performance of the instrument, according to the MicrogLacoste specifications.

Reading Resolution	1 nm/s^2
Precision	10 nm/s^2
Dynamic Range	7 10^7 nm/s^2
Feedback Range	+/- 10^6 nm/s^2
Instrument Drift	< 5 10^5 nm/s^2/month

Table 2.3 Performance of the gPhone gravimeter according to house specifications.

Since the instrument is specifically designed for monitoring tiny time-variations of gravity due to different geophysical phenomena (tides, hydrology, volcano monitoring…) it is equipped with several environmental sensors:

1) a rubidium clock, which ensures high precision timing, fundamental for tidal analysis and earthquake studies

2) temperature and pressure sensors

3) tiltmeters for leveling control

All acquired data are digitized by an accurate 24 bit A/D converter and are saved into daily files at 1 s sample rate into two formats: a binary file and also ASCII text formatted according to the TSoft specifications (Van Camp & Vauterin, 2005). The data storage is guaranteed by a modern computer linked to the instrument, which also offers the possibility to remotely access and download the data and eventually intervene in case of malfunctioning of the instrument.

The SK1 station is additionally equipped with a tripod that allows the automatic compensation of the tilts; the tripod is an in house built feature from the LIAG.

2.5.3 Auxiliary data useful for gravity modelling

As it will be shown in the next chapter, the gravity measurements are influenced by a large number of geophysical phenomena that superpose each other complicating the interpretation of the transients related to the hydrology solely. Basically every phenomenon that induces a mass redistribution (atmosphere, hydrology, oceanic circulation…) will contribute to the observed gravity signal at the station, hence the raw gravity observations usually require a forward model approach to properly remove such effects and to insulate the component of interest.

Additionally, a precise interpretation of the hydrologic related gravity transient needs further constraints on the cave geometry in order to correctly build the 4D mass model of the flood events.

In the following paragraphs I present the datasets necessary to constrain the modelling of all these geophysical effects.

Tide Gauge observations

The SK1 station is less than 30 km away from the Adriatic Sea, which is responsible of creating periodic and aperiodic mass variations both tidal and non-tidal. As we will see, the periodic variations are of less interest since the correction is already integrated in the tidal analysis processing. On the other hand, the non-tidal aperiodic variations require a model of the mass variations occurring in the Adriatic basin. In order to build such model, I took advantage of sea level measurements, recorded by tide gauges at various harbors along the Adriatic coast.

The data from 5 harbors (Figure 2.20) were exploited. Three harbors (Koper, Monfalcone and Trieste) are within 40 km from the Škocjan caves; the other two stations cover the western Adriatic coast. Unfortunately, I did not have access to any data from Croatia which has the longest coastline on the Eastern side of the Adriatic basin. The selected harbors offer continuous data coverage for the whole period of operation of the gravimeter with temporal resolution of 10 minutes (Ancona, Koper, Trieste and Venezia) or 30 minutes (Monfalcone).

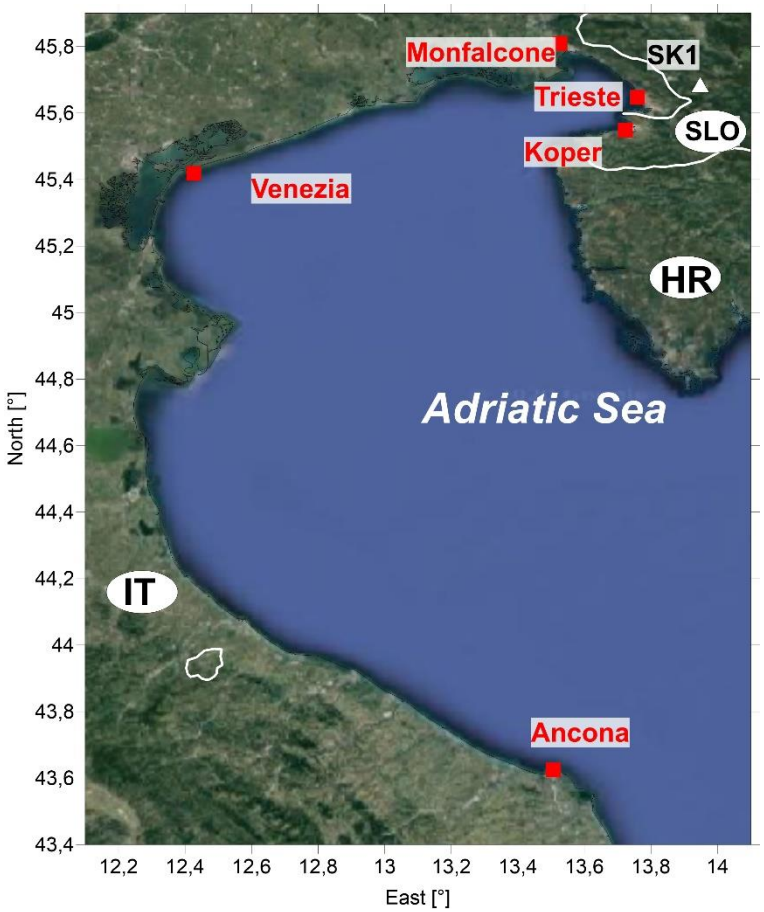

Figure 2.20 Location of the tidal gauges used for the study; the SK1 location is shown by the white triangle for reference. Basemap from Google Earth

Škocjan cave surveys and hydrology

In chapter 4 two gravity models of a flood event will be discussed: one of the simulations uses highly simplified cave geometries. The other employs a more realistic representation of the cave volumes constrained by different topographic surveys.

Figure 2.21 gives an overview of all available topographic data: the white lines show the location of 25 vertical cross-sections, while the green dots report the location of various levelling points. The whole survey is constituted by over 3000 points which mapped the internal morphologies of the cave and the topography of the dolines which host the Reka River before entering the cave system. Additionally, for the external areas I rely on the Lidar data acquired by ARSO, which covers the entire Slovenian territory with an uniform spatial resolution of 1 m.

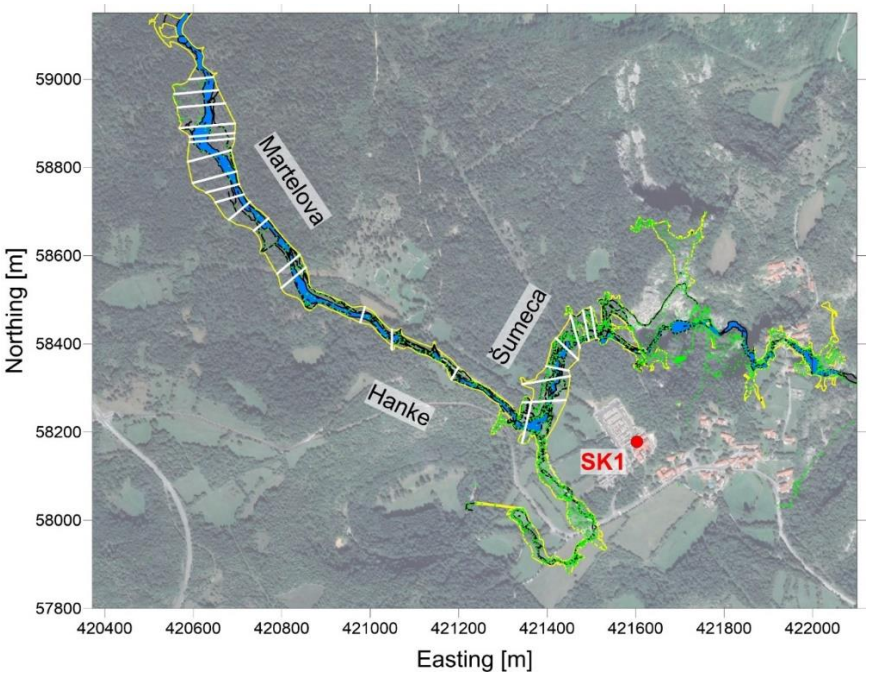

Figure 2.21 Overview of the topographic data available for the Škocjan area for the cave system. Green dots: quota heights that mapped the bed of the river; white lines: vertical sections inside the cave; yellow line: outline of the cave system. SK1 reports the gravimeter location.

Summary of datasets employed

Finally, several publicly available global databases, are exploited for correcting the gravity observations and their use is described in detail in the following chapter 3.

A summary of the auxiliary data is given in table 2.4, which reports the “source” and also spatial and temporal resolutions.

Dataset	Type	Temporal resolution	Spatial resolution	Source
Pressure measured at SK1	Pressure recorded by the gPhone barometer	1 s	-	Data of the station
Discharge Reka	Discharge Reka at Cerkvenikov Mlin	30 min	-	https://www.arso.gov.si/vode/podatki/amp/H9350_g_30.html
Diver Martelova	Water level variations in Martelova chamber	30 min	-	Data acquired by Karst Research Institute of Postojna
ATMACS model	Gravity effect of a 4D global atmospheric model calculated by the Bundesamt fur Kartographie und Geodaesie (BKG)	3 h	-	http://atmacs.bkg.bund.de/docs/lm-stations.php
GLDAS model	4D Global model of the soil moisture of the first 2 m of soil	3 h	1°	https://disc.gsfc.nasa.gov/datasets?keywords=GLDAS
Tide gauges	Tidal measurements of the sea level height at various locations	10 min or 30 min	-	Koper: https://www.arso.gov.si/vode/podatki/amp/H9350_g_30.html Trieste, Venezia, Ancona: https://mareografico.it/ Monfalcone: http://www.meteosystem.com/stazioni/fincantieri/
Lidar data	Topographic model of the Škocjan area	-	1 m	https://gis.arso.gov.si/evode/profile.aspx?id=atlas_voda_Lidar@Arso)
SRTM data	Toporgaphic model used for Classical Karst area	-	30 m	https://www2.jpl.nasa.gov/srtm/

Table 2.4 Accessory data for the SK1 station.

Chapter 3
Processing of the SK1 gravity data

Earth and marine tides, atmospheric pressure changes, non-tidal ocean components, tectonic and seismic activity are processes responsible for temporal changes of the gravity field which superpose to the hydrologic signal, the target of the study.

These phenomena occur at different temporal scales and require targeted approaches to efficiently remove their effects. For some of them, the application of suitable filtering procedures is sufficient (i.e. seismic noise), others require a modelling approach for keeping the 4D distribution of masses and loads (i.e. non-tidal ocean) into account. Finally, others require the development of empirical models estimated directly from the acquired data (i.e. Earth tides or atmospheric corrections).

In the following I detail the various processing steps used to isolate the hydrologic components. For each correction a general theoretical background is premised before discussing its effect and impact on the observed data of SK1. I begin with the largest contributions, the Earth and marine tides, succeeded by the atmospheric corrections; non-tidal ocean loading and far field hydrological effects are discussed afterwards.

3.1 Earth and Marine Tidal Correction

3.1.1 Introduction

The dominant contribution in most gravimetric recordings comes from the Earth tides which are responsible of gravity variations up to 3000 nm/s^2. The rotation of the Earth combined with the presence of a non-uniform gravity field induced by other celestial bodies results in tidal forces which cause spatial and temporal variations of the gravity field. These tidal forces are responsible also for the periodic deformation of the solid Earth, particularly evident in GNSS and tilt records, which in turn causes further gravity changes.

The temporal variations of these phenomena cover a wide spectrum of frequencies: the most important contributions in terms of amplitude are the diurnal and semi-diurnal periodicities,

however higher (ter-diurnal) and lower frequency (fortnightly, monthly…) tidal signals are also present and measurable by gravimeters. Over 200 years of tidal research have contributed in developing a solid theory which allows predicting amplitudes, frequencies and phases of over 20000 tidal constituents with high precision (< 1 nm/s^2). The study of Earth tides is an active research sector in solid Earth since they are invoked as a possible engine in driving geodynamic processes (Zaccagnino et al., 2020) and their analysis contributes to providing constraints on deep processes occurring in the mantle (Lau et al., 2017) and in the core (Rosat et al., 2017b).

The tidal forces are also responsible for exciting the marine tides which furtherly complicate the observed gravity signals. The marine tides occur at the same frequencies as the solid ones but their amplitudes and phases are rather different since they depend on the hydrodynamic response of oceans and sea to the tidal forcing. The combined effect of the solid and marine tides is observed in all gravity records and it is seen as mismatch between observed and theoretical amplitudes and phases. In continental areas, far from the sea, the marine effect is reasonably well corrected by including in the analysis a global marine tidal model (i.e. FES2014b; Carrère et al. (2016)). The model is usually accurate enough at least for the most important tidal constituents.

Body tides can be precisely predicted today by theoretical body tide models. Generally, this also holds for the effect of ocean tides provided the station is not too close to the sea coast. However, in case of the Classical Karst area even modern ocean tide models could suffer from their limited spatial resolution because of the proximity of to the Adriatic Sea. Therefore, direct forward modelling of solid Earth and marine tides would be mostly inadequate for correcting the observed data. In any case the performance of the correction should be tested with careful analysis. In order to optimally remove the tidal components, I employed the tidal analysis, a statistical approach which estimates the tidal parameters specific for a site directly from the observations. Through these site dependent tidal parameters, I can then obtain synthetic time-series of the expected tidal variation and then a residual gravity time-series.

Tidal analysis requires the knowledge of some elements of tidal theory in order to check the reliability of the obtained tidal model and also to recognize the limits of the gravimetric method. The comparison of the observed parameters with the theoretical ones could be also a good test for assessing the data quality of the station and investigate the various noise components affecting a site. Hence before discussing the SK1 tidal analysis results I present a short overview on the tidal theory and on the methods for estimating the site specific response to the tidal forcing.

3.1.2 Earth tides: tidal forces and potential

The Earth tides are the motions and changes in gravity potential occurring in the solid Earth induced by the tidal forces (e.g. Agnew, 2015). The tidal force is a differential force, induced by an external body, which appears between a point O on the Earth surface and the Earth center of mass C (Figure 3.1a). Instead of expressing the tidal forces, in gravimetry it is more convenient to work in terms of accelerations and define the vector **b** of the tidal accelerations**.** Tidal acceleration **b** results from the difference between the gravitational acceleration generated by the external body on the Earth surface ($\mathbf{a_P}$; red arrows in Figure 3.1a) and the orbital acceleration $\mathbf{a_0}$ (green arrows in Figure 3.1a). Neglecting the flattening of the Earth, **b** at the point O can be expressed mathematically as follows (Wenzel, 1996):

$$\boldsymbol{b}(O) = \mathbf{a_p} - \mathbf{a_0} = \frac{GM_m}{\rho^3}.\overline{\boldsymbol{\rho}} - \frac{GM_m}{R^3}\overline{\boldsymbol{R}} \tag{3.1}$$

where M_m is the Moon (or any external body) mass, ρ and R are the moduli of the vectors $\overline{\boldsymbol{R}}$ and $\overline{\boldsymbol{\rho}}$; R represents the distance between the two center of masses while ρ is the distance between O and the center of mass of the external body (Figure 3.1a). G is the Universal Gravitational constant equal to $6.67408\ 10^{-11}\ m^3/(kg\ s^2)$.

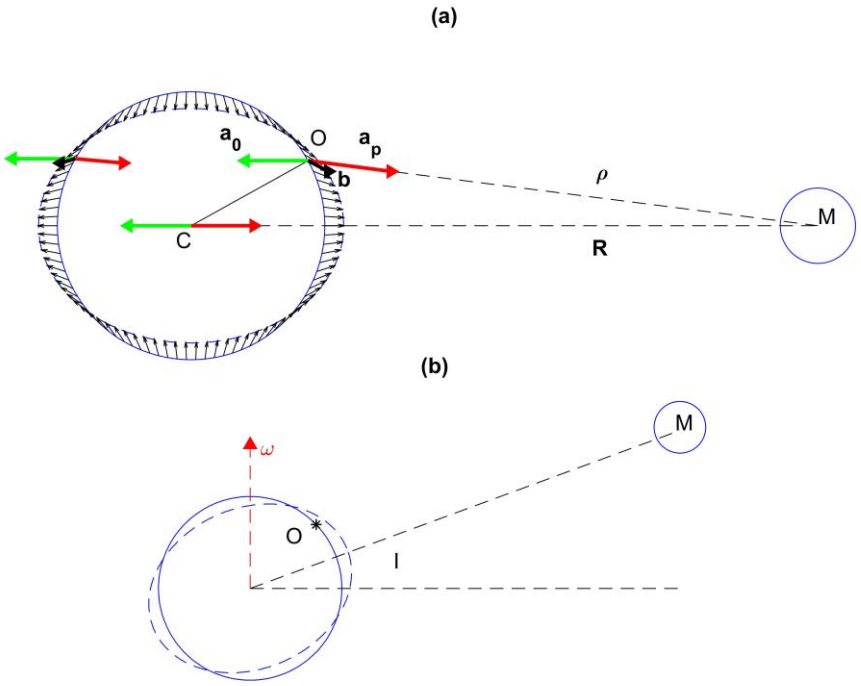

Figure 3.1 a) Effects of the tidal forces induced by the body M on the Earth. Green vector represents the orbital acceleration while the Newtonian attraction is reported in red; tidal accelerations are shown in black. b) Effect of the inclination (I) of the orbital plane of the Moon on the tidal bulge. ω reports the rotation axis of the Earth. The sketches are not representing the real proportions between the two bodies.

In Figure 3.1 I show a sketch of the Earth-Moon system as example and we see that these two accelerations ($\mathbf{a_p}$, $\mathbf{a_0}$) perfectly balance at the center of mass of the Earth. Contrarily, on the Earth's surface the gravitational acceleration varies depending on the distance to the center of mass of the tide generating body (Moon in this case); hence it could be locally larger or smaller than the orbital acceleration that is the same constant vector everywhere. Considering all points on the Earth's surface we obtain the pattern of tidal accelerations shown by the tiny black arrows in Figure 3.1a. We see that all the points in the equatorial regions are pulled radially outward while radially inward near the poles, resulting in the so-called tidal bulge.

The presence of the tidal bulge combined with the Earth's rotation (ω=Earth rotation speed in Figure 3.1) give rise to the semi-diurnal periodicity of the Earth tides, since every point of the surface experiences two tidal highs and two lows per day. We also observe that if the Moon orbital plane coincides with the equatorial plane we would observe only the semi-diurnal variations. The inclination of the lunar orbital plane, that is about 5°, introduces the diurnal variation. The sketch in Figure 3.1b illustrates the reason: due to the asymmetry of the tidal bulge with respect to the rotation axis now the point O will experience, additionally to the semi-diurnal variations, a further diurnal modulation.

The inclusion of ellipticity of Lunar and solar orbital motions further complicates the spectrum which finally includes several diurnal and semi-diurnal modulations as we will see later.

The mathematical description of the Earth tides becomes much more simplified if one introduces the Tidal potential (V'), instead of using tidal forces or accelerations, which is a scalar quantity and it is related to the tidal acceleration by:

$$\boldsymbol{b}(O) = \boldsymbol{\nabla} V'(O) \tag{3.2}$$

The gravitational potential, which is the tidal potential after the subtraction of the centrifugal potential, exerted by an external mass M in one point on the Earth surface (point O in Figure 3.1a) could be expressed by (Agnew, 2015):

$$V(O) = \frac{GM}{R}\left[1 + \left(\frac{a}{R}\right)^2 - 2aR\cos\alpha\right]^{-1/2} \tag{3.3}$$

where a is the equatorial radius and the term in the parenthesis appears from the law of cosines applied to the triangle COM in Figure 3.1a.

The term inside the square parenthesis in equation 3.3 can be expanded into a series of Legendre polynomials according to the following equation (Agnew, 2015):

$$V(O) = \frac{GM}{R}\sum_{n=0}^{\infty}\left(\frac{a}{R}\right)^n P_n(\cos\alpha) \tag{3.4}$$

In this series the term n =0 is constant in space, hence its gradient (the acceleration) is 0 (Agnew, 2015). The n =1 term corresponds to the orbital acceleration which is a constant and has to be subtracted to get the tidal acceleration (Agnew, 2015). After these considerations the expansion of the potential can be rewritten as:

$$V(O) = GM \sum_{n=2}^{\infty} \frac{a^n}{R(t)^{n+1}} P_n(\cos \alpha(t)) \tag{3.5}$$

In this formulation $\alpha(t)$ is the angle at the center of the Earth between the mass center of the tide generating body and the position O (angle between CO and CM in Figure 3.1). We can express the positions of the point O on the surface and of the external body in terms of geographic coordinates.

In particular the $\cos \alpha(t)$ term can be written as a function of latitude (φ), longitude (θ; assumed to be positive towards East) of the point O, the sidereal time (t') and other orbital parameters according to the following formula (Melchior, 1983):

$$\cos \alpha(t) = \sin \varphi \sin \delta + \cos \varphi \cos \delta \cos(\omega t' - \alpha 1 + \theta) \tag{3.6}$$

where δ is the angle of declination (angular distance north of the celestial equator; Figure 3.2), $\alpha 1$ is the so called right ascension term and ω is the sidereal velocity of Earth's rotation (see Figure 3.2).

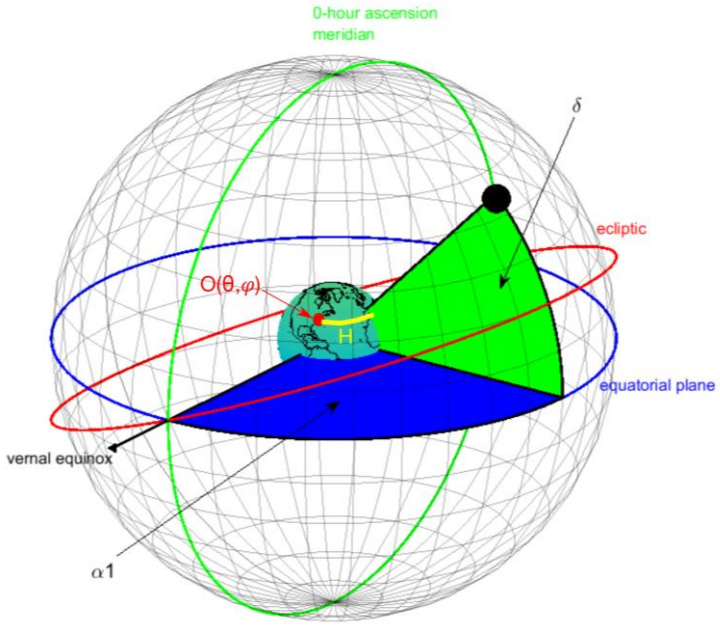

Figure 3.2 Definition of 0-h ascension meridian, right ascension angle $\alpha 1$ and declination of the Moon (shown as black dot). The observation point O (θ , φ) is reported in red and the hour angle is reported in yellow.

Inserting eq. 3.5 in eq. 3.4 and exploiting the Legendre addition theorem one could rewrite the tidal potential in terms of an expansion in spherical harmonics (SH):

$$V(t) = GM \sum_{l=2}^{\infty} \frac{a^l}{R(t)^{l+1}} \frac{1}{2l+1} \sum_{m=1}^{l} P_l^m(\sin\delta(t))\, P_l^m(\sin\varphi) \cos m(\omega t' - \alpha 1 + \theta) \tag{3.7}$$

where P_l^m are the associated Legendre functions. The term $(\omega t' - \alpha 1)$ is known as H, the local hour angle (difference in longitude between O and the tide-generating body).

Because the ratio $\frac{a}{R(t)}$ is about 1/60 for the moon and 1/23000 for the Sun the series of the potential rapidly converges. The dominant signals come from the degree 2 terms; low noise superconducting records are capable of detecting up to degree 4 terms relative to Sun and Moon. The influence of other planets is 5-6 orders of magnitude lower with respect to the lunisolar dominant components (Agnew, 2015), hence practically impossible to the detect with the actual instrumentation.

Considering only the expansion up to the second order one obtains:

$$\begin{aligned} V_2^2(\varphi,\theta,a) + V_1^2(\varphi,\theta,a) + V_0^2(\varphi,\theta,a) \\ = GM \frac{3a^l}{4R^{l+1}} \begin{cases} \cos^2\varphi \cos^2\delta \cos 2H + \\ \sin 2\varphi \sin 2\delta \cos H + \\ 3(\sin^2\varphi - 1/3)\,(\sin^2\delta - 1/3) \end{cases} \end{aligned} \tag{3.8}$$

The three terms inside the graph parenthesis are called ‘tidal species’ and correspond to different temporal periodicities and spatial patterns. The first term corresponds to the tidal potential $l = 2$ and $m = 2$ term; this functional is called ‘sectorial function’ and it is shown in the right plot of Figure 3.3. The argument of $\cos 2H$ contains 2ω which implies a semidiurnal periodicity.

The central plot of Figure 3.3 shows the tidal potential for $l = 2$ and $m = 1$, which correspond to the second term in eq. 3.8 and it is known as the ‘tesseral function’. In this case the periodicity is diurnal.

The last term is a static term, it is known as ‘zonal function’, and this is the only term in the expansion of equation 3.8 that alters the principal moment of inertia. It contains the long period tidal components.

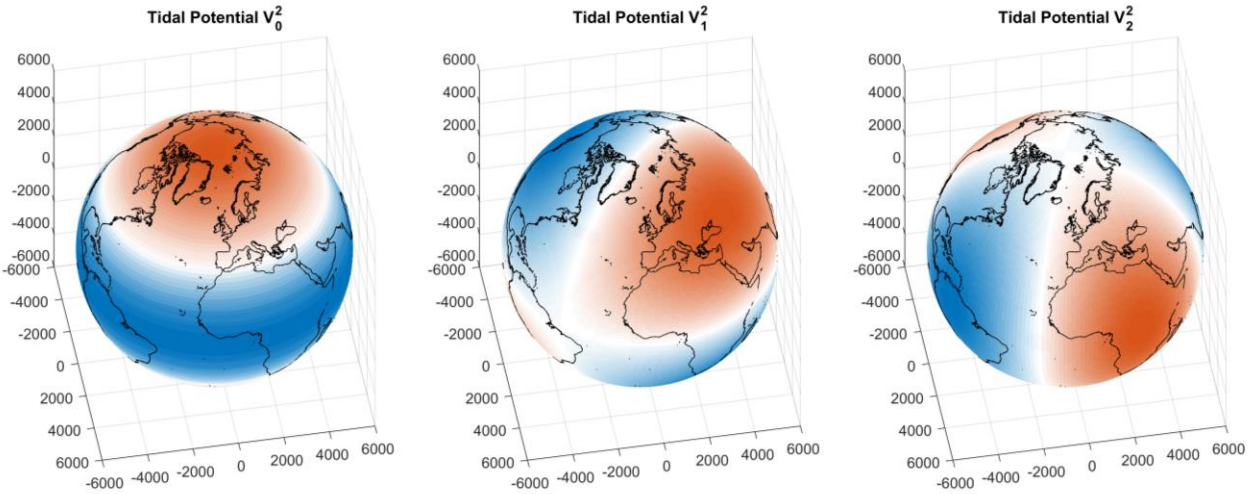

Figure 3.3 Spatial patterns of the Tidal Potential corresponding to Degree 2 and different orders. From left to right m=0 (long period tides); m=1 (diurnal variations) and m=2 (semi-diurnal variations).

In this development the gravity and tilt variations can be calculated by taking the gradient of the potential (i.e. eq. 3.7). Putting typical astronomic constants for the Moon into the expansion developed up to order 2 gives gravity variations in the range of +/- 0.082 10^{-5} m/s^2. The Sun contributes by a tidal signal of +/- 0.0379 10^{-5} m/s^2 amplitude.

To be more precise equation 3.7 allows the calculation of the potential at any point on the Earth surface by expliciting the terms $\sin\delta$, the $\frac{a^l}{R(t)^{l+1}}$ through linear combinations of small integer numbers (positive and negative) and six astronomic parameters. These six astronomic parameters describe the position of the Earth and the external bodies with respect to an absolute astronomic reference system.

The astronomic parameters which are angles, calculated with respect to the mean instantaneous vernal equinox, are reported in Table 3.1.

τ	mean lunar time
s	mean tropic longitude for Moon
h	mean tropic longitude of the Sun
p	mean tropic longitude of the lunar perigee
N'	mean tropic longitude of the ascending lunar node
p_s	mean tropic longitude of the perihelion

Table 3.1: astronomical parameters for Sun and Moon.

Previous astronomical studies (see Melchior, 1983) provided functions describing the temporal variations of these 6 angles. For instance I report the mean tropic longitude for the Moon parameter s:

$$s(T) = 270.43659° + 481.26789057° \, T + 0.000198° \, T^2 + 0.0000002° \, T^3 \qquad (3.9)$$

where T is the time in Julian centuries starting with $T = 0$ on the 31st December 1899 at 12 h.

The substitution into equation 3.7 leads to the appearance of several new tidal species. For the semi-diurnal period I report two examples, taken from Melchior (1983), of tidal species with their associated periods.

- $M_2 = 0.9208 \cos 2\dot{\tau}t$ with the argument $2\dot{\tau} = 28.9841042 \frac{^\circ}{h}$ corresponding to a period of 12 h 25 m 14 s
- $L_2 = 0.0823 \cos(2\dot{\tau} + \dot{s} - \dot{p})t$ with the argument $2\dot{\tau} + \dot{s} - \dot{p} = 30.0821372 \frac{^\circ}{h}$ corresponding to a period of 11 h 58 m 2 s

The frequencies reported above include only the lunar effect: similar calculations could be performed for the Sun and other bodies. The M_2 and L_2 represent a particular notation which was introduced by the pioneering works of Thomson and Darwin (e.g. (Agnew, 2015; Melchior, 1983)) in order to refer to particular tidal species. The notation is available only for the largest species but in any case is still widely adopted by both the geodetic and oceanographic communities. In the following table 3.2 I report the Darwin Symbols of the main diurnal and semi-diurnal species sorted by their amplitudes, according to Agnew (2015).

Amplitude[m]	Frequency [cpd]	Darwin Symbol	Amplitude[m]	Frequency [cpd]	Darwin Symbol
Diurnal			**Semi-diurnal**		
0.36864	1.0027379	K_1	0.63221	1.9322736	M_2
0.26223	0.9295357	O_1	0.29411	2	S_2
0.12199	0.9972621	P_1	0.12105	1.895982	N_2
0.05021	0.8932441	Q_1	0.07991	2.0054758	K_2
0.02062	1.0390296	J_1	0.02299	1.9008389	ν_2
0.02061	0.9664463	M_1	0.01933	1.8645472	μ_2
0.01128	1.0759401	OO_1	0.01787	1.9685653	L_2
0.00953	0.898101	ρ_1	0.01719	1.9972622	T_2
0.00801	0.8618093	σ_1	0.01602	1.8596903	$2N_2$
0.00713	0.9945243	π_1	0.00467	1.8282556	ε_2
0.00664	0.8569524	$2Q_1$	0.00466	1.9637084	λ_2
0.00525	1.0082137	ϕ_1			

Table 3.2 Largest tidal harmonics, for n = 2 (Agnew, 2015). *The amplitudes are expressed in terms of change in elevation of the geoid, which is calculated dividing the potential V by g (the gravity acceleration at the Earth's equator).*

Including the astronomical arguments into the tidal potential we obtain (Wenzel, 1996):

$$V(t) = D \sum_{l=2}^{n} \frac{a^l}{R^l} \sum_{m=0}^{l} \Gamma(\varphi)\, P_l^m(\sin\varphi) \sum_{i=1}^{N} [C_i^{lm}(t) \cos(\alpha_i(t)) + S_i^{lm}(t) \sin(\alpha_i(t))] \tag{3.10}$$

where D and $\Gamma(\varphi)$ are normalization constants C_i^{lm} and S_i^{lm} are the time dependent coefficients calculated according to:

$$\begin{cases} C_i^{lm}(t) = C0_i^{lm} + C1_i^{lm} t \\ S_i^{lm}(t) = S0_i^{lm} + S1_i^{lm} t \end{cases} \tag{3.11}$$

while $\alpha_i(t)$ is obtained from:

$$\alpha_i(t) = m\theta + \sum_{j=1}^{J} k_{ij}\, arg_j\,(t) \tag{3.12}$$

k_{ij} are small integer numbers (positive or negative) given in a specific catalogue, while the arg_j are the six astronomic arguments provided as polynomials in time, in a similar way as shown for $s(T)$ in eq. 3.9.

An example of k_{ij}, $C0_i^{lm}$, $C1_i^{lm}$, $S0_i^{lm}$, $S1_i^{lm}$ is given in Table 3.3, where I report an excerpt of the tide-generating potential (TGP) catalogue of Hartmann and Wenzel (1995). $\Gamma(\varphi)$ and D are set to unity. This catalogue, on which I rely for the calculations in SK1, contains over 12000 coefficients, but here I show only few of them near the M_2 constituent. From equation 3.10 we can calculate the gravity accelerations just taking the radial derivative of the potential:

$$b_r(t) = -D \sum_{l=2}^{n} l \frac{a^{l-1}}{R^l} \sum_{m=0}^{l} \Gamma(\varphi)\, P_l^m(\sin\varphi) \sum_{i=1}^{N} [C_i^{lm}(t) \cos(\alpha_i(t)) + S_i^{lm}(t) \sin(\alpha_i(t))] \tag{3.13}$$

Body	l	m	τ	s	h	p	N'	ps	f [°/h]	f [cpd]	C0	S0	C1	S1	name
MO	2	2	0	0	0	0	0	0	28.98410424	1.932273616	12356348081	0	130692	0	M_2
SU	2	2	0	0	0	0	0	0	28.98410424	1.932273616	1071	0	0	0	
MO	4	2	0	0	0	0	0	0	28.98410424	1.932273616	-756151	0	-910	0	
MO	3	2	0	0	0	0	1	0	28.9841062	1.932273747	0	9221	0	0	
MO	2	2	0	0	0	0	2	0	28.98410816	1.932273877	5900052	0	-974123	0	
MO	4	2	0	0	0	0	2	0	28.98410816	1.932273877	-325	0	0	0	

Table 3.3 Excerpt from the tidal potential catalogue of Hartmann & Wenzel (1995) *around M_2.*

3.1.3 Tidal Parameters and Tidal analysis

The TGP allows the direct computation of the gravity time variations on the Earth through eq. 3.13: these variations correspond to the Newtonian effect caused by the external celestial bodies to the surface of the Earth. However, correcting the gravity observations with 3.13 will lead to several periodic residuals in the exact same frequency bands. This is due mainly to other three contributions not modelled up to now:

1) Elastic response of the Earth: tidal forces cause the deformation of Earth shape which in turn results in additional gravity changes.
2) Oceanic tides: they are also responsible for further deformation (loading) and extra attraction. Moreover, they induce time-shifts, since the ocean tides are rarely synchronous with the solid Earth tides.
3) Atmospheric loading contribution

Modelling the deformation induced by tidal forces or atmosphere/oceanic load is usually done employing set of dimensionless numbers (Love-Shida numbers for a body force and load Love numbers for surface loading processes; Farrell (1972); Love (1909)) which depend on the potential degree. Through various combinations of these numbers I am able to predict the deformation and gravity variation on the surface of a spherical elastic Earth in response to a load or a tidal potential variation. The theory has progressed significantly in the past 100 years and now includes modelling of inelasticity (which leads to the appearance of complex Love numbers), Earth's flattening and non-hydrostatic conditions.

Including these effects will certainly improve the residuals, however, near coastal areas the oceanic corrections could not be enough accurate for removing all the contributions.

Hence in order to correctly estimate the tidal parameters, the classical approach is to perform the tidal analysis in which the Earth's response to TGP is estimated directly from the observations retrieving a local tidal model. Obviously if the ocean loading plays an important role in the station the response will be influenced as well by the oceanic component.

The Earth response can be described for each tidal constituent through two parameters: δ, the amplitude factor and the phase κ. According to Dehant et al. (1999), δ is defined as "the transfer function between the tidal force exerted along the perpendicular to the ellipsoid and the tidal gravity changes along the vertical as measured by a gravimeter". The phase κ, provides the time delay (expressed in °) between the observed tidal response and the theoretical tidal potential.

Figure 3.4 presents a vector representation of these quantities. **O** represents the observation vector with its δ factor and phase κ; A is the amplitude of the theoretical tidal gravity vector at the given location. Corrections for ocean loading, if supplied, could be expressed as well in terms of their amplitude and phase shifts (with respect to the solid Earth tides). In Figure 3.4 the oceanic load vector is **L**, with its amplitude L and phase λ. The vector $\mathbf{O_c}$ is the observation vector corrected for the ocean loading, while **X** is the residual vector resulting from subtracting

the theoretical response **EM** from $\mathbf{O_c}$. In a pure theoretical case of a spherical infinitely rigid Earth without oceans the δ factor will be equal to 1 and $k = 0°$. In a more realistic case, of an elastic Earth the δ factor rises to a factor about 1.16, so the contribution of the deformation is about 16 % of the attraction.

Including inelasticity causes δ to become complex number and hence $k \neq 0°$. In any case in the diurnal and sub-diurnal bands the contribution of inelasticity is very small.

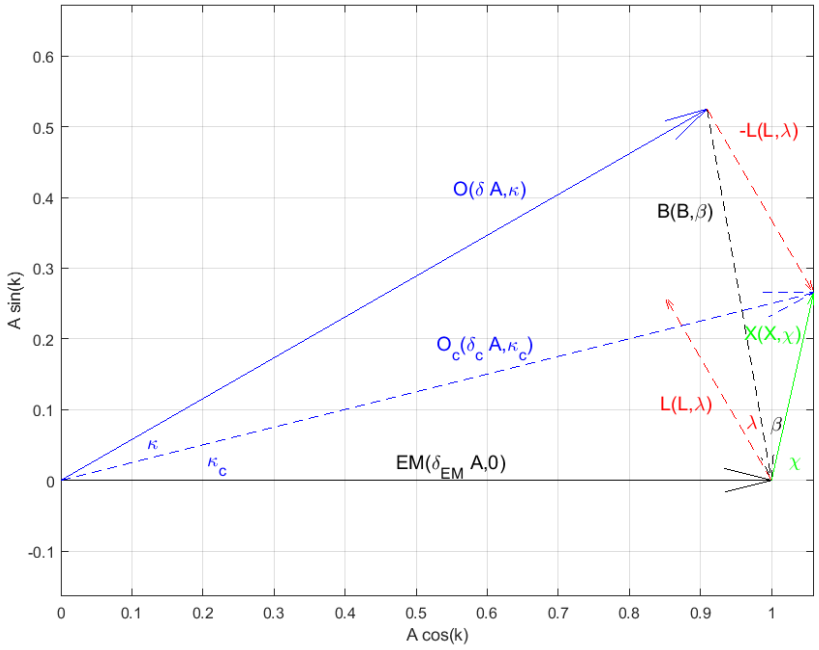

Figure 3.4 Vector diagram of tide and loading vectors. O is the observed vector, which is defined through the phase κ and the amplitude of δA where A is the theoretical amplitude and δ the delta factor from the tidal analysis. L is the oceanic loading vector. B is the vector of the residuals between O and the theoretical response. O_c is the observed vector corrected for the oceanic loading contribution; δ_c is the δ factor corrected for the oceanic loading and κ_c the observed phase corrected for the oceanic contribution. δ_{EM} is the theoretical δ factor for an Earth Model. χ is the residual vector given by the difference between the observations corrected for the oceanic effects and the theoretical response of the Earth.

We have already introduced the tidal analysis which is a procedure for estimating the tidal parameters from the gravity observations and compare the response with the theoretical predictions of the tidal theory. The theoretical response is calculated from the TGP catalogue exploiting eq. 3.12 and it is computed at a specific location and epoch. The observed amplitudes are usually obtained by fitting a set of sinusoids with known frequencies derived from the tidal catalogues in a least squares sense.

For such type of analysis, the interval length of the observations is crucial since it limits the frequency resolution of the analysis. The Hartmann and Wenzel TGP catalogue (Hartmann & Wenzel, 1995) contains over 12000 tidal waves with several different frequencies (Figure 3.5).

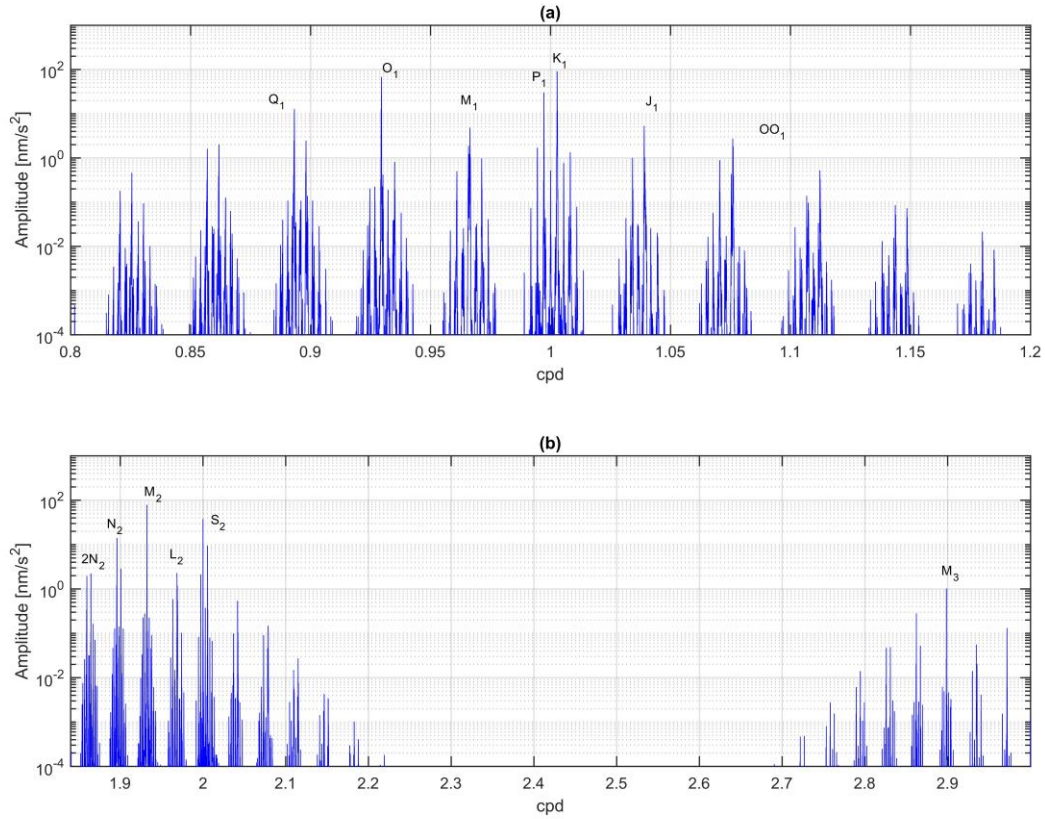

Figure 3.5 Spectrum of the tidal accelerations at SK1 from the Hartmann and Wenzel catalogue (Hartmann & Wenzel, 1995)*. a) spectrum diurnal band (1 cpd); b) spectrum of the semi-diurnal and ter-diurnal bands.*

The minimum frequency resolvable given the interval length of the record can be calculated according to the Rayleigh criterion, which states that the contribution of two waves of angular frequency ω_1 and ω_2(and periods T_1, T_2; ω_1=2π$\frac{1}{T_1}$) can be effectively separated when we have at least a record length T of:

$$T \geq \frac{2\pi}{\omega_2 - \omega_1} = \frac{T_1 T_2}{T_2 - T_1} \tag{3.14}$$

Which means that we have to record at least a period T corresponding to the modulation (beat) period. For instance to correctly estimate the L_2 and M_2 components, which have

periods of 11 h 58 m 2 s and 12 h 25 m 2 s respectively, we need at least 14 days of observations as shown in Figure 3.6.

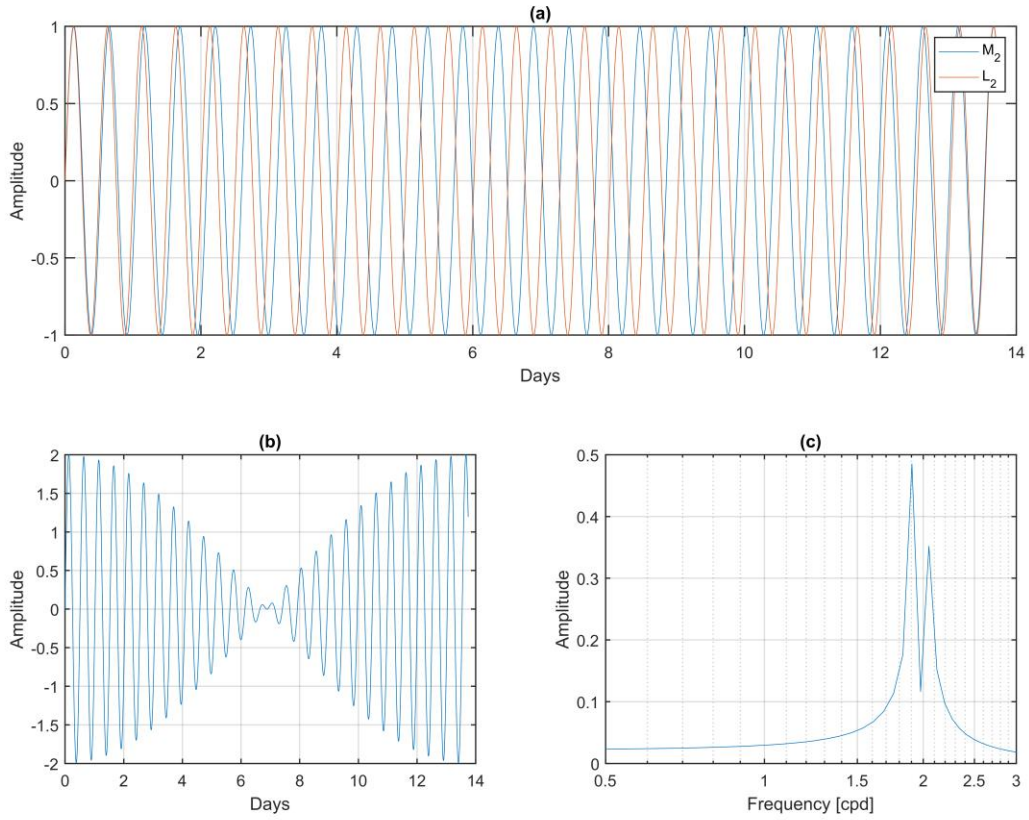

Figure 3.6 a) Two sine waves of slightly different periods (semidiurnal L_2 and M_2 tidal waves). b) Sum of the two contributions; the length of the recording is corresponding exactly to the modulation period. c) spectral analysis of the time-series in b showing two peaks corresponding to the M_2 and L_2 frequencies.

For this reason, the tidal analysis is usually performed based on "wave groups", where in each group several tidal waves with small frequency differences are collected. The tidal analysis estimates a single pair of δ and κ for each wave group.

How to group the various tidal waves efficiently depends, apart from the length of the observations, on the instrumental and site noises and obviously on the constituents which are expected to have largest amplitudes at the specific location (Ducarme & Schüller, 2018).

The implicit assumption here is that the Earth's response is smooth over frequency and that inside the wave group the tidal parameters of the various waves are constant. In general, this is not true if waves of a group originate from different degree of the tidal potential. One way to overcome this problem is to consider, within each wave group, the amplitude factors of a body tide model (Schüller, 2015), with elastic or inelastic responses.

In this project the tidal analysis was performed through the ET34-X-v73 software (Schüller, 2015; herein referred as ET34), which is an updated version of the former ETERNA software developed by Wenzel in the 90's (Wenzel, 1996) and that was the most popular software for tidal analysis in the Earth tide community. ET34 accepts different observational data such as tilts, gravity, potential (tidal gauge measurements) and estimates the tidal parameters for a specific wave group discretization provided by the user. The tidal parameters and an admittance function taking into account atmospheric pressure effects are adjusted in a least squares sense, as well as the instrumental drift (if we want to estimate also long period tidal contributions), modelled through Chebychev polynomials (Schüller, 2015). Equation 3.15 shows the model equation that is minimized in the program (Calvo Garcia-Maroto, 2015; Schüller, 2015):

$$y(t) = \sum_{i=1}^{Nwg} (X_i\, CO_i + Y_i\, SI_i) + \sum_{k=0}^{Nk} D_k\, C_k(t) + Ra(t) \tag{3.15}$$

Where X_i, Y_i are the linear forms of the amplitude (δ_i) and phase (κ_i) factors of the i-th wave group. They can be expressed as:

$$\begin{cases} X_i = \delta_i \cos(\kappa_i) \\ Y_i = \delta_i \sin(\kappa_i) \end{cases} \tag{3.16}$$

The SI_i, CO_i are expressed as follows:

$$\begin{cases} CO_i = \sum_{j=1}^{Nj} A_j \cos(2\pi f_j t + \varphi_j) \\ SI_i = \sum_{j=1}^{Nj} A_j \sin(2\pi f_j t + \varphi_j) \end{cases} \tag{3.17}$$

and represent the different tidal wave contributions in the i-th wave group: A_j, f_j, φ_j are amplitude, phase and theoretical frequency of the j-th tidal wave. Nj is the number of tidal waves of the TGP inside the i-th wave-group. D_k are the linear coefficients of the k-degree Chebychev polynomial (C_k); the maximal degree of the polynomial is Nk. Nwg represent the number of wave-groups that are considered in the analysis.

a is the atmospheric pressure time-series and R the regression parameter of the linear model. The assumption of linear relation between the gravity and the atmospheric pressure is justified by the theoretical calculations and observations, as we will discuss in the section dedicated to the atmospheric corrections.

3.1.4 Tidal Analysis of SK1 data

3.1.4.1 Pre-processing

In order to obtain reliable tidal parameters through ET34, the raw data observations require some pre-processing.

As we already pointed out, noise in the data degrades the quality of the analysis, requiring longer time-series to correctly estimate the tidal parameters. In this case noise means all gravity variations not directly linked to the tides and to atmospheric pressure variations. In the SK1 time-series, in addition to the hydrology, several other transients have been recorded due to earthquakes, seismic activity, to instrumental issues or caused by the noise of the site (vibrations caused by working machinery, windy days…). Additionally, the original sample rate of the observations (1 s) generates an enormous quantity of data which is excessively redundant for the scopes of the tidal analysis. As a consequence, filtering and attenuating part of the noise before performing the tidal analysis is a fundamental task in order to reduce the computational efforts and obtain a satisfactory result taking full advantage of the almost two years of observations. Hereinafter I detail the preprocessing phase which includes the following three stages:

1) filtering and decimation to a 1 minute sampling rate
2) cleaning the data from steps and spikes
3) filtering and decimation to 1 hour sampling rate

For the first phase I employed the decimation filter suggested by the Global Geodynamics Project for the treatment of the SG data which allows filtering and down-sampling the data from the original 1 s sample rate to a 1 minute sample rate. The filter coefficients are available at http://www.eas.slu.edu/GGP/ggpfilters.html and are plotted in Figure 3.7a. The frequency response is reported in Figure 3.7b. This filter is particularly apt for tidal analysis for three reasons. Firstly, it greatly reduces by 8 orders of magnitude the amplitudes of frequencies higher than $0.0083\ Hz$ (red dashed line of Figure 3.7b), which corresponds to the Nyquist frequency (i.e. $Nf = \frac{1}{2\Delta t}$) for a sampling rate of Δt=1 minute. Secondly it is flat in its pass band hence it does not introduce amplitude distortions in the tidal frequency band (green area in Figure 3.7b). Lastly it is not too long in the temporal domain (less than 20 minutes as seen in Figure 3.7a), so if spikes or steps are present in the raw data the spurious effects of filtering will corrupt only a small portion of data.

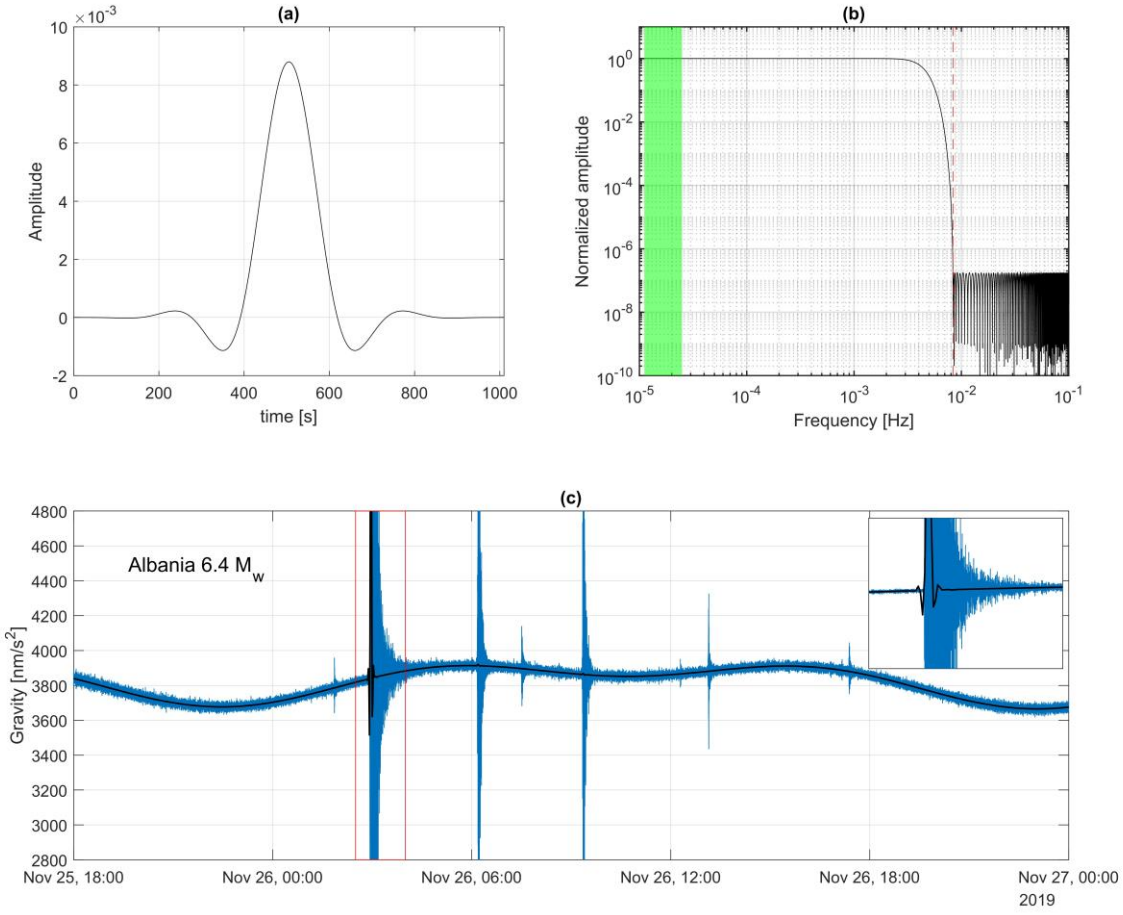

Figure 3.7 a) Coefficients of the filter used for decimation from 1 second to 1 minute data. b) Transfer function of the filter; dashed lines show the Nyquist frequency for a sampling of 1 minute. Green band shows the diurnal and semi-diurnal frequency band. c) In blue: 1.5 day long time-series in SK1 recorded at 1Hz. Notice the huge accelerations associated to the Albania earthquake. Black line: filtered and decimated time-series. The inset shows a zoom at the beginning of the earthquake.

An example of the filter performance on the SK1 data is given in Figure 3.7c, where an excerpt of 1.5 days in November 2019 is analyzed. The raw observations are reported in blue while the filtered time-series is shown in black. The raw data displays, superposed on the long period signals of the tides, a huge transient related to the 6.4 Mw earthquake occurred in Albania on 26th November 2019 at 02:54 UTC and the effects of several aftershocks. The filter has well removed the aftershocks signals, instead, the main shock effect is still present and has generated a spike (see inset).

Since the SK1 lies in a tectonically active region I recorded the effects of several earthquakes; in particular, two of them, with Mw > 4, were located within a distance of 150 km from the station. These earthquakes were responsible for the largest signals recorded and similarly to the Albania earthquake generated several spikes and disturbances in the filtered time-series.

As already hinted in the second step of the pre-processing all the steps, spikes not eliminated by filtering and gaps have to be removed.

Identifying small steps and spikes in the filtered gravity data could be complicated due to the masking effect given by the largest contributions (i.e. tides).

The "remove-restore" technique (Hinderer et al., 2007) was proposed to deal with such issue and is a standard processing step employed by the SG community. This technique is divided into two phases as suggested by its name:

1) Remove phase*:* from the original data ($g(t)$) the tides $b(t)$ are removed by means of an initial guess tidal model derived from theoretical predictions (or a previously available tidal model). Drift of the instrument $d(t)$ is removed as well through an high degree polynomial equation. The reduced time-series $r(t)= g(t) - b(t) - d(t)$ is now corrected for spikes and steps by employing a combination of interpolation and de-stepping/spiking techniques which finally allow to obtain the final corrected residual $r_c(t)$.
2) Restore phase*:* the gravity observations g_r cleaned from steps, spikes… are computed re-summing all the stripped contributions according to:

$$g_r(t)= b(t) + d(t) + r_c(t) \tag{3.18}$$

For managing such processes, I relied on TSoft software (Van Camp & Vauterin, 2005), which allows to perform the "remove and restore" technique through an interactive graphical user interface. In particular, through the software I can inspect in detail the time-series and once having identified a disturbance I can manually apply different corrections, such as steps, gaps or linear/cubic splines. The program offers also routines for automatic de-spiking and de-stepping the data, however I preferred the manual approach which allows much more control on the applied corrections.

Figure 3.8 shows for a 3-week period the remove-restore technique results. In Figure 3.8a the original data after the filtering and 1 minute decimation is shown; notice the huge spike related to the 26th November 2019 Albania earthquake. In 3.8b the tidal model $b(t)$ is plotted; in this case I use a local tide model (LTM) which was derived from a previous tidal analysis. The red line shows the drift curve, that for this limited time span is approximately linear.

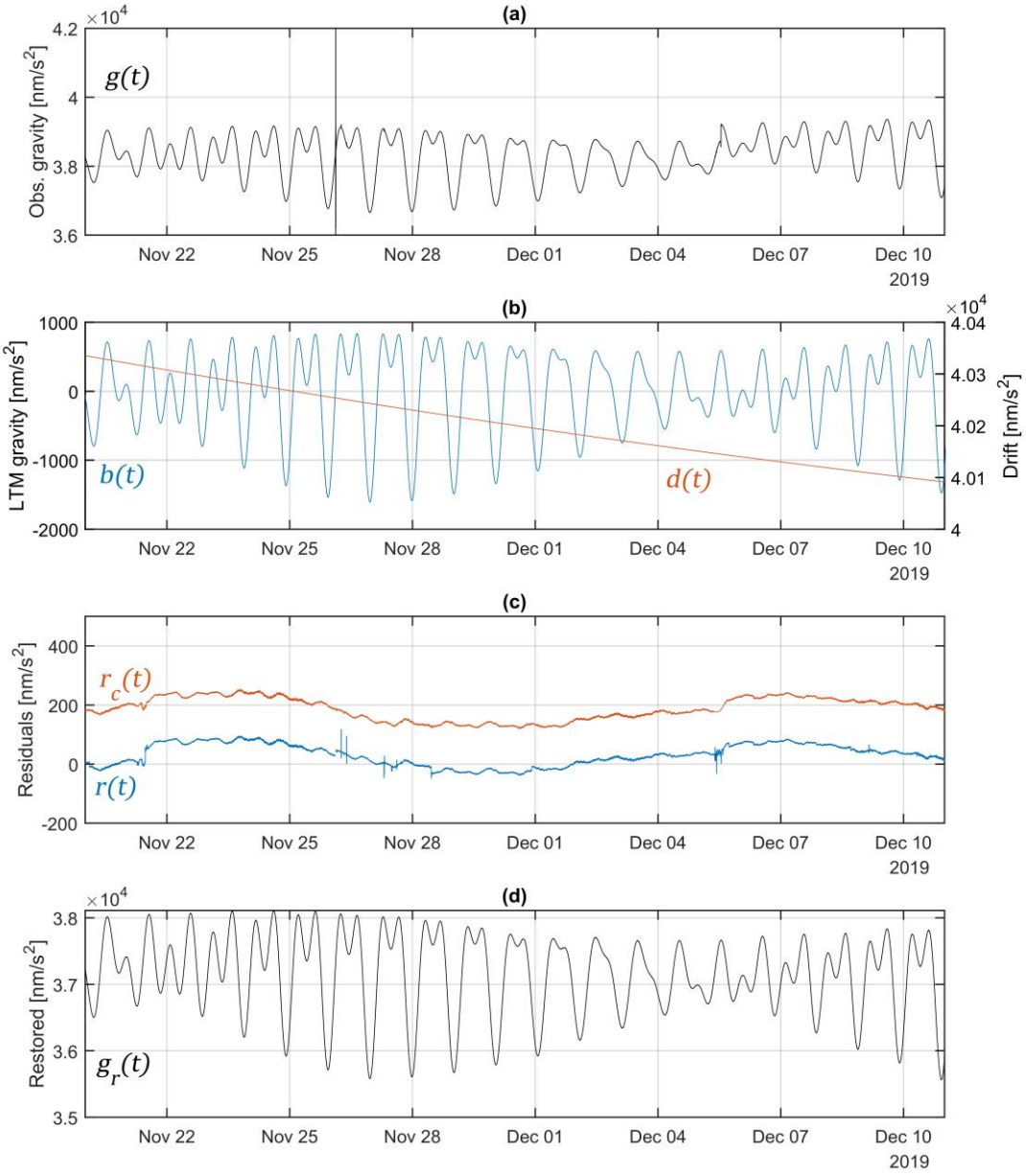

Figure 3.8 a) Observed gravity down-sampled to 1 minute data. b) Blue: synthetic Earth tides; red: instrumental drift; c) Blue: uncorrected residuals; red: despiked, destepped residuals d) restored gravity anomalies.

Figure 3.8c reports a comparison between the original $r(t)$ and de-stepped and de-spiked $r_c(t)$ residuals. The effect of the earthquake was preliminary eliminated by introducing a small gap. We see how the effect of many spikes and steps have been greatly attenuated by the procedure. The residuals unveil also a small periodic semi-diurnal component which was not perfectly estimated in the previous tidal analysis.

The last step before performing the tidal analysis is a further data decimation to 1 hour temporal sampling. Again also here we employed filter coefficients suggested by the GGP project for SG observations. The characteristics of the filter in terms of filter length and frequency response are plotted in figure 3.9a and 3.9b.

The whole time-series of almost 2 years of observations is shown in Figure 3.9c. We observe the dominant contribution of the tides and non-linear drift component. Some gaps are present in the data, mostly due to large earthquakes or issues with the acquisition system of the gravimeter. The atmospheric pressure time-series is shown in Figure 3.9d. Pressure data has been acquired together with the gravity observations and has been processed with the same filters.

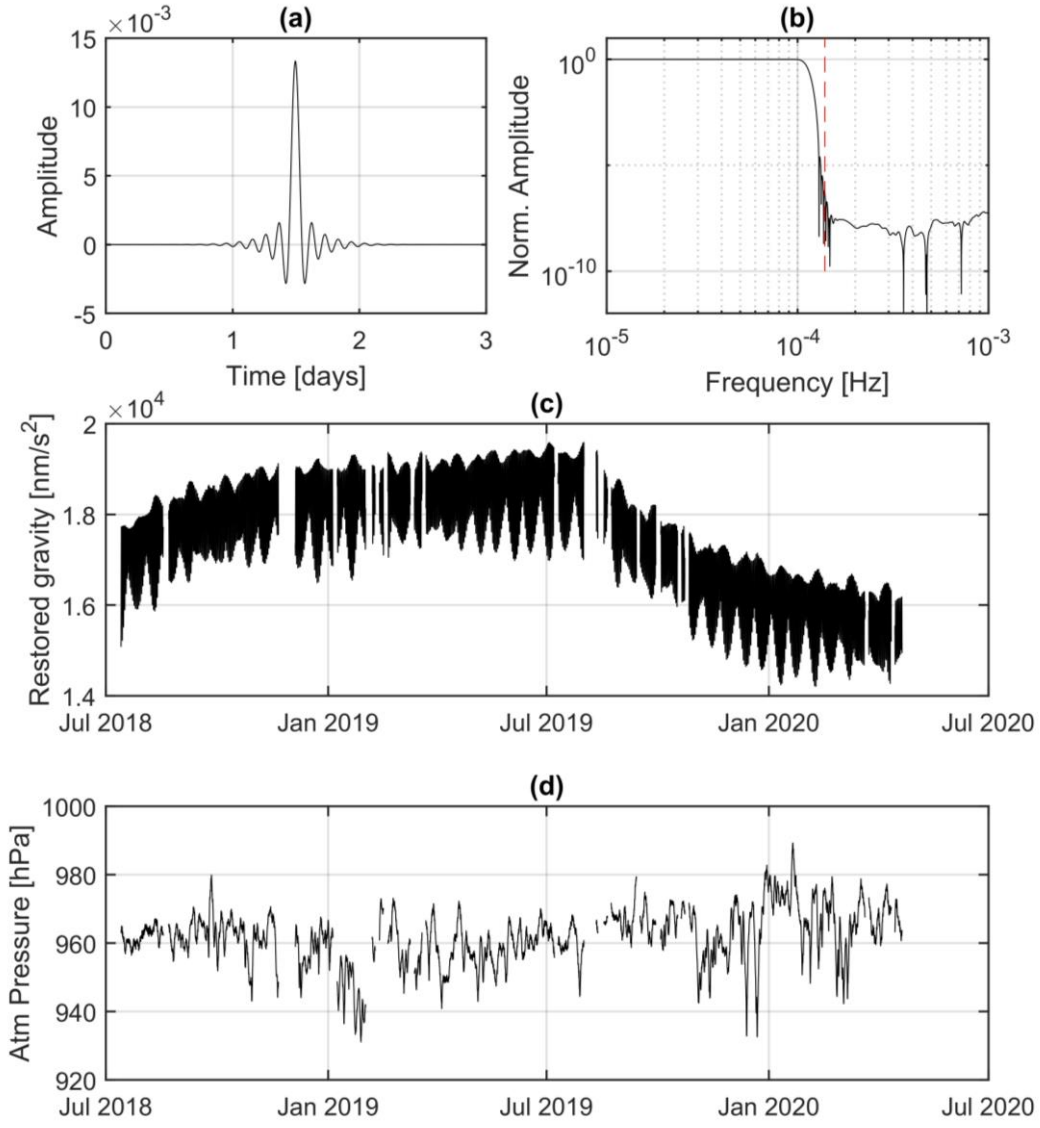

Figure 3.9 *a) Coefficients of the filter used for decimation from 1 minute to 1 hour data. b) Transfer function of the filter; dashed lines show the Nyquist frequency for a sampling rate of 1 hour. c) Filtered gravity time-series from July 2018 to May 2020. d) Atmospheric pressure variations recorded and processed with the same filters*

3.1.4.2 Tidal Analysis: Results

The tidal analysis has been performed employing the wave group discretization shown in the figure 3.10. In Figure 3.10a the diurnal components are shown, while semidiurnal waves are plotted in Figure 3.10b. Blue lines display the theoretical gravity tidal accelerations calculated at SK1 from the Hartmann & Wenzel (1995) catalogue. Through the red boxes I reported the wave groups which are defined by the first and last frequencies bounded by the box. I also included for each wave group the Darwin symbol of the largest tidal constituent. The numbers reported on top display the minimum number of days required to separate one group from another, calculated according to the Rayleigh criterion (eq. 3.14). For instance, in order to separate the contributions between wave group Q_1 and O_1, 27 days are required.

I employed a finer discretization around 1 cpd frequency where I differentiate S_1, K_1 and ψ_1 wave groups. For these tidal waves in fact, although very close in frequency, we expect non smooth variations of the tidal parameters. S_1 in fact, corresponds to the exact diurnal periodicity in which other geophysical phenomena, such as atmosphere and thermo-elastic deformation, superpose on the tidal signal. While K_1, ψ_1 and φ_1 are in the frequency band where the diurnal Free-Core Nutation (FCN) resonance occurs (Ducarme et al., 2008). I didn't include any long period component since the recordings are too short and also because of the non-linear drift of the meter which would greatly impact such constituents. So long period signals have been filtered out by the ET34 routines, applying an high pass filter before performing the analysis.

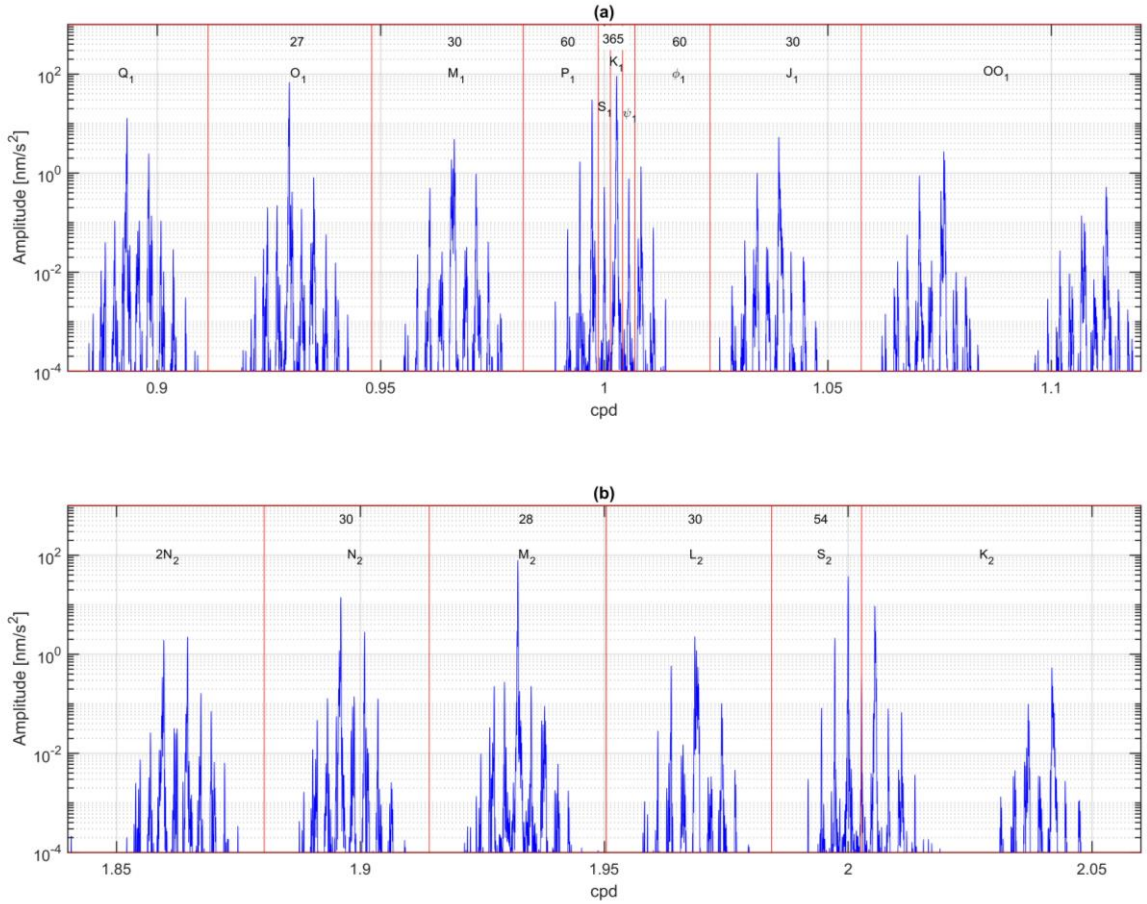

Figure 3.10 a) Amplitude spectra of tides in the diurnal band calculated at SK1 from Hartmann & Wenzel (1995)*; red vertical lines bound the different tidal groups employed in the tidal analysis. Numbers on the top report the minimum days of observations required to discriminate two successive tidal groups. Darwin notation for the main constituent of each tidal group is reported as well. b) same as a, but for the semidiurnal band.*

In order to correct the tidal parameters for the oceanic tidal component I included the effect of FES2014b (Carrère et al., 2016), which is a global model of the marine tides. I selected the FES2014b model since it includes also the Adriatic Sea. Ocean load vectors (amplitude L and phase λ) are provided by the Onsala Space Observatory (OSO ,http://holt.oso.chalmers.se/loading/): they include Newtonian and loading effects according to an elastic Earth model (Bos & Scherneck, 2013; Farrell, 1972) for the major diurnal and semi-diurnal tidal components Q_1, O_1, P_1, K_1, N_2, M_2, S_2 and K_2. A more detailed discussion on how to calculate the Newtonian and loading effects, given a 3D load distribution is provided in the following section where the atmospheric correction will be detailed. Table 3.4 gives the results for the tidal analysis considering 17 tidal groups for which the frequency of the main constituent is reported in the second column. The columns δo and κ_o report the tidal analysis results without correction for the oceanic load, while δo-OL, κ_o-OL show the tidal parameters of the gravity field corrected for this effect. The last row reports the atmospheric admittance, estimated by ET34 together with the tidal parameters.

Table 3.4 Tidal analysis results. δo= δ observed; κ_o=phase observed; δo-OL= δ observed corrected for oceanic loading (OL); κ_o-OL= phase corrected for OL; δ DDW-NIh= theoretical response; δo SF corr.-OL= δ observed corrected for Scale Factor and OL; χ: residual vector length. Rows in bold = FES2014b correction available.

Wave Group	freq.[°/h]	Amplitude Teo. [nm/s²]	Amplitude Obs. [nm/s²]	δo	δo RMS	κ_o [°]	κ_oRMS [°]	δo-OL.	κ_o-OL [°]	δ DDW-NHi	δo SF corr.-OL	χ: residual vector length %	residual vector phase
Diurnal Band													
Q_1	**13.3987**	**59.472**	**69.066**	**1.1625**	**0.0036**	**0.087**	**0.168**	**1.1682**	**0.158**	**1.15428**	**1.15360**	**12.5**	**29.5**
O_1	**13.943**	**310.616**	**361.633**	**1.1651**	**0.0007**	**0.163**	**0.033**	**1.1698**	**0.011**	**1.15427**	**1.15426**	**2.3**	**1.7**
M_1	14.49669	24.417	28.994	1.17597	0.00831	0.036	0.394		-	-	1.16102	-	-
P_1	**14.9589**	**144.506**	**169.213**	**1.1661**	**0.0014**	**0.044**	**0.023**	**1.1676**	**-0.302**	**1.14912**	**1.15336**	**58.8**	**93.2**
S_1	15	3.414	6.3253	1.46956	0.08654	-36.395	3.293	-	-	-	1.41905	-	-
K_1	**15.0411**	**436.679**	**503.759**	**1.1527**	**0.0005**	**0.396**	**0.024**	**1.1538**	**0.044**	**1.13470**	**1.13880**	**18.8**	**29.9**
ψ_1	15.08214	3.415	3.039	1.0157	0.06185	9.027	3.186	-	-	-	1.05071	-	-
φ_1	15.12321	6.217	8.254	1.28922	0.03275	2.159	1.394	-	-	-	1.26498	-	-
J_1	15.58544	24.425	28.458	1.16206	0.00854	0.906	0.406	-	-	-	1.14007	-	-
OO_1	16.1391	13.357	15.762	1.19573	0.0163	1.223	0.763	-	-	-	1.17576	-	-
Semi-Diurnal Band													
$2N_2$	27.96821	11.226	13.21	1.17766	0.00541	1.308	0.294	-	-	-	1.16198	-	-
N_2	**28.4397**	**70.292**	**83.596**	**1.19**	**0.0011**	**1.417**	**0.058**	**1.1763**	**-0.078**	**1.16194**	**1.16069**	**5.8**	**0.9**
M_2	**28.9841**	**367.124**	**439.658**	**1.1982**	**0.0002**	**1.012**	**0.012**	**1.1783**	**-0.009**	**1.16194**	**1.16282**	**1.7**	**1.5**
L_2	29.52848	10.378	12.503	1.19185	0.01078	1.785	0.585	-	-	-	1.17395	-	-
S_2	**30**	**170.79**	**204.29**	**1.1962**	**0.0005**	**0.371**	**0.329**	**1.1766**	**0.113**	**1.16194**	**1.16278**	**7.1**	**5.5**
K_2	**30.0821**	**46.398**	**55.272**	**1.194**	**0.0019**	**0.231**	**0.189**	**1.1739**	**-0.073**	**1.16194**	**1.15912**	**14.9**	**2.3**
Ter-Diurnal Band													
M_3	43.47616	5.044	5.528	1.0995	0.008	0.470	0.417				1.08118		
Atmospheric pressure admittance				-3.39 +/- 0.05 nm/s²/hPa									

The ocean load correction seems to improve both the retrieved tidal parameters, by diminishing the δ factors to values closer to 1.16 (column δo-OL) and reducing the phase κ_o. The impact of the corrections is particularly evident in the semi-diurnal band, in which the largest marine tidal contributions are observed.

However we observe that the δ factors seem to be systematically slightly higher than the theoretical ones of the Dehant-Defraigne-Wahr non-hydrostatic inelastic Earth model (δ DDW-NHi column; Dehant et al., 1999). This could be due to two effects:

a) insufficient ocean loading correction
b) calibration issues

Regarding the first option we will show in section 3.3 that the FES2014b, adequately reproduces the phases and amplitudes of the tidal waves in several harbors along the Adriatic coast. Also the discretization of the Adriatic coast employed by the model, that could be critical for calculating loading and Newtonian effects, seems not to be an issue in SK1 location as it will be shown in chapter 5.

Hence I tested the hypothesis that there could be some calibration issues and I estimated a scale factor (SF), that for the instrument in SK1 would be of 0.987. This value would imply that the observed amplitudes are smaller by about 1 %; however, to have a further confirmation of the presence of such issue, the instrument should be tested on a calibration line.

In any case, scaling the observations including the SF and applying the FES2014b correction, results in an improvement of the estimated δ factors which now are closer to the theoretical predictions (δ DDW-NHi column in Table 3.4). This also further confirmed by inspecting the residual vector lengths (in percentage with respect to the observed amplitude) and their phases.

We can have a look at the tidal analysis results and performance by looking at the plots of Figure 3.11, where the load vector (red lines) from the OSO provider is shown together with the observed (black lines) and theoretical tidal vectors (blue lines). I include also the error estimates of ET34 which are plotted at the end of the observed vectors with the error-ellipse representation. The error ellipses are barely visible, given the small uncertainty estimated by ET34, and are calculated from the errors on amplitude (A_{rms}) and phase (K_{rms}) as follows:

$$A_{rms} = RMS\delta_o \cdot A_{teo} \quad (3.19)$$

$$\kappa_{rms} = RMS\kappa_o \cdot A_{obs} \quad (3.20)$$

Where A_{teo} and A_{obs} are the theoretical and observed amplitudes of the tidal group considered, $RMSk_o$ is the root mean square error (RMSe) of k_o in radians and $RMS\delta_o$ is the RMSe of the δ_o factor.

Please notice that the x and y axis are not to scale, hence phase angles and amplitudes in the y direction are greatly exaggerated.

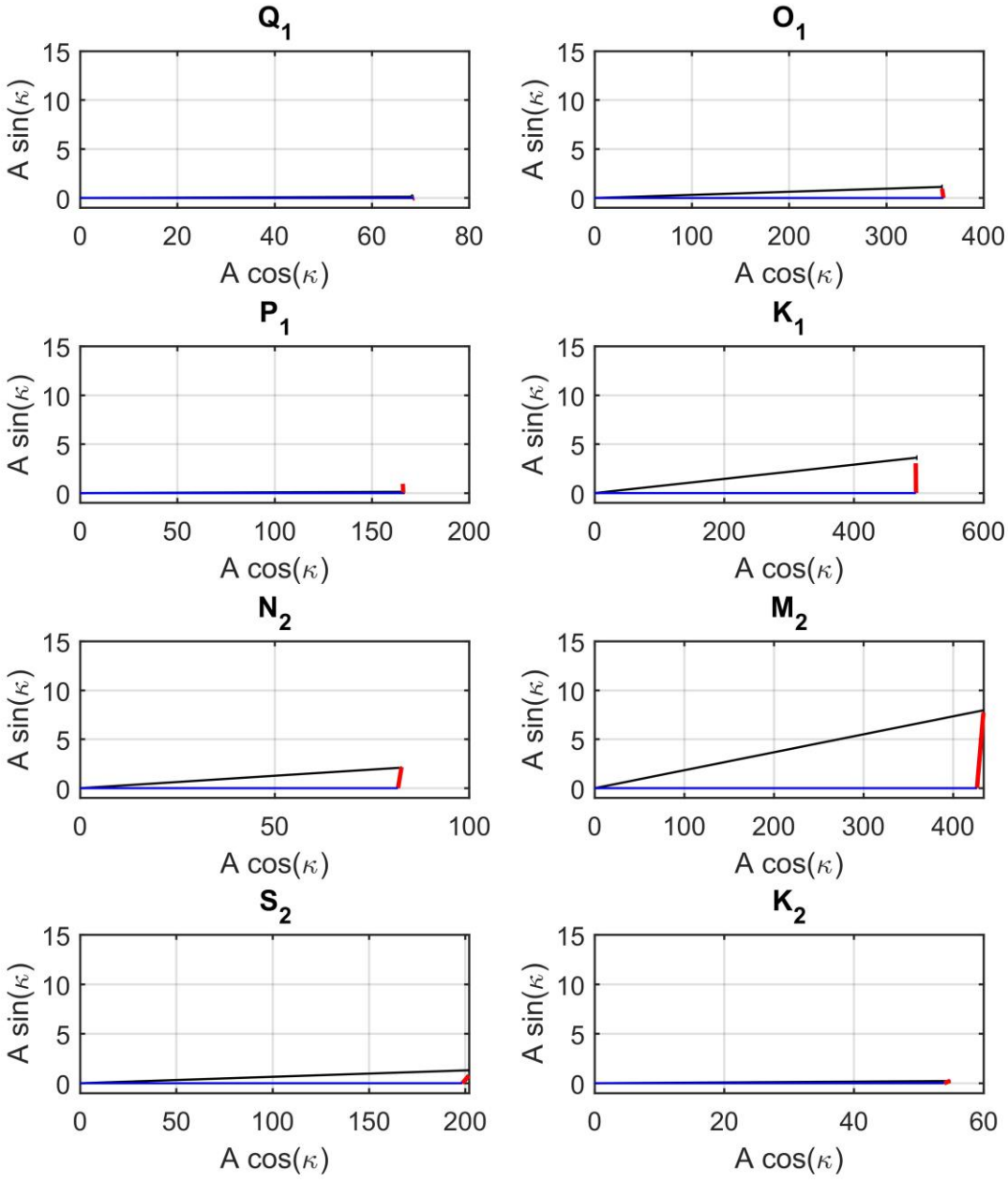

Figure 3.11 Vector diagrams for diurnal and semidiurnal tidal groups for which the oceanic correction is available. In red the load vector from OSO provider is shown; black lines report the observed data after applying the SF=0.987 and blue lines the theoretical vectors relative to the Dehant-Defraigne-Wahr non-hydrostatic inelastic Earth model (DDW-NHi). Axis units are in nm/s^2.

Apart from this, looking again at table 3.3, we observe that the most anomalous tidal coefficients are in the diurnal band and belong to those groups for which the oceanic

correction is not available. The S1 in particular has anomalous δ and k with RMS errors few orders of magnitude larger than the other waves.

The ψ_1 and φ_1 are also very noisy as observable from the RMS and show δ factors of 1.015 and 1.289 (1.26498 in case the calibration factor is employed). In addition to this all these three groups show the lowest amplitudes. As already hinted, S_1 is compromised by atmospheric pressure effects and the thermo-elastic deformation which occur at the exact same periods; for instance, I plot the spectrum of the air pressure in figure 3.12a, where we see the amplitude peaks associated with diurnal (1 cpd) and sub-diurnal harmonics (2 cpd, 3 cpd…).

Similar anomalous values are also observed in the nearby groups to S_1 such as ψ_1 and φ_1. For these tidal waves, which are in the frequency band of the FCN resonance, we expect rather different values of δ with respect to the classical 1.14-1.15. However, the retrieved parameters are still incompatible with the theoretical δ factors given by Dehant et al. (1999). The discrepancies are probably due to the combination of two effects:

1) oceanic contribution which is not available for these tidal waves
2) limited recording length of the time-series

Probably after 2-3 years of observations we will be able to discriminate more precisely the ψ_1 and φ_1 constituents.

In any case, the tidal model I obtained seems to be adequate for reducing the gravity observations; this is testified by the plots 3.12b and 3.12c where I show the performance of the local tide model (LTM) in the spectral domain.

In 3.12b the spectrum of the observed signal (blue) is shown together with the spectrum of the LTM (red). The difference between the two signals is reported in the plot 3.12c in red while the spectrum of observation is plotted in blue for comparison. Including the calibration factor improves the fit of the LTM to the theoretical predictions of Dehant et al. (1999): the impact of not including the SF could be in overestimating the amplitude of the signal up to 1 % of its true amplitude.

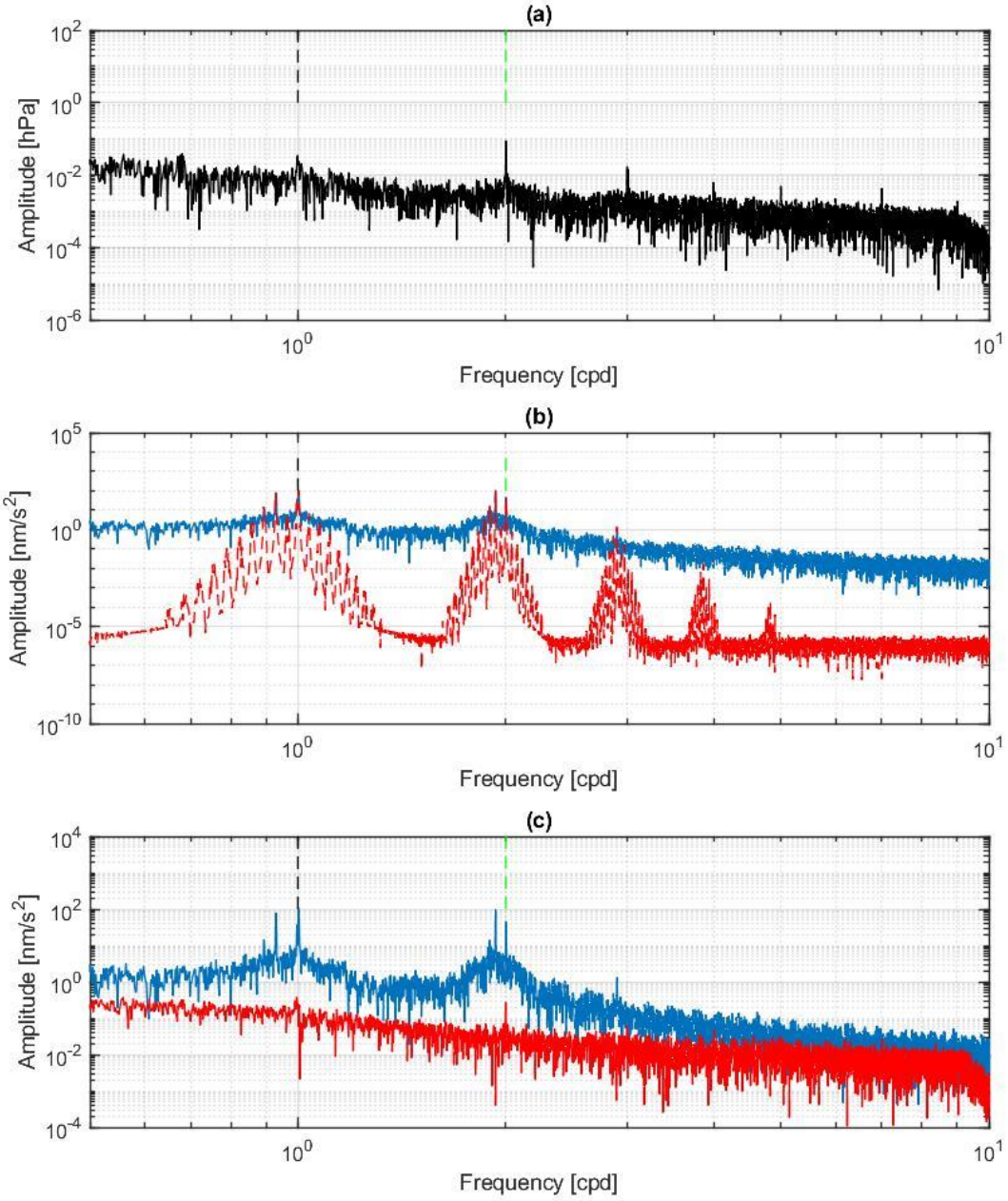

Figure 3.12 a) Spectrum in the diurnal/semi-diurnal band of the air pressure. b) in blue the spectrum of the observed signal; in red the spectrum of the local tide model. c) Blue as in b); red: de-tided observations after removing the LTM given by the difference between observed and theoretical local tidal model. In all figures black and green vertical dashed lines highlight the diurnal and semi-diurnal components.

3.1.4.3 Tidal Residuals

In order to compute the residuals, I subtracted a tidal model from the original gravity data based on the coefficients of the tidal analysis (Table 3.3), complemented by long period components (< 0.5 cpd) calculated for the theoretical body tide model by Dehant et al. (1999).

The original gravity data was decimated to hourly samples in the same way as discussed in 3.4.1; in this case I didn't apply any de-spike or de-step technique for cleaning the data as intense rainfalls could cause almost step like rapid changes in gravity (Meurers et al., 2007). However, I removed 2 large steps of clearly instrumental origin.

Additionally, I applied the pole tide and the Length Of the Day (LOD) corrections. Pole tides are induced by small perturbations of the rotation axis of the Earth, while the LOD variations are due to changes in Earth's rotation speed. The sources of these phenomena are still studied but generally are related to changes in mass distribution and momentum of the atmosphere and oceans. The changes involve different frequencies however the dominant contribution is due to the polar motion induced by the Chandler wobble, which has periods slightly superior to the year and amplitudes of several tens of nm/s^2 and an annual wobble. The LOD has amplitudes which are one order of magnitude lower. To estimate such contributions, ET34 relies on a catalogue of the instantaneous pole coordinates, provided by the International Earth Rotation and Reference Systems Service (IERS), and through the equations reported in Gross (1992) and Chen et al. (2009).

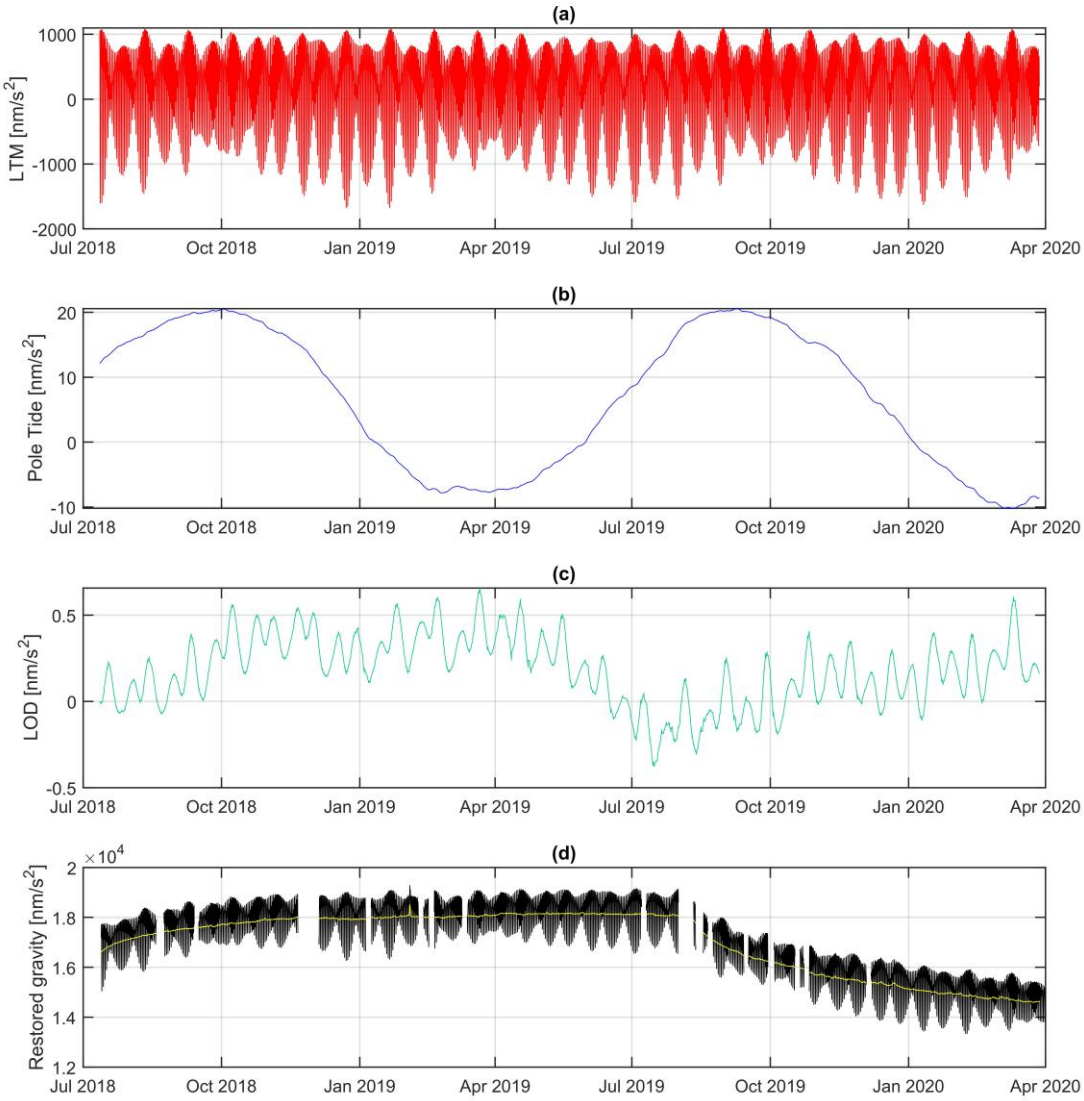

Figure 3.13 a) Predicted tides in SK1 derived from the synthesis of the parameters estimated in the tidal analysis. b) and c) Pole tide corrections and length of day gravity effects for July 2018-April 2020. d) Black: observed gravity in SK1 and residuals (in yellow) after removing a,b and c.

Figure 3.13a shows the synthetized tides for SK1 for the time-span July 2018-April 2020, while in 3.13b and 3.13c the pole tide and LOD corrections are shown.

Figure 3.13d illustrates the original data in black and the residuals with the yellow line.

3.2 Atmospheric correction

3.2.1 Introduction

Atmosphere pressure changes provide a significant contribution to the observed gravity signals with amplitudes up to 10 % of the tides (Hinderer et al., 2007). The atmosphere pressure variations involve both periodic and a-periodic temporal changes. As we already discussed previously, the periodic components pertain typically to the diurnal and sub-diurnal bands and are responsible for altering the tidal parameters. At mid-latitudes like that of Škocjan, however the effect is smaller compared to other regions of the Earth, such as tropical and subtropical regions, where most of the atmospheric changes are periodic. For instance, in Figure 3.14a I show an example of 60-days pressure time series in Škocjan (red) and Djougou (Benin; Boy et al., 2017); we see that the Škocjan site shows larger pressure variations with episodic transients exceeding 40 hPa while Djougou shows almost regularly diurnal and semi-diurnal variations. Further evidence of this can be found in Figure 3.14b, where the two spectra of 1.5 year long time-series are shown.

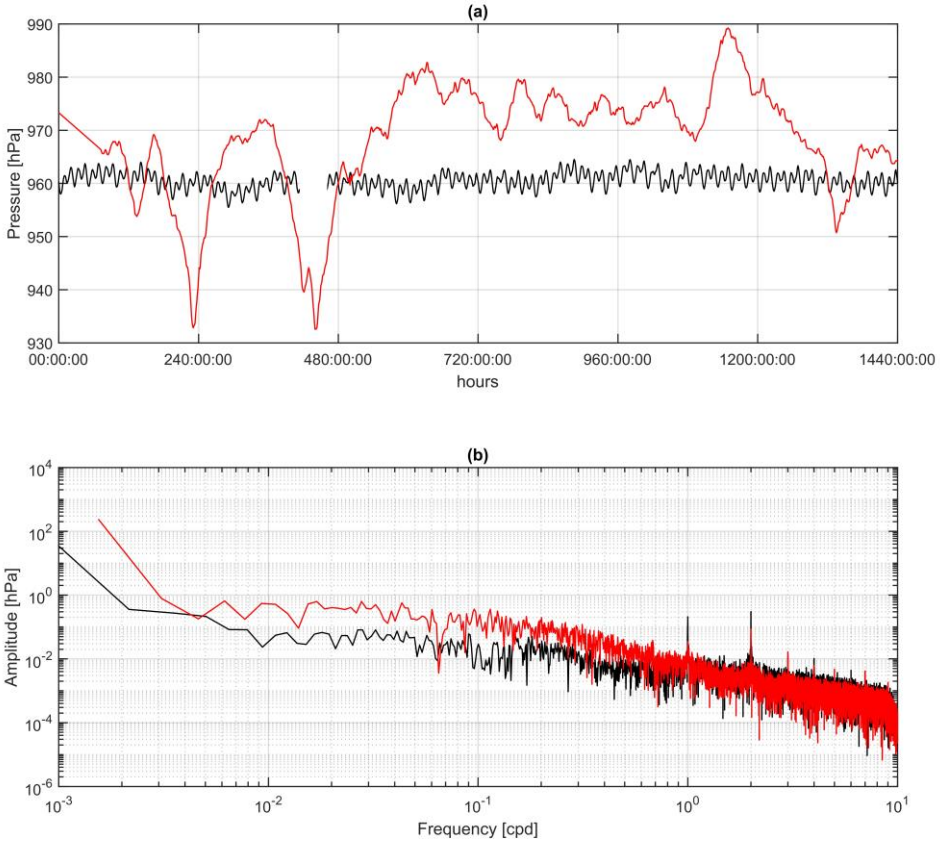

Figure 3.14 a) 60-days length time-series of pressure at Škocjan (red) and at Djougou (black). b) Spectra of the two time-series. Color code is the same as above.

Atmospheric pressure changes and the associated Earth's surface deformations are caused by mass redistribution, which in turn induces temporal gravity changes. The gravity change due to the variation of the attraction is known as Newtonian contribution while the gravity variation due to the deformation is termed as loading component. Most of the recorded gravity effects (about 90 %) come from the local zone defined as the area within 50 km from the station, while the remaining part is mostly due to a far field/global component (Merriam, 1992). Removing such signals is a fundamental task for the scopes of the work, since typically hydrological signals are correlated with atmospheric gravity changes which mask the contribution of interest.

In the past years several strategies for correcting such effects have been developed: at the beginning of the SG era most of the methods relied on a statistical analysis of co-located atmospheric pressure measurements with the residual gravity data, corrected for the tidal effects (e.g. Hinderer et al., 2007). The authors removed the atmospheric influence by the aid of empirical transfer functions in the frequency domain or by simple admittances in the time domain (Hinderer et al., 2007).

The increase of computing performances and the advent of global 4D models of the atmosphere pressure allowed the calculation of more physically based corrections. In particular, these calculations permitted to keep into account the heterogeneous state of the atmosphere far from the station.

Usually, now the SG community employs a combination of such approaches, so the local part is estimated through statistical analysis while the far field component is derived from the 4D models (Karbon et al., 2014). This is mostly due to the limitations of the 4D models in reproducing the pressure time series with sufficient spatial and temporal resolutions.

For SK1, I relied as well on such a combination of techniques, exploiting the 4D model calculation provided by the ATMospheric Attraction Computation Service (ATMACS; Klügel & Wziontek, 2009). In the following sections the corrections and the impact on SK1 gravity residuals will be presented and discussed. Firstly, a brief introduction on the atmospheric gravity effects recorded by SG and on how to calculate the Newtonian and loading effects of a 3D mass distribution will be provided. This last part in particular will be indispensable for understanding how the 4D correction based on operational weather models work.

3.2.2 Gravity response to pressure variations: observations

One of the first studies on the atmospheric effects on Superconducting gravity data was conducted in California by Warburton & Goodkind (1977). The authors observed that their gravity measurements, after removing the Earth tides, were anti-correlated with the pressure

time-series and the empirical admittance estimated through regression was about -3 nm/s^2/hPa.

The authors then calculated the Newtonian and loading contributions due to an increase of air pressure of 1 hPa occurring over circular areas of different radii around the station. The station was assumed to be in a continental area, far from the sea with no topographic reliefs. The authors found that the Newtonian attraction is the dominant contribution with respect to the loading and it causes a reduction of gravity as pressure increases. This is simply explained by the fact that higher pressures imply more mass above the meter and hence a reduction of the gravity attraction towards the Earth center of mass. In their calculation they considered an 8.84 km vertically stratified atmosphere with varying temperature and density. For the loading component the calculations lead to a positive value and it is due to the downward displacement of the instrument towards the Earth center of mass (Figure 3.15a). Considering radii > 50 km the authors found that the theoretical admittance stabilizes around the value of -3 nm/s^2/hPa which is the sum of the -4 nm/s^2/hPa Newtonian contribution and +1 nm/s^2/hPa loading. The similarity between empirical and theoretical admittances suggested that most of the transients recorded by the gravimeter were due mostly to coherent pressure variations occurring within this radius. Figure 3.15a and 3.15b show with a sketch the Newtonian (green arrows), loading (black) contributions in response to an air pressure increase (HP) or decrease (LP). The sum of the components is reported with the red/blue dashed lines.

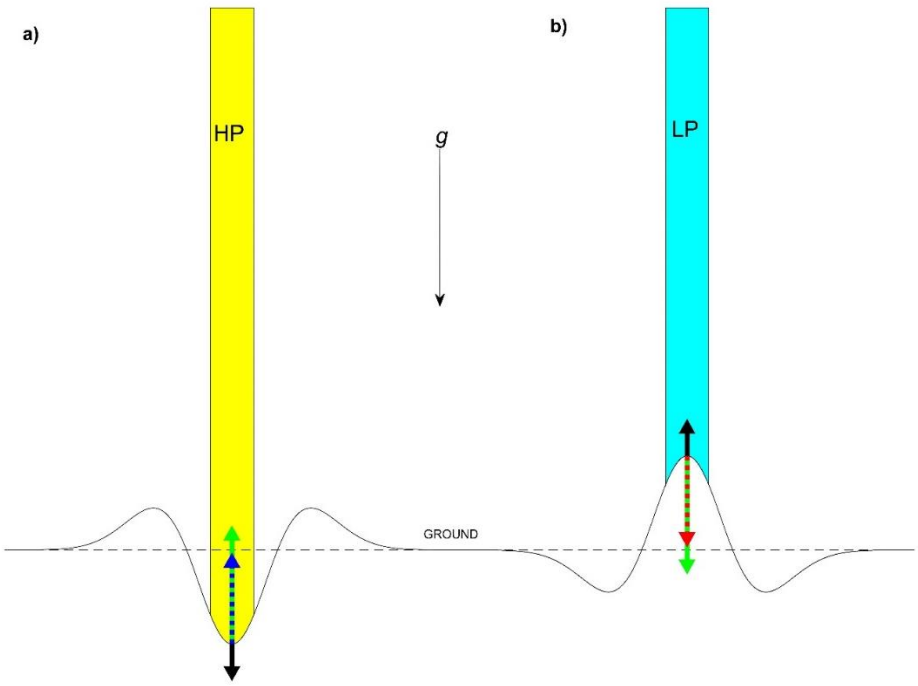

Figure 3.15 Sketch showing the gravimetric response to an increase in pressure a) and a lowering b). Green arrow: Newtonian component; black: loading. Red and blue dashed lines show the resulting vectors. Color code: blue means decrease of gravity, red increase.

Several other papers analyzed atmospheric effects on SG data and provided further evidences of these anti-correlated signals. Merriam (1992) estimated Green Functions for both loading and Newtonian components and investigated systematically the admittance behavior including far field components and the ocean, which reacts to the atmospheric loading process differently from the solid Earth. In general, the admittances found were negative and the values were expected to be in the range from -2.7 to -4.3 nm/s^2. Most of the studies pointed out that the correction through a single value admittance is problematic during the passage of weather systems when the atmospheric conditions are quite heterogeneous in time.

For this reason, in the 90's, other authors (Crossley et al., 1995) proposed to estimate frequency dependent admittances, which implied a time-variable gravimetric response to pressure transients. The approach allowed reducing the gravity residuals in many cases but it was questioned since at the same frequencies also the hydrologic signal superposes. Frequency dependent admittances in any case confirmed values around -3 nm/s^2 for cpd < 1 day while at higher frequencies there is a slight reduction up to -3.8 nm/s^2.

I would highlight that a gravimeter would record such values only if the measurement unit is sealed from the external atmospheric pressure variations. Otherwise the admittance value could be radically different. This is an issue regarding mostly old spring-based gravimeters where the measuring beam inside the chamber is subjected to buoyant forces in case of a not sealed instrument.

More recently the advent of 4D models of the atmosphere and the possibility to predict in a deterministic way the gravity changes lead to new approaches to correct the data. 4D models allow keeping into account the far field components and long period transients which were hardly accountable even with frequency dependent admittances. In the next chapter I give an overview on how the Newtonian and loading components are calculated for the ATMACS corrections which is presently adopted for the processing of several superconducting gravimeters (Karbon et al., 2014).

3.2.3 Newtonian and Loading effects of an atmospheric model

The air mass and pressure distributions are now predictable worldwide by atmospheric models which provide global grids of various physical properties (temperature, humidity distribution…) at regular time rates. The models vertically discretize the atmosphere by several layers starting from the orographic surface up to over 30 km. From these products, the density distributions are derivable applying simple thermodynamic equations. For instance, the ATMACS correction uses an atmospheric model from the German Weather

Service (DWD) and assumes the atmosphere to be approximated by an ideal gas. This leads to the following formulation of the density distribution (Klügel & Wziontek, 2009):

$$\rho_{atm}(\theta,\varphi) = \frac{p_{top}(\theta,\varphi) + p_{bot}(\theta,\varphi)}{2R \cdot T(\theta,\varphi) \cdot (1 - 0.608\, s(\theta,\varphi))} \tag{3.21}$$

Where p_{top} and p_{bot} are the pressures of the top and bottom interfaces which bound the element of mass, R is gas constant for dry air, T is the air temperature and $s(\theta,\varphi)$ the specific humidity. In this case p_{top} is calculated from p_{bot} according to:

$$p_{top}(\theta,\varphi) = p_{bot}(\theta,\varphi) \exp\left(\frac{-g(z_{top} - z_{bot})}{R \cdot T(\theta,\varphi) \cdot (1 - 0.608 \cdot s(\theta,\varphi))}\right) \tag{3.22}$$

Pressure changes and density distributions are then used to calculate the gravity changes. I remark that such variations of the gravity field are due to two processes:

1) spatio-temporal variation of $\rho_{atm}(\theta,\varphi)$ leads to variation of the Newtonian attraction.
2) variations of surface pressure induce deformations that change the mass distribution inside the Earth and also displace the instrument, inducing the so called loading contribution.

The first effect, the variation of the attraction of the air masses above the gravimeter, is usually modelled by discretizing $\rho_{atm}(\theta,\varphi)$ through a series of elementary geometries for which the gravimetric effect is known. This is an almost identical procedure to what I have employed to produce the synthetic models presented in chapter 2. However, in this former case I discretized the water mass in the cave through prisms, which are defined in planar coordinates and are commonly exploited for modelling local-scale processes. The implicit assumption of employing prisms is that the Earth curvature effect is negligible.

Obviously in the case of the global 4D atmospheric correction I could not rely only on prisms approximation and I have to find a solution to adequately represent the mass distribution far from the computation point. Usually the correction procedures are divided into two zones for which two discretization schemes are used: a global and regional/local component. For the ATMACS correction, the local component (< 70 km) is calculated by vertically stacking a pile of cylinders for which the gravity effect is known analytically:

$$g_z = 2\pi\, \rho_{atm} \mathrm{G}\left(z_{top} - z_{bot} + \sqrt{{z_{bot}}^2 + r^2} - \sqrt{{z_{top}}^2 + r^2}\right) \tag{3.23}$$

where r is the radius of the cylinder.

For the far field the mass (regional and global components in ATMACS) is discretized through spherical point masses which allow fast computation and could be calculated as follows:

$$g_z = \frac{\rho_{atm} G V}{d^2} \sin(\gamma - \beta) \tag{3.24}$$

where G is the gravitational constant, V is the volume of the spherical mass d is the distance between the mass and the computation point. The angles γ, β are defined in Figure 3.16 and can be calculated by $\beta = \alpha/2$ and $\tan(\gamma) = \cos(\beta)\,/[\left(\frac{2r}{z} + 1\right)\sin(\gamma)]$.

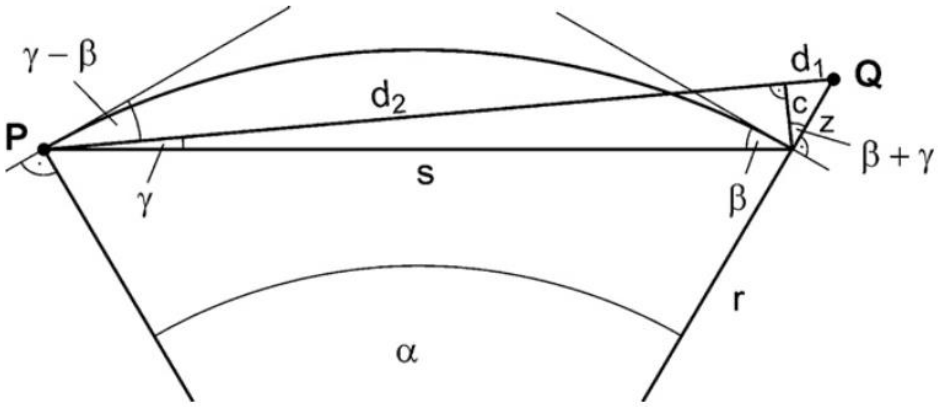

Figure 3.16 Geometrical relations between the computation point P and the atmospheric mass Q. From Klügel & Wziontek (2009).

Other softwares employ similar approaches for the discretization of the far field component but the local part could be different. In the following I will take advantage of mGlobe (Mikolaj et al., 2016) which is a software for calculating the gravity variations due to atmosphere, hydrology…, and where the local part is discretized by tesseroids (Uieda et al., 2016).

The second effect I need to model is the loading component in which I have to determine how an elastic spherical Earth responds (in terms of deformation, tilt, gravity changes…) to a point mass load. As pointed out by Farrell (1972) this is more or less equivalent to the problem of finding the Earth's response to the tidal forcing which was firstly addressed by Love (1909). The response of the Earth is defined by the three dimensionless degree dependent load Love numbers (h_n',k_n',l_n') which are calculated by resolving the linear gravito-elastic equations of motion. For a spherical radially stratified Earth model the load Love numbers depend only on the degree n and hence the computations are quite simplified. Tables of load Love numbers are available for numerous Earth models for n up to 40000 and allow calculating gravity changes, displacement, tilts… for a generic load distribution. For instance here I provide the equation for calculating the geoid change due to a surface density distribution $\Delta\sigma(\theta, \varphi)$ (Wahr et al., 1998) that loads an elastic Earth:

$$\Delta N(\theta,\varphi) = \frac{3a\rho_w}{\rho}\sum_{n=2}^{nmax}\sum_{m=0}^{n} P_{nm}\cos(\theta)\frac{1+k_n'}{2n+1}(\Delta C_{nm}\cos(m\varphi) + \Delta S_{nm}\sin(m\varphi)) \tag{3.25}$$

$$\text{With } \begin{cases}\Delta C_{nm} \\ \Delta S_{nm}\end{cases} = \frac{3}{4\pi\rho(2l+1)} \int \Delta\sigma(\theta,\varphi)\, P_{nm}(\cos\theta) \begin{cases}\cos(m\varphi) \\ \sin(m\varphi)\end{cases} \sin\theta d\theta d\varphi$$

where, ρ_w is the density of the water, ρ is the average density of the Earth and P_{nm} are the associated Legendre Polynomials.

Similar expressions can be obtained for other functionals such as gravity change.

Farrell (1972) provided an equivalent formulation of 3.25 in the spatial domain which is the so called Green Function (GF). The GF is simply the response of the Earth to a unitary load and it is computed as a combination of load Love numbers. For gravity it is reported in following eq. 3.26:

$$g(\theta) = \frac{g}{M_e} \sum_{n=0}^{\infty} (n + 2h_n - (n+1)k_n) P_n(\cos\theta) \tag{3.26}$$

where g is the average gravity acceleration on the Earth surface, M_e is the Earth mass, P_n are the Legendre polynomials and θ is the distance between the load and the computation point.

Through the Green Function formalism, we can express the gravity changes due to an arbitrary complex spatial distribution of loads through a linear combination of GF weighted by the load distribution. Mathematically this corresponds to the following convolution integral or to a summation in the discrete case:

$$G(\theta) = \int_{-\infty}^{\infty} g(\theta) l(\theta - \theta')\, d\theta' \tag{3.27}$$

$$G_m = \sum_{n=-\infty}^{\infty} g_n l_{n-m} \tag{3.28}$$

where the $l(\theta - \theta')$ is the load distribution which is a function of the angular distance $(\theta - \theta')$ from the computation point. g_n and l_{n-m} are analogous to $g(\theta)$ and $l(\theta - \theta')$ but for the discrete case. An example of the GF is given in Figure 3.17 which reports the gravity changes for a 1 hPa perturbation as a function of the radial distance from the load (Merriam, 1992).

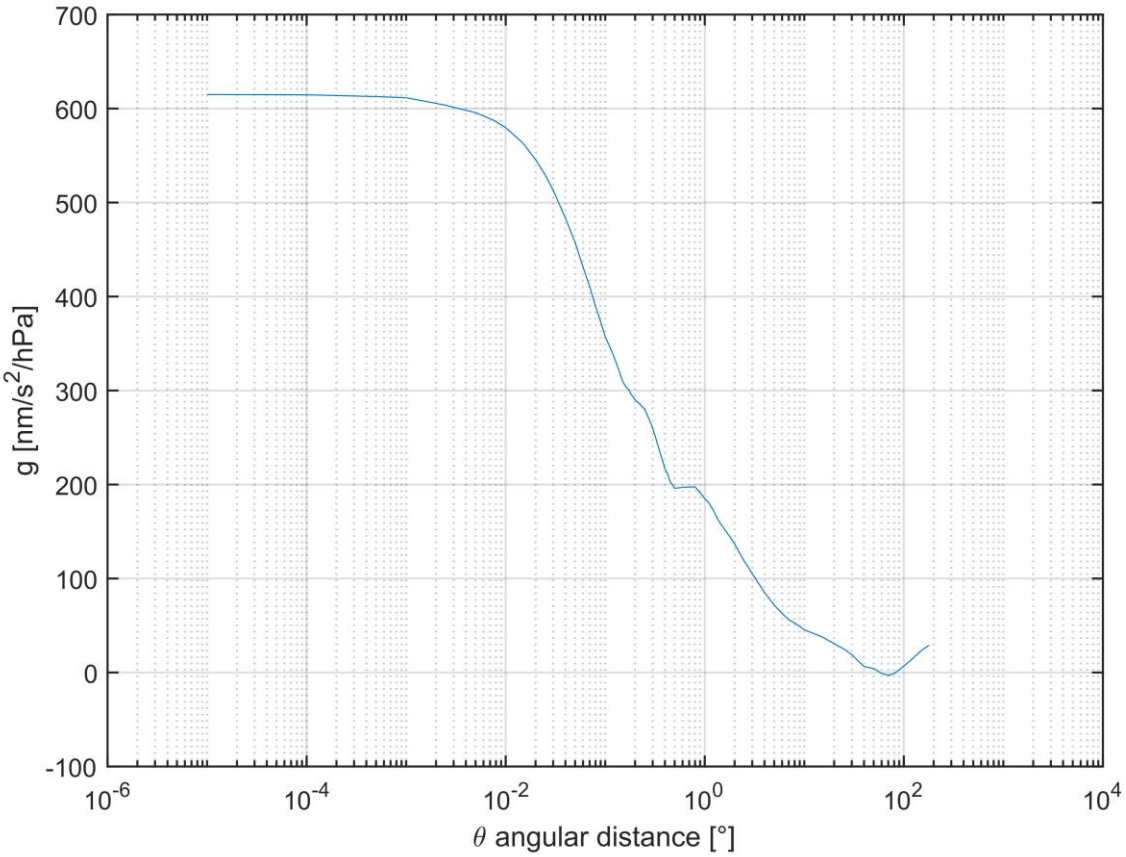

Figure 3.17 Green Function of the gravimetric response of an elastic Earth to a pressure perturbation of 1 hPa.

3.2.4 ATMACS correction implementation

The ATMACS model calculates Newtonian and loading components for the atmospheric model provided by the DWD which covers the whole Europe at spatial resolution of about 7 km and the rest of the world at a coarser resolution of about 40 km. The full resolution is exploited only for the local part (< 70 km) while the coarser grid (40 km) is used for calculating the regional correction up to 16.6° (for SK1) and the global contributions (distances > 16.6°). The correction is offered at temporal resolution of 3 h and is given as a column ASCII file, downloadable at (http://atmacs.bkg.bund.de/docs/data.php). An excerpt of the tables is given in the following table.

Local/Regional Component				Global Component	
Date (yyyymmddhh)	**model surface air pressure at station [hPa]**	**vertical atmospheric attraction of local model [nm/s²]**	**vertical atmospheric attraction of regional model**	**vertical atmospheric attraction of global model, except regional zone [nm/s²]**	**vertical deformation effect of global loading model [nm/s²]**
2018070100	987	-19.2	9.31	13.3	0.24
2018070103	987	-19.1	8.94	13.0	-0.180
2018070106	987	-17.1	8.58	12.9	-1.28
2018070109	988	-13.1	8.62	1.31	-0.199
2018070112	988	-14.6	8.84	1.36	-0.147

Table 3.5 ATMACS corrections at SK1 for 12 hours at the beginning of July 2018.

The correction could not be applied straightforward to the observations by simply subtracting the values of table 3.5 from the residuals since both spatial and temporal resolutions of the ATMACS model are inadequate to fully model local effects of the atmosphere. To overcome this problem, the SG community usually applies the ATMACS correction together with a local correction supplemented by the empirical admittance. Among the various approaches proposed in literature I followed the one reported in Karbon et al. (2014), which firstly interpolates the ATMACS loading and Newtonian components from the original 3 h sample rate to 1 h temporal resolution. Then the difference between the interpolated pressure time-series of ATMACS and the observed pressure by the barometer co-located with the meter are corrected by applying the admittance derived from tidal analysis. This way I take into account the local contributions not modelled in ATMACS.

3.2.5 Atmospheric effects and corrections in Škocjan

Figure 3.18 gives an example of the atmospheric related gravity transients recorded in Škocjan. The gravity observations reduced for the tidal components are shown in blue in 3.18a, while the pressure time series is shown in 3.18b. We observe the presence of several gravity transients anti-correlated with the pressure variations, for instance at the end of September 2018 an abrupt increase of about 30 hPa is associated with a gravity reduction of about 90 nm/s^2.

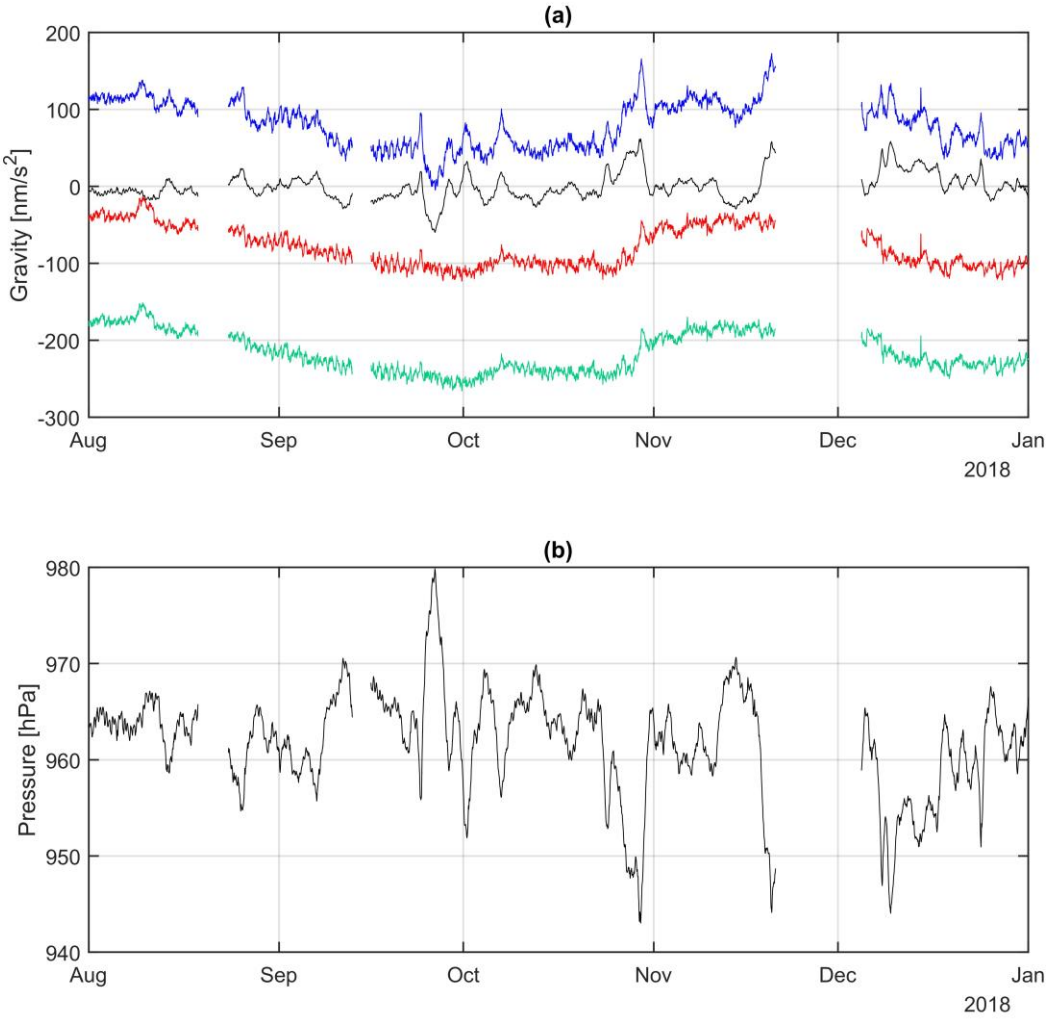

Figure 3.18 Atmospheric corrections (a) and pressure time-series (b) in Škocjan. a) In blue: gravity residuals after removing Earth tides, Pole tides and LOD signals; in black: the gravity effect modelled through the empirical admittance; in red: gravity residuals after removing the pressure signal modelled through the admittance; in green: gravity residuals after removing the atmospheric effects including ATMACS. The gravity curves are arbitrary shifted by a constant for improving readability. Note that with respect to the gravity variations in Figure 3.13d, the residuals have been further corrected for a long period linear trend.

The black line in Figure 3.18a shows the atmospheric gravity effect modelled by applying a single admittance α= -3.38 nm/s^2/hPa derived from ET34. The empirical admittance value is in the range of the theoretical predictions we discussed in the previous section and confirms that the instrument is operating correctly with the sensor box well sealed. The residuals of the gravity observations after removing the effect are shown in red, while the green line reports the residuals after subtracting the ATMACS atmospheric correction, implemented in the way as described in the previous section. By comparing red and green curves we observe that both

corrections perform well in reducing several transients, however including the ATMACS we are able to further remove energy of some transients as for instance the first occurred in August 2018. The improvement of the various corrections in this period is testified by the reduction of the Root Mean Square energy of the signals which could be computes as follows:

$$RMSe = \sqrt{\frac{1}{n}\sum_{t=0}^{n-1} r(t)r(t)} \tag{3.29}$$

Where $r(t)$ is the residual time-series, after removing the average value, n is the total number of samples constituting the signal. The original signal (blue line) has an RMSe of 28.2 nm/s^2, the residuals corrected with a single value admittance 24.3 nm/s^2 while ATMACS slightly reduces the RMSe to 24 nm/s^2.

The time-series from July 2018 to March 2020 corrected with the ATMACS correction is reported in the following Figure 3.19a in red, while the uncorrected time-series is shown in black. From both the time-series I removed the instrumental drift estimated with piece-wise polynomials; in Figure 3.19 the time-series are shifted by an arbitrary constant for improving the representation.

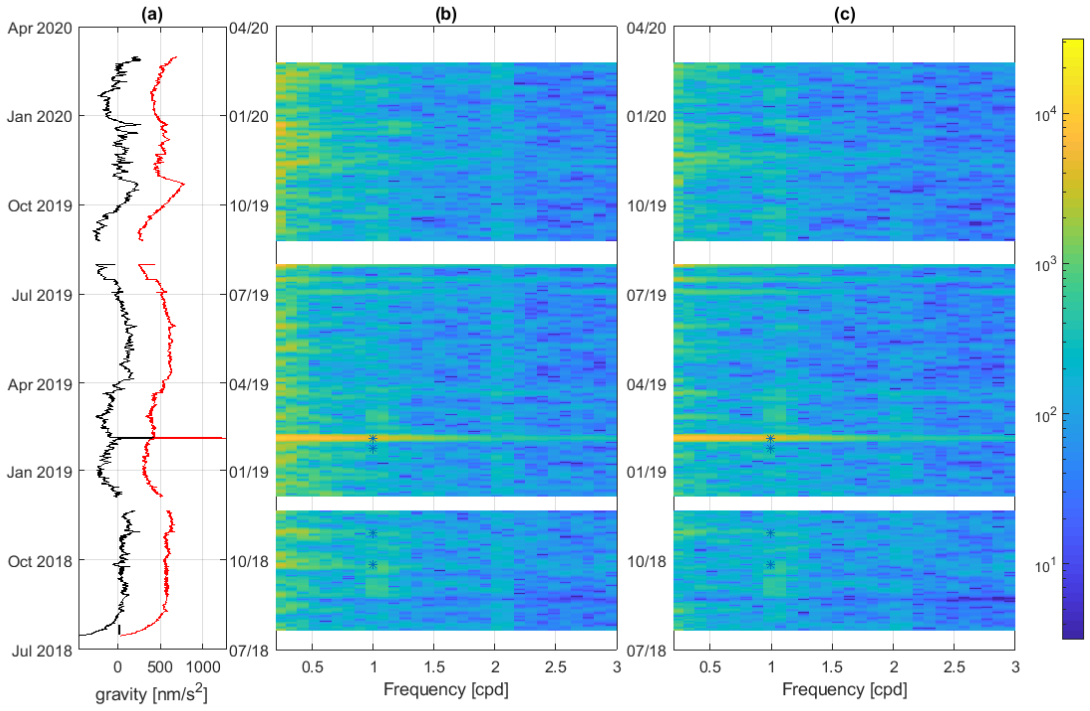

Figure 3.19 Atmospheric correction impacts. a) Original de-tided residuals (black) and atmospheric corrected residuals (red) in time-domain. The black thick short line at the beginning of the time-series shows the length of the window used for the computing the spectrograms in b and c. b) Spectrogram of the de-tided residuals; c) Spectrogram of the residuals further corrected for the atmospheric effects. Color scale proportional to the Power Spectral Density in (nm/s^2)^2/Hz.

From the comparison of the two time-series we appreciate the reduction of the signal energy of many transients associated to the atmosphere; this is testified by the reduction of RMSe which reduces from 118.6 nm/s^2 to 112.2 nm/s^2. Further evidences on the impact of the corrections can be found by Figures 3.19b and 3.19c where the spectrograms of the original residuals and the residuals corrected for the atmospheric effects are plotted. The spectrograms have been calculated by taking the Fourier Transform over sliding windows of 256 samples (about 10 days). To attenuate the spectral leakage, each time series is tapered with a Hann window.

The spectrograms clearly show that the atmospheric correction reduces the signal energy in the 0.3-1 cpd frequency band by up to 1 order of magnitude, as it is evident by inspecting the autumn-winter season in both 2018 and 2019. Part of the energy remains, principally due to hydrologic components not yet modelled; an example of this is provided by the huge transient recorded in February 2019, which caused gravity variations up to 400 nm/s^2. Furthermore, the spectral analysis shows that the atmospheric correction has notably reduced the energy of a coherent spectral peak at 2 cpd. I also computed the differences between the residuals corrected with a single admittance and those including the ATMACS model. The corrections perform similarly, however including the ATMACS model, I slightly improve the overall RMSe.

For SK1, apart from ATMACS, I didn't test any other atmospheric corrections derived from global atmospheric models. However, Mikolaj et al. (2019) compared the performance of different atmospheric corrections for different SG stations of the GGP project. They found discrepancies in the final RMSe of the time-series of few nm/s^2; the differences further attenuate including the local pressure measurements.

The Figure 3.20 shows the impact of the atmospheric corrections over a 7-days length time-series when also gravity-hydrologic related transients are expected. Figures 3.20a-b-c are relative to a flood event occurred in February 2019 which will be analyzed in detail in the following chapter; the hydrologic signal here (black curve) is the dominant contribution with amplitudes exceeding by over ten times the atmospheric corrections (blue and green lines).

Figures 3.20 d-e-f show on contrary an event in October 2018 which generated smaller gravity variations with most of the contribution coming from the atmosphere. In fact, the red curve shows the raw residuals, in which only the tidal correction has been applied, while the black is the residual after removing the atmospheric effect (blue line).

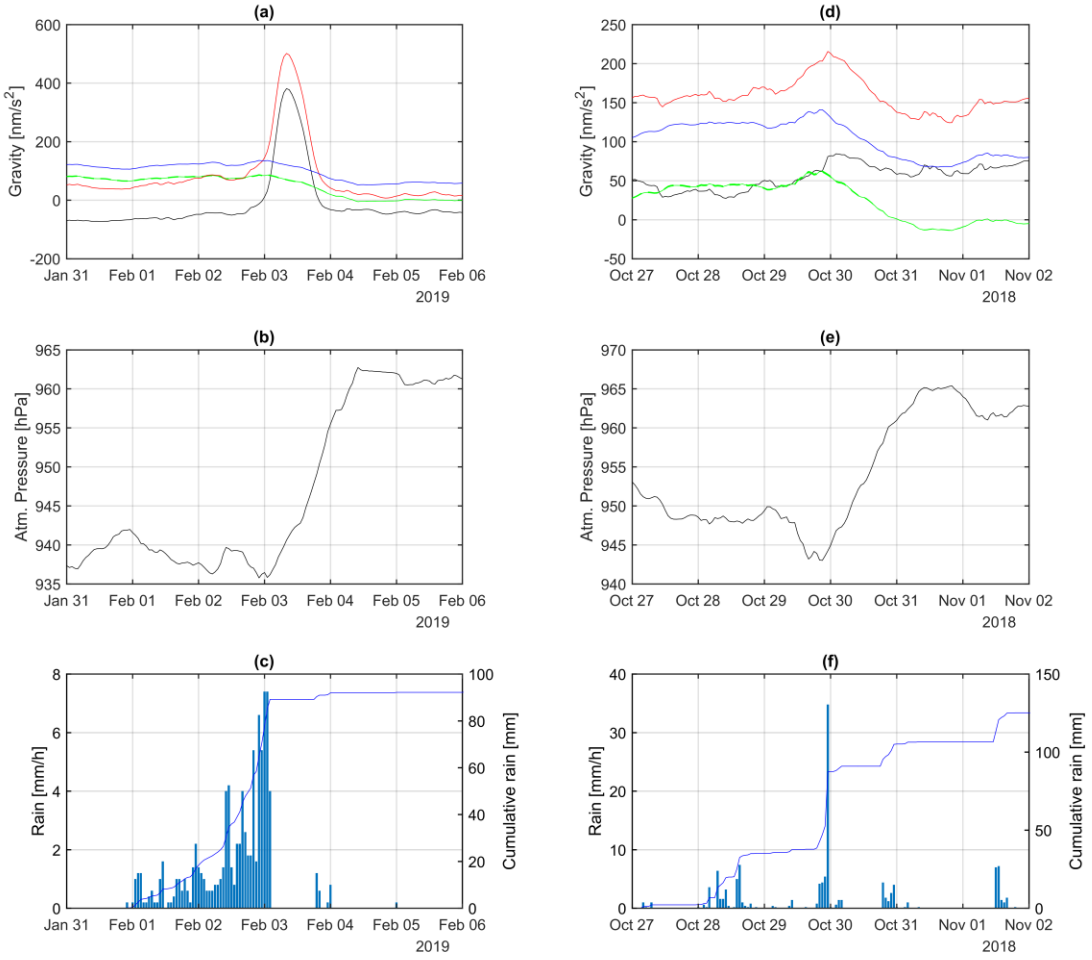

Figure 3.20 Atmospheric correction impacts in two 7-day time-series: February 2019 (a-b-c) and October 2018 (d-e-f). a) Gravity observations after removing tides (red) and atmospheric effects (black). Blue: atmospheric correction (ATMACS); green: atmospheric correction by applying the single admittance concept. b) Pressure time-series. c) Hourly rain gauge recorded at Škocjan and cumulative curve of rain (blue curve). d-e-f) as a-b-c) but for October 2018.

3.3 Non-tidal Oceanic correction

Through the tidal analysis I removed the periodic components associated to both solid Earth and oceanic tidal contributions. The atmospheric correction allowed me to remove non-periodic signals associated to the air mass circulation and redistribution and their loading effects on the solid Earth. Atmospheric pressure variations and winds are however responsible of exciting further water mass movements in oceanic basins and sea not accounted for in the previous corrections (e.g. Virtanen, (2004); Oreiro et al. (2018)). Also large scale oceanic currents cause sea level variations and water density redistribution. All these phenomena are usually referred as Non-Tidal Oceanic Loading (NTOL).

In order to predict the Newtonian and loading effects of the NTOL on gravity we need a 4D model of the water masses which is then discretized through suitable geometric elements (such as prisms or tesseroids), analogously to the procedure described in the previous section.

For the NTOL I have at my disposal global models of the sea surface variations over time; among the others the ECCO models, provided by the NASA, are the most employed by the geodetic community. The ECCO2 is the most recent model and it is obtained by minimizing the difference between sea level observations, mostly from satellite altimetry (TOPEX/Poseidon, GRACE), and a numerical simulation of the oceanic circulation in which the boundary conditions are constituted by the atmospheric forcing fields. The final product is daily solutions, offered as grids in the spatial domain with resolution of 0.25°. Such products are usually employed to remove the NTOL effects on SG time-series in continental areas.

Figure 3.21 shows the sea level heights for the North Adriatic Sea according to the ECCO2 model: in Figures 3.21a and 3.21b we observe two snapshots at on 28th and 29th October 2018 when an important storm surge event occurred in the North Italy, VAIA, which was associated with strong winds, a large scale low-pressure atmospheric front and abundant precipitations (Biolchi et al., 2019; Forzieri et al., 2020).

An 18-days long time-series of the non-tidal sea level variations in Trieste extracted from the ECCO2 model is shown by the blue line in Figure 3.21c. For comparison the de-tided sea level variations from the Trieste harbor are shown in red while time-series, filtered by a 48-hours moving average window, are plotted in green.

However, as it is evident from this figure the ECCO2 model lacks both in temporal and spatial resolution: the representation of the coastline, and consequently the mass distribution, near Trieste is quite rough and also the amplitudes of the NTOL seem to be underestimated. Hence following the approach of Oreiro et al. (2018) I produced an independent model of the NTOL constrained by various tidal gauges observations recorded at 5 different harbors located along the Adriatic coast. In the following I detail the procedure to build this model: first I performed a tidal analysis of the sea level gauges in order to isolate the NTOL contribution. Then from the various NTOL time-series I produced an empirical model of the sea level variations for the whole Adriatic Sea. This model is then used to calculate the Newtonian and loading effects.

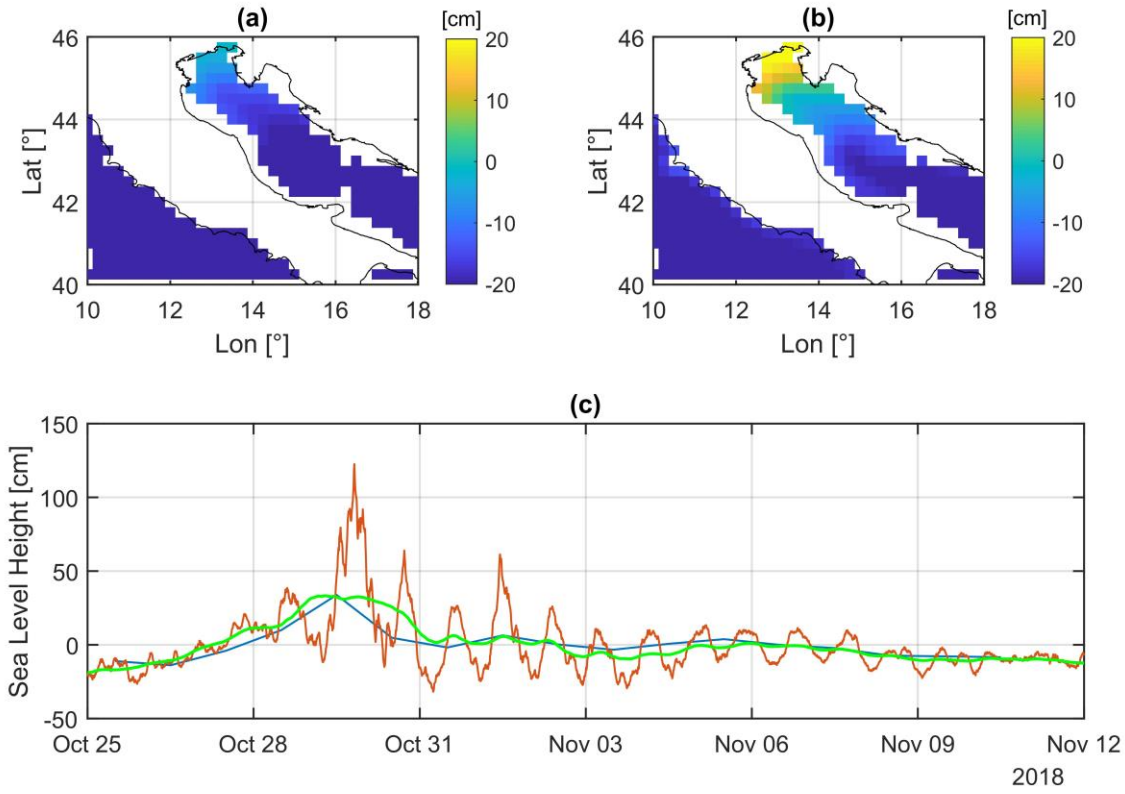

Figure 3.21 Non-tidal marine components in the Adriatic Sea. a) and b) Sea level height according to the non-tidal ocean model ECCO2 for two days in October 2018 when a huge storm surge ("VAIA") occurred in the North Adriatic basin. c) 18-days time-series in October-November 2018 during the "VAIA" storm surge: blue line reports the ECCO2 model time-series extracted for Trieste, while the red line shows the non-tidal component derived from the analysis of the Trieste harbor data, provided at 1 hour temporal resolution (see following section for details). The green line is the Trieste data low pass filtered with a 48 hours moving average window.

3.3.1 Tidal Analysis of Sea level observations

In order to perform the tidal analysis of the sea level gauges I relied on the UTide software (Codiga, 2011) which is a collection of Matlab routines apt for optimally treat the tidal oceanographic observations. The software adjusts in a least-squares sense the phase and amplitude coefficients for a set of tidal constituents selected by the user. Together with the tidal coefficients the program provides the confidence intervals and various statistical parameters for error assessment. The principle of the analysis is similar to ET34 however the software is designed specifically for the treatment of sea level observations, which are in general much noisier than geodetic data.

For the tidal analysis I rely on 1-year long time-series of sea level variations recorded in five harbors. The data have been down-sampled to 1 hour temporal resolution in case of Trieste and analyzed after interpolating small gaps and after removing large spikes. I employed the same frequency discretization as the one used for the gravimeter SK1. The tidal analysis results are shown in Figures 3.22 and 3.23, where the amplitudes and phases are shown together with the error estimates and the theoretical amplitudes and phases derived from the FES2014b model. As observable the obtained tidal models are reliable since they are in very good agreement with the theoretical predictions of the FES2014b model.

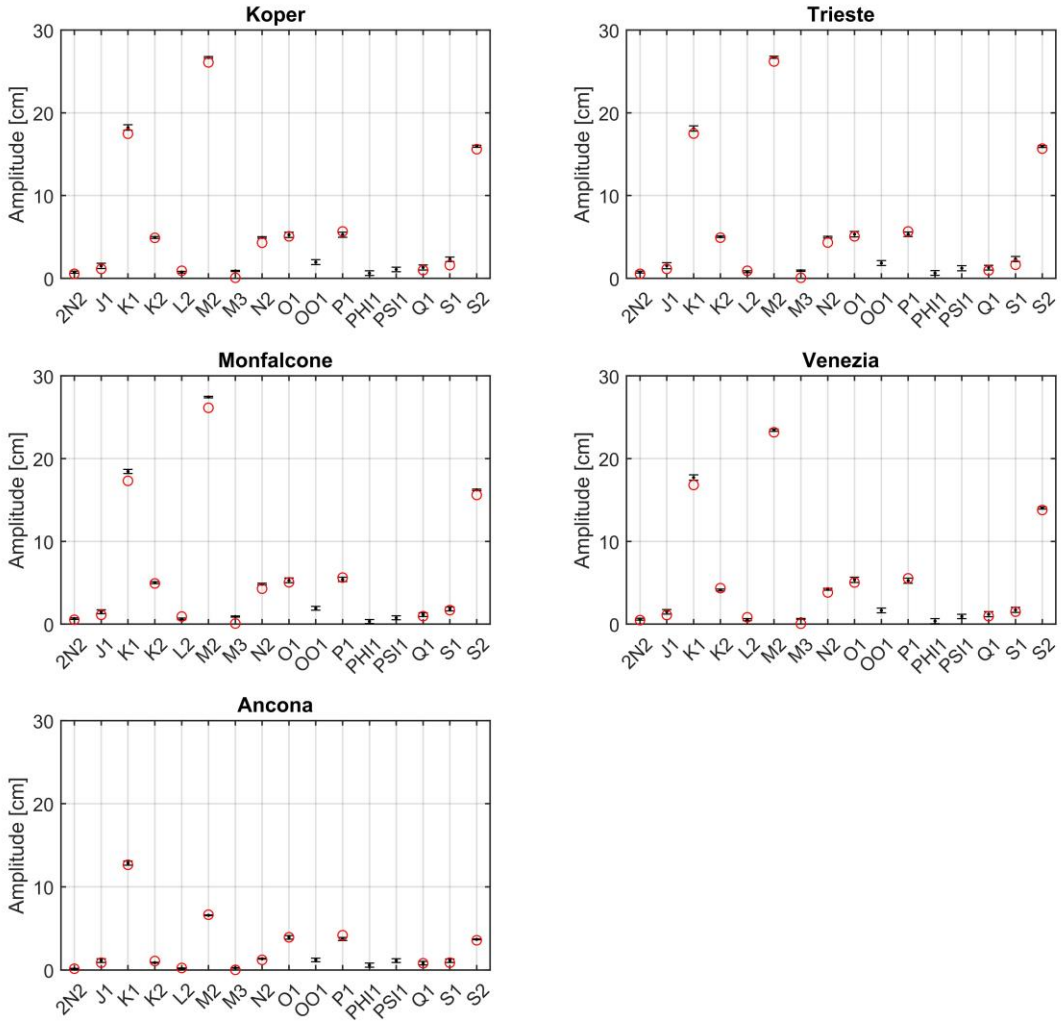

Figure 3.22 Amplitudes of 16 tidal components for 5 harbors in the Adriatic Sea. Black dots report the amplitudes derived from the tidal analysis; the bars report an error estimate (95 % confidence interval). The red circle shows the amplitude according to the FES2014b model.

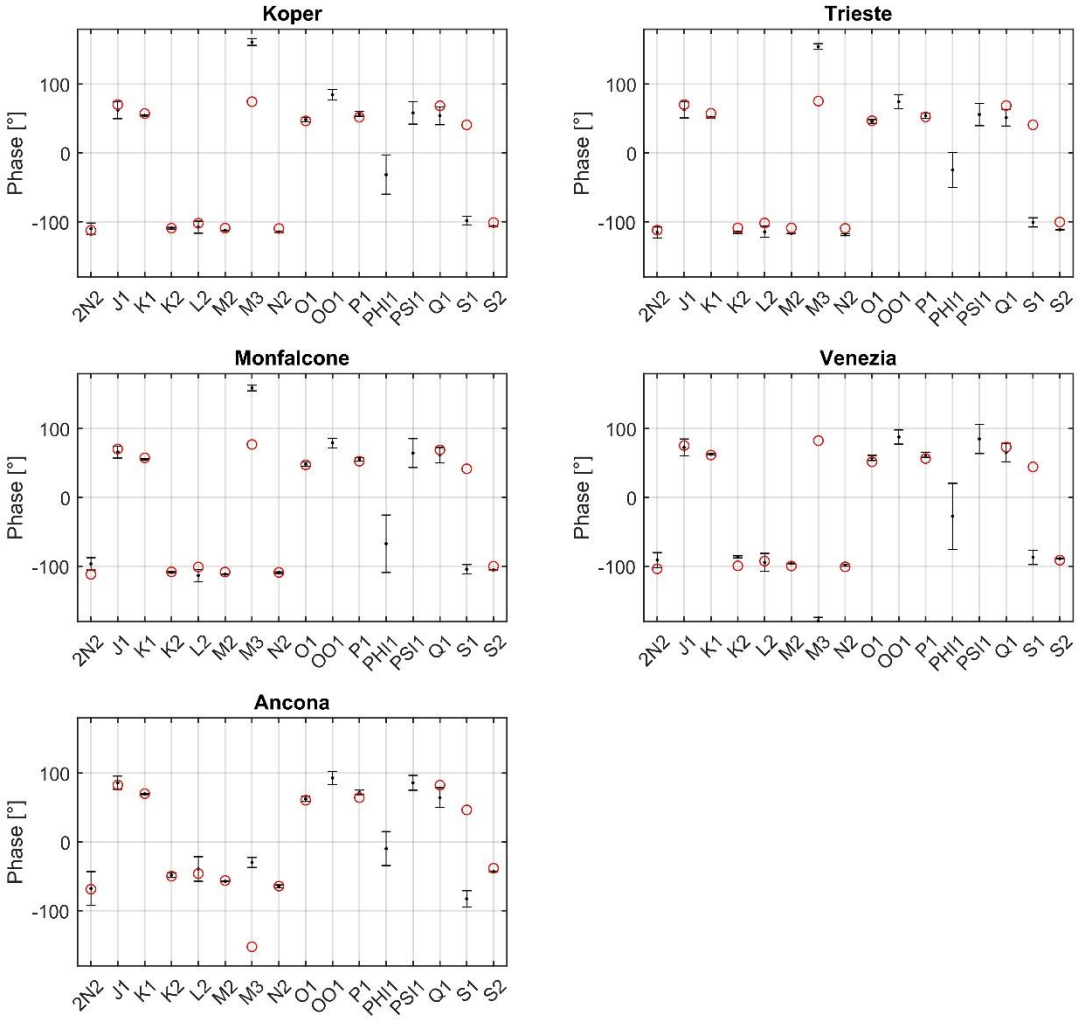

Figure 3.23 Phases of 16 tidal components for 5 harbors in the Adriatic Sea. Black dots report the phases derived from the tidal analysis; the bars report an error estimate (95 % confidence interval). The red circle shows the phase according to the FES2014b model.

With the tidal parameters for each harbor I can obtain a synthetic tidal prediction which can be subtracted from the original observations obtaining the non-tidal residuals. In Figure 3.24 the prediction and residuals are plotted in red and yellow lines while the original data are shown in blue. Regarding the residuals, we appreciate highly coherent sea level variations recorded at all the harbors, especially in the northern Adriatic basin (Trieste, Koper, Monfalcone and Venezia). The similarity between the non tidal time-series is testified by the values of the correlation coefficients, calculated between pairwise stations, and which are plotted in Figure 3.25.

The correlation coefficient between two time-series x, y is defined as:

$$\rho(x,y) = \frac{1}{N-1}\sum_{i=1}^{N}\left(\frac{x_i - \mu_x}{\sigma_x}\right)\left(\frac{y_i - \mu_y}{\sigma_y}\right) \tag{3.30}$$

where N is the number of samples and μ_x, $\sigma_x$are respectively the average value and standard deviation of the time-series x and μ_y σ_y are the same for y.

As evident from Figure 3.24 the non-tidal sea level component could exceed the 1.2 m in several harbors during exceptional meteorological events and the anomalous transient could last for several hours (as shown in Figure 3.21c).

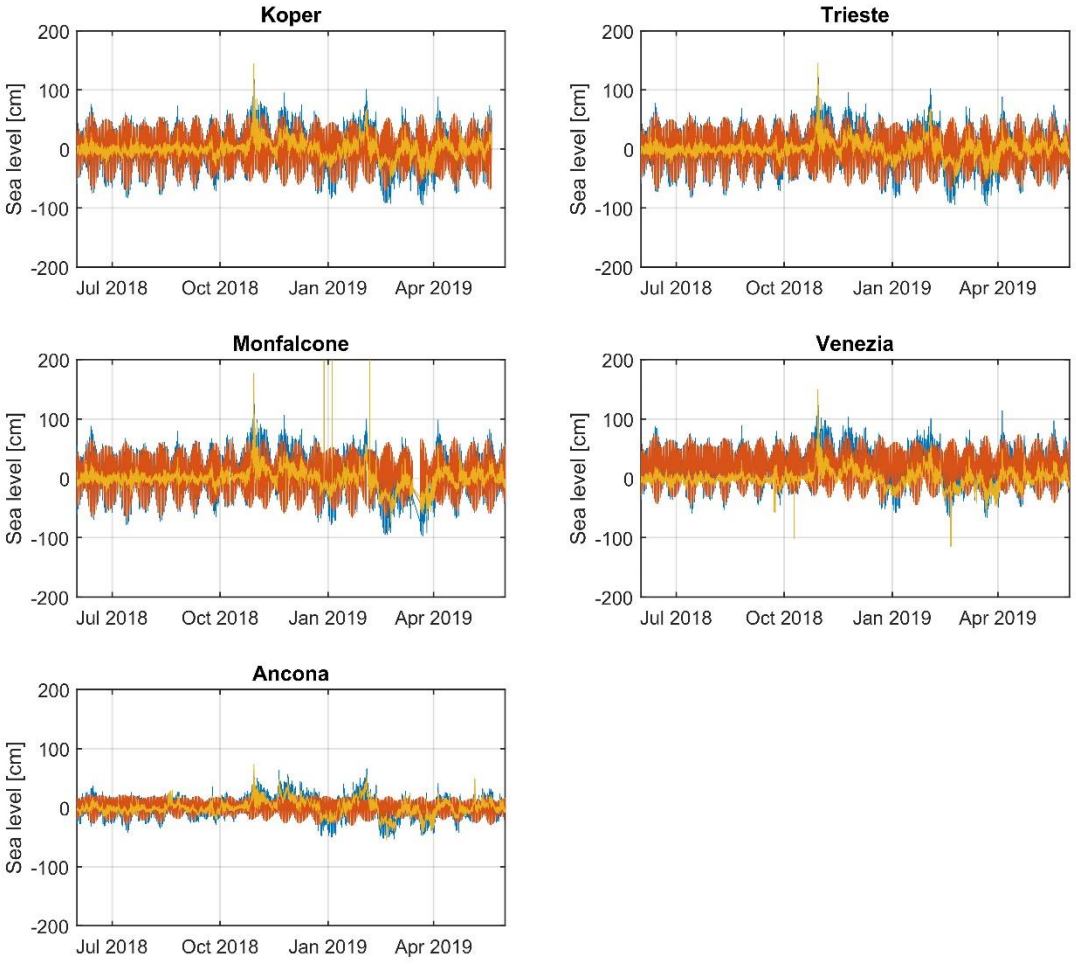

Figure 3.24 Tide gauge observations (blue), tidal predictions (red) and residuals (yellow) for 1 year long time-series of 5 harbors in the Adriatic Sea.

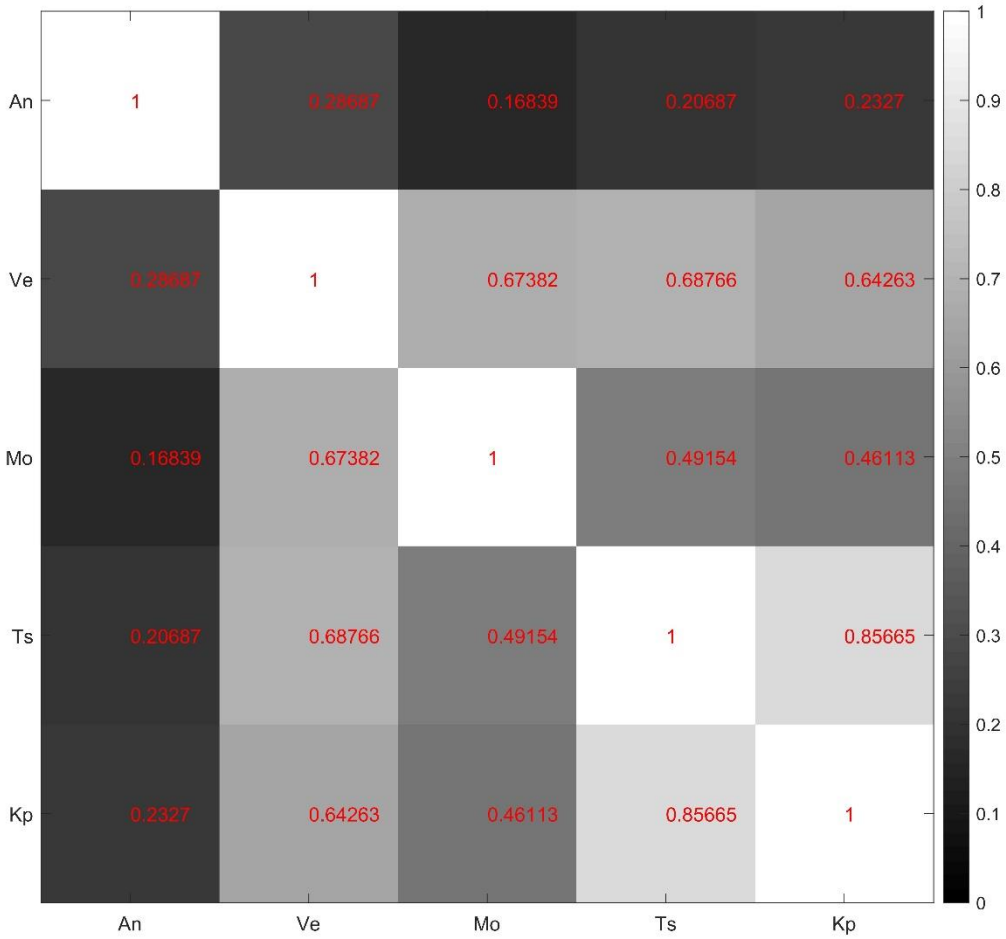

Figure 3.25 Correlation coefficient matrix plotted with color proportional to correlation coefficient. An=Ancona, Ve=Venezia, Mo=Monfalcone, Ts=Trieste, Kp=Koper.

3.3.2 Non-Tidal Oceanic model of the Adriatic Basin

In order to estimate the gravity effects due to Newtonian and loading contributions of the Adriatic basin I interpolated the sea level heights for each time step of the 5 time-series of the Non-tidal sea level on a regular grid. I used an inverse distance interpolator applied to regular grid that covers the whole Adriatic Sea with 0.01° spatial resolution. I discretized the basin up to a distance of 2.5° from the SK1 station, since I did not have at disposal adequate data from other harbors to constrain the empirical model (i.e. in Croatia and Southern Italy). In any case this distance is adequate for capturing over the 75 % of the local non-tidal contribution, as

testified by the Figure 3.26b which shows the gravity effect at SK1 as a function of the radial distance which encloses the considered water masses. The gravity variation is calculated discretizing the basin by tesseroids and considering a uniform layer of water 1 m thick. We see that masses farther than 2.5° contribute maximally by about 5 nm/s^2. This is a worst case scenario, however, since typically the largest non-tidal contributions are recorded in the Northern Adriatic Sea, while in Ancona for instance the transients are usually smaller.

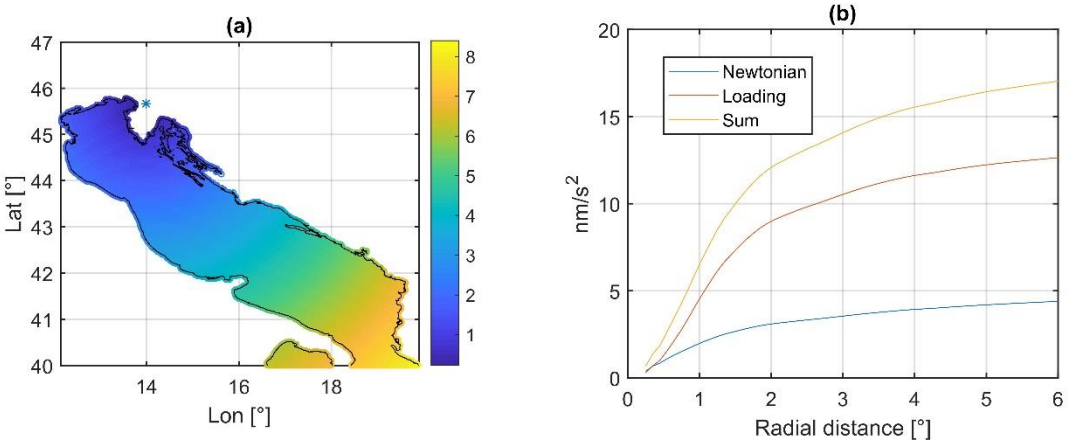

Figure 3.26 a) Radial distances of the Adriatic basin from SK1 (blue star). b) Gravity effect at SK1 due to the Newtonian (blue) and loading effects (red). The sum is reported in yellow

As an example the left plot of Figure 3.27 shows the interpolated sea level heights on the 3rd February 2019 at 4 am when a strong meteorological forcing was acting on the sea surface. We see that Ancona area shows the lowest sea level variations compared to the North Adriatic where in Trieste, Koper and Monfalcone the level exceeded the 50 cm. The plot on the left depicts the situation during high atmospheric pressure conditions where the sea surface is mostly flat.

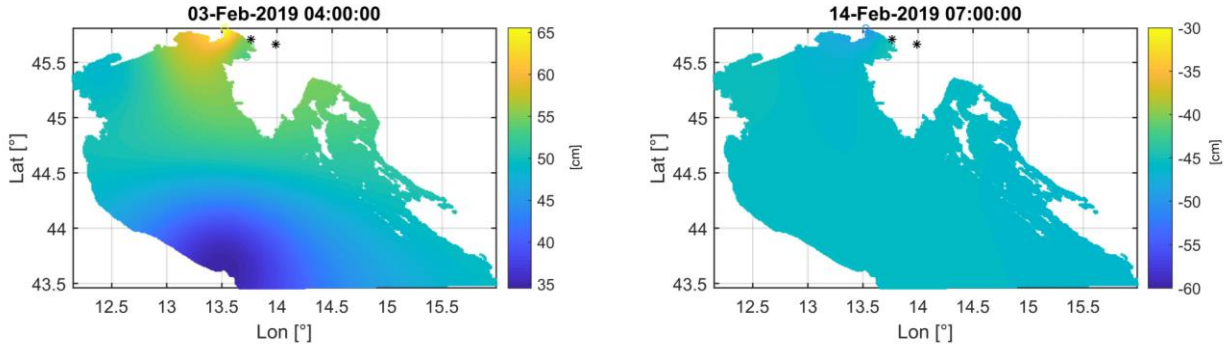

Figure 3.27 Empirical model of the sea level variations constrained by tide gauge observations. Left: in a day of strong meteorological forcing; right: during a quiet day. Black dots show position of SK1 (Eastern dot) and Grotta Gigante.

In addition to the Newtonian component I calculated the loading effects as well, exploiting the equations presented in the chapter 3.2.3. Figure 3.28b shows both Newtonian and loading the non-tidal effects calculated at SK1 for a time-span of 1 month, together with the ECCO2 model used for estimate the far field effects at distances larger than 2.5° from SK1. The comparison with the observed gravity signals is reported in figure 3.28c while the Non tidal contributions at the different harbors are plotted in 3.28a.

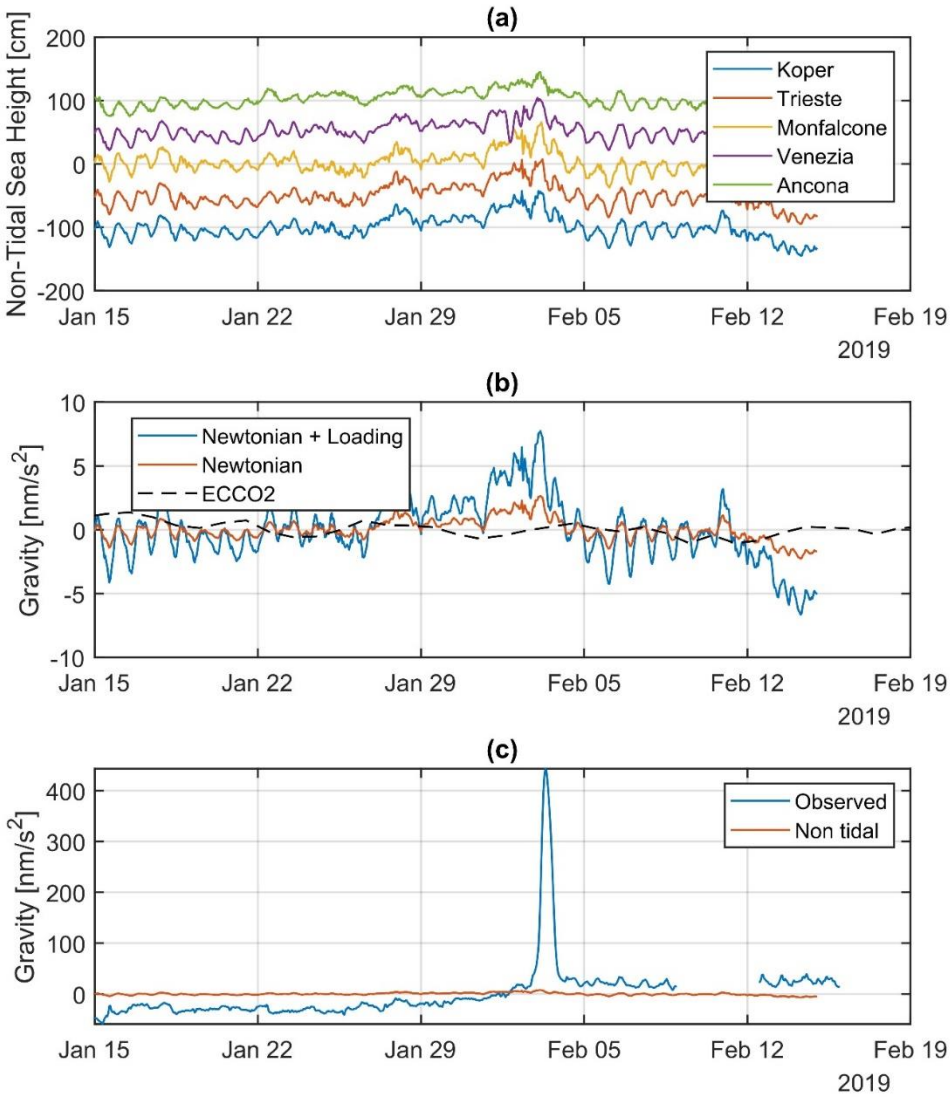

Figure 3.28 a) Non-tidal level variations at 5 harbors in the Adriatic basin. The levels are arbitrarily shifted by a constant for clarity. b) Modelled NTOL gravity contribution at SK1: in red only Newtonian; in blue Newtonian component and loading; dashed line: ECCO2 model far field contribution (i.e. distances > 2.5°). c) Comparison of the observed transients in January-February 2019 with the NTOL loading effect (Newtonian + loading). The large gravity transient is due to the hydrologic signal of a flood event.

We see that the loading effect is larger than the Newtonian one. In general, the NTOL contribution compared to the recorded transients is generally smaller and in the case of the February 2019 hydrologic transient its amplitude is almost two orders of magnitude lower. From the point of view of the improvement of the residuals the NTOL correction for the time-span considered in Figure 3.28 seem to slightly reduce the RMS from 54.5 nm/s^2 to 54 nm/s^2.

3.4 Local and Non local hydrologic contributions

Far field continental hydrology and also local contribution of the immediate surroundings of the gravimeter could generate further gravity contributions that could correlate and superpose with the signal due to the Reka floodings. Hence these contributions should be evaluated and subtracted before modelling the hydrologic transient of interest.

3.4.1 Continental hydrologic gravity variations

The hydrologic effect of the far field continental water mass variations was estimated exploiting the GLDAS (Global Land Data Assimilation Systems) products. GLDAS is a project that offers several databases of the land surface state and fluxes in the whole world, at different spatial and temporal resolutions (Rodell et al., 2004). Surface temperature, snow cover, soil moisture, vegetation index are examples of the physical parameters that could be extracted. Each of these is provided at monthly, daily and also 3 h temporal resolutions, while 0.25° and 1° are the spatial resolutions available. The database is constructed incorporating direct observations of the various phenomena from satellite or from ground based observations and modelling procedures. I employed the integrated soil moisture of the first 2 m of soil, which has been already used for correcting geodetic time-series from hydrologic effects: some applications with GRACE could be found in Matsuo & Heki (2010) or for GNSS in Yi et al. (2016). The 3-hours resolution models are also employed for correcting superconducting gravimeter observations (Mikolaj et al., 2016).

An example of 2 snapshots of the GLDAS model is given in Figure 3.29, which reports the integrated soil moisture mass (in kg/m^2) for 3rd February and 3rd August 2019 at both at 6:00 am.

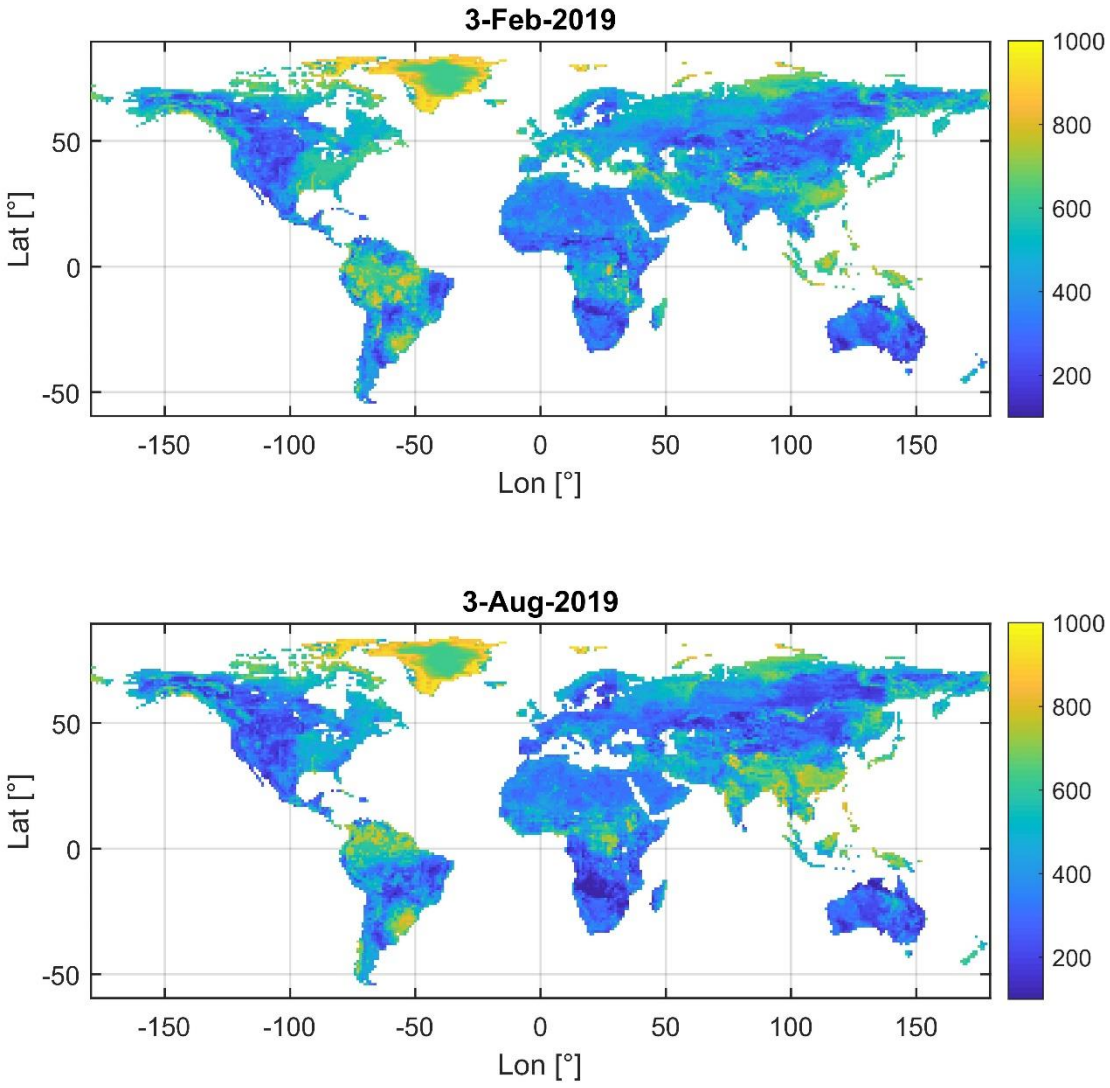

Figure 3.29 Two snapshots of the GLDAS model of the integrated soil moisture, expressed in kg/m^2 and shown with the color code reported on the side.

From the GLDAS grids I calculated both the Newtonian and loading components exploiting the mGlobe Matlab routines (Mikolaj et al., 2016). Through this package the time-series of the global hydrologic contribution could be calculated at SK1. The program allows including or excluding certain areas, such as Greenland or a local area around the station for which the models have inadequate temporal and spatial resolution. A detailed DEM model of the station could be included in order to keep into account the local topography and the height of the station. In the local area the contributions are calculated on an interpolated grid at higher resolution with respect to the available hydrologic models.

I exploited the 3-hours resolution GLDAS soil moisture model globally, with a spatial resolution of 1°. I tested also the higher spatial resolution model, for which the calculation doesn't differ significantly. I excluded from the calculation the contributions coming from masses at distances < 0.1°, as I expect these to be mostly due to the Reka contribution, target of the study.

The figure 3.30 shows the hydrologic contribution for the whole time-series considered: we see that the dominant signal is a yearly component which has 20 nm/s^2 amplitude and superposed there are other smaller contributions due to specific rain events. In general, such variations rarely exceed 5 nm/s^2 in few days; one example of this is the sudden variation at the end of October 2018. The impact on the time-series is very small as observable in the whole time-series in Figure 3.30b or in Figure 3.31, where a zoom in January-Febraury 2019 shown. In this one month long time-series there is only a slight improvement of the RMS error that decreases from 20.5 to 19.9 nm/s^2. In this figure we can also compare the difference in the magnitude between global hydrology and the local hydrologic effect due to the Škocjan flood event, which is about 200 times larger.

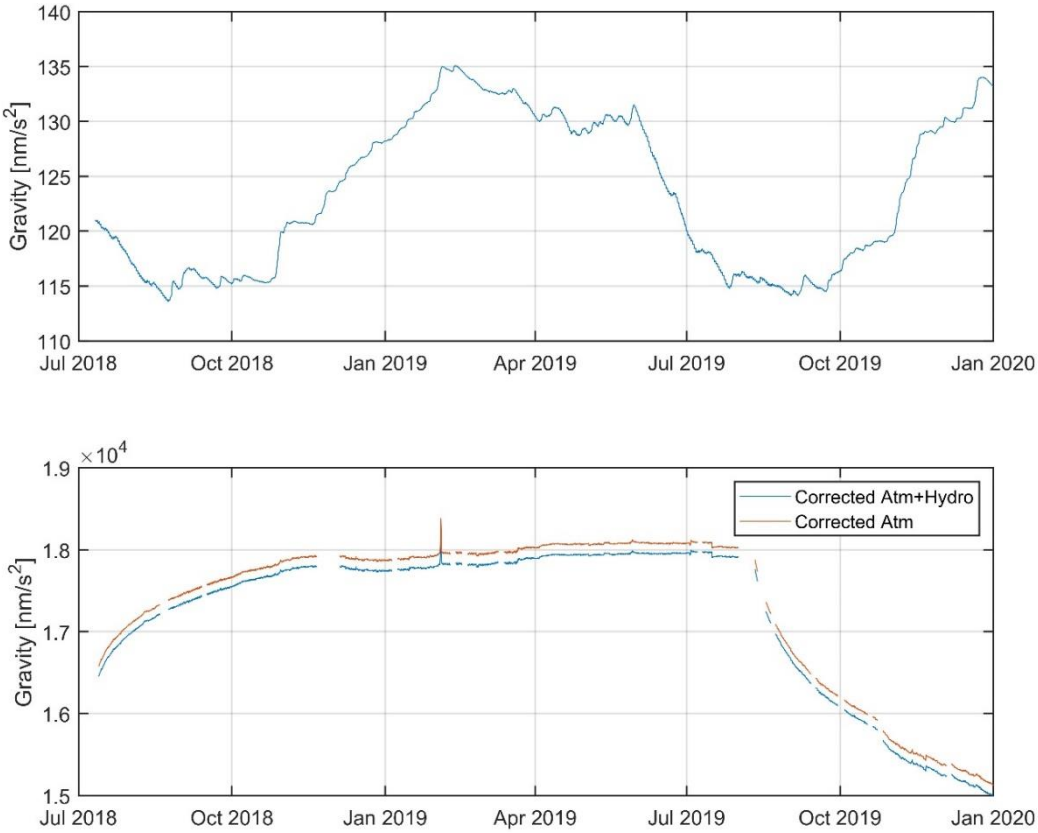

Figure 3.30 a) Gravity contribution of the global hydrologic component at SK1 due to the GLDAS model. b) Corrected time-series for the global hydrologic component.

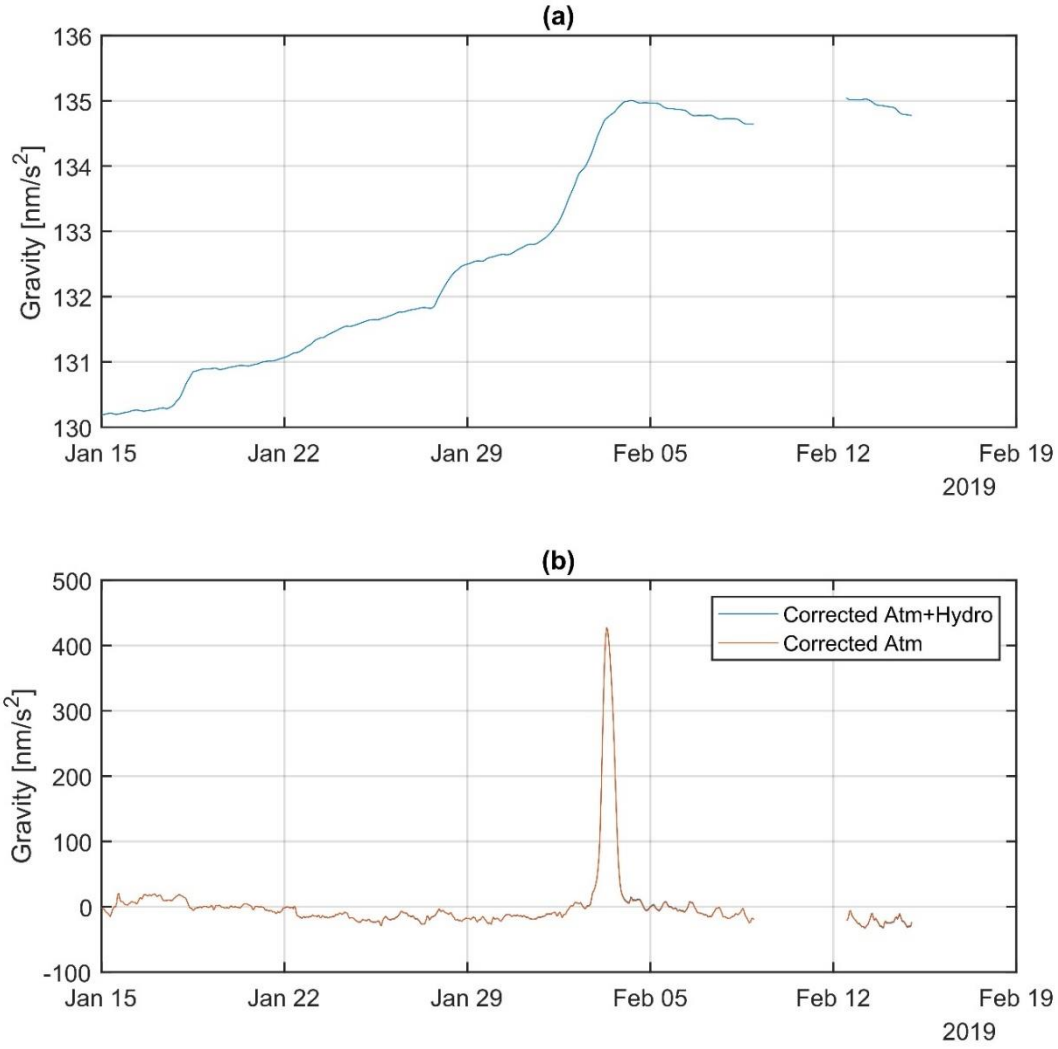

Figure 3.31 Detail of the global hydrologic correction for January-February 2019. a) Global hydrologic contribution. b) Corrected and un-corrected time-series. Note that a linear trend was removed from both the time-series.

3.4.2 Local hydrologic contribution

As pointed out by many authors (Meurers et al., 2007; Mikolaj et al., 2015; Reich et al., 2019) the gravity effect of the local water storage in the immediate surroundings of the meter (< 10 m) during a rain event could be very large and should be estimated and eventually accounted for. Modelling such local effect is challenging, since it requires detailed knowledge of soil characteristics and of the mechanism of water infiltration. Usually such constraints are lacking

and this is up to now also a limit in the Škocjan study case where also the extremely inhomogeneous superficial epikarst structure further complicates the modelling.

In any case I tried to estimate at least what could be maximally the gravity contribution due to short term atmospheric events associated to heavy rainfalls. This could be done, as outlined in Meurers et al. (2007), by calculating the gravity response to a 1 mm rain event (admittance) using a high resolution topographic model. Then for each rain event the maximal effect would be simply calculated by multiplying the rain gauge measurements and the admittance value. I say maximal effect because in my case the gravimeter is located on the surface and the calculation implicitly assumes the water to be stored in the first cm of soil with no water infiltration. No run-off is modelled and no surface deformation is accounted for. I exploited 3 DEMs at different spatial resolutions for the areas surrounding the station: I take advantage of the Lidar acquisition for the topography within a radius of 250 m, a 20 m resolution model is employed up to 4 km while a 90 m spatial resolution DEM model is exploited for the external ring up to a 15 km distance from SK1 (Figure 3.33a).

Two possible scenarios are investigated: one considering the “umbrella effect” which assumes the immediate surrounding of the meter to be shielded (in this case a 4 m x 4 m area) and hence not able to temporarily store water masses, the other assuming the umbrella effect to be negligible. The first simulation is the most realistic in the Škocjan case since the instrument is located in a building (surrounded by parking lots and several other infrastructures) that shields the ground. The two admittance curves are plotted in Figure 3.32d. The no umbrella effect scenario predicts larger gravity variations compared to the other situation: the difference in magnitude is about a factor 20. The other striking difference is the sign of the correction, which in the case of absence of umbrella effect is negative. This is due to the fact that the meter is hosted in a building that is partly excavated on the limestone rocks and hence the topographic level is located at higher elevations with respect to the meter (Figure 3.32b and 3.32c). As a consequence, during rain events the additional water mass accumulated above the instrument causes a gravity decrease.

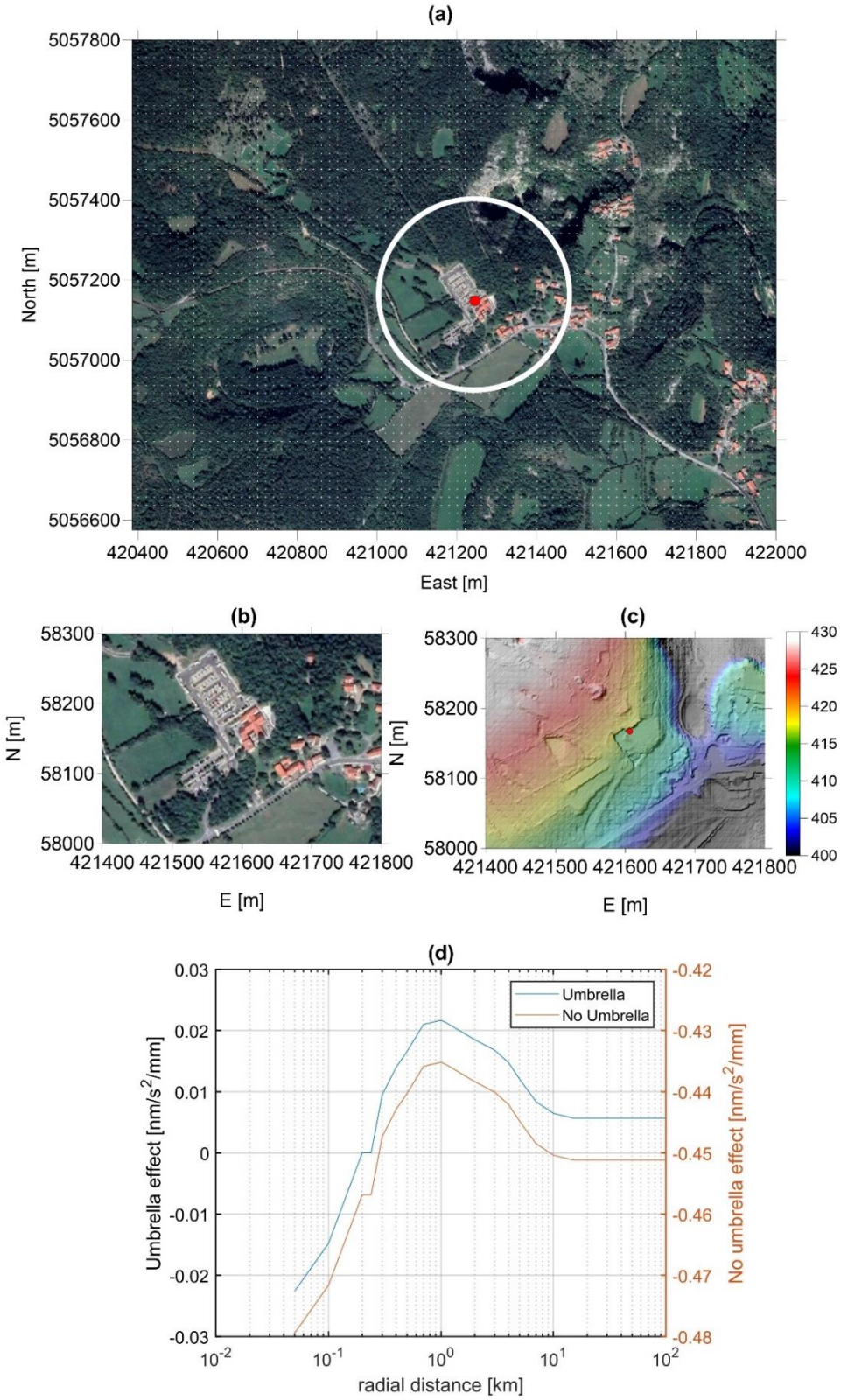

Figure 3.32 a) Aerial view of the Škocjan area. White circle marks the 250 m radius around SK1 (red dot). Reference system (UTM-33; WGS84). b) Detail into the info-center; c) DEM of the area. d) Gravity response to 1 mm rain event at SK1 as a function of the radius of the area where it is supposed to rain; blue curve: umbrella effect considered; red: no umbrella effect.

For two selected events I calculated the gravity response to the rainfall, by simply multiplying the cumulative rain by the value of the admittance corresponding to the area of radius 10 km.

Figures 3.33a and 3.33b show the results for the February 2019 event while Figures 3.33c and 3.33d detail the calculations for October 2018. Both in Figures 3.33b and 3.33d the red and green lines show the gravity response to the rainfall with and without considering the umbrella effect respectively.

If the umbrella effect is considered the gravity corrections are insignificant and generally below the 1 nm/s^2. Disregarding the umbrella effect provides substantial variations, which, however are generally not observed in real data, a part on the 15th January in which a small decrease in gravity is observed and that seems coherent with the modeled effect of the rain. During important rain events the gravity variations observed are usually positive, suggesting that other hydrologic contributions, such as Reka, are dominant with respect to the local effects.

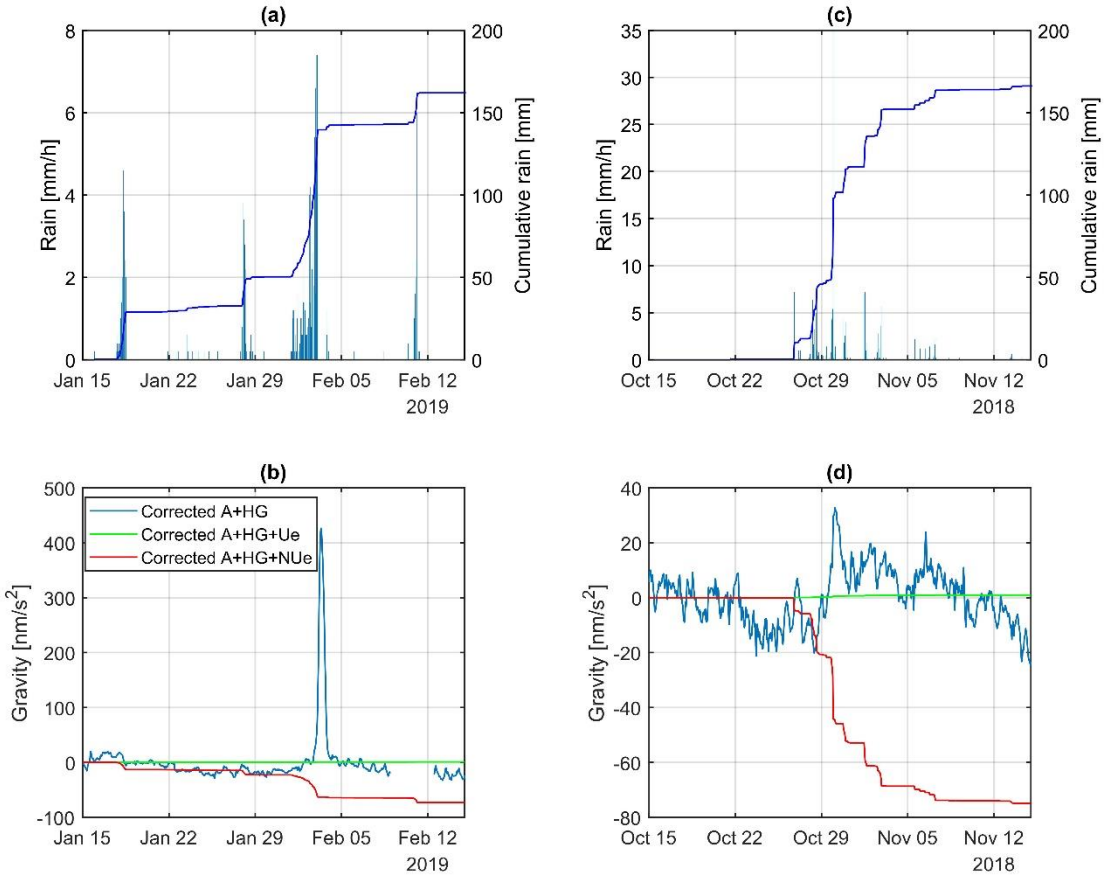

Figure 3.33 a) and c) Rain and cumulative curve of the rain for 2 time-series in Škocjan. b) and d) Corrected gravity effects: blue curve reports the gravity data corrected for atmospheric effects (A) and global hydrology (HG); correction for the local hydrology with and without considering the umbrella effect, respectively in green and red.

3.5 Gravity residuals due to flood events

After removing all these contributions, several residuals correlated with the hydrologic signal of the Škocjan caves are evident in the time series. The following Figures 3.34 and 3.35 show three examples of such transients. All figures show on top the rain together with the discharge recorded at Cerkvenikov Mlin; the graphs in the middle display the water level recorded in the Martelova chamber while the bottom plots illustrate the observed gravity variations.

The January-February 2019 event is the largest with amplitudes exceeding 400 nm/s^2; it is associated with intense rain in the recharge basin of the Reka that caused an impressive increase of the discharge of the river up to more than 300 m^3/s. The other two events are smaller: the first happened at the end of October 2018 when the rainfall amounted to more than 100 mm within few hours with a peak of almost 30 mm/hr. The Reka discharge increased up to 220 m^3/s causing a rise of 20 m of the water level in the Martelova chamber. The gravity transient associated to the event is about 50 nm/s^2.

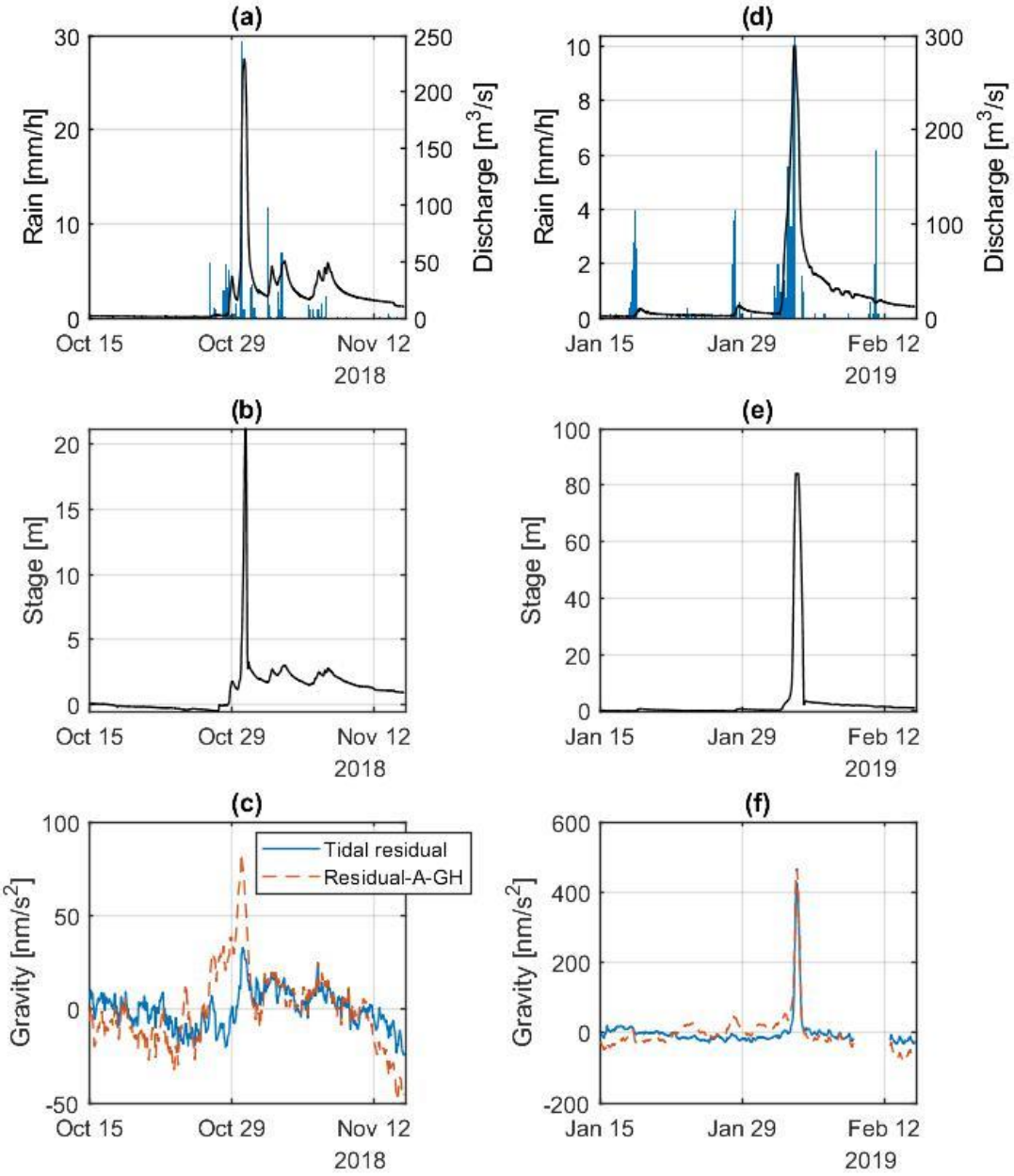

Figure 3.34 Hydrologic signals related to flooding of the Škocjan caves: a), b) and c) October 2018 event; d), e) and f) February 2019 event. a) Hourly rain in Škocjan (blue bars) and Reka discharge at Cerkvenikov Mlin. b) Water level variations recorded in Martelova. c) Gravity residuals after the subtraction of Earth and marine tides (blue) and after the subtraction of atmospheric effects and global hydrology. d) e) and f) as a) b) and c) but for February 2019 event.

The last meteoric event shown by Figures 3.35a-b-c caused a peak discharge of the Reka of less than 200 m^3/s and a modest variation water level variation in the Škocjan caves (less than 10 m). However the SK1 give a clear peak of 35 nm/s^2 correlated with the stage in Martelova.

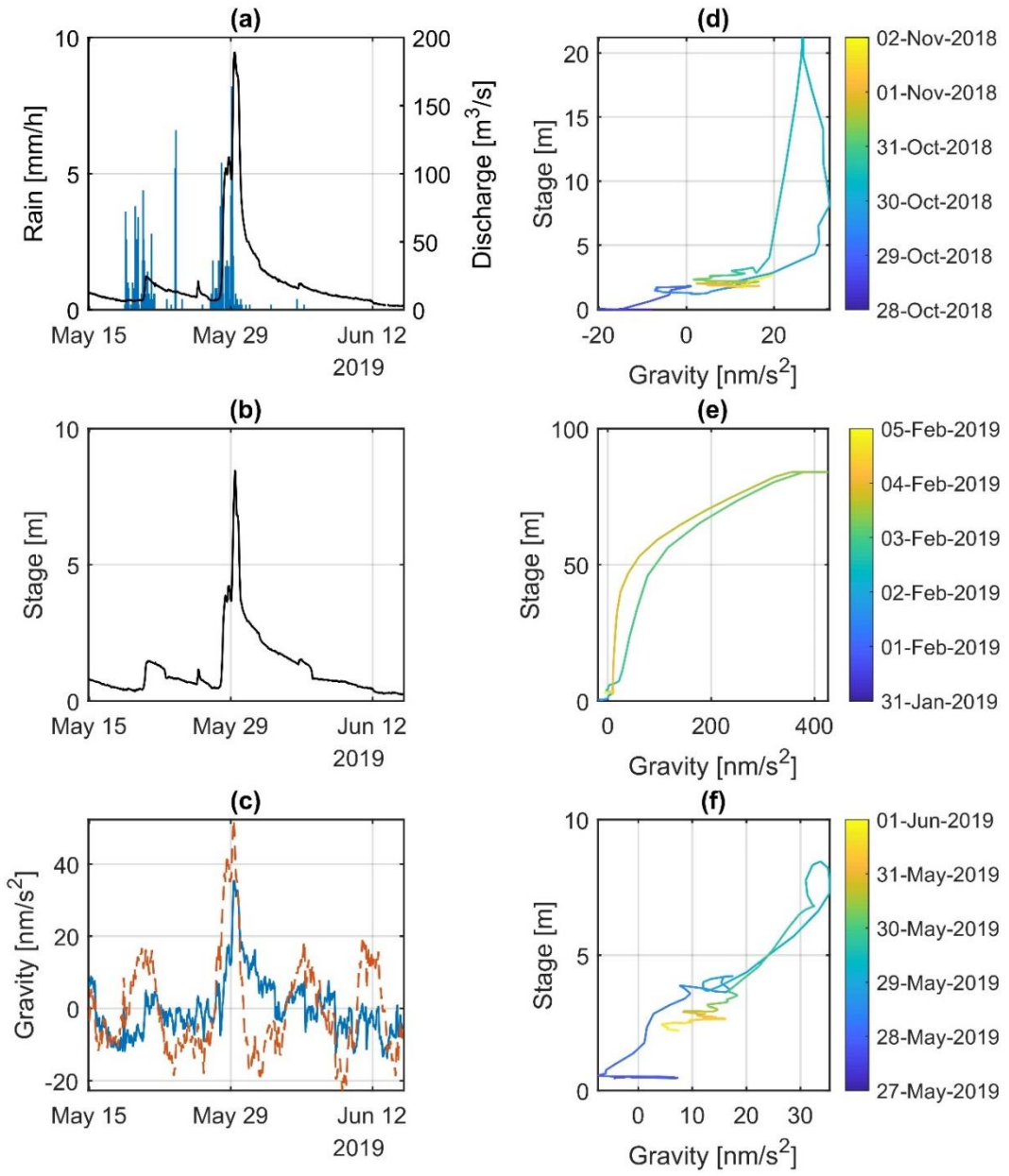

Figure 3.35 Hydrologic signals related to flooding of the Škocjan caves on May 2019. a) Hourly rain in Škocjan (blue bars) and Reka discharge at Cerkvenikov Mlin. b) Water level variations recorded in Martelova. c) Gravity residuals after the subtraction of Earth and marine tides (blue) and after the subtraction of atmospheric effects and global hydrology. d), e) and f) correlation between water level and gravity for the three events considered. Color code proportional to date.

The last plots demonstrate the relation between stage and the gravity: we see that for this last event there is a strong and almost linear relation between the two measurements (Figure 3.35f), while for the large event of February 2019 (Figure 3.35e) a hysteretic behavior appears

and which will be discussed in the next chapter. The transient in October 2018 shows an almost linear relation at the beginning of the event while at the flood peak in Martelova, gravity decreases rapidly, suggesting that probably other unmodelled geophysical phenomena are superposing.

Chapter 4
Joint hydraulic gravimetric model of a flood event in the Škocjan caves

To validate the relation between the hydraulic and gravimetric signal, I have modelled both responses. Hereinafter, two hydraulic and gravimetric models of the 2019 flooding event are discussed: the first is derived by Gabrovšek et al. (2018) in which the channel geometries are very simple and the drainage system is approximated by rectangular prisms.
The second model, includes a more realistic approximation of the Škocjan-Kačna system and the channel cross-sections are constrained by the available topographic data acquired inside and outside the cave system.
In both cases I discuss the mass balances for the system and prove the importance of including the gravimeter observations in the modelling procedure. By the first model I also demonstrate that reliable results, in terms of water mass balances, are obtainable by rather simplified hydraulic models, which are an important outcome for exporting the methodology to less known karstic contexts, where the underground void distribution is poorly known.
In all the cases discussed in the following, the hydraulic simulations are performed exploiting the SWMM software which was already presented and employed for the synthetic simulations shown in chapter 2. The gravimetric simulations are constrained by the water volumes estimated from the hydraulic model and, similarly to the preliminary synthetic models, a prisms discretization is employed to calculate the gravity field variations at the SK1 location.

4.1 Simplified Model

A plan view of the model is shown by the black outlines in Figure 4.1a while the model of Gabrovšek et al. (2018) is reported for comparison in 4.1c. Two vertical cross sections along the axis of the models are shown in Figures 4.1b and 4.1d.
Evidently, the model presents a more detailed representation of the Škocjan and Kačna caves system than the Gabrovšek et al. (2018) model.

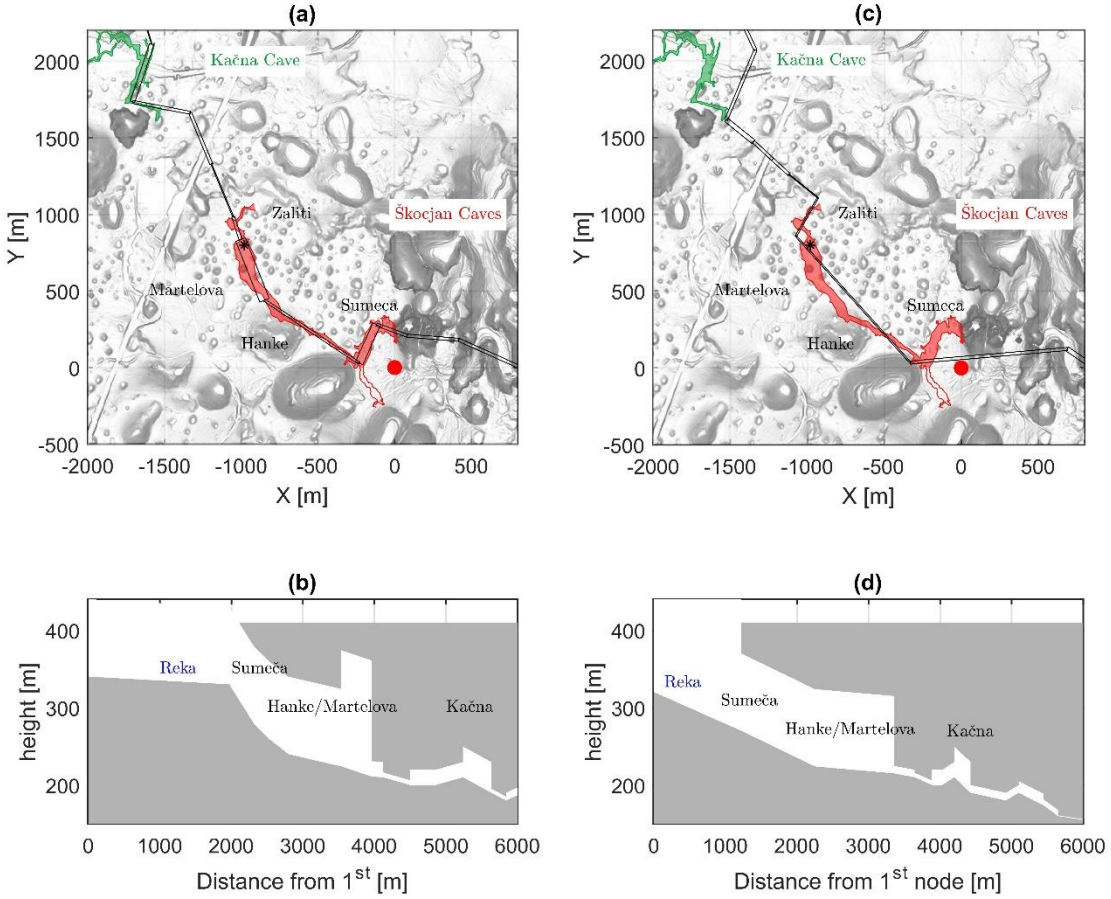

Figure 4.1 a) Hillshade of the Škocjan area from laser-scan with the outlines of Škocjan (red line) and Kačna cave systems (green line). The red areas show the portions of the caves where water is stored during extreme events. Names of the channels and halls are reported for Škocjan. Red dot: location of SK1. Black star: location of P1. Black lines show the plan view of the new hydraulic model discussed in the chapter. b) Vertical cross section along the axes of the channels. c) and d) same as a) and b) but for the Gabrovšek et al. (2018) *model.*

Both the Figures 4.1a and 4.1b show through the red lines the outline of the cave system: the shaded red areas illustrate the portions of the caves subjected to the Reka flooding events. As evident a sector of the Škocjan cave system located SW from SK1 is not included in the floodable areas and in the hydraulic model. This sector is known as Tiha Jama (Silence cave) and it is constituted by a large gallery about 30 m wide and 250 m long that develops in the SE-NW direction and it is linked to the Hanke and Sumeča channels. This gallery is located at higher quotas with respect to both Hanke and Sumeča channels and to my knowledge it has never been flooded, even during important Reka events with peak discharge exceeding 300 m^3/s. The inclusion of such channel in the modelling procedure would not affect the results hence it is simply omitted from the hydraulic model.

In order to perform the simulation, I provided the discharge hydrographs of the Reka River gauging station as input flow to the 1st node of the model.

Using the measured discharge value recorded at Cerkvenikov Mlin (Figure 4.2a), the simulated time series of water levels in P1 were compared to the measured ones (Figure 4.2c). The observed data (black line) show a large plateau at the flood peak, which is due to the fact that the water level exceeded the measurement range of the diver. In general, the model fits the observed data well; the main difference is, that the onset of the flood in the model precedes the recorded one. This time difference is attributable to imperfect modelling of the Kačna cave for which the more complex water circulation is less known than for Škocjan. The final RMS difference between the observed and modelled data amounts to 8 m for the time span of 5 days (1st-6th February 2019) considered in Figure 2.2c.

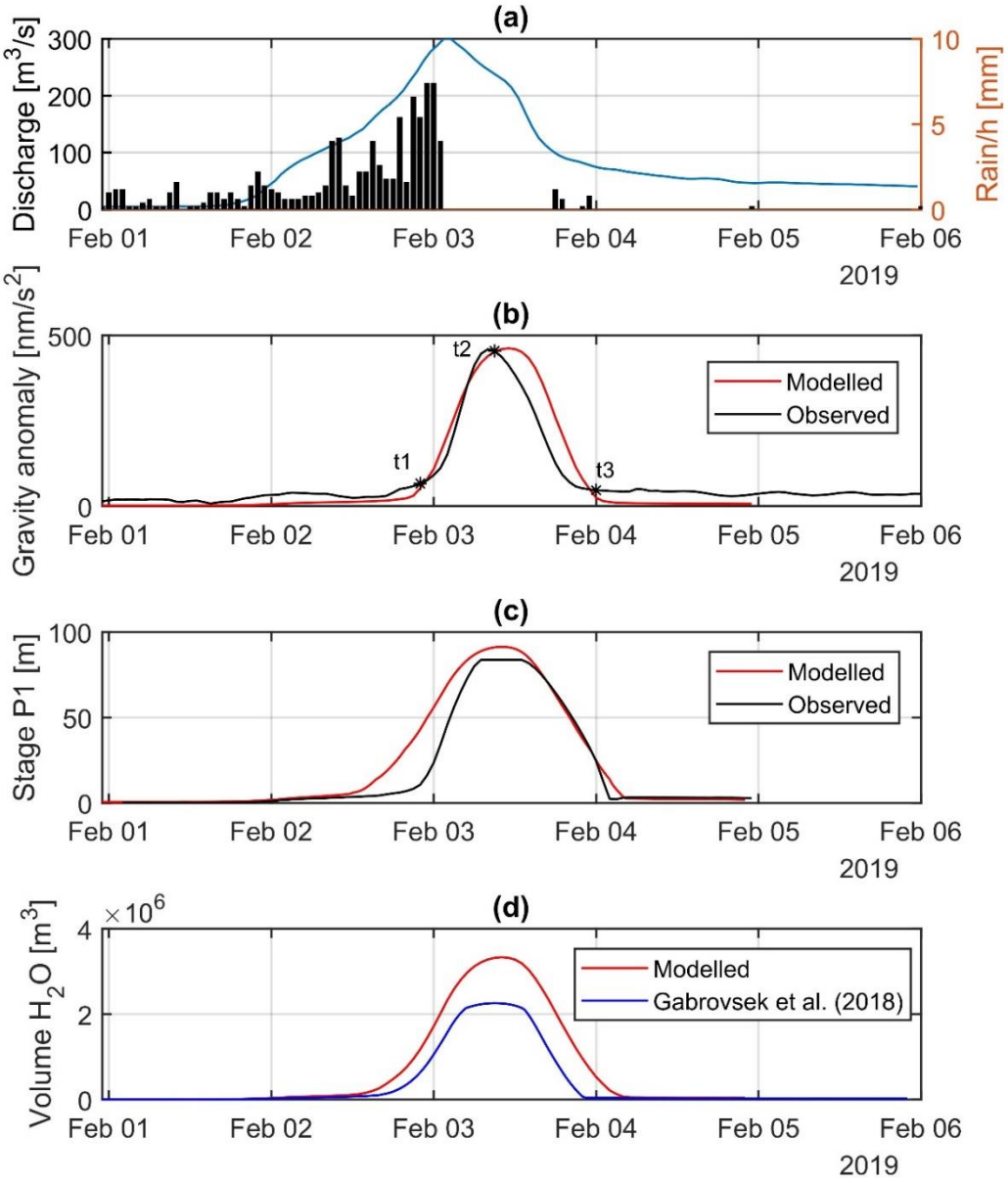

Figure 4.2 Observed and modelled time series of the flood event in 02/2019. a) Hydrological data: rain (black) recorded in Škocjan and discharge (blue line) at Cerkvenikov mlin. b) Observed and modelled gravity signals (black and red) at SK1; t1, t2 and t3 indicate three different phases of the flood event (rising, peak, falling). c) Stage time-series recorded and modelled at P1 (black and red). d) Water volume accumulation during the event in the whole Škocjan system according to the new model (red) and based on Gabrovšek et al. (2018; blue line).

For calculating the gravity effect I discretized the water mass distribution occurring in the conduits at each time-step by a series of small prisms: the base area of each prism is set to be

5 m x 5 m, while the height is equal to the simulated water level in the conduit. To each prism I assigned a unique density value for the water equal to 1000 kg/m^3.

Figure 4.2b shows the comparison between the observed gravity residuals and the model predictions. The model over-estimates a bit the duration of the flood event by less than 5 hours, while the magnitude and the overall shape are well reproduced. The RMS error amounts to 40 nm/s^2 for the 5 days time-span.

The plots of Figure 4.3 show three snapshots (t1,t2 and t3, see Figure 4.2b) of the simulated water levels in the caves during different phases of the flood: the top graphs show the situation in plan view while the bottom graphs show a vertical section along the channels axes. At time t1, the discharge of the Reka is increasing and the high flow conditions have already caused the flooding of the Kačna cave. A back-flooding wave starts to propagate towards Škocjan, however in Martelova and in the other chambers the flow is still mostly in an open channel regime. As new water input from the Reka is provided, the back flood becomes more vigorous and starts affecting the Škocjan caves: now the water level in the caves rapidly raises at rates exceeding 10 m/h. The following time-step t2 shows the situation when the Reka discharge has already reached the peak and it is on the falling limb (about 250 m^3/s), but the back flood is still sustained and the water level in the caves has just reached the maximum as observable in both P1 and SK1 plots (Figures 4.3b-4.3c). During this phase most of the gravity signal originates from the Sumeča (Figure 4.4a), which is the closest cave to the gravimeter, while Hanke and Martelova contribute respectively with 50 nm/s^2 and 10 nm/s^2. Another gravity contribution arises from the channel located before the entrance of the system, which further contributes with 80 nm/s^2. Contribution of conduits downstream Martelova and by the Kačna system are negligible.

The last snap-shot (t3) depicts the situation during low flow conditions, when Martelova and the drainage system towards Kačna is slowly emptying. By comparing these three snapshots we observe the different storage periods in Sumeča/Hanke chambers with respect to Martelova; this is also testified by the differences in the duration of the transients recorded in P1 and SK1.

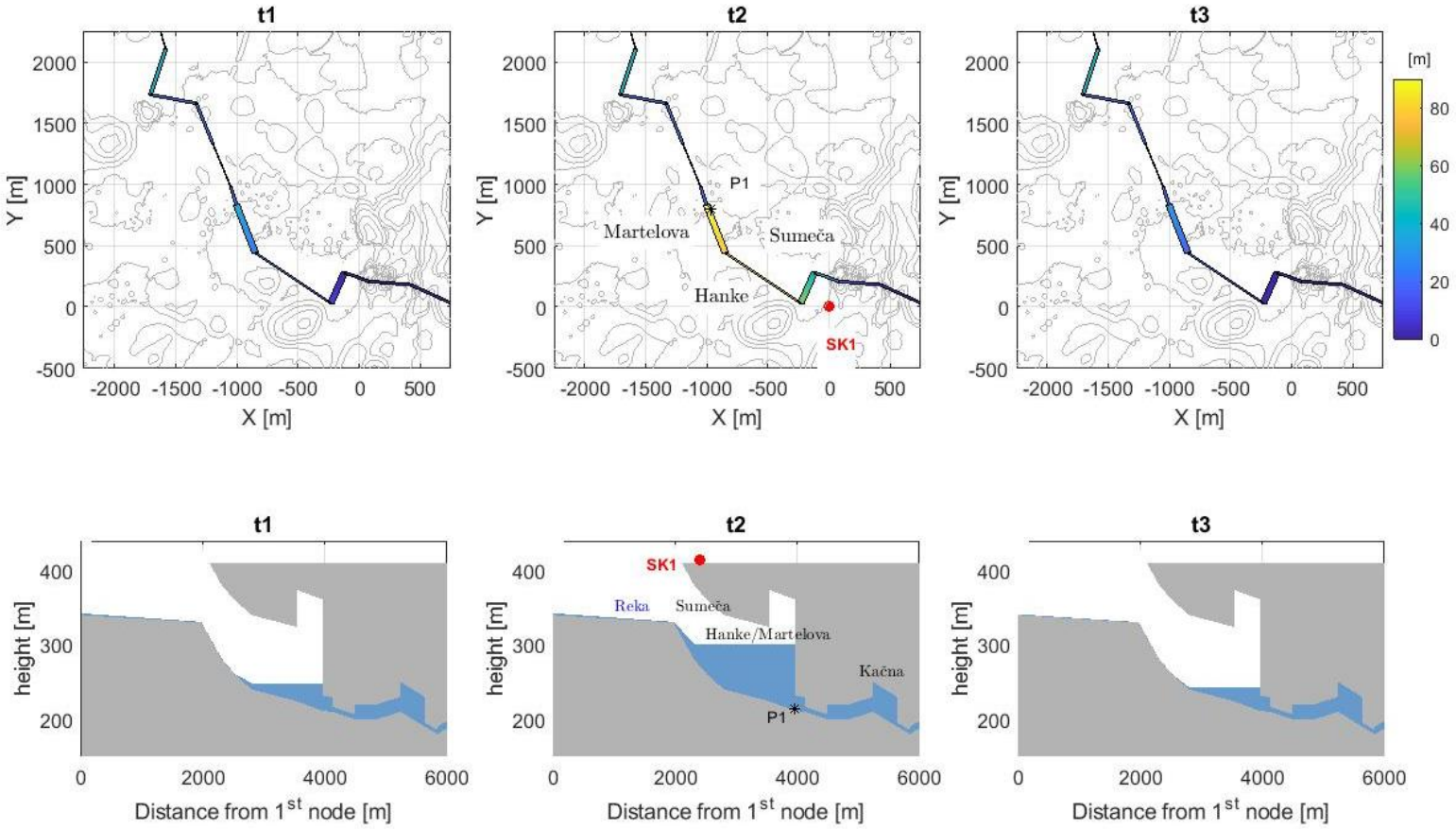

Figure 4.3 Water distribution in the caves at three snapshots (refer to Figure 4.2b): for each time-step, a cross section and a plan view of the water levels in the caves are displayed. Note that in the cross sections the vertical scale is exagerated by a factor of about 10. The colour code is proportional to the water level height in the conduits. The contours of the DEM are shown in grey.

Our hydraulic model predicts an accumulation of more than 3.5 10^6 m^3 of water in the whole cave system at t2: most of the water volume, i.e. 1.8 10^6 m^3, is stored in the Martelova (Figure 4.4b) while Hanke and Sumeča chambers represent smaller storage volumes (0.7 10^6 m^3 each).

The total volume stored in the caves predicted by the new model is almost 30 % bigger compared to the estimated volume predicted by the model of Gabrovšek et al. (2018).

I tried to assess the error on the water budget of the system by considering the P1 to be representative of the level in the whole last chamber of the Škocjan caves and SK1 to be a proxy of the level in Sumeča. I assumed the RMS between observed and modelled gravity signals (40 nm/s^2) as a proxy of the error on the water level in Sumeča Jama: considering a distance of 250 m between the gravimeter and the chamber a 40 nm/s^2 gravity variation translates to a water variation of about 10 m. This means a water volume uncertainty of 1.3 10^5 m^3. For the Hanke channel, since it has a similar volume to Sumeča, I can assume the same uncertainty.

I estimated a water volume uncertainty of 2 10^5 m^3 for Martelova, considering the RMS of the model (8 m) as an estimate on the water level error. As a consequence, the total mass budget error, in a worst case scenario, could sum up maximally at +/- 4.5 10^5 m^3.

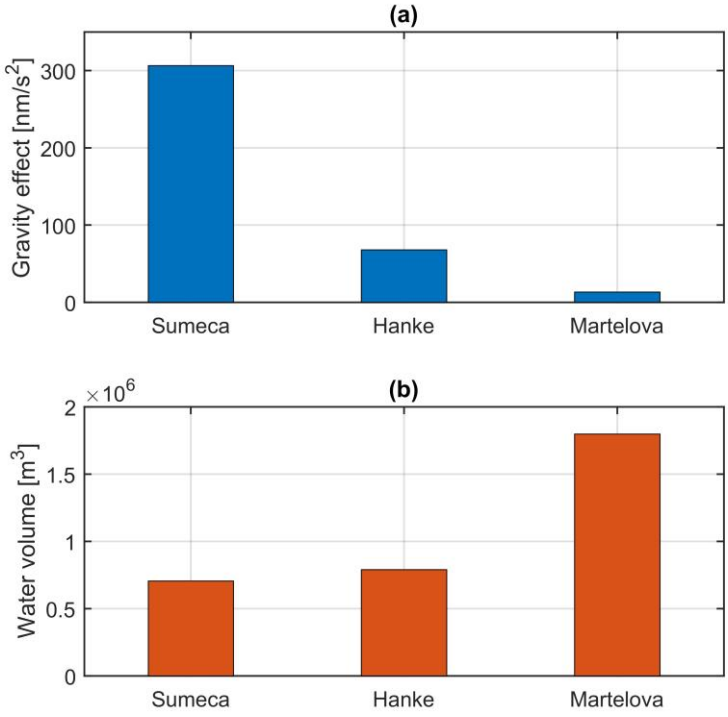

Figure 4.4 a) Gravity contribution of each of the three chambers at the flooding peak t2. b) Stored water volume in each chamber at the flooding peak.

4.2 Model II

The satisfactory fit of the hydrologic and gravimetric records by the model discussed before suggests that a limited number of conduits and restrictions mainly controls the hydraulics of such a system. However, to strengthen and prove this argument I calculated the hydraulic and gravimetric response of a model that includes a more realistic approximation of the channel geometries. The model relies on several topographic measurements that mapped both the areas surrounding the Škocjan caves and the main internal morphological structures and which have been already presented in the chapter 2. In the following I first give a brief overview on how the topographic surveys data are implemented for constraining the hydraulic and gravimetric models; subsequently simulations and results are discussed.

4.2.1 Hydraulic model

The hydraulic response to the flood event was calculated employing the SWMM routines: in this case I discretized the Škocjan caves canyon with 12 conduits of differently shaped cross section, each of them constrained by the internal topographic survey. The hydraulics downstream Martelova, which include Kačna cave, have been taken into account with the same parameters as the model discussed in the previous section 4.1. Since SWMM implements 1D flow modelling routines, the channel cross-section should be symmetric with respect to the vertical axis. For the Škocjan cave system such approximation is quite reasonable as evident from the Figure 4.5 that shows 6 vertical cross sections traced along the cave system (location in Figure 4.6). In this figure the black lines report the morphology according to the topographic survey, while the blue lines plot the equivalent cross sections, implemented for the SWMM calculation. I obtained these equivalent sections by subdividing the height of each vertical section into 10 intervals (dz in the first plot) and then I calculated the average width of the cave inside each dz interval. The equivalent section is built assigning to each dz interval the average width of the channel symmetrically distributed with respect to the z-axis. In this procedure particular attention was posed in assuring the conservation of the flow cross sectional area. In general, the differences between the surveyed cross section areas and the equivalent sections implemented in SWMM are very small and on average about 6 %; the largest deviations lie within +/-20 % interval as also reported in Figure 4.7b.

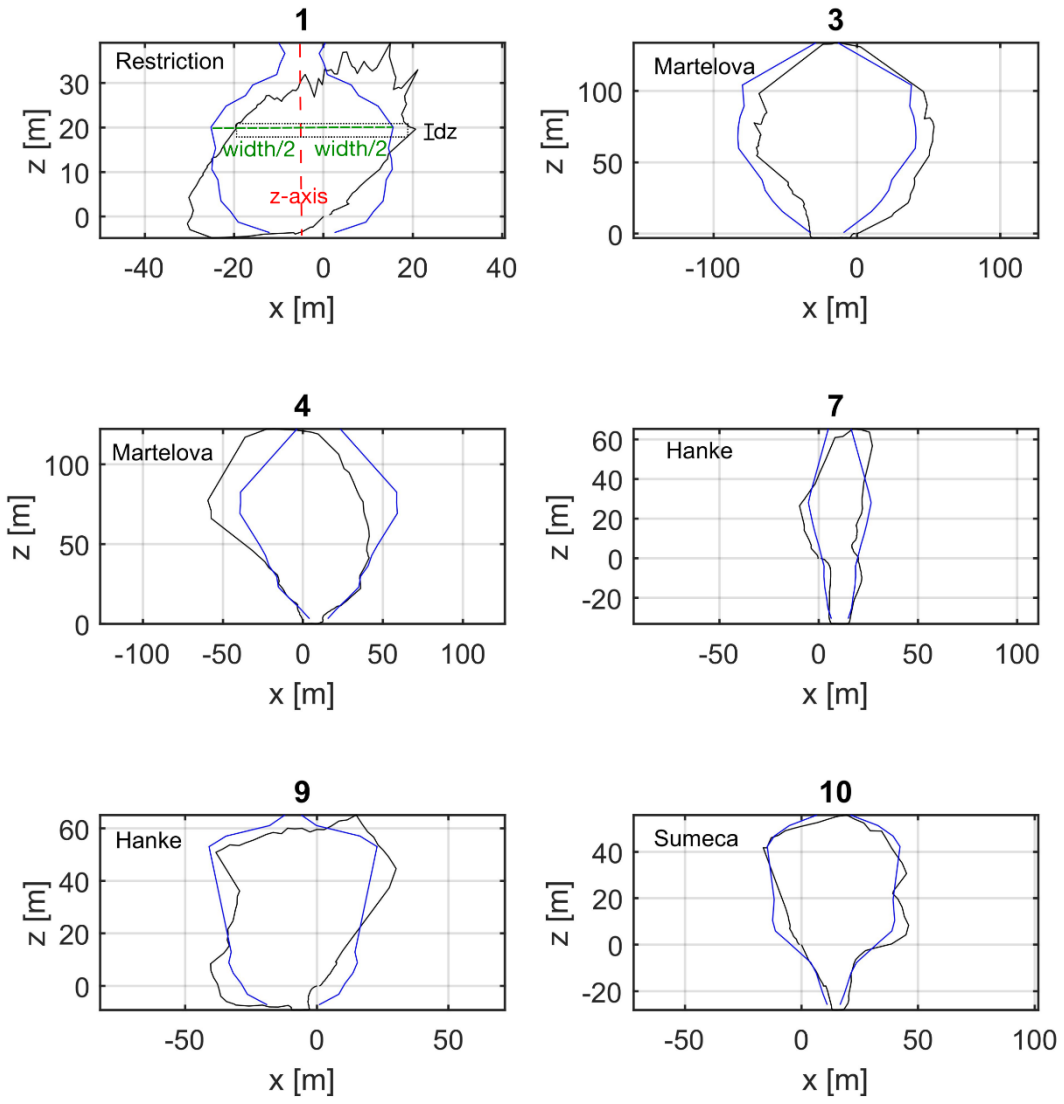

Figure 4.5 Vertical cross-sections inside the Škocjan caves (for location see Figure 4.6): Black lines: real geometry according to the topographic survey; blue lines: the implementation in SWMM software.

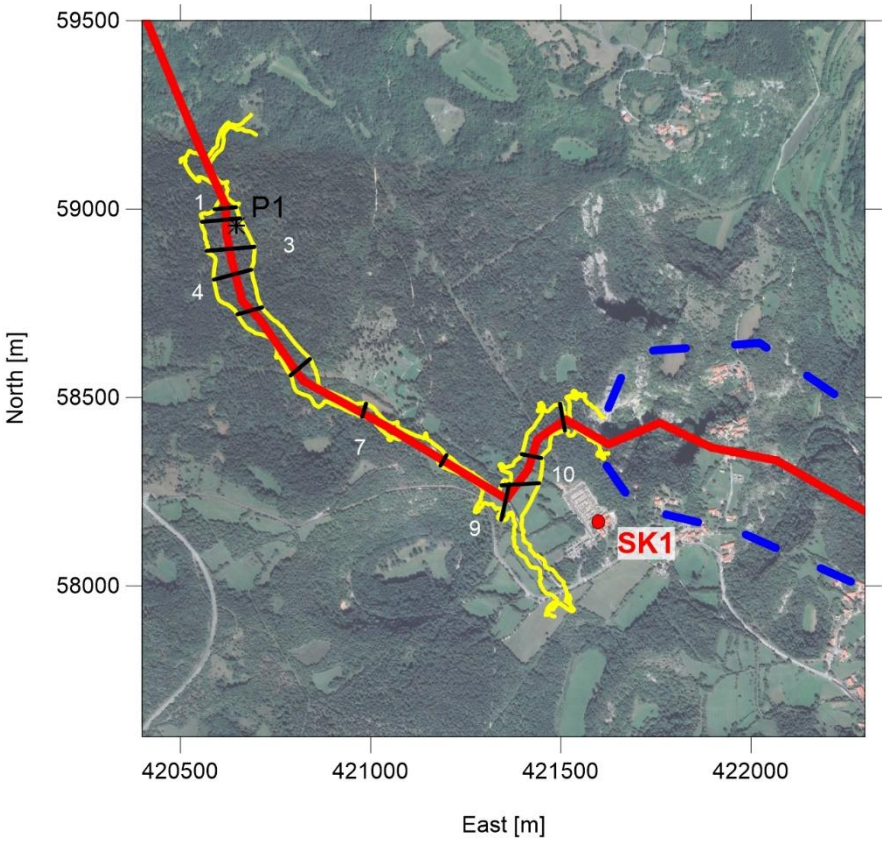

Figure 4.6 Hydraulic model geometry. Red line: axes of the channels; black lines show the location of the vertical cross sections; white numbers indicate the sections shown in 4.5. blue stippled line indicates the external area of the cave.

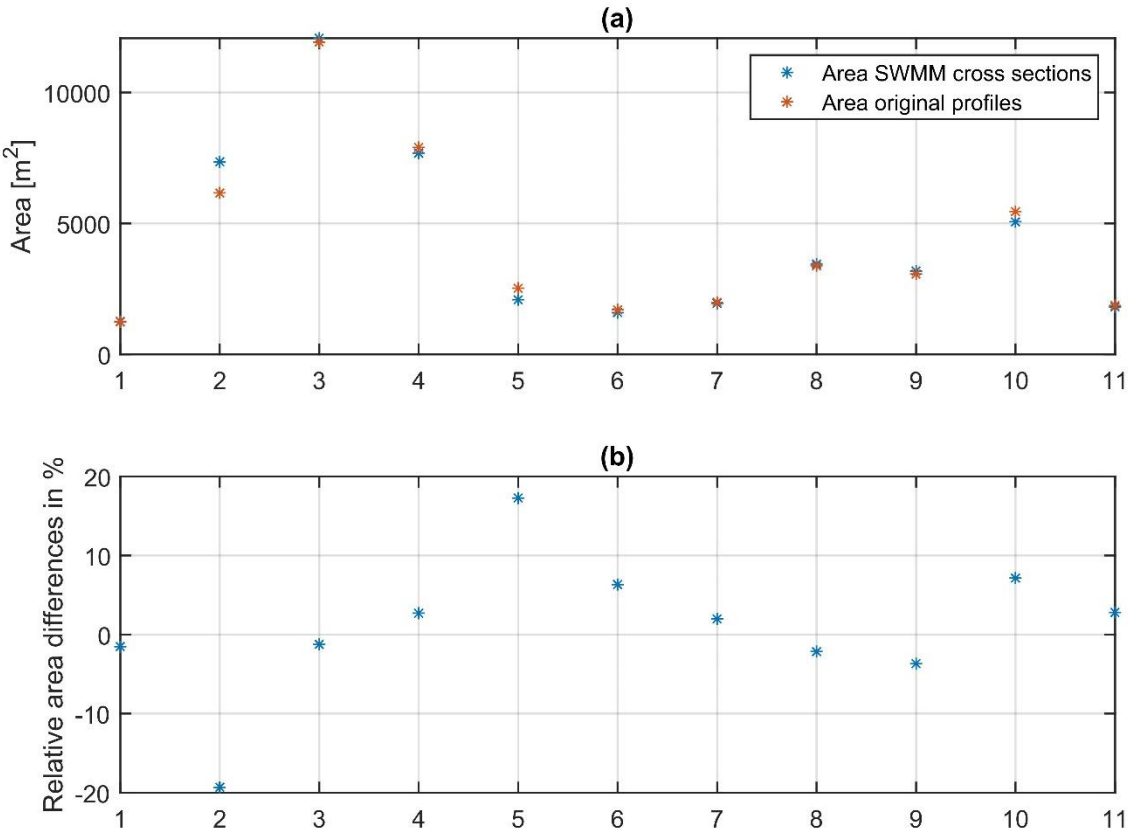

Figure 4.7 a) Comparison between the flow cross sectional areas as derived from the topographic surveys (red stars) and the areas implemented in SWMM (blue star). b) Percentage difference in the areas between the survey and the SWMM implementation.

For the external areas, the channel geometry was derived from 3 topographic profiles taken from the DEM model (ARSO).

The data from the hydrograph at Cerkvenikov Mlin was set as input flow at the first node of the model which is located 5 km away from Škocjan. I simulated the water heights in the different conduits from the 1st February to the 5th February with 15 min resolution.

4.2.2 3D model of the Škocjan caves

For calculating the gravimetric effects, rather than using the geometry of the SWMM model, I built an independent model of the cave internal morphologies which relaxes the assumption on the channel symmetry along the vertical axis. This change in the model is not so impacting for most of the sectors of the cave, as testified by Figure 4.5, but slight differences are present at the entrance of the cave system.

The calculation of the gravimetric effect requires the definition of two surfaces for determining the geometry of the channels: one for the bottom where the river is flowing, and the other for the ceiling of the cave. I obtained these two surfaces elaborating the 25 vertical sections inside the cave that were firstly georeferenced obtaining a cloud point representation of the cavity. Subsequently the cloud points have been divided between points pertaining to the ceiling from those associated to the bottom: I exploit a smooth surface that locally follows the median plane of the cave to divide the point cloud. The surface has been calculated through a local regression (Loess surface), in a similar way as done by Pivetta & Braitenberg (2015) to process the laser-scan data from the Grotta Gigante. In this study the authors used such method for a similar problem, since the surface was employed in order to define top and bottom interfaces of the cavity which were then used to define a prism model and calculate the gravimetric effect. A 3D view of the Škocjan point cloud together with the Loess surface is shown in Figure 4.8 while Figure 4.9 reports the performance of the method along some vertical cross-sections.

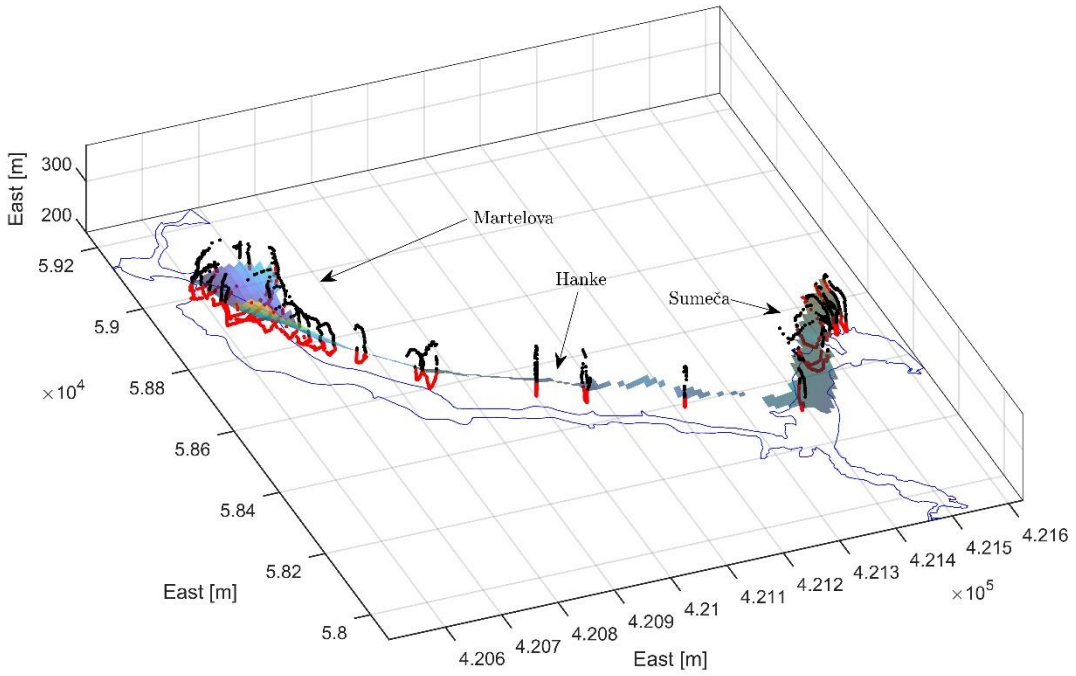

Figure 4.8 3D view of 25 vertical cross sections of the Škocjan cave system. Red: points classified as bottom; black: point pertaining to the top. The Loess interface, used for separation of top/bottom is also reported. The outline of the cave system is shown with the blue line.

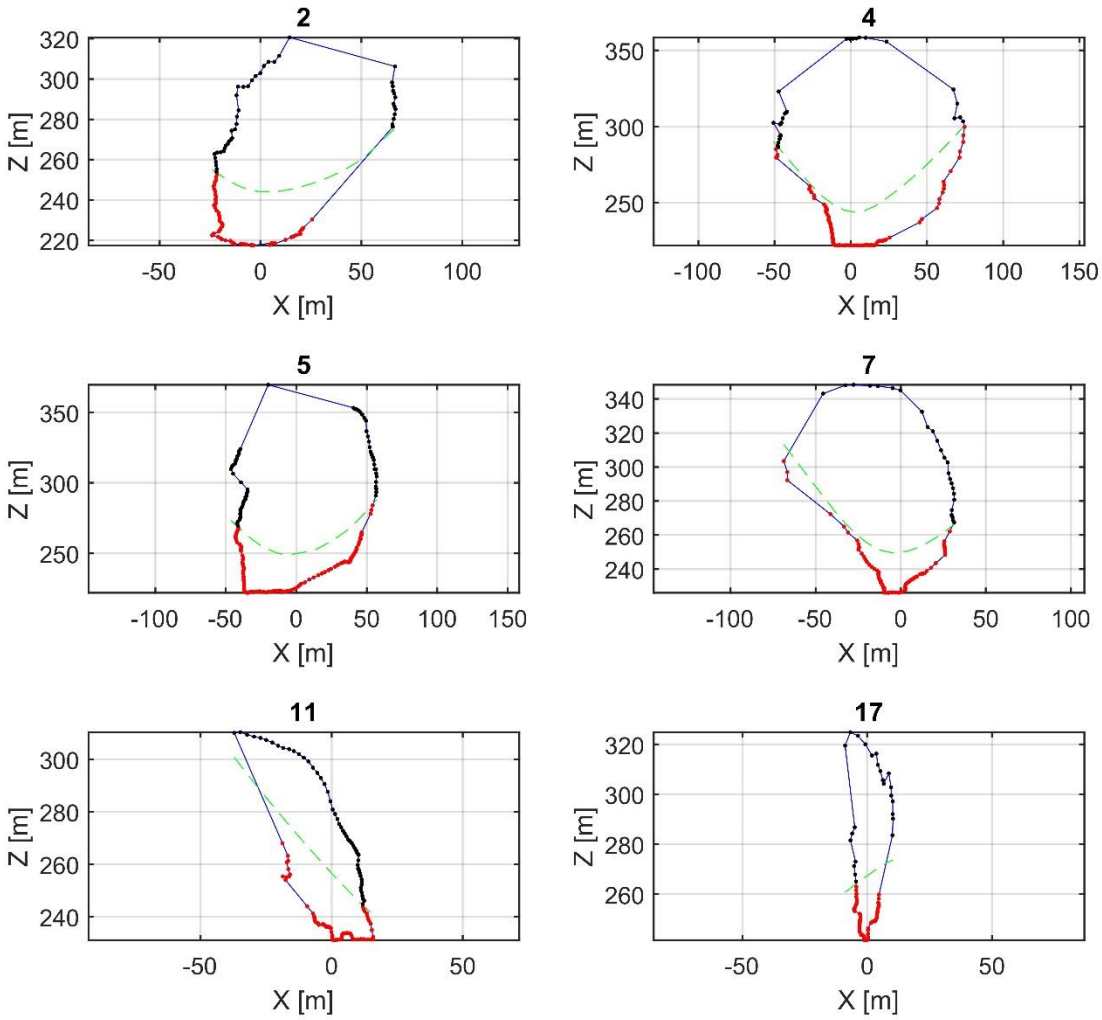

Figure 4.9 Performance of the Loess surface along some vertical sections of the cave. Green dashed line: Loess. Black dots: points classified as top; red points assigned to the bottom. Labels on top report cross-section number: 2-4-5-7 (Martelova); 11-17 (Hanke).

Then I interpolated the scattered points separately into two regular grids with spatial resolution of 2 m x 2 m: for the definition of the bottom interface, in addition to the points derived from the vertical sections, I included also the 3000 points of the topographic survey. For the areas external to the caves, the bottom surface of the river bed is obtained by integrating the topographic survey with the model derived from the laser-scan (ARSO).

The two surfaces are plotted in Figure 4.10a and 4.10b; 4.10d reports also the topography used for the external areas. In all these figures the color code is proportional to the quota of the surface above the sea level. Obviously, the ceiling (plot 4.10b) appears to be smoothed since it is constrained by fewer observations with respect to the bottom. The total volume of

the caves from this model is about 5 10^6 m^3, which is fairly in accordance with previous estimations.

Figure 4.10c reports the sensitivity of the gravimeter, located at SK1 location, to a 1 m water level variation in the cave: similarly to the synthetic tests, we see that in SK1 most of the gravity contribution comes from Sumeča chamber.

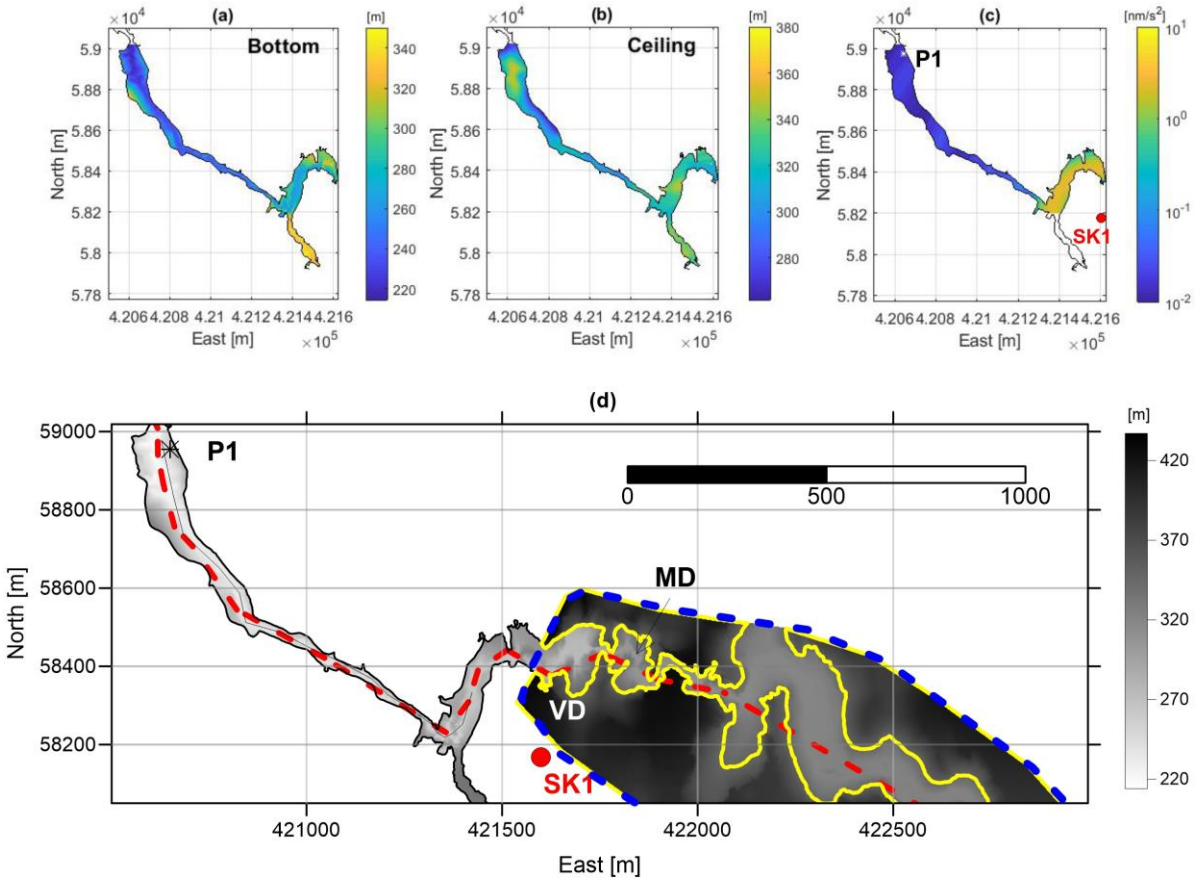

Figure 4.10 a) and b) Bottom and ceiling of the Škocjan cave system according to the model. c) Sensitivity of the gravimeter to 1 m level variation in the cave. d) Bottom of the channel system including the external areas (bounded by dashed line) of the cave system derived from integration of Lidar and topographic surveys. SK1 and P1 locations reported with black star and red dot. Yellow line reports the 350 m contour line which clearly outlines the two dolines, Mala and Velika Dolina (MD and VD) located just before the cave system entrance. Red dashed line reports the hydraulic model channel axis.

With respect to the simple model presented before, in which the conduits were approximated by rectangular prisms, in this model the flooded area in a specific sector of the cave could change as a function of the water level in the conduit. The base area of the each prism is 2 m

x 2 m. An example is given by Figure 4.11, where the plots to the right illustrate the flooded areas, depicted in black, as a function of the water level in P1.

With such model of the internal geometries I calculated the curve in Figure 4.11a, where the flooded water volume is plotted as a function of the water level in P1. I approximate the water level in the cave to be a constant (i.e. the water surface is a horizontal plane), which is realistic for large flood events when the difference between the water level in P1 and water level at the beginning of the cave system is of few meters (see the cross sections in Figure 4.3). For low water levels the estimate is less accurate, since we are neglecting the contribution of the chambers not yet flooded.

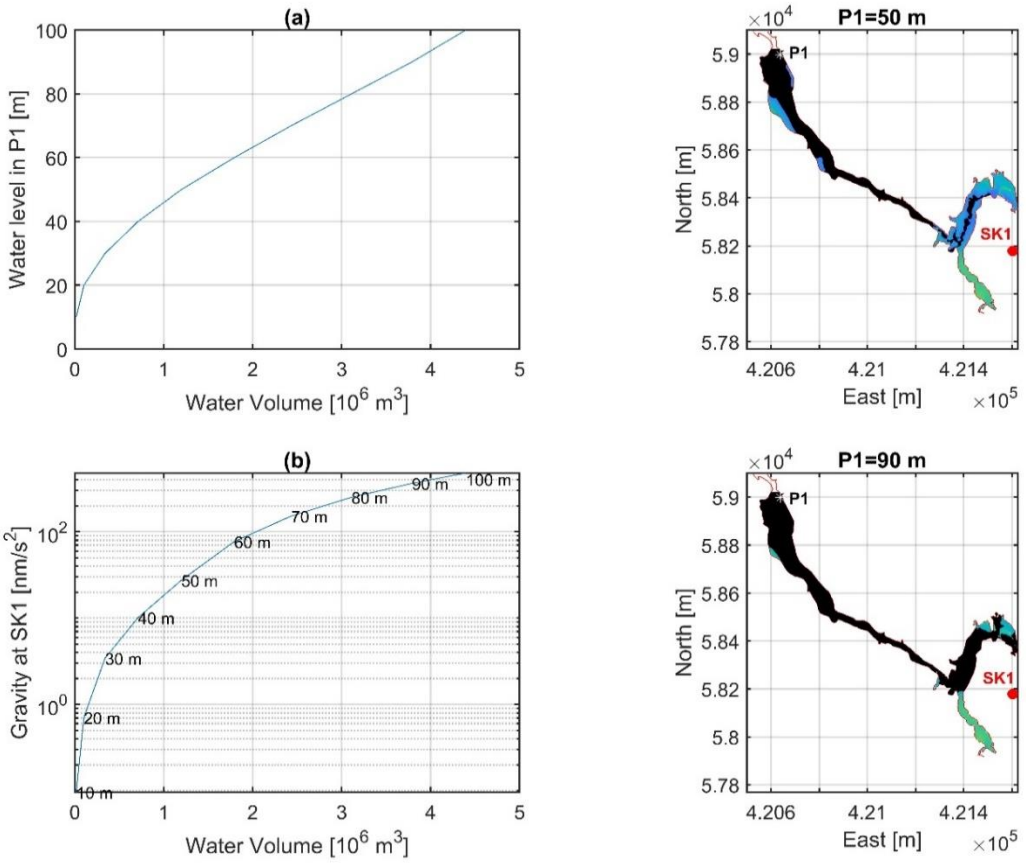

Figure 4.11 a) Water volume in the cave vs. Stage in P1, calculated for the cavity model. b) Gravity effect expected at SK1 as function of the water volume in the Škocjan system. Labels report the corresponding water levels in P1. The plots on the right show the flooded areas (black) when the water level in P1 is 50 m and 90 m. Location of P1 and SK1 are reported with the white star and red circle.

The plot in Figure 4.11b shows the gravity contribution at SK1 for the various flooded volume estimates: the calculation was done exploiting the usual prisms discretization setting the water density to be 1000 kg/m^3. From the plots 4.11a-b we see that a flood event with water level variations of 90 m in P1, similar to the February 2019, is able to store a water volume of

about 3.5 10^6 m^3 in the whole cave system and generate gravity variations of about 350 nm/s^2. The calculation is in fair agreement with the estimates of the simplified model at the peak of the flood event.

4.2.3 Hydraulic and gravimetric responses to the flood event

Finally, I modelled both the hydraulic and gravimetric responses to the Reka flood event employing the SWMM routines.

I have additionally considered the Mala and Velika Dolina (See Figure 4.10) as well as a portion of the meander of the Reka River in the modelling domain. Velika and Mala dolina are two large collapse dolines located just before the entrance of the cave system (outlined in the yellow in Figure 4.10d); presently they host the Reka river before it enters the Škocjan caves. Velika dolina is the largest doline (about 150 m diameter), while Mala has a diameter of about 100 m. When large flood events hit the Škocjan caves, as the event of February 2019, in addition to the cavity also external these two dolines may be subjected to flooding, up to several meters of level variation. Unfortunately, in this area the lack of gauge observations in the dolines prevents me to precisely control the hydraulic simulation here. In any case I included both the Reka meander and the dolines in the simulation in order to give a rough estimation of their contribution to the observed gravity signal. In these external areas the hydraulic simulation is constrained by realistic cross sections derived from the DEM model which are then implemented in the SWMM modelling procedure.

The plot 4.12c shows the hydraulic modelling results, comparing the observations at P1 and the simulated water level in Martelova. The performance of the modelling procedure, in terms of fitting is similar to the simple model. The presence of an early rise of the simulated water table with respect to the observations, similar to the one already observed in the simple model, is a further confirmation that its origin is due to the simplifications in the Kačna conduit system rather than approximations in the geometry of Škocjan.

Figure 4.12a shows the results for the gravity simulations. I calculated the effect at SK1 exploiting the prism discretization: for each time step of the simulation the density model is constrained by the hydraulic model results, which provide the water levels in different conduits, and by the cave's bottom and ceiling surfaces. In Figure 4.12a the red line illustrates the simulated gravity signal caused by considering only the water masses inside the cave while the blue line reports the effect including the contributions of Mala and Velika Dolina and of the Reka meander. The model reproduces fairly well the shape of the observed gravity transient while it underestimates a bit the magnitude of the event. The final RMS error for the gravity time-series considering all the masses amounts to 50 nm/s^2.

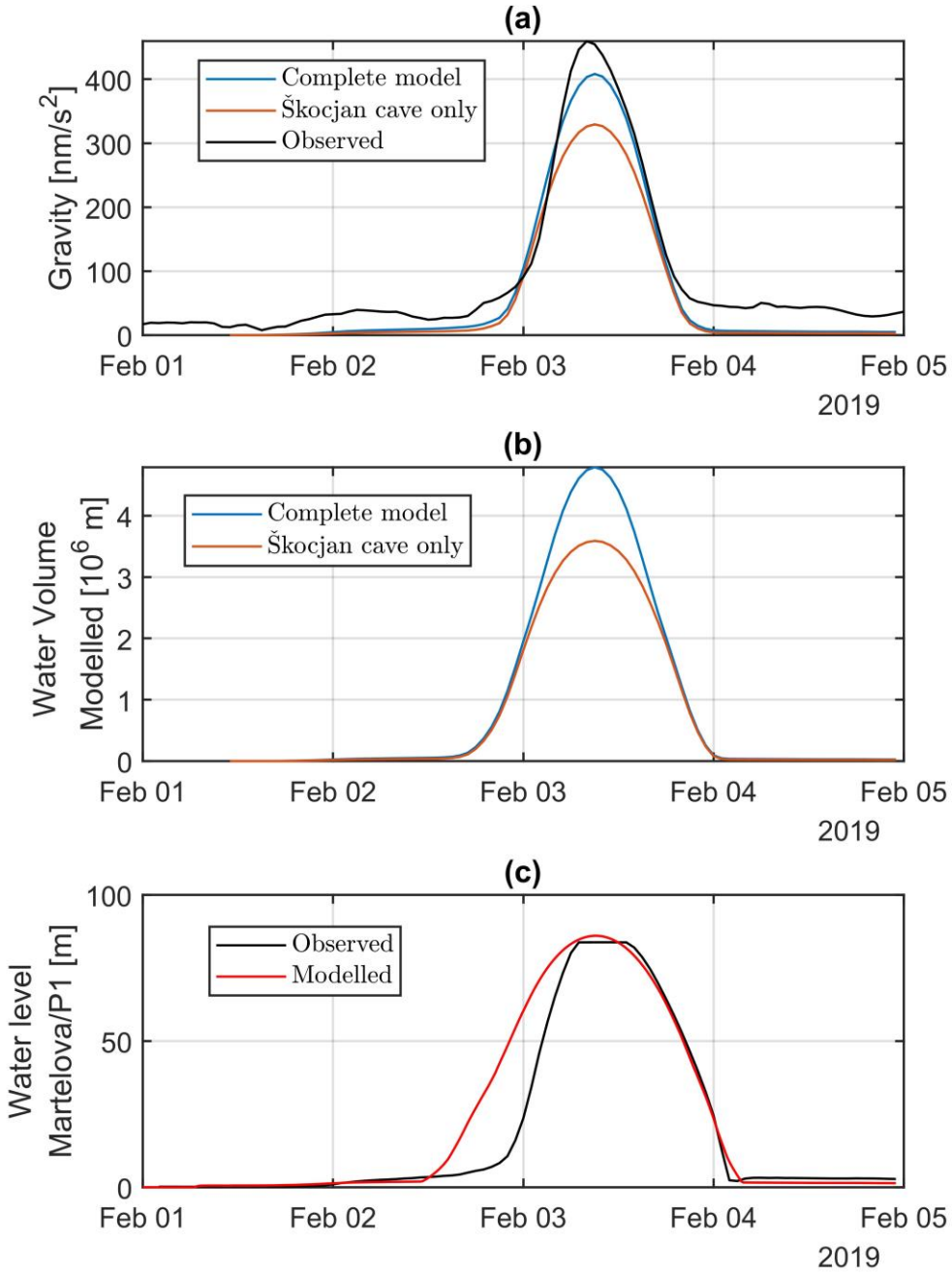

Figure 4.12 a) Observed gravity transient (black), complete model signal (blue) and gravity contribution due solely to mass variations in the Škocjan caves. b) Modelled volume storage in Škocjan (cave), and in the complete model which considers also the Mala Dolina, Velika Dolina and Reka meander contributions. c) Observed and modelled water levels in P1 (Martelova).

The difference in the misfits between gravity and hydrologic data could be attributed to the fact that gravity is practically insensitive to water level variations in Martelova as long as these

are below 50 m: above this threshold significant water volumes start to accumulate in Sumeca giving rise to gravity signal. In the model we see that fit between the observed and modelled level in P1 improves generally as we approach the peak flood, where we the largest gravitational effects are expected.

In order to discriminate the various gravity contributions during the flood and to verify that the domain modelling is sufficiently extended I performed a sensitivity analysis on the water mass distribution during the peak's flood (actually on 3/2/2019 at 4:00). Figure 4.13a shows a snapshot of the spatial distribution of the water masses colored proportionally to the water height.

Apart from the water volume accumulated in the cave we observe flooded areas both in the Mala Dolina and Velika Dolina as well as in the external parts of the modelling domain (> 600 m). Here the Reka has flooded large areal portions, increasing the bed width up to 50-80 m, but with very tiny variations in water level. This is because in these areas the topographic gradient is less steep than downstream, where the channel system becomes steeper and water is forced to flow into narrower conduits.

Through this snapshot I calculated the gravimetric effect at SK1 and inspect what the various contributions sensed by the gravimeter are. In Figure 4.13c the red dashed line reports the gravity effects as we increase the radius of integration from SK1 (the y-axis of this plot is shown on right). Up to 85 % of the signal (250 nm/s^2) is due to the mass variations occurring in the nearby areas within 400 m from the instrument; then the gravity contribution slowly decays. Masses at distances larger than 1200 m practically do not show effects at SK1.

To inspect more specifically the origin of the signals I investigated the variation of the gravity contribution as a function of the azimuthal angle. Figure 4.13b shows how I performed the calculation: the SK1 is located at the center of a circular sector (of 200°) which includes all the masses of the calculation domain. The circular sector is further divided into sectors of 20° (an example is shown by the black dashed lines). Then for each sector I calculated the cumulative gravity contributions progressively increasing the radius of integration. The resulting 10 curves are plotted in Figure 4.13c: the curves confirm that the largest contributions are within 400 m and predominantly are associated to Sumeča and Hanke channels (yellow-green lines; Azimuths 60°-80°). The contribution of the channel that links Martelova to Kačna (green curve from about 1200 m to 2000 m) is practically null. Velika and Mala Dolina produce lower effects compared to the signals from the cave, with amplitudes of about 20-30 nm/s^2 each one. The contribution of the Reka meander (Azimuths between -70° and -90°) is negligible and well below the 10 nm/s^2; Reka River masses at azimuths < -90° and radial distances > 900 m contribute with even smaller gravity variations (< 5 nm/s^2).

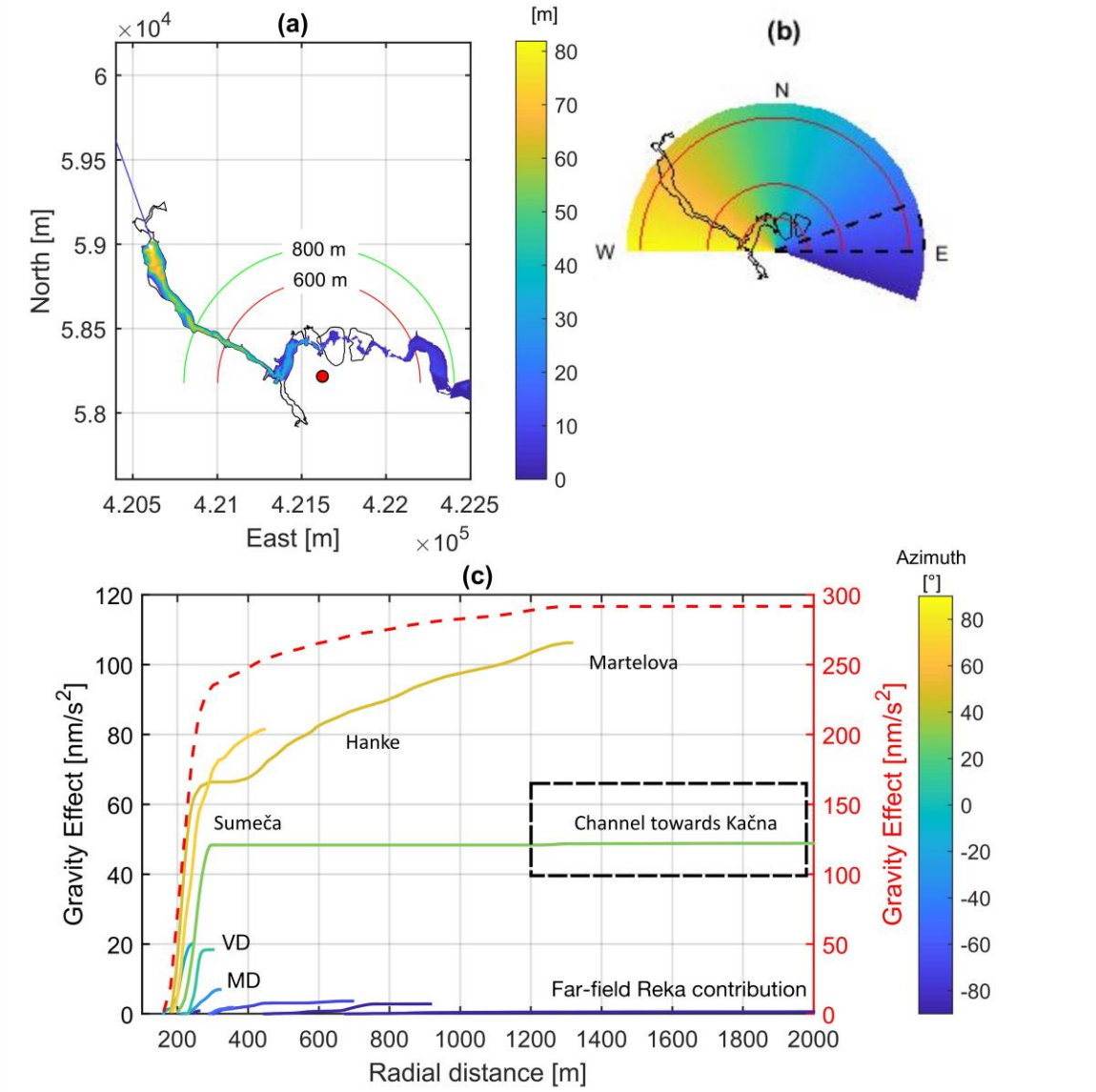

Figure 4.13 a) Water level height simulated in Škocjan; purple and green lines mark the 600 m and 800 m radial distances from the station. Note that the simulation includes further masses of the Reka meander at East, not included for clarity. b) In black: outline of the Škocjan system; three half-circumferences report the 300 m 600 m and 1200 m radial distances from the SK1 station (assumed to be in the center of the circumference). The color code reports the azimuth angle with respect to the North (same as the scale in plot c). c) Red dashed line: gravity effect of the water masses shown in a) as a function of the integration radius. Colored lines: gravity effect of the water masses included in a sector of the half-circle of 20° as a function of the integration radius.

This analysis testifies that the modelling domain seems to be sufficiently extended to capture all the significant gravity contributions due to the flooding of the Škocjan caves. The slight

discrepancies we observe in Figure 4.12a will likely reflect nearby processes not perfectly modelled: for instance, the absence of stage observations in the nearby dolines (Mala Dolina and Velika Dolina) doesn't allow us to constrain well the model in this area.

In any case we cannot completely rule out that the small gravity contributions could be due to the presence of further minor underground flow paths presently unknown as well gravity contributions arising from other un-modelled geophysical phenomena such as:

1) transport of the suspended sediment or through bedload (non-negligible effect as reported in Mouyen et al., 2020)
2) slow infiltration of seepage waters in the massif

Interestingly, regarding this last effect, we observe that the gravity seems to be slightly more positive at the end of the flood event with respect to the beginning. Similar effects are also observed in the flood event occurred in Autumn 2018 (Figure 3.34c). This could be an evidence of the autogenic component, as suggested by Watlet et al. (2020), which is caused by the delayed rainwater infiltration in the fracture system of the karst massif. Since the flooding of the Škocjan caves is delayed with respect to the precipitations, such effect could superpose on the flood related gravity signal, slightly amplifying the gravity maximum. However, up to now this is just a speculation and further data analysis and modelling is required to prove the presence of this effect.

4.3 Summary of the results

The gravimetrically constrained hydraulic model shed new light on the water dynamics of the Škocjan cave system. Here I summarize the main results:

1) The detailed hydraulic model confirmed the role of the Kačna cave in regulating the flooding events in Škocjan: the Kačna cave system is firstly saturated avoiding the drainage of the Reka River downstream the Martelova;
2) The back-flooding wave that propagates from Kačna to Škocjan takes about 6-8 hours to reach the Martelova chamber. This is evident when comparing the Reka peak discharge with both gravity and stage peaks observed in SK1 and P1;
3) Joint modelling of both observables evidenced a huge water accumulation in the system during the flood's peak, with over 3 10^6 m^3 of water stored in the cave for more than 12 hours;
4) The different duration of the transients recoded by P1 and SK1 suggests that the instruments sense different storage units of the cave system: P1 depicts the water dynamics at the end of the cave, in the Martelova chamber; SK1 is more sensitive to the storage variations at the beginning of Škocjan, in the Sumeča chamber. This is also confirmed by the sensitivity simulations made on the cave's geometric model and by the hysteresis of the curve in the plot gravity vs. water level in Martelova (Figure 3.35e);

5) Including the gravity observations in the modelling procedure improved the mass estimates; SK1 acts as a further independent observation with respect to P1 and constrains the mass fluxes in a different sector of the cave;
6) Apart the dominant contribution of the Sumeča chamber and of Hanke and Martelova, SK1 senses further gravity contributions. The most important seems to be attributable to water accumulation occurring outside the cave system in the two coalescent dolines of Velika and Mala Dolina. At the flood's peak they could generate signals up to 60-80 nm/s^2;
7) Since there are no observations to constrain the model outside the cave, reliable mass flux estimates of the MD and VD are difficult to obtain;
8) The persistence of slight positive anomalies after the flood event could suggest the presence of water masses slowly released by the infiltration process. Supplemental analysis is however needed to prove the presence of such process;
9) The good correspondence in terms of water fluxes in the cave between the two hydraulic models confirms that adequate estimates of the mass balances are obtainable by rather simplified geometries of the drainage system.

Chapter 5
Detectability of water storage units in karst by gravimetry

The occurrence of large voids in the epiphreatic zone connected by networks of conduits is not a unique characteristic of the Škocjan area, but is a common feature of the Classical Karst and also of many karstic regions all over the world. For instance, similar hydrologic conditions are observed near the River Lomme in Belgium as testified by the studies of Van Camp et al. (2006) and Watelet et al. (2020). Whether such voids can be detected and studied by gravimetry, depends on their volume, extent of groundwater variation and their distance from the surface. Obviously the noise of the instrument employed for the monitoring and the noise of the site are additional factors to be considered, as well as the presence of further geophysical phenomena that superpose their effects in the same spectral band of the hydrology. In the following I discuss all these aspects in order to assess the detection limits of storage units by gravity monitoring.
I start by evaluating the noise level of the SK1 station with the aim to define the smallest signals detectable with a continuous spring gravimeter in a karstic region. Then I simulate the hydrologic induced gravity signals for some caves in the Classical Karst in order to estimate the expected signal magnitudes for storage units with different volumes and depths of the vadose zone.
Finally, I discuss the feasibility of monitoring these storage units by a combination of continuous gravity observations and time lapse measurements.

5.1 Noise level of SK1

The noise spectrum of the SK1 station was assessed by taking advantage of the whole time-series which is almost 2 years long. The estimate is valid for the frequency range between 10 and 0.1 cycles per day (cpd), which is most interesting for hydrologic applications.
The spectrum was calculated in a similar way as done by Rosat et al. (2017a), who compared the noise performance of a seafloor gravimeter and a similar instrument installed on surface.

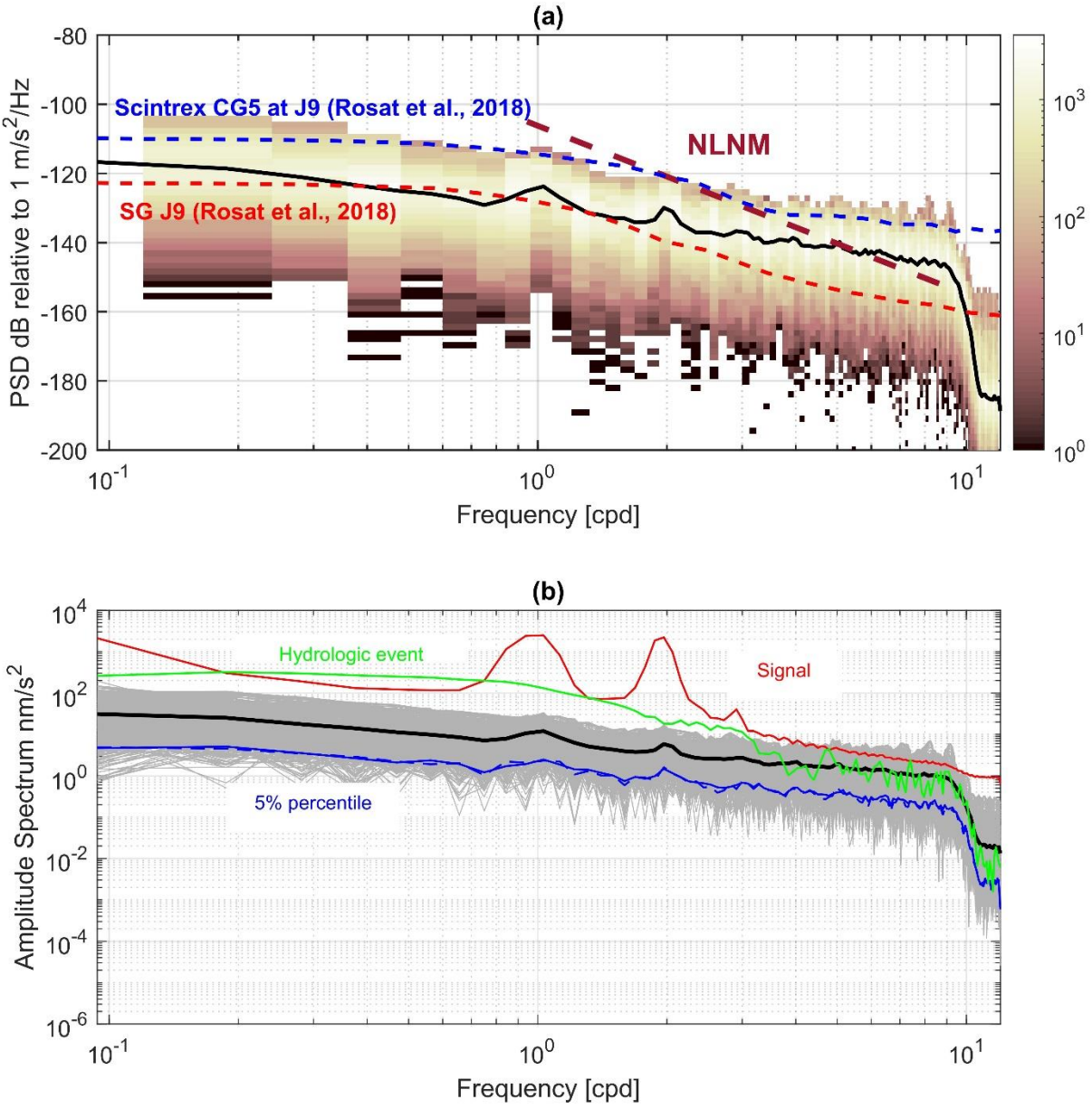

Figure 5.1. a) Power Spectral Density (PSD) of the Škocjan residuals. Colored patches: histogram showing the distribution of the PSDs; color code proportional to the number of PSDs for a given interval of frequency and dB. Black solid line: median PSD. Red dashed line: median PSD of the SG at J9 (Rosat et al., 2017a)*; blue dashed line: PSD of the Scintrex CG5 at J9. Brown thick dashed line: New Low Noise Model according to* Peterson (1993). *b) Amplitude spectrum of the Škocjan residuals. Grey lines: individual spectral estimates. Black Solid line: median PSD. Green curve: PSD associated to the flood event in February 2019; red line: PSD for observed hourly observations without removing tidal contribution and atmospheric effects.*

Similarly to that study, I estimated the Power Spectral Density (PSD) by computing the Fourier transform (FT) on 10-days sliding windows, analysing the hourly data after removing tidal and atmospheric contributions. Before performing the FT each window was tapered by a Hann

window and the linear trends were removed by least squares fitting. I discarded periods when particularly strong hydrologic signals were recorded (as the February 2019 event). For each frequency interval I obtained a distribution of the PSDs from which I extracted the median value. In Figure 5.1a the distribution of the PSDs is reported with a 2D histogram: each bin of the histogram (a coloured patch) covers a frequency interval of 0.12 cpd and 2 dB interval along the PSD axis; the colour is proportional to the number of spectrograms inside the bin. The median of the distribution is reported with the black line. For comparison I report the New Low Noise Model (NLNM; Peterson, 1993) and the noise estimates of a Scintrex CG5 and of the superconducting gravimeter at the site J9, in Strasbourg: data are taken from Rosat et al. (2017a).

We see that SK1 performs better than the Scintrex CG5, which is systematically noisier by about 10 dB in the whole frequency range. In the diurnal frequency band, the noise level of SK1 is similar to the SG, while the SG shows lower noise levels both at higher and lower frequencies. At frequencies higher than 10 cpd in SK1 we observe the effect of the decimation filter, which has not been applied to the Strasbourg data: obviously noise comparisons between the sites in this band do not make sense.

The spectral analysis reveals also some small residuals in both diurnal and semi-diurnal frequency bands of SK1 not completely removed by the tidal analysis. Probably adopting a finer frequency discretization in the tidal analysis procedure I could further improve the residual spectrum removing the remaining energy.

I am aware that the best option would be to compare co-located instruments because they would sense the same signals and the differences in the PSD would be attributable exclusively to instrumental noise. However, I believe that also the comparison I propose is significant since the atmospheric contribution has similar spectral energies at the latitudes of Trieste and Strasbourg (compared for instance to Djougou) and the most striking differences between the two sites are probably related to the hydrology. We expect to record larger hydrologic contributions in Škocjan and for this reason I discarded days when large flood events occurred.

Figure 5.1b shows the amplitude spectrum of SK1: the grey curves report the Amplitude Spectra (AS) for all the windowed data while the black thick line is the calculated median AS curve. For comparison I report the amplitude spectra of the data without the tidal and atmosphere corrections, and the AS estimate of the February 2019 event, calculated from a 10-day window centred on the flood event.

From this plot we see that the noise level in the diurnal band is about 10 nm/s^2 and is even lower (down to 5 nm/s^2) in the semi-diurnal band. The signal to noise ratio (SNR) between the largest hydrologic signal (February 2019) and the noise level is about 20-25.

5.2 Expected hydrologic gravity signals for other cavities

I estimated the gravity contribution for other possible water reservoirs in the karst, simulating the induced gravity effect of water filled voids (Figure 5.2a). The caves are approximated by spherical masses with density of 1000 kg/m^3, which represents the density contrast between an empty and a fully saturated cavity. I investigated the signal strengths and inspect the detectability of the storage units by varying their water volume and the centroid depth of the cavity.

I considered storage volumes from 50,000 m^3 to 1,000,000 m^3, which are clearly lower than those accumulated in the Škocjan cave system, but indeed they are more representative of the typical volumes of other Classical Karst caves.
Moreover, I report the simulated gravity variations due to water accumulation in three specific caves of the Classical Karst area: Kačna Cave (for location see P2 in the following Figure 5.3a), Trebiciano Abyss (P4 in Figure 5.3a) and the Lindner cave (P7 in Figure 5.3a). Kačna Cave is sub-superficial system of caves and it is able to store more than 500,000 m^3; it is a typical example of the drainage system at the beginning of the Reka underground path near Škocjan.

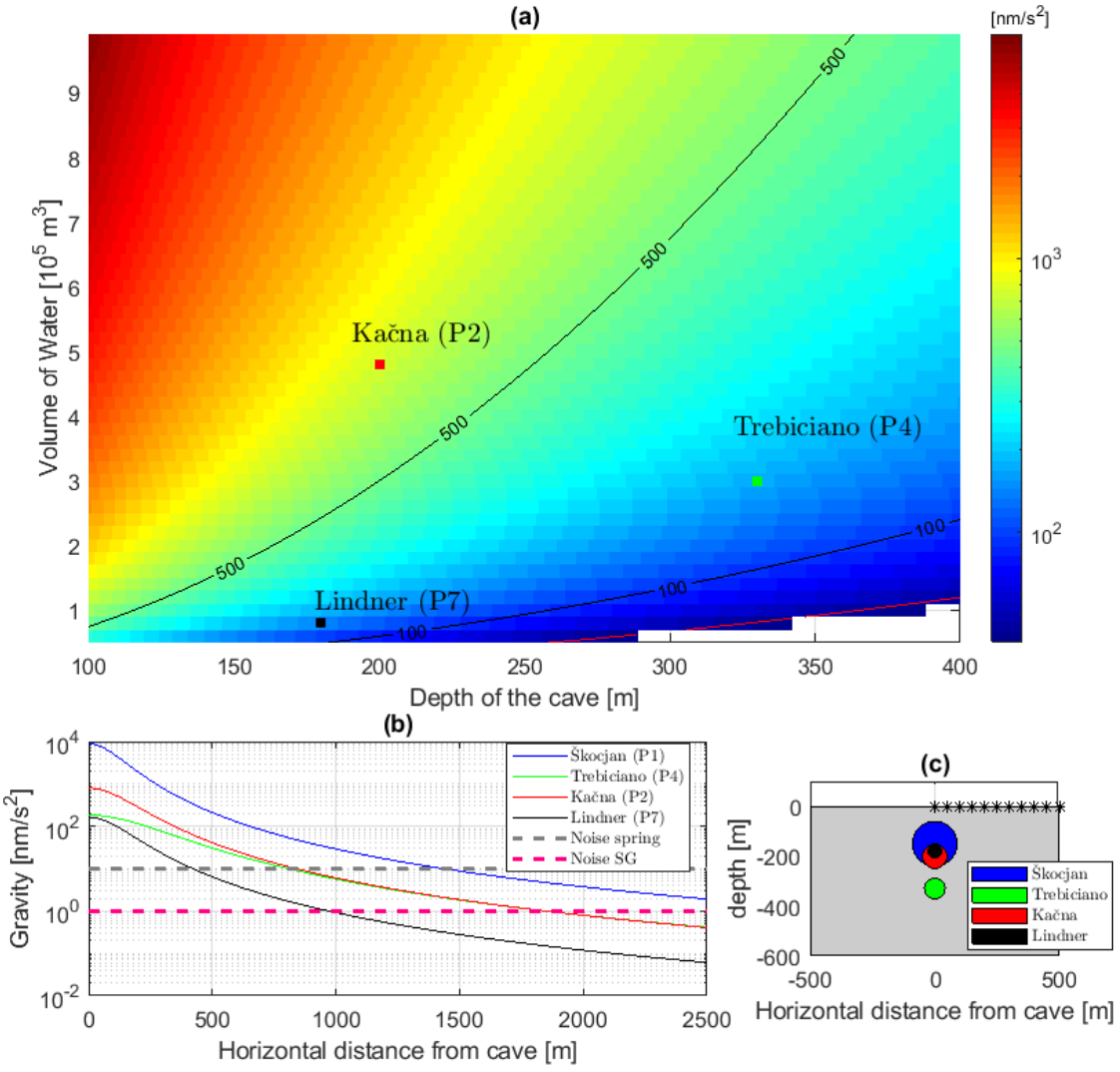

Figure 5.2 Detectability of gravity signals related to hydrology in karstic areas. a) Gravity signals simulated for various water volumes stored and depths of the caves. b) Gravity anomalies for 3 different cavity volumes filled with water at different depths as a function of the horizontal distance from the cavity centre. Noise levels for a common spring gravimeter and a SG are reported with the dashed lines. c) Vertical cross-section of the spherical cavities used for approximating the hydrologic gravity effects: black stars report the surface locations where gravity anomalies have been simulated.

The Trebiciano Abyss is an over 330 m deep cave reaching the groundwater flow about 10 km NW from Škocjan Caves. There, a system of small vertical shafts leads to a large chamber with volume > 300,000 m^3 about 300 m below the surface. The Lindner cave is located in the final path of the Reka-Timavo path and it is constituted by a large gallery located few meters above the sea level connected to a large sub-superficial chamber by a vertical shaft. The galleries and the shaft are located at about 180 m below the topography and are frequently flooded by the waters of the Reka-Timavo system. (Casagrande & Zini, 2004) observed that during flood events the water level could rise up by over 10 m. The storage unit is smaller compared to both Trebiciano and Kačna and from the internal surveys I estimate a capacity of about 80,000 - 100,000 m^3.
During flood events Kačna Cave generates a clearly detectable gravity signal at surface (> 500 nm/s^2), while in Trebiciano the gravitational signal triggered by a large flood event would be lower (200 nm/s^2) but still clearly detectable by a common spring gravimeter. The gravity signal associated to the Lindner cave is about 100 nm/s^2. I remark that in these simulations the implicit assumption is that the gravimeter is located exactly above the cave's centroid, since as the gravimeter is moved away from the cavity axis, the signal amplitude decays.
Figure 5.2b plots an estimate of the sensitivity of gravimetry to the Škocjan, Kačna and Trebiciano water storage units as function of the horizontal distance from the caves axis (assumed to be in 0 m). Dashed grey and purple lines report the expected noise thresholds for a spring gravimeter similar to the SK1 (10 nm/s^2) and for a SG. For the SG I take as representative values the one reported in Figure 5.1a for SG J9, where the SG showed better noise performances at both long periods and in the semi-diurnal spectral band with respect to spring based gravimeters. The improvement in these frequency ranges with respect to SK1 is about 10 dB and hence we could assume to lower the noise level by about 1 order of magnitude, reaching the 1 nm/s^2.
The plot 5.2b suggests that hydrological signals are detectable by common spring gravimeters also few hundreds of meters away from the water filled cavity: the effect of Škocjan caves would be easily observable for horizontal distances exceeding 1000 m; Kačna and Trebiciano show their effects up to 700-800 m.
Considering a SG meter, the radius of detectability is easily increased by a factor larger than 2, which allows detecting significant gravity variations of smaller storage units (as Kačna and Trebiciano) up to almost 2000 m.

5.3 Other geophysical effects in the hydrologic spectral band

The gravity transient associated to the February 2019 flood event had a duration slightly minor to 1 day: hence its energy is mostly confined in the diurnal band. This is also evident from the spectrum (green line) in the plot 5.1b where we see the signal has significant energy up to 1-2 cpd, rapidly decaying at higher frequencies.
In Škocjan other geophysical effects in the same spectral band of the hydrology, apart from the Earth tides, are due to the atmospheric contributions and to the marine non-tidal contribution. The atmospheric effects are dominant in terms of amplitude; however, they can be corrected with sufficient accuracy by the method shown in chapter 3.2 which is also easily applicable for any other continuous gravity observations in the karst.

The non-tidal contribution from the Adriatic Sea, estimated by the empirical model shown in chapter 3, seems to represent a minor effect in Škocjan in comparison to the magnitude of both atmospheric and hydrologic signals.
For other sectors of the Classical Karst the NTOL amplitudes are expected to be larger and could reach the order of magnitude of the hydrologic signal. Near the coastal areas we should also take into consideration that the uncertainties on the empirical NTOL model could be critical.
Figures 5.3a and 5.3b report the calculation of the Newtonian and loading effects in the whole Classical Karst plateau due to the "VAIA" event, occurred on 29th October 2018 (Figure 5.3c). During this event the tide gauges recorded the highest non-tidal marine transients in the last two years, with variations exceeding the 100 cm in Trieste and Koper and reaching the 150 cm in Monfalcone.
In order to calculate the gravity effect, the non-tidal mass was discretized through tesseroids, for which the outline is reported in both plots 5.3a and 5.3b; the height of the tesseroids is shown in greyscale. The mass model comprises the whole North-Central Adriatic Sea, which includes also Venezia and Ancona harbours. I calculated the loading component due to this mass model in the same way as done in chapter 3. From the maps we observe that the Newtonian component has the largest amplitudes close to the coastline but it rapidly decays with the distance; the loading effect is responsible of a smooth long-period trend with amplitude in the order of ten nm/s^2.

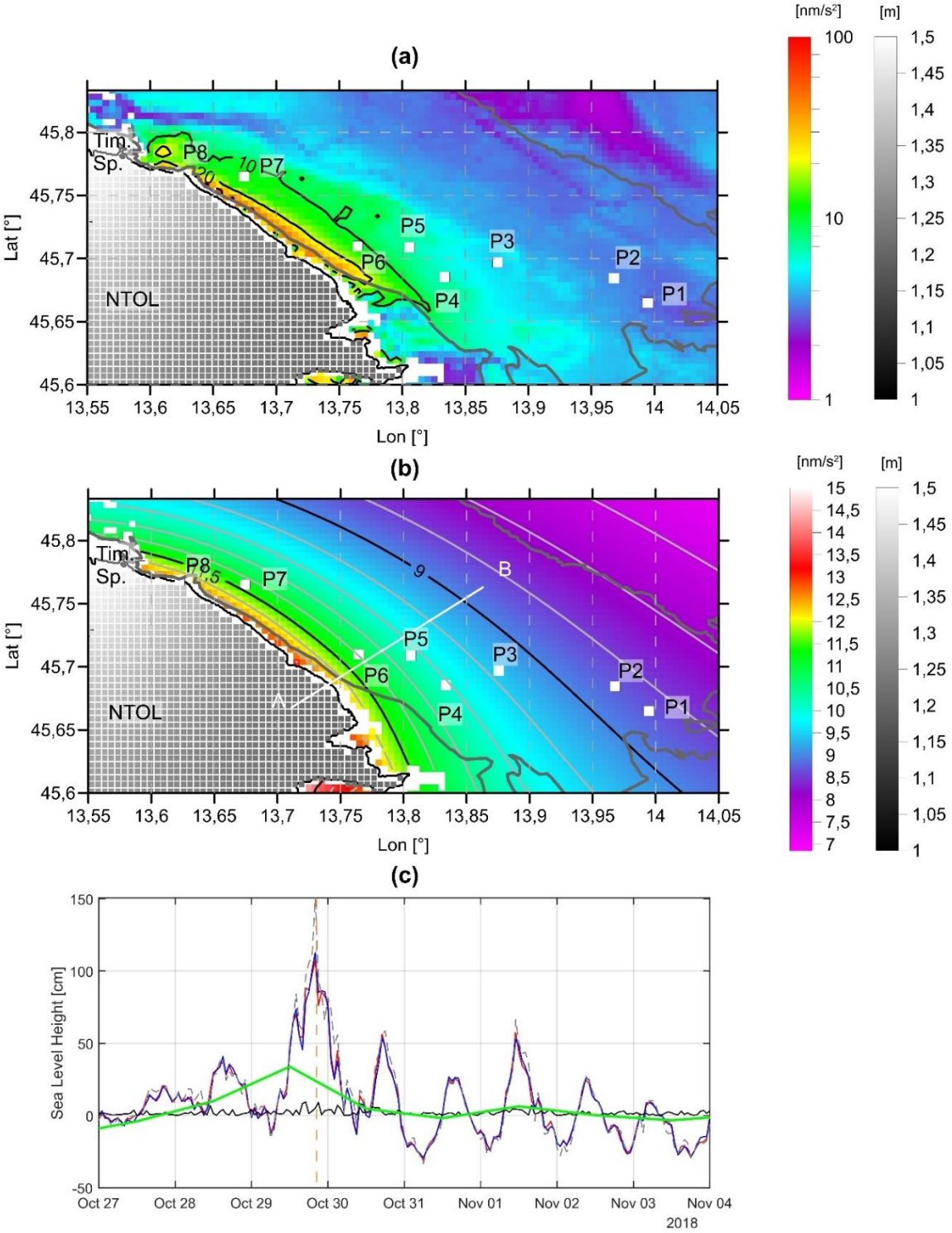

Figure 5.3 Marine Non-Tidal contribution of the Adriatic Sea in the Classical Karst area. a) Inland areas: Newtonian contribution of the NTOL derived from the empirical model of the Adriatic Sea. Marine areas: tesseroid discretization of the NTOL for 29th October 2018 (orange dashed line in plot c), greyscale proportional to water height. White squares: location of the main caves in the Classical Karst- P1: Škocjan caves; P2: Kačna Jama; P3: Kanjaduce; P4: Trebiciano; P5: Lazzaro Jerko; P6: Grotta Gigante; P7: Lindner cave. Grey thick solid line: boundary of the Carbonates (i.e. Classical Karst) according to Jurkovsek et al. (2016); b) as a) but for the loading component; white line: trace of profile of Figure 5.4. c) time-series of NT component: blue line= Trieste; red line: Koper; grey dashed: Monfalcone; green line: ECCO2 model black line: difference between Trieste and Koper.

This is more evident from Figure 5.4 which shows the Newtonian and loading components along a profile orthogonal to the coastline that passes close to Grotta Gigante (P6) and Lazzaro Jerko (P5).
We see that moving from the coast up to P6 the Newtonian component reaches amplitudes over 30 nm/s^2 while the loading effect is about 2 - 3 times lower. This results in a maximal NT contribution of over 40 nm/s^2 (black line in Figure 5.4). In Grotta Gigante I expect contributions exceeding 20 nm/s^2 while in Lazzaro Jerko (P5) and Trebiciano (P4) slightly less than 20 nm/s^2. At the Lindner cave (P7) the NTOL is likely to have the same magnitude as in P4.
For Trebiciano the NTOL contribution is almost 1/10 of the hydrologic signal amplitude due to a large flood event; for Lindner the ratio is probably larger and could be in the order of 1/5.

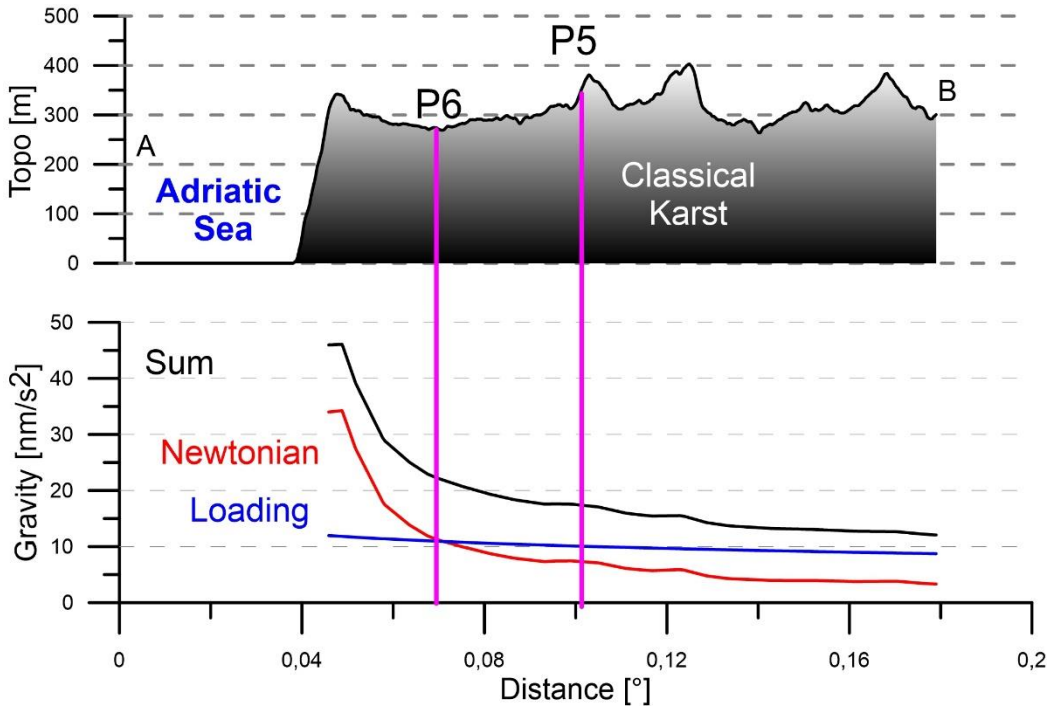

Figure 5.4 Non tidal contributions as a function of the distance from the Adriatic Sea. Top: topography of a representative cross section of the Classical Karst. Bottom: Newtonian (red), loading (blue) effects and their sum (black). Location of the Grotta Gigante (P6) and of Lazzaro Jerko (P5) are reported with the vertical purple lines.

At the sites P6 and P7 the uncertainties on the empirical tidal model could also be a limit since we are very close to the sea and there are no tide gauges observations nearby.
Assuming an uncertainty of 20 cm on the non-tidal model this translates into gravity uncertainties of about 5 nm/s^2 for the internal areas in the Classical Karst plateau. Obviously for caves closer to the coastline this value rises up to 10-15 nm/s^2 since the NTOL signal reaches amplitudes of 40-50 nm/s^2.

5.4 Sensitivity of gravimetry to water storage units in karst

In this work I have shown that temporary water accumulation in the Classical Karst caves could exceed 3.5 10^6 m^3 in the extreme case of the Škocjan caves; in other known storage units the volumes are usually smaller (in the order of 10^5 m^3) but still relevant.
Gravimetry could offer a support to classical hydrologic techniques by monitoring such storage units and eventually contribute in identifying unknown ones. Different approaches, depending on the instruments at disposal and modalities of data acquisition, could be exploited. We could identify chiefly two of them:

1) Continuous gravity observations
2) Time-lapse and "hybrid gravimetry" approaches

In this thesis I discussed the data from a single station equipped with a spring based gravimeter which pertains to the first approach. Hereinafter I give a brief discussion on possible further applications of the methods in the study area, reviewing the possible advantages as well as the critical aspects of both configurations.

5.4.1 Continuous gravity observations

In continuous gravity observations the meter is installed in a fixed site and it is left measuring for an arbitrary interval of time which depends on the number of flood events we want to record.
The method has the advantage of being the most accurate and it is the best for retrieving small hydrologic signals.
As I have shown, the continuous data allows completely removing Earth and marine tidal components with high precision, as well as the response of the instrument to atmospheric effects.
The data, after removing the non-hydrologic components, revealed in the case of SK1 some gravity residuals linked to the local storage process which were quantitatively interpreted by including a hydraulic modelling procedure.
A similar approach could be applied to study or monitor other sectors of the Classical Karst, where the underground water dynamics are only hypothesized and no direct access to the vadose zone is possible. Near the Škocjan area we would likely observe the largest gravity effects, given the shallower level of the water circulation and presence of a well-developed channelized system (see Kačna system for instance).
Obviously the positioning of the instrument is a critical factor: the best option would be to put it directly above the storage unit; however, I have demonstrated that for large flood events the induced gravity signal could be detected few hundred meters away. The instrument requires continuous power supply and also an internet connection is recommended: this could represent a further limitation in the site selection.
Moreover, in order to quantitatively model the gravity signals and to give an estimate of the mass fluxes insisting over an area, the single station approach requires building a hydraulic model, similar to the Škocjan cave. Some constraints on the underground voids distribution

are necessary and they could come from a preliminary gravity static survey around the station, which offers sufficiently accurate volume estimates (Braitenberg et al., 2016).
Two possible areas of interest could benefit from the application of this method and are shown in Figure 5.5.

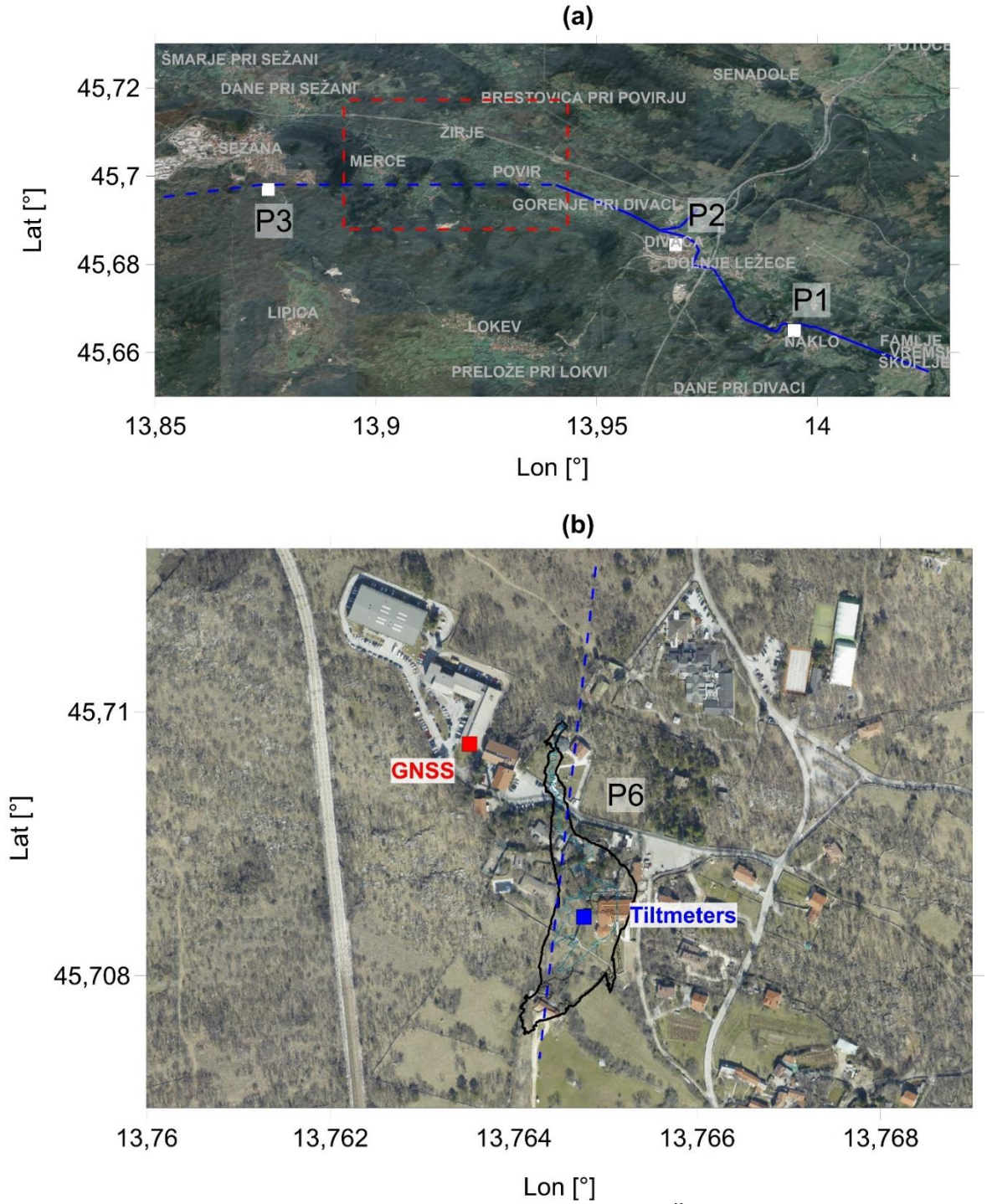

Figure 5.5 Possible location of continuous gravity measurements. a) Škocjan - Sežana area; blue trace of the hydraulic model employed in the thesis; red dashed line bounds the Povir - Merce area where there are indirect evidences of underground water mass movements during Reka flood events. Name of towns reported in gray. Photo from Google maps. b) Grotta Gigante cave (black outline) area. Blue square: tiltmeters; red square: GNSS antenna. Blue dashed line: approximate location of underground conduit hypothesized by Braitenberg et al. (2019).

The first (Figure 5.5a) is outlined by the red dashed line and bounds a sector between Kačna (P2) and Kanjeduce (P3). Here certainly some karstic structures exist related to the Reka underground drainage system. Particularly in the village of Povir the activation of blowholes during Reka flood events suggests the presence of quite big underground cavities. Up to now the access to the vadose zone here is limited hence at least a superficial gravity survey would be crucial to depict the main underground structures and optimally select the site of installation. Since we are in a village, all the facilities for the functioning of the instrument are easily available. In this area the interpretation of the recorded gravity transients could benefit from the hydraulic model discussed in the thesis.
The second location (Figure 5.5b) is on the bottom of the Grotta Gigante cave (P6 in maps 5.3a-b). With respect to the Škocjan and Povir caves, here the water circulation is deeper, occurring at few meters above the sea level. The site is interesting since two horizontal pendulums, two clinometers and a GNSS are co-located. All the instruments revealed hydrologic signals which were correlated to the Reka flood events. The site offers excellent noise conditions as well as facilities for power supply and internet connection. Apart from Reka contribution, here also the diffuse infiltration, prevalently a "vertical" water mass movement, could play a significant role with respect to the Škocjan area.

5.4.2 Time-lapse approach

The time-lapse approach employs a portable gravimeter to perform repeated measurements above the target storage unit. The temporal resolution is obviously lower than a continuous instrument, but multiple locations could be monitored by this approach during a single flood event. If a spring based gravimeter is employed, a reference station is required. A reference station could be a continuous recording station or eventually a stable point far from the storage unit where no or only small hydrologic effects are expected. Usually the best option is to have a continuous instrument as the reference station. The overall best configuration is given when, in addition to the reference station and the portable meter, some repeated absolute measurements are available for calibrating the long period trends of the continuous station. In this case the combination is referred as hybrid-gravimetry (Portier et al., 2018).
The processing of the time-lapse measurements is similar to continuous data: drift, tidal correction and atmospheric corrections are applied obtaining the residual signal. Depending on the instrument employed for the monitoring and on its conditions the accuracy of the measurement is usually above 10 nm/s^2: for Scintrex CG5 (linear gravimeter) it is estimated to be 50 nm/s^2 (Portier et al., 2018), for instruments employing the Zero-Length Spring suspension it could be better and reach 10 nm/s^2 (Jentzsch et al., 2018; Schulz, 2018).
In the hybrid-gravimetry concept the continuous observations are also employed for retrieving a Local Tidal Model (LTM) which is then used for correcting the time-lapse observations as well. Obviously we assume to know the transfer function of the instrument, hence to have a precise and stable calibration at the level of 1‰.
Then, the further assumption is that inside the study area the variation of the solid Earth tidal contribution is smaller than the precision of the instrument. The marine contribution can be accounted for by including the effect of a global model as the FES2014b (Carrère et al., 2016).

The SK1 data demonstrated, albeit a calibration issue, that such models are accurate enough, at least for the internal areas of the Classical Karst, however for other caves very close to the sea (e.g P6-P7), the spatial resolution of the model can be a limiting factor that has to be considered. I say spatial resolution because the amplitudes and phases of the model seem to reproduce very well the observed data at the various harbours, as shown in chapter 3.3.
I performed a simple experiment for estimating such error on the discretization: the gravity effects due to the M_2 marine tidal wave were simulated in several locations of the karst plateau taking advantage of the FES2014b model (Carrère et al., 2016). The original resolution of the FES2014b model (0.0625°) was increased by interpolating the phases and amplitudes into a finer grid (0.01°) up to a distance of about 2° from SK1 (P1 in Figure 5.6c).

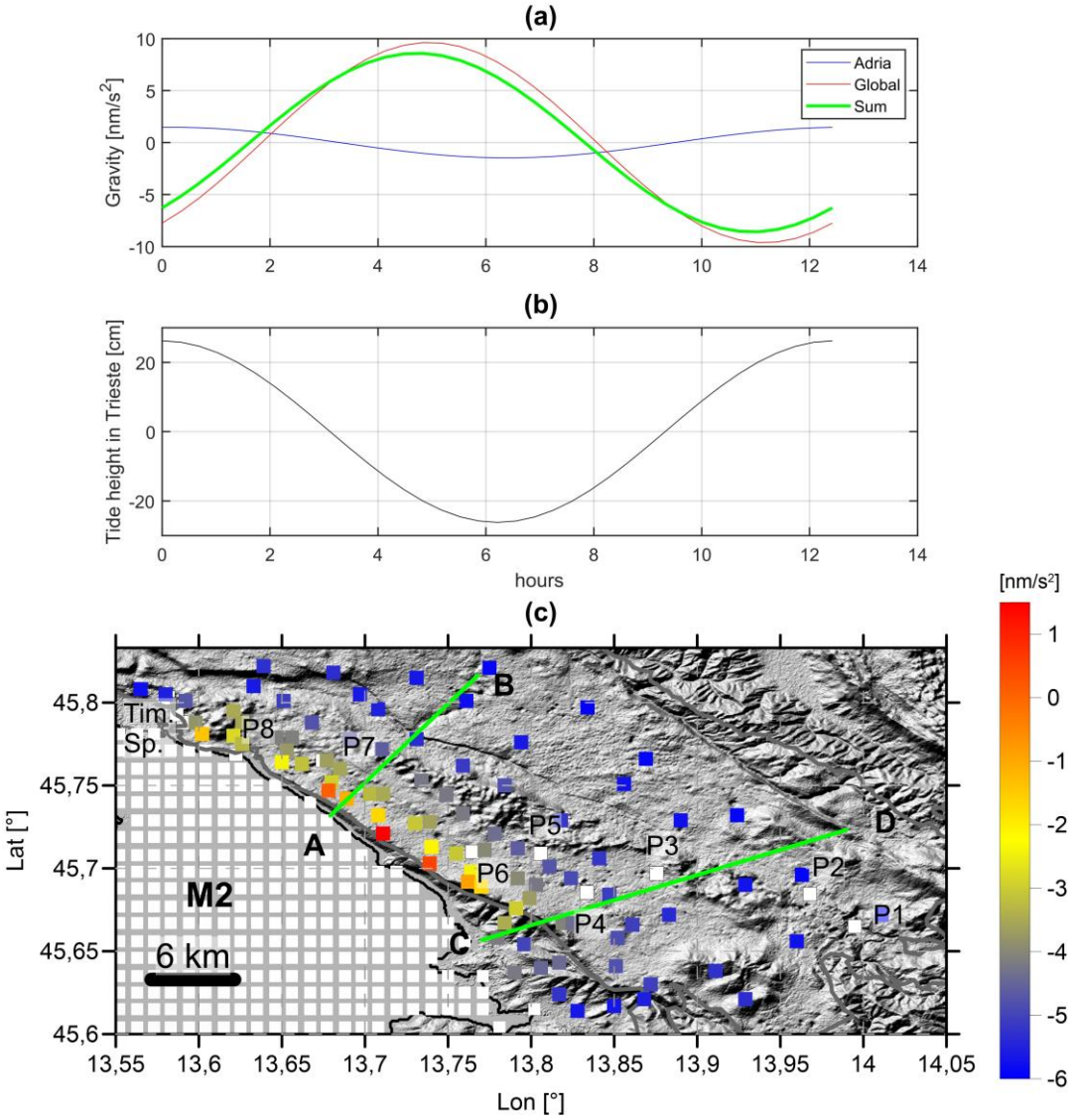

Figure 5.6 a) Gravity effect of M_2 component at SK1 calculated from FES2014b. Blue: Newtonian and loading effects of the North Adriatic Sea calculated with the finer grid; red: global contribution (Newtonian and loading) of FES2014b employing the global resolution. Green: sum of the two effects. Note that the maximum effect of the North Adriatic is temporal shifted with respect to the maximum effect of M_2. b) Tidal height in Trieste according to FES2014b model. c) Gravity effect in several points of the Classical Karst due to the M_2 marine wave. The discretization in tesseroids is reported with the white patches. Green lines: profiles; white squares: location of important cavities. Shaded relief map from SRTM. For SK1 the effect is relative to the instant 0 hour of the plot 5.6a.

For farther distances the FES2014b model original resolution is employed. I selected the M_2 wave since it is the largest component in the North Adriatic region, and in SK1 I clearly saw its influence in the tidal analysis.
I computed the M_2 effect at the epoch corresponding to the maximal height of the tidal wave in the Trieste Gulf (hour 0 in figure 5.6a and 5.6b). The gravity effects at this epoch are shown for the various locations through the colour scale (Figure 5.6c).
The Figure 5.6 clearly shows a bimodal distribution of the values: close to the coastline we have mostly positive values, slightly above 1 nm/s^2, while going towards the internal areas of the plateau the effect is stably negative around -5/-6 nm/s^2. This is due to the fact that near the coast the Newtonian effect of the Adriatic Sea is dominating, while farther away the stations are more sensitive to far field oceanic contributions which contribute with a marked negative gravity anomaly. The profiles AB and CD (Figure 5.7) report the various contributions to the signal, testifying the different sensitivity of internal and coastal areas to the Adriatic contribution. In these profiles I also report the effects calculated with the original FES2014b spatial resolution (purple line).

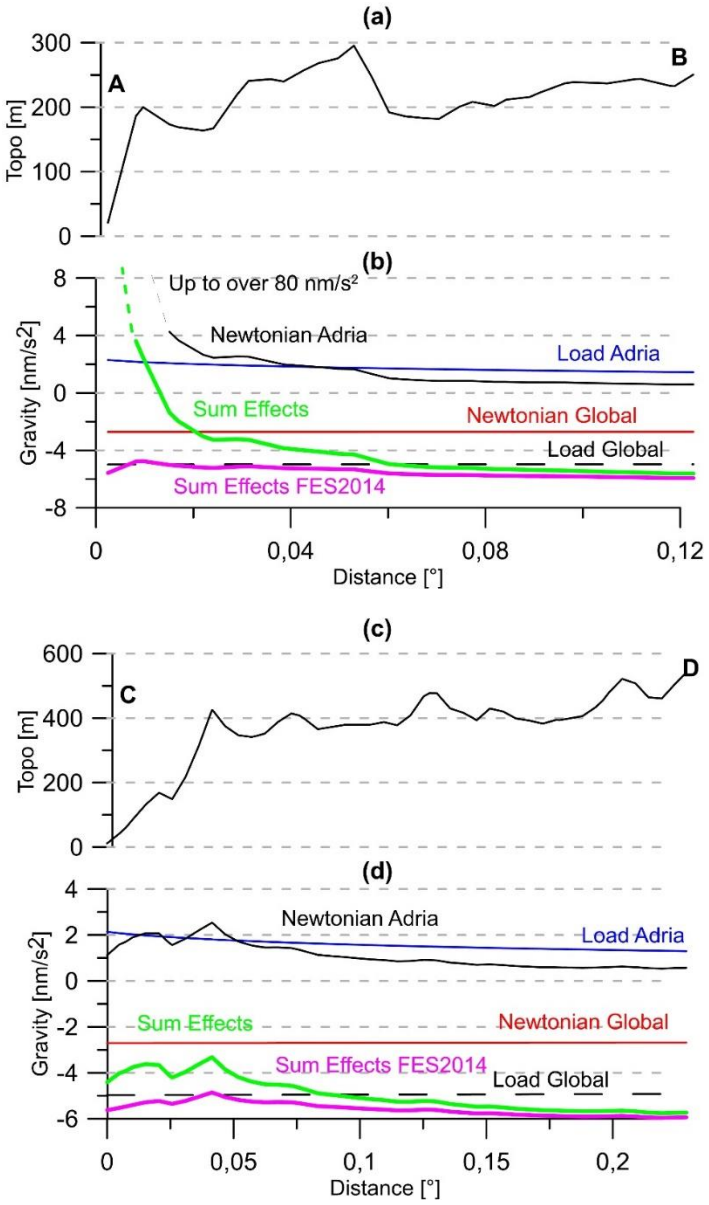

Figure 5.7. Gravity profiles along traces AB and CD (see Figure 5.6c) of the M_2 marine effects. Newtonian and loading effects for the near field contribution (black and blue lines; labelled Adria) and the global far-field contributions (red: Newtonian; black dashed: loading). Green line: sum of all the contributions. Purple: gravity effect of the original FES2014b model, without the finer discretization of the North Adriatic water masses. a) and c) report the topographic profiles; b) and d) the gravitational contributions. Note that in Figure b the y-axis is clipped: the Newtonian contribution (black line) and the sum of the effects (green) exceed the 80 nm/s² at the beginning of the profile.

By comparing the green and purple lines we observe relevant differences (on average 3-5 nm/s^2 but locally can be up to more than 80 nm/s^2) up to distances of 0.02° (about 2 km) from the coastline (profile AB). Further away from the coast, in the internal sectors of the Karst plateau, the difference is lower suggesting that here gravity observations can be reasonably well corrected by employing the original FES2014b resolution. The errors are maximal in situations where the instrument is located nearby steep cliffs directly plunging into the sea (i.e. profile AB), instead a gravimeter placed on the surface of gently dipping shore platforms

seem to be less sensitive to the sea level variations occurring in the Adriatic Sea. This could be explained by the fact that gravity observations are mostly sensitive to mass variations occurring below the instrument rather than mass redistribution occurring at the sides of the instrument.
In this simulation I have considered only the M_2 wave, which is the largest component (25 cm); however, K_1 and S_2 are also responsible of contributions of almost 20 cm each one and K_2, O_1, N_2 and P_1 further contribute with amplitudes of about 10 cm. Considering the sum of all the components we obtain a maximal tidal oscillation of almost 1 m which translates into errors that could be easily larger than 20 nm/s^2 near the coastline. For stations P6 and P7, which are within 5 km from the sea, such effects could be relevant, impacting the time-series in case the oceanic tidal correction is performed employing the original FES2014b spatial resolution.
I have shown by this synthetic example, that a large portion of the plateau could benefit from a time-lapse monitoring of the storage units employing the tidal model of a reference station. In this case, before employing the LTM of SK1, we need to properly estimate the transfer function of the instrument, since the presence of a scale factor, as reported in chapter 3.1, limits us to export the LTM to other stations. We also need longer data in order to correctly estimate the ψ_1 and φ_1 constituents, for which the tidal oceanic correction is not available.
In case the cavity is within 5 km from the coastline the FES2014b correction, calculated with the original spatial resolution, seems to be inadequate to fully remove all the marine tidal components.
An additional reference station in these areas can be used to test the effective influence of the marine tidal contribution of the Adriatic Sea and eventually provide a specific LTM for correcting the effects nearby the stations.
The benefit of including time-lapse observations in a monitoring network is that we can monitor the storage unit in different locations with obvious advantages to constrain the hydraulic model.

Chapter 6
Conclusions

In karst aquifers, a conduit-chamber structure combined with a highly irregular recharge process results in transient accumulation of huge water masses in localized storage units.

The gravity data in Škocjan allowed to obtain a refined estimate of the water flux in the cave during an extreme flood event of the Reka River. I demonstrated that the gravity measurements were complementary to the hydrologic observations and gave information of a sector of the cave not yet monitored by hydrologic observations. The recorded transient, when interpreted with hydraulic models, unveils rather complex hydrodynamic mechanisms, such as back-flooding effects which are responsible for the accumulation of large water volume in the system. Additionally, the gravity is also informative of other processes occurring in the vadose zone as the slow seepage of infiltrated waters within the massif that seem to cause the slight positive anomaly after the flood event. Such anomaly has been observed in other similar allogenic contexts (Watlet et al., 2020) and in future, modelling such signal could help in getting constraints on the vadose flow velocity and on the water mass of the autogenic contribution.

The Classical Karst offers several other examples of rapid accumulation of water in chambers of various storage volumes. Among the known, Škocjan is the upper limit with more than 3 10^6 m^3 stored in few hours.

I have shown that such spatial heterogeneity of the storage units can be investigated by deploying a continuous gravimeter as well as performing time-lapse gravity measurements.

Continuous observations with spring-gravimeters offer high precision measurements, capable of detecting small gravity signals with amplitudes down to 10 nm/s^2 at frequencies around 1 cpd, the most relevant for hydrologic purposes. In several caves of the Classical Karst the expected gravity signals are at least 1 order of magnitude larger. Such big signals would be also detectable by time-lapse gravity measurements which in general offer lower performance in terms of measurement accuracy. The advantage in this case is the possibility to monitor multiple sites almost simultaneously, depending on the number of instruments available, and obtain 4D gravity observations.

The time-lapse approach benefits from continuous observations, which can help in identifying other geophysical phenomena superposing on the hydrologic signal and provide a local tidal model. Karstic areas near the sea, such as the Classical Karst, represent a challenge for the application of marine tidal corrections since usually the global models used to compute their

effects could not reproduce correctly both the amplitude and phase of the constituents as well as the spatial distribution of the masses. For the North Adriatic region, I have shown that phases and amplitudes are in good accordance with the tide-gauges observations. The mass discretization of the model is also adequate for correcting the SK1 data, as revealed by the tidal analysis. These considerations seem to suggest that the global models can be employed for correcting the gravity time-series (also the time-lapse applications) of most of the sites of potential interest located in the plateau interior. There could be some issues for monitoring targets close to the sea (i.e. for distances < 5 km), where the effect of the mass discretization could result in differences in the order of 10-20 nm/s^2. Additionally, I have estimated the marine non tidal contribution of the Adriatic Sea from an empirical model: in SK1 the effect seemed to be limited, but I remark that we do not have a complete model with sufficient spatial and temporal resolution to fully evaluate the effect of the whole Adriatic Sea. In other sectors of the Classical Karst the NTOL of the nearby Adriatic Sea is markedly larger with amplitudes that could reach easily the 50 nm/s^2. Including the results of a hydro-dynamic simulation of the non-tidal component as proposed by Donatini et al. (2015) could be a future approach for improving the correction to all the measurements in the Classical Karst.

Regarding the Classical Karst region, based on all the considerations reported above, I proposed two further locations that could benefit from a gravity monitoring: one close to the Škocjan caves, in Povir, which could also employ the SK1 local tidal model, once corrected with the coefficients for the transfer function of the instrument. The other site is in Grotta Gigante, where the water circulation occurs surely at deeper levels compared to Povir: in any case there are sound evidences of strong hydrological influence on other geodetic instrumentation. At this site the NTOL will likely play an important role in the observations given the proximity of the Adriatic Sea (about 3 km).

A similar integrated gravity and hydrologic approach, as the one presented in this thesis, could be employed to characterize the water circulation in other similar contexts such as in the evaporite karst, which bear a natural hazard in many regions worldwide.

Acknowledgements

I wish to thank the Regione Friuli Venezia Giulia that provided me the fellowship, 50% cofunded by the European Social Fund.

I wish to thank Prof. Gerald Gabriel, Prof. Laurent Longuevergne and Prof. Bruno Meurers for their constructive and inspiring comments which contributed to improve the final version of the thesis.

A special thank to Škocjanske Jame Park and to Dr. Borut Peric for the interest in the project and for housing the instrument.

I wish to thank the Leibniz Institue for Applied Geophysics for sharing the acquired gravity data and Dr. Detlef Vogel, Jan Bergmann Barroccas for support in maintenance of the instrument.

I thank Prof. Meurers and Prof. Bokelmann for supporting me during my period abroad at the University of Vienna.

I thank the Karst Research Institute of Postojna for support through the whole project and my period abroad.

Thanks to Dr. Alberto Pastorutti, Francesca Maddaloni, Marco Bartola for help, comments and support throughout these years. Thanks also to all my colleagues of the PhD course in EFSM.

A special thank to my supervisor Prof. Carla Braitenberg and my co-supervisor Prof. Franci Gabrovšek for the excellent guidance and support during the whole PhD period.

References

Abdelmohsen, K., Sultan, M., Save, H., Abotalib, A. Z., & Yan, E. (2020). What can the GRACE seasonal cycle tell us about lake-aquifer interactions? *Earth-Science Reviews*, *211*, 103392. https://doi.org/10.1016/j.earscirev.2020.103392

Agnew, D. C. (2015). Earth Tides. In *Treatise on Geophysics* (pp. 151–178). Elsevier. https://doi.org/10.1016/B978-0-444-53802-4.00058-0

Beven, K. (2006). A manifesto for the equifinality thesis. *Journal of Hydrology*, *320*(1–2), 18–36. https://doi.org/10.1016/j.jhydrol.2005.07.007

Biolchi, Denamiel, Devoto, Korbar, Macovaz, Scicchitano, et al. (2019). Impact of the October 2018 Storm Vaia on Coastal Boulders in the Northern Adriatic Sea. *Water*, *11*(11), 2229. https://doi.org/10.3390/w11112229

Blatnik, M., Mayaud, C., & Gabrovšek, F. (2019). Groundwater dynamics between Planinsko Polje and springs of the Ljubljanica River, Slovenia. *Acta Carsologica*, *48*(2). https://doi.org/10.3986/ac.v48i2.7263

Blatnik, M., Culver, D. C., Gabrovšek, F., Knez, M., Kogovšek, B., Kogovšek, J., et al. (2020a). Deciphering Epiphreatic Conduit Geometry from Head and Flow Data. In M. Knez, B. Otoničar, M. Petrič, T. Pipan, & T. Slabe (Eds.), *Karstology in the Classical Karst* (pp. 149–168). Cham: Springer International Publishing. https://doi.org/10.1007/978-3-030-26827-5_8

Blatnik, M., Culver, D. C., Gabrovšek, F., Knez, M., Kogovšek, B., Kogovšek, J., et al. (2020b). Late Cretaceous and Paleogene Paleokarsts of the Northern Sector of the Adriatic Carbonate Platform. In M. Knez, B. Otoničar, M. Petrič, T. Pipan, & T. Slabe (Eds.), *Karstology in the Classical Karst* (pp. 11–31). Cham: Springer International Publishing. https://doi.org/10.1007/978-3-030-26827-5_2

Bonacci, O., Ljubenkov, I., & Roje-Bonacci, T. (2006). Karst flash floods: an example from the Dinaric karst (Croatia). *Natural Hazards and Earth System Sciences*, *6*(2), 195–203. https://doi.org/10.5194/nhess-6-195-2006

Bos, M. S., & Scherneck, H.-G. (2013). Computation of Green's Functions for Ocean Tide Loading. In G. Xu (Ed.), *Sciences of Geodesy - II* (pp. 1–52). Berlin, Heidelberg: Springer Berlin Heidelberg. https://doi.org/10.1007/978-3-642-28000-9_1

Boy, J.-P., Rosat, S., Hinderer, J., & Littel, F. (2017). Superconducting Gravimeter Data from Djougou - Level 1 [Data set]. GFZ Data Services. https://doi.org/10.5880/IGETS.DJ.L1.001

Braitenberg, C. (2015). Exploration of tectonic structures with GOCE in Africa and across-continents. *International Journal of Applied Earth Observation and Geoinformation*, *35*, 88–95. https://doi.org/10.1016/j.jag.2014.01.013

Braitenberg, C., Sampietro, D., Pivetta, T., Zuliani, D., Barbagallo, A., Fabris, P., et al. (2016). Gravity for Detecting Caves: Airborne and Terrestrial Simulations Based on a Comprehensive Karstic Cave Benchmark. *Pure and Applied Geophysics*, *173*(4), 1243–1264. https://doi.org/10.1007/s00024-015-1182-y

Braitenberg, C., Pivetta, T., Barbolla, D. F., Gabrovšek, F., Devoti, R., & Nagy, I. (2019). Terrain uplift due to natural hydrologic overpressure in karstic conduits. *Scientific Reports*, *9*(1). https://doi.org/10.1038/s41598-019-38814-1

Calvo Garcia-Maroto, M. (2015). *Analysis of long-term gravity records in Europe; consequences for the retrieval of small amplitude and low frequency signals including the Earth's core resonance effects.* (Universidad Complutense de Madrid Université de Strasbourg). Retrieved from http://hdl.handle.net/10261/116033

Carrère, L., Lyard, F., Cancet, M., Guillot, A., & Picot, N. (2016). FES 2014, a new tidal model—Validation results and perspectives for improvements. *Proceedings of the ESA Living Planet Symposium 2016,Prague, Czech Republic, 9–13 May 2016.*

Casagrande, G., & Zini, L. (2004). Variazioni del livello delle acque al fondo della grotta Lindner (829/3988 VG) in relazione alle piene del Timavo. *Atti e Memorie Della Commissione Grotte "E. Boegan," 40*, 37–44.

Chen, X., Kroner, C., Sun, H., Abe, M., Zhou, J., Yan, H., & Wziontek, H. (2009). Determination of gravimetric parameters of the gravity pole tide using observations recorded with superconducting gravimeters. *Journal of Geodynamics*, *48*(3–5), 348–353. https://doi.org/10.1016/j.jog.2009.09.020

Chen, Z., Auler, A. S., Bakalowicz, M., Drew, D., Griger, F., Hartmann, J., et al. (2017). The World Karst Aquifer Mapping project: concept, mapping procedure and map of Europe. *Hydrogeology Journal*, *25*(3), 771–785. https://doi.org/10.1007/s10040-016-1519-3

Christiansen, L., Binning, P. J., Rosbjerg, D., Andersen, O. B., & Bauer-Gottwein, P. (2011). Using time-lapse gravity for groundwater model calibration: An application to alluvial aquifer storage: TIME-LAPSE GRAVITY FOR MODEL CALIBRATION. *Water Resources Research*, *47*(6). https://doi.org/10.1029/2010WR009859

Codiga, D. L. (2011). Unified Tidal Analysis and Prediction Using the UTide Matlab Functions.Technical Report 2011-01. Graduate School of Oceanography, University of Rhode Island, Narragansett, RI.

Courant, R., Friedrichs, K., & Lewy, H. (1967). On the Partial Difference Equations of Mathematical Physics. *IBM Journal of Research and Development*, *11*(2), 215–234. https://doi.org/10.1147/rd.112.0215

Creutzfeldt, B., Güntner, A., Klügel, T., & Wziontek, H. (2008). Simulating the influence of water storage changes on the superconducting gravimeter of the Geodetic Observatory Wettzell, Germany. *GEOPHYSICS*, *73*(6), WA95–WA104. https://doi.org/10.1190/1.2992508

Crossley, D. J., Jensen, O. G., & Hinderer, J. (1995). Effective barometric admittance and gravity residuals. *Physics of the Earth and Planetary Interiors*, *90*(3–4), 221–241. https://doi.org/10.1016/0031-9201(95)05086-Q

Dehant, V., Defraigne, P., & Wahr, J. M. (1999). Tides for a convective Earth. *Journal of Geophysical Research: Solid Earth*, *104*(B1), 1035–1058. https://doi.org/10.1029/1998JB900051

Deville, S., Jacob, T., Chéry, J., & Champollion, C. (2013). On the impact of topography and building mask on time varying gravity due to local hydrology. *Geophysical Journal International*, *192*(1), 82–93. https://doi.org/10.1093/gji/ggs007

Devoti, R., Zuliani, D., Braitenberg, C., Fabris, P., & Grillo, B. (2015). Hydrologically induced slope deformations detected by GPS and clinometric surveys in the Cansiglio Plateau, southern Alps. *Earth and Planetary Science Letters*, *419*, 134–142. https://doi.org/10.1016/j.epsl.2015.03.023

Donatini, L., Lupieri, G., Contento, G., Feudale, L., Pedronicini, A., Cusati, L., & Crosta, A. (2015). A high resolution wind and wave forecast model chain for the Mediterranean & Adriatic Sea. In *Towards Green Marine Technology and Transport* (Tayor and Francis). London: Guedes Soares, Dejhalla and Pavletic.

Dreybrodt, W., Gabrovšek, F., & Romanov, D. (2005). *Processes of a Speleogenessis [sic]: A Modeling Approach* (Založba ZRC, Vol. 4).

Ducarme, B., & Schüller, K. (2018). Canonical wave grouping as the key to optimal tidal analysis. *Bulletin d'Informations Des Marees Terrestres (BIM)*, *150*, 12131–12244.

Ducarme, B., Rosat, S., Vandercoilden, L., Jian-Qiao, X., & Heping, S. (2008). European Tidal Gravity Observations: Comparison With Earth Tide Models And Estimation Of The Free Core Nutation (Fcn) Parameters. In M. G. Sideris (Ed.), *Observing our Changing Earth* (Vol. 133, pp. 523–532). Berlin, Heidelberg: Springer Berlin Heidelberg. https://doi.org/10.1007/978-3-540-85426-5_62

Ebbing, J., Haas, P., Ferraccioli, F., Pappa, F., Szwillus, W., & Bouman, J. (2018). Earth tectonics as seen by GOCE - Enhanced satellite gravity gradient imaging. *Scientific Reports*, *8*(1), 16356. https://doi.org/10.1038/s41598-018-34733-9

Farrell, W. E. (1972). Deformation of the Earth by surface loads. *Reviews of Geophysics*, *10*(3), 761. https://doi.org/10.1029/RG010i003p00761

Ford, D., & Williams, P. (2007). *Karst Hydrogeology and Geomorphology*. John Wiley & Sons,Chichester, England.

Fores, B., Champollion, C., Le Moigne, N., Bayer, R., & Chéry, J. (2017). Assessing the precision of the iGrav superconducting gravimeter for hydrological models and karstic hydrological process identification. *Geophysical Journal International*, *208*(1), 269–280. https://doi.org/10.1093/gji/ggw396

Fores, Benjamin, Klein, G., Le Moigne, N., & Francis, O. (2019). Long-Term Stability of Tilt-Controlled gPhoneX Gravimeters. *Journal of Geophysical Research: Solid Earth*, *124*(11), 12264–12276. https://doi.org/10.1029/2019JB018276

Forzieri, G., Pecchi, M., Girardello, M., Mauri, A., Klaus, M., Nikolov, C., et al. (2020). A spatially explicit database of wind disturbances in European forests over the period 2000–2018. *Earth System Science Data*, *12*(1), 257–276. https://doi.org/10.5194/essd-12-257-2020

Gabrovšek, F., & Peric, B. (2006). Monitoring the Flood Pulses in the Epiphreatic Zone of Karst Aquifers: The Case of Reka River System, Karst Plateau, SW Slovenia. *Acta Carsologica*, *35*(1). https://doi.org/10.3986/ac.v35i1.241

Gabrovšek, F., Knez, M., Kogovšek, J., Mihevc, A., Mulec, J., Otoničar, B., et al. (2015a). Caves. In M. Knez, M. Petrič, T. Slabe, & S. Šebela (Eds.), *The Beka-Ocizla Cave System* (pp. 23–48). Cham: Springer International Publishing. https://doi.org/10.1007/978-3-319-04456-9_3

Gabrovšek, F., Knez, M., Kogovšek, J., Mihevc, A., Mulec, J., Otoničar, B., et al. (2015b). Karst Waters. In M. Knez, M. Petrič, T. Slabe, & S. Šebela (Eds.), *The Beka-Ocizla Cave System* (pp. 49–71). Cham: Springer International Publishing. https://doi.org/10.1007/978-3-319-04456-9_4

Gabrovšek, F., Peric, B., & Kaufmann, G. (2018a). Hydraulics of epiphreatic flow of a karst aquifer. *Journal of Hydrology*, *560*, 56–74. https://doi.org/10.1016/j.jhydrol.2018.03.019

Gabrovšek, F., Peric, B., & Kaufmann, G. (2018b). Hydraulics of epiphreatic flow of a karst aquifer. *Journal of Hydrology*, *560*, 56–74. https://doi.org/10.1016/j.jhydrol.2018.03.019

Goldscheider, N., & Drew, D. (2014). *Methods in karst hydrogeology*. Retrieved from https://nls.ldls.org.uk/welcome.html?ark:/81055/vdc_100058316053.0x000001

Gross, R. S. (1992). Correspondence between theory and observations of polar motion. *Geophysical Journal International*, *109*(1), 162–170. https://doi.org/10.1111/j.1365-246X.1992.tb00086.x

Güntner, A., Reich, M., Mikolaj, M., Creutzfeldt, B., Schroeder, S., & Wziontek, H. (2017). Landscape-scale water balance monitoring with an iGrav superconducting gravimeter in a field enclosure. *Hydrology and Earth System Sciences*, *21*(6), 3167–3182. https://doi.org/10.5194/hess-21-3167-2017

Hartmann, T., & Wenzel, H.-G. (1995). The HW95 tidal potential catalogue. *Geophysical Research Letters*, *22*(24), 3553–3556. https://doi.org/10.1029/95GL03324

Hinderer, J., Crossley, D., & Warburton, R. J. (2007). Gravimetric Methods-Superconducting Gravity Meters. *Treatsie in Geophysics: Geodesy*, 65–122.

Jacob, T., Bayer, R., Chery, J., Jourde, H., Moigne, N. L., Boy, J.-P., et al. (2008). Absolute gravity monitoring of water storage variation in a karst aquifer on the larzac plateau (Southern France). *Journal of Geophysical Research: Solid Earth*, 13.

Jacob, T., Chery, J., Bayer, R., Moigne, N. L., Boy, J.-P., Vernant, P., & Boudin, F. (2009). Time-lapse surface to depth gravity measurements on a karst system reveal the dominant role of the epikarst as a water storage entity, 14.

Jacob, T., Bayer, R., Chery, J., & Le Moigne, N. (2010). Time-lapse microgravity surveys reveal water storage heterogeneity of a karst aquifer. *Journal of Geophysical Research*, *115*(B6). https://doi.org/10.1029/2009JB006616

Jentzsch, G., Schulz, R., & Weise, A. (2018). Automated Burris gravity meter for single and continuous observation. *Geodesy and Geodynamics*, *9*(3), 204–209. https://doi.org/10.1016/j.geog.2017.09.007

Jurkovšek, B., Biolchi, S., Furlani, S., Kolar-Jurkovšek, T., Zini, L., Jež, J., et al. (2016). Geology of the Classical Karst Region (SW Slovenia–NE Italy). *Journal of Maps*, *12*(sup1), 352–362. https://doi.org/10.1080/17445647.2016.1215941

Karbon, M., Böhm, J., Meurers, B., & Schuh, H. (2014). Atmospheric Corrections for Superconducting Gravimeters Using Operational Weather Models. In C. Rizos & P. Willis (Eds.), *Earth on the Edge: Science for a Sustainable Planet* (Vol. 139, pp. 421–427). Berlin, Heidelberg: Springer Berlin Heidelberg. https://doi.org/10.1007/978-3-642-37222-3_56

Kaufmann, G., Gabrovšek, F., & Turk, J. (2016). Modelling flow of subterranean Pivka river in Postojnska jama, Slovenia. *Acta Carsologica*, *45*(1). https://doi.org/10.3986/ac.v45i1.3059

Kennedy, J., Ferré, T. P. A., & Creutzfeldt, B. (2016). Time-lapse gravity data for monitoring and modeling artificial recharge through a thick unsaturated zone: *Water Resources Research*, *52*(9), 7244–7261. https://doi.org/10.1002/2016WR018770

Klügel, T., & Wziontek, H. (2009). Correcting gravimeters and tiltmeters for atmospheric mass attraction using operational weather models. *Journal of Geodynamics*, *48*(3–5), 204–210. https://doi.org/10.1016/j.jog.2009.09.010

Kobe, M., Gabriel, G., Weise, A., & Vogel, D. (2019). Time-lapse gravity and levelling surveys reveal mass loss and ongoing subsidence in the urban subrosion-prone area of Bad Frankenhausen, Germany. *Solid Earth*, *10*(3), 599–619. https://doi.org/10.5194/se-10-599-2019

Lau, H. C. P., Mitrovica, J. X., Davis, J. L., Tromp, J., Yang, H.-Y., & Al-Attar, D. (2017). Tidal tomography constrains Earth's deep-mantle buoyancy. *Nature*, *551*(7680), 321–326. https://doi.org/10.1038/nature24452

Llubes, M., Florsch, N., Hinderer, J., Longuevergne, L., & Amalvict, M. (2004). Local hydrology, the Global Geodynamics Project and CHAMP/GRACE perspective: some case studies. *Journal of Geodynamics*, *38*(3–5), 355–374. https://doi.org/10.1016/j.jog.2004.07.015

Longuevergne, L., Boy, J. P., Florsch, N., Viville, D., Ferhat, G., Ulrich, P., et al. (2009). Local and global hydrological contributions to gravity variations observed in Strasbourg. *Journal of Geodynamics*, *48*(3–5), 189–194. https://doi.org/10.1016/j.jog.2009.09.008

Longuevergne, L., Florsch, N., Boudin, F., Oudin, L., & Camerlynck, C. (2009). Tilt and strain deformation induced by hydrologically active natural fractures: application to the tiltmeters installed in Sainte-Croix-aux-Mines observatory (France). *Geophysical Journal International*, *178*(2), 667–677. https://doi.org/10.1111/j.1365-246X.2009.04197.x

Love, A. (1909). The yielding of the earth to disturbing forces. *Proceedings of the Royal Society of London. Series A, Containing Papers of a Mathematical and Physical Character*, *82*(551), 73–88. https://doi.org/10.1098/rspa.1909.0008

Matsuo, K., & Heki, K. (2010). Time-variable ice loss in Asian high mountains from satellite gravimetry. *Earth and Planetary Science Letters*, 7.

Mayaud, C., Gabrovšek, F., Blatnik, M., Kogovšek, B., Petrič, M., & Ravbar, N. (2019). Understanding flooding in poljes: A modelling perspective. *Journal of Hydrology*, *575*, 874–889. https://doi.org/10.1016/j.jhydrol.2019.04.092

Melchior, P. J. (1983). *The tides of the planet earth* (2nd ed). Oxford [Oxfordshire] ; New York: Pergamon Press.

Merriam, J. B. (1992). Atmospheric pressure and gravity. *Geophysical Journal International*, *109*(3), 488–500. https://doi.org/10.1111/j.1365-246X.1992.tb00112.x

Meurers, B., Van Camp, M., & Petermans, T. (2007). Correcting superconducting gravity time-series using rainfall modelling at the Vienna and Membach stations and application to Earth tide analysis. *Journal of Geodesy*, *81*(11), 703–712. https://doi.org/10.1007/s00190-007-0137-1

Meurers, B., Papp, G., Ruotsalainen, H., Benedek, J., & Leonhardt, R. (2021). Hydrological signals in tilt and gravity residuals at Conrad Observatory (Austria). *Hydrology and Earth System Sciences*, *25*(1), 217–236. https://doi.org/10.5194/hess-25-217-2021

Middlemiss, R. P., Samarelli, A., Paul, D. J., Hough, J., Rowan, S., & Hammond, G. D. (2016). Measurement of the Earth tides with a MEMS gravimeter. *Nature*, *531*(7596), 614–617. https://doi.org/10.1038/nature17397

Mikolaj, M., Meurers, B., & Güntner, A. (2016). Modelling of global mass effects in hydrology, atmosphere and oceans on surface gravity. *Computers & Geosciences*, *93*, 12–20. https://doi.org/10.1016/j.cageo.2016.04.014

Mikolaj, M., Reich, M., & Güntner, A. (2019). Resolving Geophysical Signals by Terrestrial Gravimetry: A Time Domain Assessment of the Correction-Induced Uncertainty. *Journal of Geophysical Research: Solid Earth*, *124*(2), 2153–2165. https://doi.org/10.1029/2018JB016682

Mikolaj, Michal, Meurers, B., & Mojzeš, M. (2015). The reduction of hydrology-induced gravity variations at sites with insufficient hydrological instrumentation. *Stud. Geophys. Geod.*, 14.

Mouyen, M., Longuevergne, L., Chalikakis, K., Mazzilli, N., Ollivier, C., Rosat, S., et al. (2019). Monitoring of groundwater redistribution in a karst aquifer using a superconducting gravimeter. *E3S Web of Conferences*, *88*, 03001. https://doi.org/10.1051/e3sconf/20198803001

Mouyen, M., Steer, P., Chang, K.-J., Le Moigne, N., Hwang, C., Hsieh, W.-C., et al. (2020). Quantifying sediment mass redistribution from joint time-lapse gravimetry and photogrammetry surveys. *Earth Surface Dynamics*, *8*(2), 555–577. https://doi.org/10.5194/esurf-8-555-2020

Nagy, D., Papp, G., & Benedek, J. (2000). The gravitational potential and its derivatives for the prism. *Journal of Geodesy*, *74*(7–8), 552–560. https://doi.org/10.1007/s001900000116

Oreiro, F. A., Wziontek, H., Fiore, M. M. E., D'Onofrio, E. E., & Brunini, C. (2018). Non-Tidal Ocean Loading Correction for the Argentinean-German Geodetic Observatory Using an Empirical Model of Storm Surge for the Río de la Plata. *Pure and Applied Geophysics*, *175*(5), 1739–1753. https://doi.org/10.1007/s00024-017-1651-6

Peterson, J. (1993). Observations and Modelling of Seismic Background Noise.Open-File Report 93–332. U.S. Department of Interior, Geological Survey.

Petrič, M., & Kogovšek, J. (2016). Identifying the characteristics of groundwater flow in the Classical Karst area (Slovenia/Italy) by means of tracer tests. *Environmental Earth Sciences*, *75*(22). https://doi.org/10.1007/s12665-016-6255-4

Petrič, M., Ravbar, N., Zini, L., Calligaris, C., Corazzi, R., Žitko, Z., et al. (2020). Determining the directions and characteristics of underground water flow in karst for the purpose of traffic routes construction: the case of the new Divača-Koper railway line (SW Slovenia). *Acta Carsologica*, *49*(1). https://doi.org/10.3986/ac.v49i1.8582

Piccolroaz, S., Majone, B., Palmieri, F., Cassiani, G., & Bellin, A. (2015). On the use of spatially distributed, time-lapse microgravity surveys to inform hydrological modeling: MICROGRAVITY AND HYDROLOGICAL MODELING. *Water Resources Research*, *51*(9), 7270–7288. https://doi.org/10.1002/2015WR016994

Pivetta, T., & Braitenberg, C. (2015). Laser-scan and gravity joint investigation for subsurface cavity exploration — The Grotta Gigante benchmark. *GEOPHYSICS*, *80*(4), B83–B94. https://doi.org/10.1190/geo2014-0601.1

Placer, L., Vrabec, M., & Celarc, B. (2010). The bases for understanding of the NW Dinarides and Istria Peninsula tectonics. *Geologija*, *53*(1), 55–86. https://doi.org/10.5474/geologija.2010.005

Portier, N., Hinderer, J., Riccardi, U., Ferhat, G., Calvo, M., Abdelfettah, Y., et al. (2018). Hybrid gravimetry monitoring of Soultz-sous-Forêts and Rittershoffen geothermal sites (Alsace, France). *Geothermics*, *76*, 201–219. https://doi.org/10.1016/j.geothermics.2018.07.008

Reich, M., Mikolaj, M., Blume, T., & Güntner, A. (2019). Reducing gravity data for the influence of water storage variations beneath observatory buildings. *GEOPHYSICS*, *84*(1), EN15–EN31. https://doi.org/10.1190/geo2018-0301.1

Rodell, M., Houser, P. R., Jambor, U., Gottschalck, J., Mitchell, K., Meng, C.-J., et al. (2004). The Global Land Data Assimilation System. *Bulletin of the American Meteorological Society*, *85*(3), 381–394. https://doi.org/10.1175/BAMS-85-3-381

Rosat, S., & Hinderer, J. (2018). Limits of Detection of Gravimetric Signals on Earth. *Scientific Reports*, *8*(1), 15324. https://doi.org/10.1038/s41598-018-33717-z

Rosat, S., Escot, B., Hinderer, J., & Boy, J.-P. (2017). Analyses of a 426-Day Record of Seafloor Gravity and Pressure Time Series in the North Sea. *Pure and Applied Geophysics*. https://doi.org/10.1007/s00024-017-1554-6

Rosat, S., Lambert, S. B., Gattano, C., & Calvo, M. (2017). Earth's core and inner-core resonances from analysis of VLBI nutation and superconducting gravimeter data. *Geophysical Journal International*, *208*(1), 211–220. https://doi.org/10.1093/gji/ggw378

Rossman, L. (2017). Storm Water Management Model Reference Manual Volume II – Hydraulics. U.S. Environmental Protection Agency. Washington, DC, EPA/600/R-17/111, 2017. Retrieved from https://cfpub.epa.gov/si/si_public_record_report.cfm?Lab=NRMRL&dirEntryId=337162

Rožič, P. Ž., Čar, J., & Rožič, B. (2015). Geological Structure of the Divača Area and its Influence on the Speleogenesis and Hydrogeology of Kačna jama, 16.

Sambridge, M. (1999). Geophysical inversion with a neighbourhood algorithm-I. Searching a parameter space. *Geophysical Journal International*, *138*(2), 479–494. https://doi.org/10.1046/j.1365-246X.1999.00876.x

Schüller, K. (2015). ET34-X-V73 Program System for Earth Tide Analysis and Prediction. Retrieved from software and manual at http://ggp.bkg.bund.de/eterna

Schulz, H. R. (2018). A new PC control software for ZLS-Burris gravity meters. *Geodesy and Geodynamics*, *9*(3), 210–219. https://doi.org/10.1016/j.geog.2017.09.002

Šebela, S. (2009). Structural geology of the Škocjan Caves. *Acta Carsologica*, *38*(2–3), 165–177.

Tapley, B. D., Chambers, D. P., Bettadpur, S., & Ries, J. C. (2003). Large scale ocean circulation from the GRACE GGM01 Geoid: LARGE SCALE OCEAN CIRCULATION. *Geophysical Research Letters*, *30*(22). https://doi.org/10.1029/2003GL018622

Taylor, R. G., Scanlon, B., Döll, P., Rodell, M., van Beek, R., Wada, Y., et al. (2013). Ground water and climate change. *Nature Climate Change*, *3*(4), 322–329. https://doi.org/10.1038/nclimate1744

Tenze, D., Braitenberg, C., & Nagy, I. (2012). Karst Deformations Due To Environmental Factors: evidences from the horizontal pendulums of Grotta Gigante, Italy. *Boll. Geofis. Teor. Appl.*, *53*(3), 331–345. https://doi.org/10.4430/bgta0049

Thomas, B. F., & Famiglietti, J. S. (2019). Identifying Climate-Induced Groundwater Depletion in GRACE Observations. *Scientific Reports*, *9*(1), 4124. https://doi.org/10.1038/s41598-019-40155-y

Uieda, L., Barbosa, V. C. F., & Braitenberg, C. (2016). Tesseroids: Forward-modeling gravitational fields in spherical coordinates. *GEOPHYSICS*, *81*(5), F41–F48. https://doi.org/10.1190/geo2015-0204.1

Van Camp, Michael, Meus, P., Quinif, Y., Kaufmann, O., van Ruymbeke, M., Vandiepenbeck, M., & Camelbeeck, T. (2006). Karst aquifer investigation using absolute gravity. *Eos, Transactions American Geophysical Union*, *87*(30), 298. https://doi.org/10.1029/2006EO300005

Van Camp, Michel, & Vauterin, P. (2005). Tsoft: graphical and interactive software for the analysis of time series and Earth tides. *Computers & Geosciences*, *31*(5), 631–640. https://doi.org/10.1016/j.cageo.2004.11.015

Van Camp, Michel, de Viron, O., Pajot-Métivier, G., Casenave, F., Watlet, A., Dassargues, A., & Vanclooster, M. (2016). Direct measurement of evapotranspiration from a forest using a superconducting gravimeter: EVAPOTRANSPIRATION AND GRAVITY. *Geophysical Research Letters*, *43*(19), 10,225-10,231. https://doi.org/10.1002/2016GL070534

Van Camp, Michel, de Viron, O., Watlet, A., Meurers, B., Francis, O., & Caudron, C. (2017). Geophysics From Terrestrial Time-Variable Gravity Measurements: Time-Variable Gravity Measurements. *Reviews of Geophysics*, *55*(4), 938–992. https://doi.org/10.1002/2017RG000566

Virtanen, H. (2004). Loading effects in Metsa¨hovi from the atmosphere and the Baltic Sea. *Journal of Geodynamics*, 16.

Wahr, J., Molenaar, M., & Bryan, F. (1998). Time variability of the Earth's gravity field: Hydrological and oceanic effects and their possible detection using GRACE. *Journal of Geophysical Research: Solid Earth*, *103*(B12), 30205–30229. https://doi.org/10.1029/98JB02844

Warburton, R. J., & Goodkind, J. M. (1977). The influence of barometric-pressure variations on gravity. *Geophysical Journal International*, *48*(3), 281–292. https://doi.org/10.1111/j.1365-246X.1977.tb03672.x

Watlet, A., Van Camp, M., Francis, O., Poulain, A., Rochez, G., Hallet, V., et al. (2020). Gravity Monitoring of Underground Flash Flood Events to Study Their Impact on Groundwater Recharge and the Distribution of Karst Voids. *Water Resources Research*, *56*(4). https://doi.org/10.1029/2019WR026673

Weise, A., & Jahr, Th. (2017). The Improved Hydrological Gravity Model for Moxa Observatory, Germany. *Pure and Applied Geophysics*. https://doi.org/10.1007/s00024-017-1546-6

Wenzel, H.-G. (1996). The nanogal software: earth tide data preprocessing package. *Bull. Inf. Marées Terrestres*, *124*, 9425–9439.

White, W. B. (2002). Karst hydrology: recent developments and open questions. *Engineering Geology*, *65*(2–3), 85–105. https://doi.org/10.1016/S0013-7952(01)00116-8

Yi, S., Freymueller, J. T., & Sun, W. (2016). How fast is the middle-lower crust flowing in eastern Tibet? A constraint from geodetic observations: FLOW IN EASTERN TIBET. *Journal of Geophysical Research: Solid Earth*, *121*(9), 6903–6915. https://doi.org/10.1002/2016JB013151

Zaccagnino, D., Vespe, F., & Doglioni, C. (2020). Tidal modulation of plate motions. *Earth-Science Reviews*, *205*, 103179. https://doi.org/10.1016/j.earscirev.2020.103179

Zini, L., Calligaris, C., & Zavagno, E. (2014). Classical Karst hydrodynamics: a shared aquifer within Italy and Slovenia. *Proceedings of the International Association of Hydrological Sciences*, *364*, 499–504. https://doi.org/10.5194/piahs-364-499-2014